Photophysical properties of bi- and multichromophoric supramolecule-based systems

Sergey Denisov

université de BORDEAUX

THÈSE PRÉSENTÉE

POUR OBTENIR LE GRADE DE

DOCTEUR DE

L'UNIVERSITÉ DE BORDEAUX

ÉCOLE DOCTORALE DES SCIENCES PHYSIQUES ET DE L'INGÉNIEUR (SP1)

LASERS, MATIÈRE ET NANOSCIENCES

Sergey Alexandrovich DENISOV

Propriétés photophysiques des systèmes supramoléculaires bi- et multichromophoriques

Photophysical properties of bi- and multichromophoric supramolecule-based systems

Sous la direction de : Dr. Gediminas JONUSAUSKAS
(co-directeur : Dr. Nathan D. MCCLENAGHAN)

Soutenue le: 13 novembre 2014

Membres de jury :

M. OBERLÉ, Jean	Université de Bordeaux	Président
Mme. FEDOROVA, Olga A.	INEOS RAS	Rapporteur
M. BEEBY, Andrew	Durham University	Rapporteur
M. LIMA, João Carlos	Universidade NOVA de Lisboa	Examinateur
M. JONUSAUSKAS, Gediminas	Université de Bordeaux	Directeur
M. MCCLENAGHAN, Nathan D.	Université de Bordeaux	Co-directeur

Titre : Propriétés photophysiques des systèmes supramoléculaires bi- et multichromophoriques

Résumé : En utilisant les spectroscopies d'absorption UV-vis et d'émission stationnaire et résolue dans le temps (femto- et sub–nanoseconde, caméra à balayage de fente), nous avons étudié, au cours de cette thèse, les processus photophysiques au sein de différentes molécules et supramolécules. Les propriétés photophysiques de nouveaux complexes de Ru(II) polypyridine et de Ir(III) cyclométallé présentant un transfert d'énergie électronique réversible entre le noyau métallique et les chromophores organiques auxiliaires énergétiquement appariés (anthracène et pyrène) ont été analysées en détail. Les caractéristiques de la séparation de charge entre un donneur d'électron (OPV) et un accepteur (PB) à travers un pont d'oligoquinoline au sein de foldamères de longueurs croissantes ont été précisées dans une échelle de temps inférieure à la nanoseconde. De nouvelles sondes luminescentes à base de lanthanides ont été réalisées pour la détection en temps réel de l'ion Cu(I), leurs propriétés optiques étant modulées par effet «d'antenne» par le biais d'interactions cations-nuage π. L'étude de sondes fluorescentes off-on en proche IR formées de colorants BF_2-AzaBODIPY fixés de manière covalente sur des nanoparticules (100 nm) polymériques a été réalisée, et étendue à de nouvelles sondes sensibles au pH émettant dans le proche IR. Des études de photoisomérisation ont été effectuées sur deux systèmes azobenzéniques capables de libérer/capturer des ions Ca(II) (azobenzène-éther «lasso», azobenzène-BAPTA) – l'impact de l'eau sur la photoisomérisation *cis-trans* d'hydroxychalcones a été mis en évidence dans CH_3CN et H_2O/CH_3OH (v/v=1/1).

Mots clés : Transfert d'électron photo-induit, transfert d'énergie électronique, photoisomerization, absorption transitoire, émission résolue dans le temps

---

Title: Photophysical properties of bi- and multichromophoric supramolecule-based systems

Abstract: In the present work photophysical processes of different molecular and supramolecular systems were studied using steady-state and time-resolved femto- and sub-nanosecond (streak-camera detection) UV-vis absorption and emission spectroscopies. Detailed photophysical studies of novel Ru(II) polypyridine and cyclometalated Ir(III) complexes showing reversible electronic energy transfer between metallic core and auxiliary organic energetically-matched chromophores anthracene and pyrene, respectively were performed. Time-resolved characterization of charge separation between electron donor (OPV) and acceptor (PB) in the sub-nanosecond timescale through an oligoquinoline bridge in foldamers of increasing oligomeric length was carried out. Novel lanthanide-based luminescent probes were investigated for time-gated detection of Cu(I) ion, being modulated by an antenna effect through cation-π interactions. The study on NIR fluorescent *off-on* probes, based on BF_2-aza-BODIPY dyes, covalently attached to the surface of polystyrene 100 nm nanoparticles, along with related novel NIR pH-responsive fluorescence probes were conducted. Photoisomerization studies focused on azobenzene-based (azobenzene-lariat ether, azobenzene-BAPTA) Ca(II)-ion release/capture systems, while the impact of water on the *cis−trans* photoisomerization of hydroxychalcones was studied in CH_3CN and H_2O/CH_3OH (v/v=1/1).

Key words: Photoinduced electron transfer, electronic energy transfer, photoisomerization, transient absorption, time-resolved emission

---

Unité de recherche

[Laboratoire Ondes et Matière d'Aquitaine Université de Bordeaux, UMR CNRS 5798 351 cours de la Liberation, 33405 Talence, France]

Dedicated to my beloved family.

Preface

Ce que nous connaissons est **peu de chose**, ce que nous ignorons est **immense**.

French mathematician and astronomer,
Pierre-Simon de Laplace (1749–1827)

Il piacere della vita è imparare.

Italian scholar and poet, Francesco Petrarca
(1304–1374)

This PhD thesis at the beginning, in 2011, appeared to be the first and the only one. But I made an effort, sat and analyzed results of 6 years of work devoted to the study of nanodiamonds' chemical surface modification and its electrophysical (conductivity and dielectric permability) properties. The output of it was my first PhD thesis in physical-chemistry [1][1].

Writing the manuscript was a hard, but interesting and cognitive time for me. Even so this work is my second PhD thesis, it is also very important for me. If it is appropriate to compare: the first thesis was as firstborn child – long waited and desirable, second one is accompanied by a more mature emotions, without any false expectations from it and thus more valuable.

[1] It could be downloaded from https://www.researchgate.net/profile/Sergey_Denisov2/publications/. Date of defence 7.11.2013, Frumkin Institute of physical chemistry and electrochemistry RAS, Moscow, Russia.

Acknowledgments

I wish to express my grateful acknowledgement to all the people who helped me during the work on the dissertation.

I believe I am truly lucky person if both of my research supervisors: Dr. Gediminas Jonusauskas and Dr. Nathan D. Mcclenaghan are people of rare tenderness and humanity, not only willing to help in the resolution of experimental problems, but also for solving everyday problems of ”Russian in France”.

I am grateful to my colleagues in the laboratory and University: Dr. Luca Scarpantonio, Dr. Ivan Veshchunov, Arnaud Tron, Guillaume Raffy, Dr. Peter Verwilst, Dr. Robin Bofinger for their advices and suggestions in setting up experiments.

I would like to express my gratitude to French ministry of education for financing this research (Ministère de l’Éducation nationale – Bourse qualité recherche), as well as Université de Bordeaux for providing good working conditions.

Apart of said I would like say my tender thanks to my family for their patience and love.

Résumé

1 Introduction

Les propriétés photophysiques de systèmes moléculaires et supramoléculaires (émission de lumière, absorption électronique spécifique, transfert de charge et d'énergie) mettent souvent en jeu des interactions avec l'environnement ou entre sous-unités moléculaires. En portant, suite à l'absorption d'un photon, ces systèmes (supra)moléculaires à l'état excité de telles interactions peuvent être modifiées ou déclenchées.

Les chercheurs s'intéressent principalement à cinq phénomènes distincts qui permettent la modélisation d'édifice moléculaires / supramoléculaires de types différents : organique, inorganique, les systèmes biomimétiques photoactifs pour *in fine* améliorer les systèmes existants. Ces phénomènes sont énumérés ci-dessous :

1. Formation de liaison photoinduite ou de liaison thermique réversible :
   - Cyclisation thermique ou photocyclisation ;
   - Réactions thermiques ou photoactivées ;
   - ...
2. Transfert d'Électron Photoinduit (TEP) ;
3. Transfert d'Énergie Électronique (TEE) ;
4. Transfert d'Énergie Électronique Réversible (TEER) ;
5. Isomérisation thermique ou photoisomérisation.

Au cours de nos recherches, nous allons nous intéresser à des systèmes moléculaires et supramoléculaires activés par la lumière qui ont été conçus en mettant à profit des processus différents (voir les éléments énumérés en italique). Nous allons examiner les processus photophysiques des systèmes sélectionnés. Dans le premier chapitre, les aspects fondamentaux de photophysique et de photochimie sont rappelés, ainsi que les techniques expérimentales utilisées pour étudier les processus photophysiques inhérents aux systèmes (supra)moléculaires.

Le deuxième chapitre est consacré au transfert d'énergie électronique réversible, qui a été utilisé pour prolonger considérablement la durée de vie d'émission de complexes de Ru(II) à base de ligands tridentates et de complexes cyclométallés de Ir(III), sans altérer les rendements quantiques de luminescence. Une nouvelle approche de l'utilisation du TEER est par ailleurs décrite. Elle permet remonter à la conformation et à la distance entre chromophores après interaction avec une deuxième espèce. Effectivement, pour contrôler l'efficacité du TEER dans le processus en fonction du degré de complexité illustré entre un foldamère récepteur à double hélice et un fil moléculaire invité.

Les processus de transfert d'énergie et d'électron photoinduit sont étudiés dans le troisième chapitre. Les processus de transfert d'énergie et d'électron photoinduit ont été abordés en tant que séparation de charge entre un donneur d'électrons (OPV) et un accepteur (PB) dans une échelle de temps inférieure à la nanoseconde, à travers un pont d'oligoquinoline dans des foldamères de tailles croissantes (9, 14, 19 unités dans l'oligomère), de 180 à 303 K. De nouvelles sondes luminescentes a effet «d'antenne» à base de lanthanide siège du transfert d'énergie, pour la détection de Cu^+ en temps réel et *in situ*, ont été explorées par le biais d'interactions cations-π.

Le quatrième chapitre décrit sur une gamme de systèmes moléculaires et supramoléculaires

photoactifs à plusieurs états. L'étude de sondes PIR fluorescentes «OFF-ON» a été effectuée sur des colorants aza-BODIPY, fixés de manière covalente à la surface de NP (copolymère(styrène/acide méthacrylique)) avec une taille caractéristique de 100 nm, présentant des réponses prononcées (fluorescence activée) en présence d'agents tensioactifs, tels que le Triton X-100 et le DOPC, ce dernier étant un phospholipide biologique. Des études photophysiques ont été réalisées sur les nouvelles sondes nanoscopiques à pH, basées sur une variante nitrée de molécules aza-BODIPY comprenant un site phénoxyde, qui pourraient être utilisées comme senseurs de pH adaptés à l'imagerie par fluorescence. Enfin, les processus de photoisomérisation pour les systèmes capture / libération d'ions à base d'azobenzène (azobenzène-éther lariat, azobenzène-BAPTA), ainsi que l'impact de l'eau sur la photo-isomérisation *cis-trans* d'hydroxychalcones dans CH_3CN et dans H_2O/CH_3OH (1/1, v/v) ont été étudiés à l'aide de mesures de spectroscopie d'absorption transitoire ultra-rapide.

2 Transfert d'énergie électronique réversible dans les systèmes supramoléculaires inorganiques

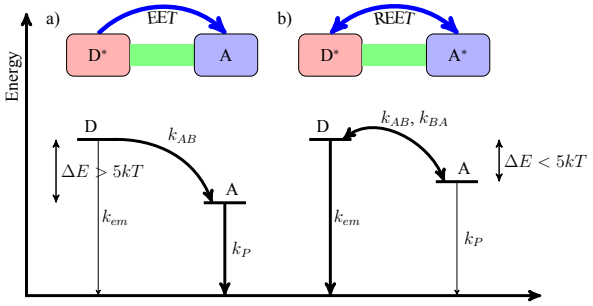

Figure I. Représentation schématique de complexes bichromophoriques et d'états excités dans l'architecture moléculaire «chromophore A-espaceur chromophore B» ; a) Transfert unidirectionnel d'énergie électronique (constant de vitesse, k_{AB}) à une sous-unité organique avec des chromophores énergiquement différent ; b) transfert d'énergie électronique réversible entre états excités énergiquement similaires.[2]

La gestion de l'énergie après absorption lumineuse est d'une importance fondamentale pour le développement de dispositifs optoélectroniques efficaces [3, 4], la séparation de charge et le stockage d'énergie sous forme d'énergie chimique. Les systèmes photosynthétiques naturels sont d'excellents exemples d'architectures complexes multiporphyrinique pouvant absorber l'énergie lumineuse, la transférer de façon unidirectionnelle vers un site distant pour conduire à un processus de transfert de charge et finalement transformer l'énergie lumineuse en énergie chimique via des processus multiélectroniques. En ce qui concerne le stockage temporaire d'énergie, il a été démontré récemment que dans les systèmes moléculaires à base de composants multiples, les procédés de transfert d'énergie réversible peuvent être utilisés [5, 6] pour stocker temporairement l'énergie d'excitation électronique au sein de la molécule, par exemple en donnant lieu à une émission retardée. Dans la littérature, ce processus est souvent désigné comme transfert d'énergie réversible ou transfert d'énergie électronique réversible (TEER).[5–8]

D'un point de vue énergétique, pour qu'un transfert d'énergie inter-chromophore réversible ait lieu (par exemple du chromophore A au chromophore B), plutôt qu'un transfert d'énergie unidirectionnel, les états excités les plus bas en énergie des deux chromophores doivent être mutuellement thermiquement accessibles (Figure I). La différence d'énergie (ΔE) entre ces états attenants ne doit généralement pas être supérieure à quelques kcal/mol ($\sim$ 0,1 eV) pour rendre le TEER efficace à température ambiante. Lorsque la différence d'énergie entre les deux états augmente, le taux de transfert retour d'énergie diminue jusqu'à ce qu'il devienne non-compétitif avec les autres processus, et que le TEER ne soit plus possible. Si la différence d'énergie entre les états interagissent est suffisamment faible pour permettre un repeuplement efficace des états émissifs, et si les transferts d'énergie sont beaucoup plus rapides que les voies de désexcitation, alors le rendement quantique d'émission du système bichromophorique sera comparable à celui de son précurseur.[2]

2.1 Complexes de Ru(II) et Ir(III) de luminescence à longue durée de vie

Il est bien connu que les principales propriétés des complexes de métaux de transition sont intimement liées aux aspects électroniques et stériques des ligands dans la sphère de coordination primaire, incluant les propriétés redox et l'absorption et l'émission de la lumière. En outre, dans les complexes supramoléculaires où des chromophores spatialement distincts sont introduits, ces derniers peuvent intervenir dans les propriétés photophysiques déterminantes, par exemple le transfert d'électron ou d'énergie.[9]

En ce qui concerne l'émission, le rendement quantique et la durée de vie de luminescence sont des caractéristiques importantes qui au final définissent l'applicabilité dans des architectures détectant et émettant de la lumière. Nous et d'autres avons déjà appliqué une approche en mettant à profit un processus de TEER entre paires de chromophores énergiquement appariés [6, 10, 11] présentant un comportement cinétique complémentaire, afin d'améliorer la performance de certains complexes de métaux luminescents sous-performants à base de Ru, Os, Cu et Re comme luminophores et agents photosensibilisants.[7, 12–18].

2.1.1 Complexes de Ru(II) [7]

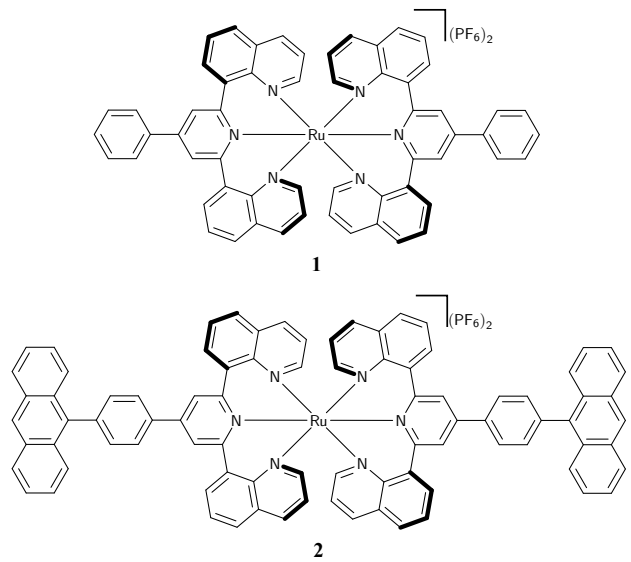

Figure II. Complexes sans- **1** et avec anthracène **2**.

Les complexes polypyridiniques de métaux de transition, et en particulier de Ru(II), ont été largement étudiés pour mieux comprendre et exploiter leurs processus d'absorption visible, redox et photochimiques [19] ; ils ont trouvé des applications dans divers domaines en tant que photosensibilisateurs, colorants, capteurs, diodes, catalyseurs ainsi qu'en nanotechnologies.[20–23] La modification des ligands est cruciale pour ajuster les nombreuses propriétés-clés des états excités de ces complexes, leur luminescence étant la plus étudiée (rendement quantique d'émission et durée de vie). Les ligands polypyridiniques se lient généralement d'une façon bidentate ou tridentate, conduisant des complexes de géométries, coordination et propriétés différentes. Ainsi, les ligands tridentates permettent d'accéder à des complexes de géométries 1D linéaires (barres et fils moléculaires), mais leurs propriétés luminescentes sont perturbées par les états du centre métallique thermiquement accessible qui diminuent l'intensité de la luminescence.[19]

Beaucoup d'attention a été portée sur la conception et la synthèse de nouveaux complexes Ru(II) aux propriétés d'émission améliorées (durée de vie prolongée et rendement quantique élevé). Les différentes approches sont basées sur des stratégies limitant les pertes par acti-

Tableau I. Propriétés photophysiques des complexes **1** et **2** dans l'acétonitrile.

complex	$\lambda_{em.}$, nm	Φ_{air} [a]	Φ_{degas} [a]	τ,[b] μs	τ_{eq},[c] ps
1	686	2.2×10^{-3}	1.3×10^{-2}	2.7 ± 0.3	–
2	686	4×10^{-4}	9.5×1.3^{-2}	42 ± 2	75

[a] Rendement quantique de luminescence.
[b] Durée de vie de luminescence.
[c] Durée de vie de processus de equilibrium.

vation thermique.[13, 24–26]

Une percée importante a été effectuée en remplaçant deux groupements pyridiniques externes du «terpy» par des quinoléines, donnant alors des complexes de ruthénium octaédriques à base de ligands tridentates plus émissifs, avec une durée de vie augmentée et dont le comportement photophysique a pu être rationalisé par le calcul.[26, 27]

Pour notre part, nous avons étudié en détail un nouveau complexe de Ru(II), produit par une modification structurale simple de ce dernier type de complexe (voir complexe de modèle **1** Figure II), impliquant l'intégration judicieuse d'un chromophore auxiliaire adapté[1], voir prototype **2** dans la Figure II, dans le but de donner accès à un complexe luminescent d'une durée de vie beaucoup plus longue, tout en conservant un rendement quantique d'émission similaire (Tableau I).

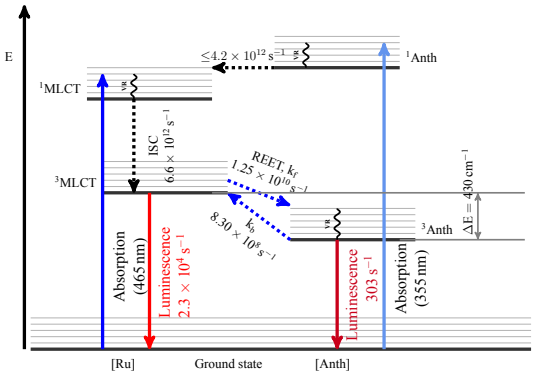

Figure III. Diagramme Perrin-Jablonski montrant les niveaux d'énergie pertinents et la cinétique du TEER et la luminescence retardée de **2**.

Le chromophore auxiliaire est prévu pour exercer le rôle souhaité tant que les paramètres énergétiques et cinétiques spécifiques sont respectés (le niveau du triplet organique introduit présente une désexcitation lente, et est quasi-isoénergétique avec l'état ^{3}MLCT émissif). En suivant ce cahier des charges, le TEER sera permis (Figure III) avec la sous-unité organique jouant le rôle de réservoir d'énergie, et l' émission provenant de la sous-unité métallique aura une durée de vie de luminescence prolongée. Les complexes bichromophoriques de Ru(II) à base de ligands tridentates offrent un environnement de coordination optimal qui, combiné avec un auxiliaire organique approprié, donnent des complexes à ligands tridentates avec des durées de vie de luminescence sans précédent ($\tau = 42\ \mu$s), sans modifier l'efficacité de l'émission. Les spectroscopies résolues dans le temps montrent qu'un équilibre à l'état excité est atteint en moins de 100 ps grâce au processus TEER, avec en moyenne 94 % d'énergie stockée sur le réservoir organique. Il est intéressant de noter que ce phénomène a été produit de façon prédéterminée en se basant sur une connaissance rudimentaire des énergies des états excités des sous-unités moléculaires mises en jeu.

2.1.2 Complexes cyclométallés d'Ir(III) [8]

La modification des propriétés photophysiques de complexes d'iridium cyclométallés a un intérêt particulier dû à leur rôle central dans de nombreuses applications nécessitant une émission très efficace, telle que l'électroluminescence, la détection et la bioimagerie [29–32].

Nous avons modifié un complexe d'iridium cyclométallé (voir complexe de modèle **3**, Figure IV), impliquant l'intégration judicieuse d'un chromophore auxiliaire organique adapté[2], afin d'obtenir les complexes luminescents **4** et **5** d'une durée de vie beaucoup plus longue, tout en conservant un rendement quantique d'émission similaire (Tableau II). La clé du succès repose sur l'introduction d'un espaceur aliphatique non conjugué entre le groupe pyrène et la 2,2-bipyridine adjacente, car la fixation directe du pyrène au ligand auxiliaire peut modifier les propriétés du centre excité Ir(III).[33]

[1] L'anthracène a été sélectionné en tant que candidat approprié agissant comme réservoir d'énergie ($E_T = 1.8$ eV ; $\tau_{phos} = 3.3$ ms) [28].

[2] Le pyrène a été choisi comme réservoir d'énergie ($E_T = 2.09$ eV ; $\tau_{phos} = 11$ ms) [28].

Des études spectroscopiques résolues dans le temps ont clairement montré pour la première fois que l'équilibration de l'état excité est atteinte dans un complexe cyclométallé d'Ir(III) bichromophorique après quelques nanosecondes seulement *via* un TEER, et que l'émission observée provenant de **4** et **5** est retardée ($\tau = 225\ \mu$s et $\tau = 430\ \mu$s), respectivement, sans modifier les rendements quantiques d'émission (Tableau II). Ces durées de vie extrêmement longues de l'état excité nous ont permis de détecter l'oxygène à faible concentration (résultats préliminaires).

Tableau II. Propriétés photophysiques des complexes Ir(III) **3**, **4** et **5** dans l'acétonitrile.

complex	$\lambda_{em.max}$, nm	Φ_{air} [a]	Φ_{degas} [a]	τ, [b] μs	τ_{eq}, [c] ns
3	576, 617, 654	4×10^{-3}	10×10^{-2}	8.3 ± 0.3	–
4	576, 617, 654	5×10^{-4}	9.5×10^{-2}	225 ± 15	5
5	576, 617, 654	1×10^{-4}	9.6×10^{-2}	430 ± 15	2.8

[a] Rendement quantique de luminescence.
[b] Durée de vie de luminescence.
[c] Durée de vie de processus de equilibrium.

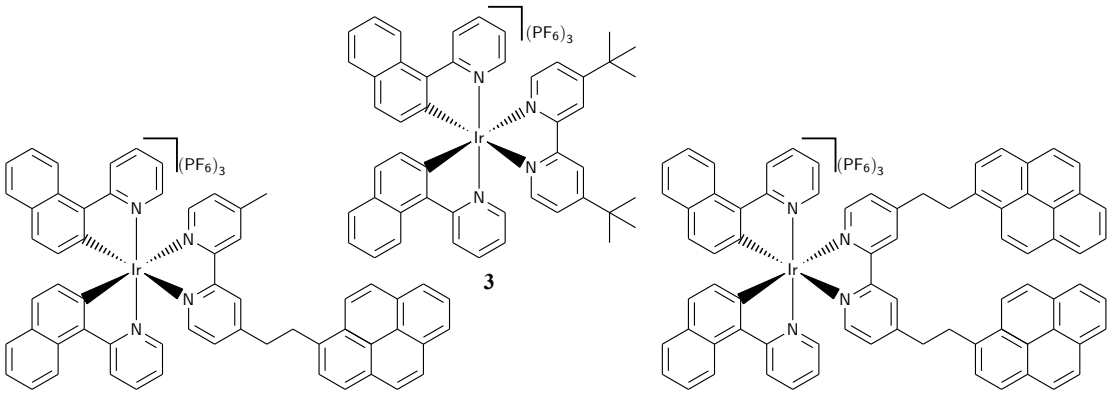

Figure IV. Formules structurales des complexes d'iridium **3**, **4** et **5**.

2.2 TEER dans des complexes hélice-tige de type hôte-invité

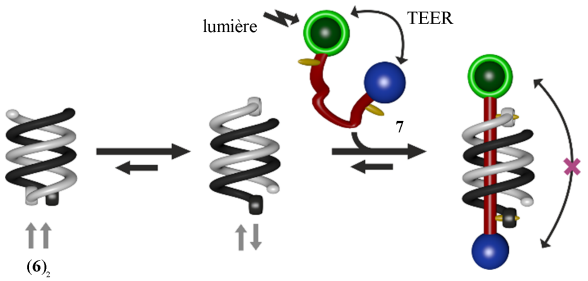

Figure V. La formation du complexe $\mathbf{7}\subset(\mathbf{6})_2$ de type hôte-invité démontrant le processus du TEER ; la boule verte représente un luminophore complexe organique à base de Ru(II) et la boule bleue – un chromophore pyrène. À l'équilibre, une boule antiparallèle $(\mathbf{6})_2$ est prédominante.

Les foldamères appartiennent à une classe d'oligomères synthétiques qui ont récemment attiré l'attention en raison principalement de leurs applications potentielles en sciences biomédicales.[34] Huc et ses collègues ont démontré [35] que les foldamères hélicoïdaux double-brin enroulés autour de molécules invitées en forme de tige peuvent effectuer un mouvement de type vis, phénomène inhabituel non observé pour d'autres machines moléculaires.

Nous avons été particulièrement intéressés par les structures à double hélice pour étudier par TEER des complexes de type invité-hôte de structure spécifique. L'idée de base est présentée dans la Figure V. La molécule invitée (pour raison de simplicité, elle sera dénommée «fil») a été synthétisée avec un luminophore basé sur le centre émissif Ru(II) (i. e. $[Ru(bpy)_3]^{2+}$, bpy – 2,2'-bipyridine) fixé à une extrémité du fil (chaîne flexible) avec un réservoir d'énergie (pyrène) à son autre extrémité. La liaison flexible entre le centre Ru(II) et le chromophore pyrène permet à la molécule d'adopter une

conformation dans la solution telle, que le transfert d'énergie peut se produire d'une manière réversible. Le TEER est donc «ON» et la durée de vie de l'émission est allongée. Lorsque le fil et la double hélice sont en interaction – la conformation du fil se rapproche de celle d'une tige découplant le centre émissif Ru(II) et le chromophore pyrène, et ainsi diminue le transfert d'énergie. Dans ce cas, le TEER est «OFF», avec une raccourcissement du déclin de l'émission du système supramoléculaire. Un tel système supramoléculaire pourrait être utilisé comme sonde de conformation et remplacer les sondes FRET [36] avec une sensibilité plus grande pour les courtes distances.

En utilisant des spectroscopies résolues en temps il a été montré, que dans les complexes hélice-tiges (type hôte-invité), l'efficacité du TEER peut être modulée par le degré de complexité entre le foldamère hôte et la molécule invitée.

3 Transfert d'énergie et d'électron photoinduit dans des systèmes supramoléculaires

3.1 Transfert d'électron photoinduit dans des foldamères hélicoïdaux d'oligoamides aromatiques

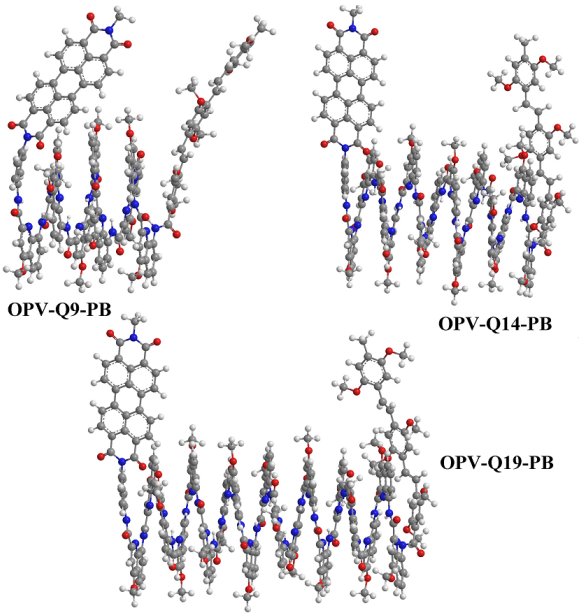

Figure VI. Structures d'échantillons étudiés: **OPV-Q9-PB**, **OPV-Q14-PB**, **OPV-Q19-PB** (MOPAC, PM7 calculs).

Certaines molécules photoexcitées deviennent de puissants donneurs ou accepteurs d'électrons.[37] Ce phénomène peut donner lieu à un transfert d'électron photoinduit. La nature et la façon dont la charge se propage à travers les molécules, les systèmes et les matériaux moléculaires sont à la base de l'électronique moléculaire. Elles sont aussi d'une importance fondamentale pour la modélisation des dispositifs photovoltaïques organiques et des diodes électroluminescentes, et pour la compréhension du fonctionnement des centres réactionnels photosynthétiques. Les processus de transfert de charge et leur dynamique dans les systèmes moléculaires ont fait l'objet de nombreuses recherches, en particulier sur des systèmes incluant deux centres redox : un donneur et un accepteur liés de façon covalente par un pont pour conduire à des architectures donneur-pont-accepteur.[38–40].

De nombreux modèles ont été conçus pour étudier la dépendance entre la distance et la recombinaison des charges produites après excitation lumineuse.[40–44] En raison de la rigidité des ponts utilisés et quelles que soient les positions cofaciales et/ou colinéaires des chromophores, leur distance reste fixe et correspond à la longueur du pont. Selon les propriétés du pont et la façon dont les chromophores y sont fixés, le transfert d'électron peut procéder par superéchange [38, 45] ou par multiples sauts de charge («hopping»).[44–46]

Dans l'équipe de Huc[1], des foldamères hélicoïdaux à conformations stables et anticipées ont été utilisés comme pont dans les structures donneur-pont-accepteur [40], où l'hélicité permet

[1] Institut Européen de Chimie et Biologie

d'organiser les chromophores dans l'espace.

Nous avons poursuivi le travail entrepris par Huc et ses collègues en 2009 [40] concernant la caractérisation de foldamères d'oligoquinoline hélicoïdaux à base d'amide aromatique[1] agissant comme pont hélicoïdal entre un donneur d'électron, l'oligo (p-phénylène vinylène) (OPV), et un accepteur d'électrons, le pérylène bisimide (PB). Le couple de transfert de charge (OPV-PB) a été choisi car la photophysique des composés isolés et la paire de transfert de charge ont été soigneusement étudiées et leurs propriétés sont bien connues.[47–53]

La caractérisation de la séparation de charge, résolue dans de temps à une échelle inférieure à la nanoseconde, entre le donneur d'électrons (OPV[2]) et l'accepteur (PB) a été effectuée avec un pont foldamère dont la longueur oligomère passe de 9, 14 et 19 unités, et dans des solvants de polarité différente : toluène, $CHCl_3$, CH_2Cl_2. Le mécanisme général du transfert d'électrons proposé pour des systèmes similaires consiste en quatre étapes distinctes : excitation de l'accepteur, injection d'un électron à partir de l'HOMO de l'unité quinoléine vers l'HOMO à un électron de l'accepteur excité ; puis transfert du trou formé au site donneur d'électrons par un saut aléatoire réversible entre les unités quinoléine énergiquement dégénérées où il se trouve irréversiblement piégé. Un mécanisme de superéchange pour les foldamères plus courts n'est pas exclu.

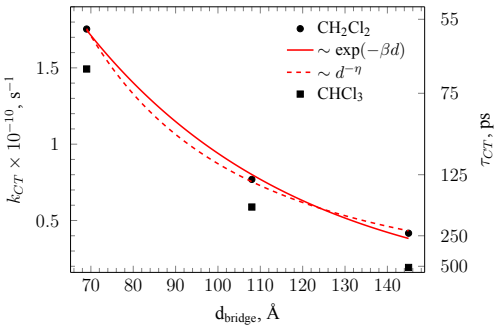

Figure VII. Dépendance de la vitesse d'oxydation d'OPV en fonction de la la distance déterminée de données TRABS (CH_2Cl_2, $CHCl_3$; RT).

En outre, un superéchange pourrait se produire entre le pont et le site OPV. Une longue et exceptionnelle durée de vie de l'état OPV^+-Q_n-PB^- (par exemple $\tau_{CSS} > 80\,\mu$s, CH_2Cl_2) a été observée. Il a également été démontré que dans les systèmes OPV-Q_n-PB étudiés, le site OPV du donneur d'électrons pourrait jouer le rôle d'une antenne collectrice de lumière. L'OPV excité pourrait transférer l'énergie d'excitation à un site PB grâce à une interaction de type dipôle-dipôle dont le taux de transfert d'énergie dépend de selon $1/d_{DA}^6$ [3].

3.2 Sondes luminescentes à base de lanthanide pour la détection *in situ* en temps-réel d'ions Cu(I)

Les ions métalliques jouent un rôle essentiel dans la physiologie humaine car il est considéré qu'au moins un tiers de toutes les protéines exigent un ion métallique comme cofacteur pour leur fonctionnement. Le cuivre est un élément nutritif essentiel impliqué dans des processus biologiques, y compris la respiration mitochondriale, le métabolisme osseux, la cicatrisation, la formation du tissu conjonctif, la mobilisation et l'absorption de fer.[54]

Il n'y a que quelques sondes spécifiques du Cu^+ dans la littérature, et elles souffrent de plusieurs inconvénients, en raison de leur nature organique. Les inconvénients principaux sont une faible solubilité dans l'eau, des spectres d'excitation et d'émission se situant dans la gamme UV-visible où l'absorption et la fluorescence des milieux biologiques sont importantes.[55]

Pour réaliser une sonde luminescente pour le Cu^+ qui lie sélectivement le métal et s'affranchit des problèmes de solubilité, le groupe de Sénèque[4] s'est inspiré de la protéine de cuivre CusF

[1] La longueur des ponts de foldamère a été choisie de telle façon que les donneur et l'accepteur soient orientés l'un à l'autre d'une manière cofaciale. La distance entre le donneur et l'accepteur par le pont d_{pont} a été estimée à : 69, 108 et 145 Å, respectivement pour 9-mer (4 tours complets d'hélice), 14-mer (6 tours) et 19 mer (8 tours) ; dans l'espace d_{DA} : 14, 21 and 28 Å, respectivement, selon les données publiées précédemment [40].

[2] En fonction de la longueur du pont foldamère, la vitesse d'oxydation d'OPV diminue (Figure VII).

[3] d_{DA}^6 étant l'écart entre OPV et PB.

[4] Laboratoire de Chimie et Biologie des Métaux, équipe Physicochimie des Métaux en Biologie, Institut de Recherches en Technologies et Sciences pour le Vivant (iRTSV), Grenoble, France

impliquée dans la résistance au cuivre et à l'argent dans Escherichia coli.[56] La protéine CusF lie un ion Cu^+ dans une boucle à deux méthionines, une histidine et un tryptophane par des interactions π-cation.[57] Ces interactions modifient les propriétés électroniques du tryptophane, de sorte que son absorption est décalée vers le rouge et la fluorescence désactivée en raison du peuplement du triplet du tryptophane. Plusieurs sondes peptidiques ont été synthétisées[1].

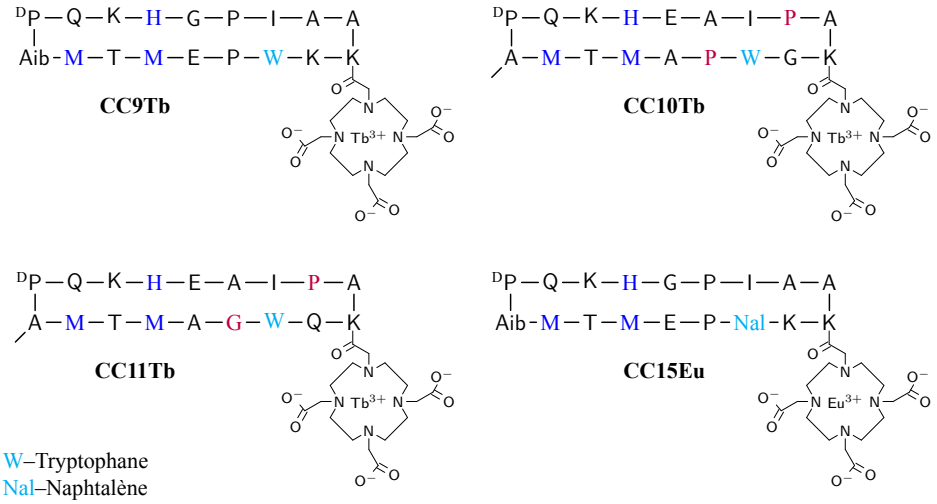

Figure VIII. Séquence des peptides: **CC9Tb**, **CC10Tb**, **CC11Tb** et **CC15Eu**, à base de protéine CusF.

Afin de réaliser une activation/désactivation luminescente d'une sonde ionique pour Cu^+, l'ion émissif Tb^{3+} a été incorporé dans le peptide à proximité de l'antenne de lumière tryptophane. Il est connu que l'énergie de l'état triplet du tryptophane ($E_{T_1} = 24600\,cm^{-1}$ [58]) peut être transférée à l'état $^5D_4$ de Tb^{3+} ($E = 20500\ cm^{-1}$), qui se relaxe à l'état fondamental par émission de lumière (Figure IX). Sans ion Cu^+, une voie de désactivation importante de l'état excité de la sonde est la fluorescence du tryptophane. L'interaction avec l'ion Cu^+ désactive la fluorescence du tryptophane, par passage à l'état triplet. L'efficacité du passage intersystème S-T est favorisée par des interactions π-cation [59]), il est suivi du transfert d'énergie vers l'ion Tb^{3+}, dont la luminescence est activée (Figure X).

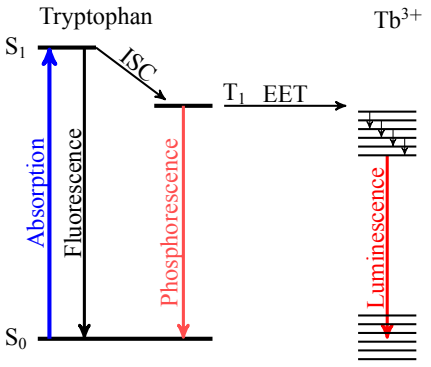

Figure IX. Schéma du principe de fonctionnement de la sonde **CC9Tb**.

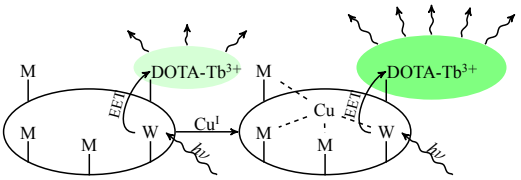

Figure X. Schéma du principe de fonctionnement de la sonde Cu(I).

Nous avons étudié les processus photophysiques de nouvelles sondes à base de Tb^{3+} et d'Eu^{3+} pour la détection *in situ* d'ions Cu^+ mimant la structure peptidique de CusF. Les sondes

[1]Le remplacement de tryptophane par le naphtalène (décroissance de fluorescence monoexponentielle) donnerait un modèle simplifié pour comprendre le processus photophysique régissant l'activation de fluorescence de sondes pour Cu^+. Pour cette raison, la sonde **CC15Eu** a été synthétisée (Figure VIII). L'ion Eu^{3+} a été utilisé comme luminophore au lieu de l'ion Tb^{3+}, car il est mieux adapté énergiquement à l'état triplet du naphtalène ($E_T = 22000\,cm^{-1}$ [28]). (Figure VIII).

à base de Tb^{3+} ont montré que l'émission du luminophore lanthanide est activée en présence des ions Cu^{+} et Ag^{+}. La sonde à base d'Eu^{3+} a seulement montré une réponse à l'ion Ag^{+}, ce qui est un résultat prometteur, car à ce jour à notre connaissance, aucune sonde est connue pour discriminer *in situ* les ions Ag^{+} des ions Cu^{+}. Les spectroscopies stationnaires et dynamiques ont montré qu'en présence des cations précités, le passage intersystème singulet-triplet pour l'antenne collectrice de lumière de la sonde (tryptophane pour la sonde à base de Tb^{3+} et naphtalène pour celle à base d'Eu^{3+}) a augmenté, en raison des interactions cation–π entre chromophores organiques (hydrocarbures aromatiques) et les ions Ag^{+} et Cu^{+}. Les interactions cation–π ont causé la diminution d'énergie du niveau triplet pour le tryptophane et le naphtalène à des degrés divers, important pour Cu^{+} et faible pour d'Ag^{+}. Un mécanisme général basé sur des données photophysiques expérimentales a été proposé pour expliquer l'activation de luminescence du lanthanide en présence des ions Ag^{+} et Cu^{+}. Une explication de la sélectivité de la sonde à base d'Eu^{3+} pour Ag^{+}, par rapport aux ions Cu^{+}, a été proposée.

4 Systèmes moléculaires multi-états

4.1 Nanoparticules fluorescentes *OFF-ON* pour l'imagerie *in vivo*

Aujourd'hui, l'imagerie de fluorescence utilisant des fluorophores moléculaires est un outil central pour l'étude des processus biologiques dans les cellules et les tissus, et offre un énorme potentiel pour l'imagerie couplée à des procédures thérapeutiques.[60, 61] Une des principales limites de l'imagerie de fluorescence est un problème complexe lié à l'émission de fond qui recouvre celle du fluorophore localisé à un point particulier. Il serait bénéfique de moduler l'émission de fluorescence de la sonde d'un état *OFF* à un état *ON* en réponse à un événement biologique spécifique, cela aurait pour avantage d'imager un tel événement en temps réel sans interférence de fond.[62]

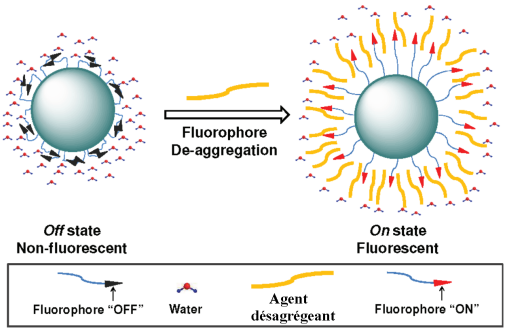

Figure XI. Mécanisme de commutation proposé pour les nano-sondes fluorescentes *OFF-ON* [62].

L'immobilisation de fluorophore sur ou à l'intérieur de particules peut apporter des avantages photophysiques significatifs ; cette approche est de plus en plus étudiée pour la nano-médecine, les nano-biotechnologies et l'imagerie de fluorescence.[63] Des études approfondies sont menées sur des fluorophores à colorants liés de manière non covalente sur des particules de polymère. En revanche, la mise au point de nanoparticules avec fluorophores liés de manière covalente à la surface est plutôt limitée, malgré l'avantage de réagir aux stimuli dans leur microenvironnement.[62] Le principe de fonctionnement de telles architectures fluorescentes nanométriques *OFF-ON* est présenté dans la Figure XI. La surface de la nanoparticule (NP) est recouverte de fluorophores PIR hydrophobes plongés dans un milieu aqueux polaire, ce qui définit une particule à l'état off. La fluorescence d'une particule peut être activée dans un milieu aqueux en réponse a divers agents tensioactifs.[62]

Dans ce travail, nous nous sommes spécialement intéressés à l'étude du mécanisme gouvernant le processus d'activation de la fluorescence de colorants greffés sur la surface de NP[1] à base de copolymère(styrène acide méthacrylique) après ajout d'agents tensioactifs (qui favorisent la désagrégation). Nous avons étudié plusieurs systèmes :

[1]NP de polystyrène avec des groupes de surface carboxylate a augmenté la solubilité des de la sonde fluorescente hydrophobe.

– Système modèle **NP-P** avec un groupement à base de pyrène[1], greffé sur la surface de nanoparticules de polymère de $d=100$ nm.
– Le boron-difluodipyrrométhène (BODIPY) qui a produit des NP polymères (diamètre$=$ 100 nm) : **NP-B1** et **NP-B2** (Figure XII).

L'étude de sondes *OFF-ON* fluorescentes en PIR, à base de colorants aza-BODIPY, liés de manière covalente à la surface de NP (copolymère(styrène acide méthacrylique)) de taille caractéristique $d=100$ nm a été effectuée en solutions aqueuses. De même, nous avons étudié un système modèle incluant des unités pyrène, fixées de manière covalente à la surface de la même NP. Il a été montré que les systèmes étudiés présentaient des réponses nettes (fluorescence activée) en présence d'agents tensioactifs (désagrégeants), tels que le Triton X-100 (Figure XIII et XIV)[2] et le DOPC. En raison de leur excellente photostabilité [64], de leurs propriétés d'émission et de leur bonne réponse à un stimulus, ces systèmes pourraient trouver des applications dans l'imagerie cellulaire par fluorescence. Nous avons proposé un mécanisme de fluorescence activée, qui fait intervenir une interaction directe de l'agent tensioactif sur l'organisation spatiale des fluorophores fixés à la surface des NP, provoquant l'élimination des voies de désexcitation non radiatives et en conséquence une augmentation du rendement quantique d'émission de fluorescence, jusqu'à $0,13$ et $0,4$ dans le cas du pyrène et de l'aza-BODIPY, respectivement.

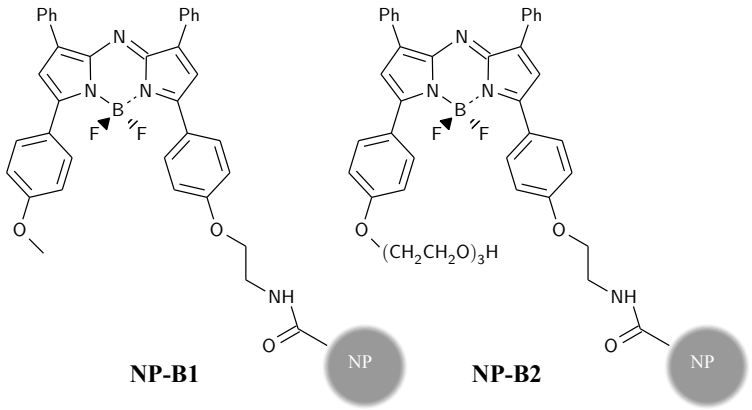

Figure XII. Structure d'aza-BODIPY : **B1** et **B2** ont recouvert les NPs.

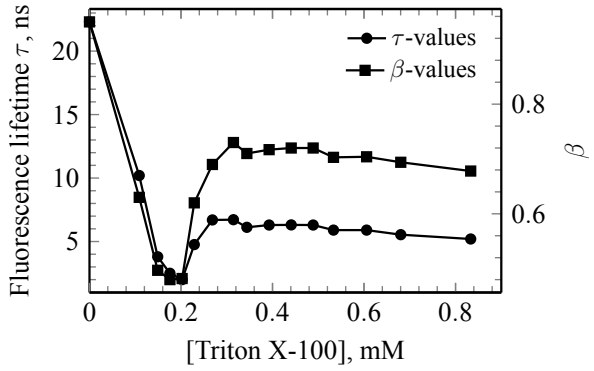

Figure XIII. Dépendance des paramètres τ et β en fonction de la concentration de Triton X-100 dans la solution **NP-P**, 0.0025 mg/mL ($\lambda_{exc}=355$ nm, $\lambda_{obs}=410$ nm).

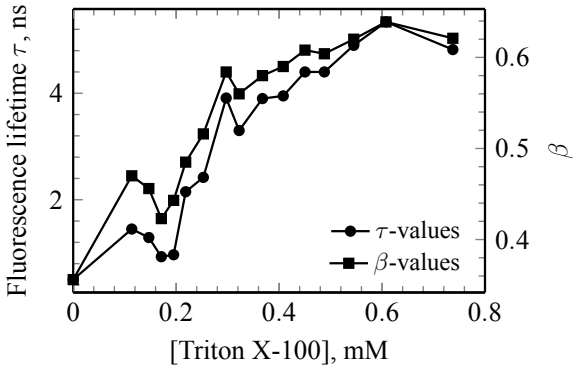

Figure XIV. Dépendance des paramètres τ et β en fonction de la concentration de Triton X-100 dans la solution **NP-P**, 0.01 mg/mL ($\lambda_{exc}=355$ nm, $\lambda_{obs}=410$ nm).

[1]Le pyrène a été utilisé comme fluorophore en raison de son rendement quantique d'émission élevé et de son émission qui se situe dans un domaine spectral commode pour les études in vitro. De même son émission double monomère / excimère donne de plus amples informations sur les interactions interchromophores. En outre, le processus FRET entre le Triton X-100 et le pyrène devrait fournir plus d'informations sur l'interaction tensioactif-chromophore.

[2]Une méthode simple utilisant la fonction exponentielle étirée ($A\exp\left(-(kt)^{\beta}\right)$) a été utilisée pour décrire l'interaction qui se produit entre les fluorophores et leur environnement.

4.2 Colorant fluorescent aza-BODIPY sensible au pH émettant dans le PIR pour l'imagerie *in vivo*

La durée de vie de fluorescence de la sonde a été considérée pour l'imagerie optique *in vivo*, contrairement aux mesures d'intensité, comme alternative pour surmonter le problème de la dépendance de concentration et également améliorer le contraste et surmonter d'autres problèmes : dispersion de la lumière, turbidité de l'échantillon, auto-fluorescence.[65]

Afin d'avoir un système fluorescent *OFF-ON* répondant au pH (Figure XV), le colorant **B3** (Figure XVI) a été imaginé et synthétisé en collaboration avec le groupe de O'Shea (Royal College of Surgeons Ireland). La chaîne polyéthylène glycol (PEG) (masse moléculaire moyenne de 5000 g/mol) a été introduite pour augmenter l'hydrosolubilité. Dans les applications futures, le colorant **B3** pourrait être immobilisé par une liaison covalente avec la NP, en fournissant un système solide et efficace pour la microscopie fluorescente *in vivo* similaire aux systèmes fluorescents *OFF-ON* décrits dans la section 4.1.

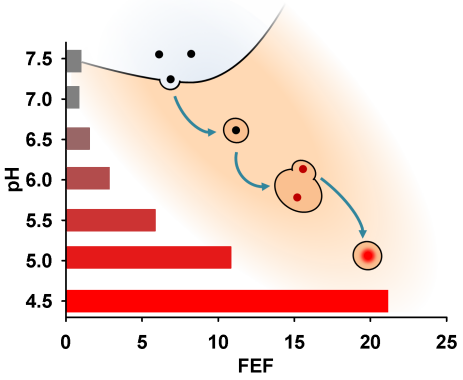

Figure XV. Mécanisme de commutation pour une sonde *OFF/ON* fluorescente sensible au pH. FEF – facteur d'amélioration de fluorescence.

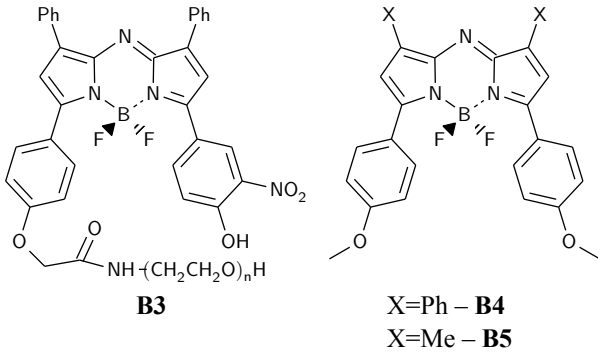

B3

X=Ph – **B4**
X=Me – **B5**

Figure XVI. Structure de **B3** (poids moléculaire ~ 5630 g/mol), **B4** [64] et **B5** [66].

L'efficacité de cette sonde fluorescente sensible au pH a été démontrée par notre collaborateur O'Shea dans des études in vitro, toutefois sans que l'ensemble des processus photophysiques aient été complètement élucidés. L'objectif principal de ce travail consistait à comprendre les processus photophysiques inhérents aux molécules **B3** à différentes valeurs de pH, et après une excitation lumineuse.

La valeur élevée du FEF (80) pour **B3** prouve que l'introduction du groupe NO_2 dans le fluorophore **B3** assure une commutation efficace (de *OFF* à *ON*) du signal de fluorescence, du pH physiologique au pH acide. En d'autres termes, une molécule **B3** resterait non fluorescente dans le milieu extracellulaire et deviendrait extrêmement fluorescente après introduction et localisation dans un compartiment cellulaire acide (par exemple, dans les endosomes et les lysosomes). Il a été prouvé que **B3** pourrait être utilisée à la fois comme sonde fluorescente à pH longue durée de vie, et d'intensité sensible au pH pour l'imagerie. Les molécules **B3** étudiées présentent des voies de relaxation subnanoseconde, ce qui réduit ainsi leur photostabilité par rapport à la molécule **B4** et diminue leur rendement quantique d'émission ; ceci pourrait être amélioré par remplacement du groupe NO_2 par un autre groupe électro-accepteur, pour lequel la formation de liaisons hydrogène sera empêchée par des facteurs stériques.

4.3 Systèmes à base d'azobenzène pour la capture / libération d'ions calcium [67]

Une multitude de récepteurs macrocycliques synthétiques a été décrite au cours des dernières quarante années, ces récepteurs ayant montré des affinités variables envers différents hôtes, notamment les ions métalliques.[68] Parmi ces récepteurs, les espèces modulées par un stimulus

(lumière, chaleur, pH, etc.), où l'affinité de liaison peut être modifiée, représentent un domaine de recherche en pleine expansion. Il existe en effet une grande variété d'applications potentielles en nanotechnologie biomimétique, ainsi qu'en biologie moléculaire, où la capture / libération d'un agent chimique à un moment donné est nécessaire pour permettre l'étude de voies biologiques spécifiques. Ainsi, les cellules font appel à une grande variété de médiateurs chimiques pour la signalisation. L'ion calcium (Ca^{2+}) est un des supports d'information les plus importants de la cellule.[69] Le développement de structures chimiques efficaces pour la capture / libération contrôlée sélective de l'ion Ca^{2+}, combinant vitesse et stabilité dans les cellules vivantes est un défi pour la chimie moderne.[67]

Dans notre groupe, nous avons conçu et étudié deux systèmes différents [67, 70] à base de l'éther lariat (Figure XVII) et BAPTA[1] incorporant une unité azobenzène photochrome pour la capture / libération de Ca^{2+} sous un stimulus lumineux (Figures XVII and XVIII).

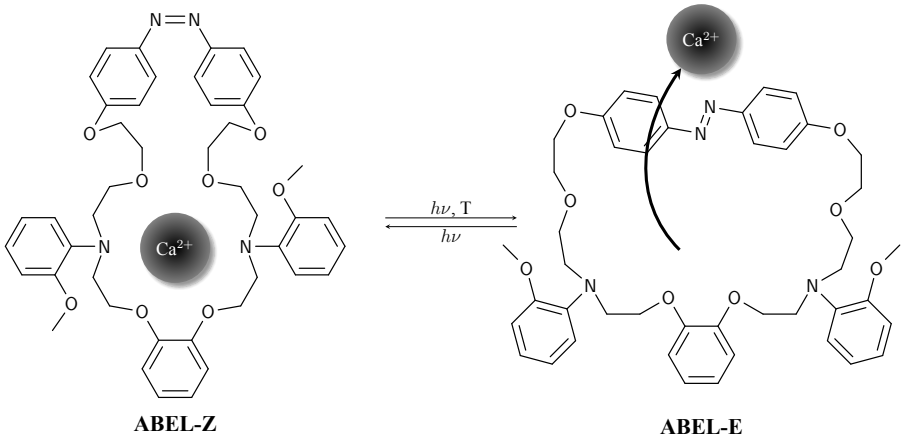

Figure XVII. Photo-commutation de "photo-lassos" prototypes **ABEL**.

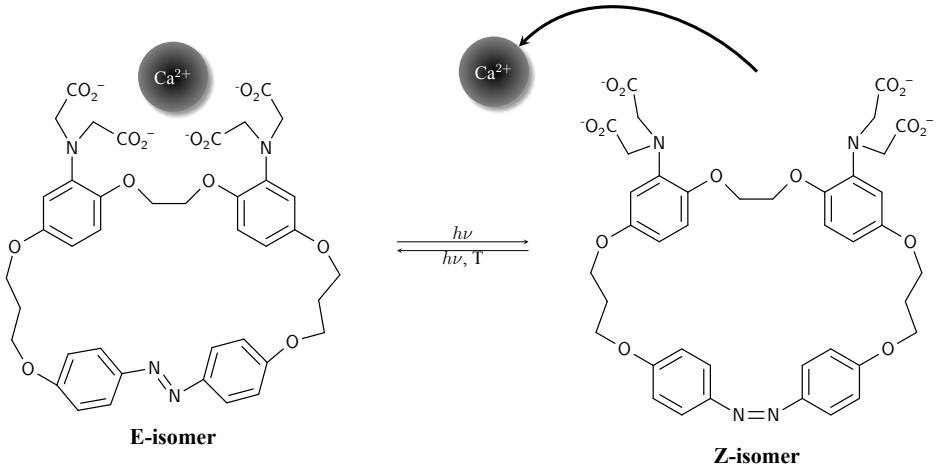

Figure XVIII. Photo-commutation d'azobenzène - BAPTA.

Des mesures ultrarapides d'absorption transitoire des processus de la photo-isomérisation pour la capture / libération de l'ion par des systèmes à base d'azobenzène (azobenzène - éther de lariat, azobenzène-BAPTA) ont été effectuées. Les taux d'isomérisation ont été déterminés pour les systèmes en présence et en absence de l'ion Ca^{2+}. Il a été observé que les systèmes azobenzène - éther lariat n'ont montré aucune différence significative dans la cinétique de la photo-isomérisation avec ou sans liaison avec Ca^{2+}. Cela peut s'expliquer par la faiblesse de la liaison entre l'hôte **ABEL** et l'ion invité Ca^{2+}, ce qui se traduit par une constante d'association

[1]BAPTA est un chélateur sélectif de Ca^{2+} bien connu et largement utilisé en biologie.

assez faible $K = 1,7$ pour la forme Z et $K \sim 0$ pour la forme E. Le complexe azobenzène-BAPTA avec Ca^{2+}, présente une constante K plus élevée ~ 5 pour la forme E, et montre le retentissement (4 fois) de la photo-isomérisation de l'azobenzène.

4.4 Impact de l'eau sur la photo-isomérisation *cis-trans* d'hydroxychalcones [71]

L'impact de l'eau sur la photoisomérisation cis-trans d'hydroxychalcones a été étudié dans l'acétonitrile et dans un mélange H_2O/CH_3OH (1/1, v/v) par spectroscopies (sous-picoseconde et nanoseconde) résolues dans le temps. Dans les deux types de milieux, la première étape après excitation est la même et fait intervenir la relaxation à partir du singulet excité à l'état tordu $^1P^*$ en quelques picosecondes. Dans l'acétonitrile, cet état se désactive pour former une hydroxychalcone de formes *cis* et *trans* en proportions identiques, situation classique pour la photoisomérisation d'une double liaison. La présence d'eau affecte considérablement la voie photochimique par formation d'un intermédiaire tautomère entre l'état $^1P^*$ et les photoproduits. La voie photochimique principale de ce tautomère est une électrocyclisation qui produit un chromène, tandis que toutes les autres voies mènent à l'hydroxychalcone sous la forme *trans* ; c'est pourquoi aucun isomères *cis* n'est formé par la voie photochimique.

5 Conclusions

Dans cette thèse, les études photophysiques ont été réalisées sur une multitude de systèmes moléculaires, notamment des systèmes à base d'une supramolécule bi- et multichromophorique, fonctionnant via des mécanismes différents : transfert d'électron et d'énergie électronique photoinduit, transfert d'énergie électronique réversible et isomérisation photoinduite.

- Plusieurs applications du Transfert d'Énergie Électronique Réversible (TEER) ont été discutées. L'approche TEER a été utilisée pour améliorer considérablement la durée de vie d'émission de complexes Ru(II) à base, respectivement, de ligands tridentates et de complexes cyclométallés Ir(III), sans pour autant diminuer les rendements quantiques. La modulation des propriétés photophysiques de ces chromophores peut être pertinente pour des applications comme capteurs de gaz (par exemple O_2) et dans les dispositifs électroluminescents. Une nouvelle approche du TEER dans la perspective de sonder les conformations / distances a été proposée. Le contrôle de l'efficacité du processus du TEER par le degré de complexité a été illustré entre un foldamère hôte à double hélice et une molécule fil invitée.
- La caractérisation de la séparation de charge résolue dans le temps entre un donneur d'électrons (OPV) et un accepteur (PB) à une échelle de temps inférieure à la nanoseconde (dans les foldamères oligoquinoliniques de tailles variables) a été réalisée dans des solvants de polarités différentes : le toluène, $CHCl_3$, CH_2Cl_2. Nous avons proposé un mécanisme général pour le transfert d'électrons dans ces systèmes, composé de 4 étapes distinctes : excitation de l'accepteur, injection d'électron à partir d'un état HOMO de l'unité quinoléine à l'HOMO à un électron de l'accepteur excité ; ce trou est transféré au site du donneur d'électrons par un saut stochastique et réversible entre les unités modulaires de quinoléines énergiquement dégénérées, où il est irréversiblement piégé. Une durée de vie exceptionnellement longue de l'état OPV^+-Q_n-PB^- $\tau_{CSS} > 80\,\mu$s dans CH_2Cl_2 a été observée. Il a également été démontré que dans les systèmes OPV^+-Q_n-PB^- étudiés, le site OPV du donneur d'électrons pourrait jouer un rôle d'antenne collectrice de lumière, transférant l'énergie d'excitation vers un site de PB à travers une interaction de type dipôle-dipôle.
- De nouvelles sondes *in situ* à base de Tb^{3+} et Eu^{3+} pour la détection d'ions Cu^+, mimant la structure de peptides CusF, ont été étudiées. Les sondes à base de Tb^{3+} ont montré une

exaltation important de l'émission du luminophore lanthanide en présence des ions Cu^+ et Ag^+. La sonde à base de Eu^{3+} a montré une réponse seulement à l'ion Ag^+, ce qui est un résultat prometteur car à ce jour, à notre connaissance, des sondes discriminant entre les ions Ag^+ et Cu^+ *in situ* n'ont pas été décrites. Nous avons proposé un mécanisme général basé sur des données expérimentales photophysiques pour expliquer l'activation de luminescence du lanthanide en présence des ions Ag^+ et Cu^+, il est basé sur des interactions cation–π entre les fluorophores organiques (tryptophane pour la sonde à base de Tb^{3+} et naphtalène pour celle à base d'Eu^{3+}) et les ions Ag^+, Cu^+. Une explication de la sélectivité de la sonde à base d'Eu^{3+} envers Ag^+, par rapport aux ions Cu^+ a été proposée.

- L'étude de sondes PIR fluorescentes *OFF-ON* a été effectuée en phase aqueuse. Ces sondes sont à base de colorants aza-BODIPY fixés de manière covalente sur une surface de NP (poly(styrène-co-acide-méthacrylic)) avec une taille caractéristique de d=100 nm. De même, nous avons étudié un système modèle avec des unités de pyrène analogues, fixées de manière covalente à la surface d'une même NP. Il a été montré que les systèmes étudiés présentaient des réponses claires (fluorescence activée) en présence d'agents tensioactifs (désagrégeants), tels que le Triton X-100 et les DOPC. En raison de leurs excellentes photostabilités, de leurs propriétés d'émission et de leur bonne réponse à un stimulus, ces systèmes pourraient trouver des applications dans l'imagerie cellulaire de fluorescence. Nous avons proposé un mécanisme pour l'activation de fluorescence. Il fait intervenir directement le tensioactif sur l'organisation spatiale du fluorophore fixé à la surface de la NP, supprimant les voies de désactivation non-radiatives et, en conséquence, augmentant le rendement quantique d'émission, jusqu'à $0,13$ et $0,4$ dans le cas du pyrène et de l'aza-BODIPY, respectivement.
  Les études photophysiques ont été réalisées sur les nouvelles sondes PIR fluorescentes à pH, basées sur une variante nitrée de molécules aza-BODIPY. Il a été prouvé qu'elles pourraient être utilisées en imagerie en tant que sonde à pH en durée de vie et en intensité de fluorescence avec une valeur FEF relativement élevée (80) pour la molécule étudiée. Une stratégie pour améliorer l'émission de fluorescence d'une sonde a été suggérée.
- Les processus de photoisomérisation pour des systèmes dédiés à la capture / libération d'ion à base d'azobenzène (azobenzène-éther lariat, azobenzène-BAPTA) ont été étudiés au moyen de mesures spectroscopiques ultrarapides (absorption transitoire). Les taux des processus d'isomérisation ont été déterminés en présence et en absence de l'ion Ca^{2+}. Il a été observé que les systèmes azobenzène-éther lariat n'ont montré aucune différence significative dans la cinétique de photoisomérisation avec ou sans Ca^{2+}, ce qui s'explique par la faiblesse de la liaison entre le complexe hôte et l'ion invité Ca^{2+} ($K=1,7$ en forme Z et $K\sim0$ en forme E). Le complexe azobenzène-BAPTA avec le Ca^{2+} a une constante d'association plus élevée ($K\sim5$ en forme E), et montre le ralentissement (4 fois) de la photoisomérisation de l'azobenzène.
- L'impact de l'eau sur la photoisomérisation *cis-trans* d'hydroxychalcones a été étudié dans l'acétonitrile et dans un mélange H_2O/CH_3OH (1/1, v/v) par les spectroscopies (sous-picoseconde et nanoseconde) résolues dans le temps. Dans les deux milieux, la première étape après excitation lumineuse est la même et correspond à la relaxation du singulet excité de l'état tordu $^1P^*$ (quelques picosecondes). Dans l'acétonitrile, cet état se désactive pour former une hydroxychalcone de formes *cis* et *trans* en proportions identiques, la situation classique pour la photoisomérisation d'une double liaison. La présence d'eau affecte considérablement la voie photochimique par formation d'un intermédiaire tautomère entre l'état $^1P^*$ et les photoproduits. La voie photochimique principale de ce tautomère est une électrocyclisation pour former un chromène, tandis que toutes les autres voies mènent à l'isomère trans de l'hydroxychalcone.

Contents

List of Figures

List of Tables

Chapter 1

Introduction

L'art c'est **moi** – la science c'est **nous**.

french physiologist, Claude Bernard
(1813–1878)

Useful properties (light emission on stimulus, specific electronic absorption, charge and energy transfer, etc.) of molecular and supramolecular systems imply intricate through interactions with environment or between molecular sub-units. Most systems do not interact with each other or do not show interaction between their internal parts and environment in the ground state. By translating them into an excited state, such interactions could be observed. One of the most often used stimulus in chemistry and physics is light excitation.

In modern **photo**chemistry researchers actively use 5 distinct approaches, which allow the design of molecular/supramolecular systems of different origin: organic, inorganic; biomimetic natural photo-active systems, to improve already existing systems. These approaches are listed below:

1. Thermal- or photo- reversible bond formation:
   - Thermal or photocyclization;
   - Thermal or photoactivated reactions;
   - ...
2. *Photoinduced Electron Transfer (PET)*;
3. *Electronic Energy Transfer (EET)*;
4. *Reversible Electronic Energy Transfer (REET)*;
5. *Thermal or photoisomerization*.

In this research we will be dealing with molecular and supramolecular systems which are activated by light excitation, designed using different approaches (see the listed items in italics). In particular we will be interested in studying photophysical processes of the cited systems.

In the first chapter the fundamental aspects of photophysics and photochemistry will be highlighted, as well as experimental techniques, which were used to study photophysical processes of supramolecular and molecular systems.

The second chapter is focused on Reversible Electronic Energy Transfer (REET), which was used to dramatically enhance emission lifetimes of Ru(II) complexes based on tridentate ligands and cyclometallated Ir(III) complexes, respectively, without diminishing luminescence quantum yields . Equally a new approach of using REET in the perspective of probing conformation/distance is discussed: to control the efficiency of the REET in the process by the degree of complexation, exemplified between a host double-helix foldamer and guest thread molecule.

In the third chapter the photoinduced energy and electron transfer processes are studied. The photoinduced electron and energy transfer processes were studied by the example of charge separation between electron donor (OPV) and acceptor (PB) in the sub-nanosecond timescale through an oligoquinoline bridge in foldamers of increasing oligomeric length (9, 14, 19 units) in the temperature range $180-303\,\mathrm{K}$. The energy transfer occurring in novel lanthanide-based luminescent probes for time-gated *in situ* detection of Cu(I) ions, being modulated by an antenna effect through cation-π interactions were investigated.

Chapter four covers a range of multi-state photoactive molecular and supramolecular systems. The study of NIR fluorescent *OFF-ON* probes, based on aza-BODIPY dyes, covalently attached to the surface of NP (poly(styrene-co-methacrylic acid)) with characteristic size of $d=100\,\mathrm{nm}$ was conducted, showing pronounced responses (fluorescence turning *ON*) to the presence of surfactant (de-aggregating) agents, such as Triton X-100 and DOPC micelles. Photophysical studies on novel NIR pH fluorescent probes, based on a nitrated variant of aza-BODIPY molecules was carried out, which could be used for pH sensitive intensity fluorescence probe in fluorescence imaging. And finally the photoisomerization processes for azobenzene-based (azobenzene-lariat ether, azobenzene-BAPTA) ion release/capture systems, as well as the impact of water on the cis−trans photoisomerization of hydroxychalcones in CH_3CN and in H_2O/CH_3OH (1/1, v/v) were investigated by means of ultrafast transient absorption spectroscopy measurements.

1.1 Chemistry and physics in research

We need to revisit various definitions to remind briefly readers what stands behind the words *chemistry* and *physics*, despite their apparent familiarity. Part of this information we will use after to explain how chemistry and physics fused together in this research.

Explanatory dictionaries give these definitions for the word *chemistry*:

1. The science of the composition, structure, properties and reactions of matter, especially of atomic and molecular systems.[72]
2. The branch of science concerned with the substances of which matter is composed, the investigation of their properties and reactions, and the use of such reactions to form new substances.[73]
3. The science that systematically studies the composition, properties and activity of organic and inorganic substances and various elementary forms of matter.[74]

All of these definitions are very similar in their meaning and allow us to say that *chemistry* chiefly deals with atoms and molecules and their *interactions* with each other. The interactions between atoms, molecules should be considered together with other phenomena: electrons and various forms of energy, which are involved in such processes as chemical, photochemical, oxidation-reduction reactions, changes in phases of matter, separation of mixtures, etc.

Most crucial for understanding what is the essence of *chemistry* – are the electron processes happening while matter is interacting. These interactions, which *chemistry* studies happen in a rather narrow energy range and with absolute values not exceeding 1 eV [1](see Table 1.1), so only electrons of the atom[2], namely how they behave in reaction with other atoms are truly objects of ***chemistry*** studies.

Now lets look what explanatory dictionaries tell us for definitions of the word physics:

1. The science of matter and energy and of interactions between the two, grouped in traditional fields such as acoustics, optics, mechanics, thermodynamics, and electromagnetism, as well as in modern extensions including atomic and nuclear physics, cryogenics, solid-state physics, particle physics and plasma physics.[72]
2. The branch of science concerned with the nature and properties of matter and energy. The subject matter of physics includes mechanics, heat, light and other radiation, sound, electricity, magnetism and the structure of atoms.[73]
3. The science that deals with matter, energy, motion, and force.[74]

The *physics* studies different phenomena in vast range of energies uprising from Planck's energies (quantum physics) up to galactic energies (astrophysics) (see Table 1.1). Physics attempts to describe processes in systems of various complexity by the same laws and often consistent patterns, that evolves in very different areas of our observable world.

Table 1.1. Characteristic time, distance and energy ranges for chemistry and physics.

	Time range, s	Size range, m	Energy range, eV
Chemistry	10^{-15}–*	$10^{-10} - 10^{1}$ (11 orders)	$10^{-4} - 10^{0}$ (4 orders)
Physics	$10^{-44} - 10^{18}$ (>50 orders)	$10^{-35} - 10^{-18} - 10^{26}$ (>40 orders)	up to 10^{70}

There is an opinion that *chemistry* could be named as part of such huge and spacious science as *physics*? To disprove this statement let us consider the work of Dr. Bunge. "Is chemistry a branch of physics?" [75] and make some citations from this work:

"At the first sight chemistry is included in physics because chemical systems would seem to constitute a special class of physical systems. But this impression is mistaken, for what is

[1]These energies cannot cause any significant effect on nuclei.

[2]The proton (H^+) is a special case.

physical about a chemical system is its components *rather that the system itself, which possesses certain emergent (though explainable) properties in addition to physical properties. Indeed, a chemical system may be defined as a system where chemical reactions occur, i. e. a system whose atomic and molecular composition is variable. The composition of a chemical system is then a set of atoms or molecules, each of which may be regarded as a physical system. Since system and components do not share all their properties, they do not belong to the same kind of thing. (Likewise the components of a social system are animals and the chemical and physical systems they use, but the social system itself is not alive and does not engage in metabolic reactions or in physical processes.)"*

"Doing laboratory chemistry is not the same as doing physics, regardless of the amount of physical methods that may be employed. (Remember the old chestnut: Physics handles impure substances with pure methods; chemistry handles pure substances with impure methods[1]*). Nor is doing classical theoretical chemistry – e. g. posing and solving systems of chemical kinetics equations coupled with a diffusion equation – the same as doing theoretical physics. Classical theoretical chemistry is centrally interested in the description of macroprocesses – typically those occuring in a test tube or in a chemical reactor – rather than in understanding them in terms of atomic components.*

On the other hand doing quantum chemistry does look very much like doing quantum physics..."

Later in the article Dr. Bunge showed, that "*Quantum chemistry is weakly reducible to quantum physics... Quantum chemistry is not a part of quantum physics although it is based on the latter."*

We'd like to generalize:

- *"Some chemical concepts, such as that of chemical structure, are definable in quantum-theoretic terms in a straightforward manner. Other chemical concepts, such as that of rate constant, are definable in quantum-theoretic terms provided certain extra assumptions back them up. (Their reduction is then partial rather than total.) However, a final decision on this matter will have to await the axiomatization of quantum chemistry.*
- *Quantum theory, by itself, fails to entail quantum chemistry: the latter follows only when the former is adjoined, not only linking definitions, but also extra assumptions concerning the composition of molecules, the nature of chemical reactions, and certain mathematical idealizations and approximations. In short, quantum chemistry is based on quantum physics but is not part of it.*
- *"Chemistry, as a field of inquiry – not just as a collection of results of inquiry – has a number of traits it fails to share with physics. Among them are a peculiar domain or reference class, a peculiar problem system, and goals and methods of its own. Hence chemistry* ***is not a branch*** *of physics.*
- *Nor is chemistry an autonomous science: it is based on physics. However, chemistry in turn feeds physics a number of data, ideas, and problems. So, physics and chemistry are* ***interdependent****."*[75]

1.2 Objects of study

Object of study – in science is meant to be the one of most important points to which scientists apply their forces. The correct determination of the object of study reduces quantity of errors during research for a scientist and research worker, what represents in reducing of unnecessary experiments or even the wrong ones, resulting in an economy of time and energy. Sometimes the object of study is concretized at every step of research, what happens often in unknown or unstudied fields of science.

[1] Author remark: Physical-chemistry deals with impure substances with impure methods.

1.2.1 Molecular and supramolecular systems

Molecular systems – are basically systems made up of molecules. But almost every system, surrounding us could be described as molecular. Considering the molecular system from a chemistry point of view compels us, firstly, to impose dimensional constraints on the molecular system (molecular size of its components less than tens of nanometers[1], see Table 1.1 and Appendix 1.1); secondly, energies for such systems are limited[2]; in third place, we will focus on properties of such system as a whole, but not as a sum of its part's properties, while interactions of its parts form a system. The interaction between components is the main factor, defining a system[3], for example: energy transfer from one chromophore[4] to another in solution. In this particular research the objects of study could be assigned as well as supramolecular systems.

Lehn [77] gave this definition for supramolecular chemistry: "Supramolecular chemistry is the chemistry of the intermolecular bond, covering the structures and functions of the entities former by the association of two or more chemical species."

Vögtle" [78] said this: "In contrast to molecular chemistry, which is predominantly based upon the covalent bonding of atoms, supramolecular chemistry is based upon intermolecular interactions, i. e. on the association of two or more building blocks, which are held together by intermolecular bonds. Supramolecular chemistry is defined as chemistry beyond the molecule, as chemistry of tailor-shaped intermolecular interaction. In supramolecules, information is stored in the form of structural peculiarities. Moreover, not only the combined action of molecules is called supramolecular, but also the combined action of characteristic parts of one and the same molecule".[78]

Both these definitions and comments, taking in account what said about molecular systems, leads us to conclusion that the supramolecular system differs from a molecular system only by strength of interaction between the system's parts. In both aforementioned citations authors stress the importance of interaction between system's parts. The author would like to stress, that from the point of chemistry, not every ensemble of molecules could be called as a molecular *system*. A highly diluted solution of sugar molecules is not molecular system, if we only are not interested in interaction between dissolved molecules and solvent molecules, but this interaction is not usually an interest in chemistry.

Some molecules in their ground state do not interact with each other or do not show interaction between their internal parts. By translating them into an excited state, such interaction could be observed:

1. Thermal- or photo- reversible bond formation:
   - Thermal or photocyclization;
   - Thermal or photoactivated reactions;
   - ...
2. *Electronic Energy Transfer (EET) see Chapter 3, p. 59;*
3. *Reversible Electronic Energy Transfer (REET) see Chapter 2, p. 31;*
4. *Photoinduced Electron Transfer (PET) see Chapter 3.2, p. 61;*
5. *Thermal or photoisomerization see Chapter 4.3 and 4.4, p. 105 and p. 111.*

One of the most often used stimulus in chemistry and physics is a light excitation. In this research we will be dealing with systems which are activated by light stimulus. In modern

[1] Exceptions are molecules of DNA, polymer molecules, reaching macroscopic sizes. Although even in these cases the reactive centres of molecules have characteristic molecular size.

[2] not exceeding > 1 eV

[3] A group of interacting, interrelated, or interdependent elements forming a complex whole could be named as system (www.thefreedictionary.com).

[4] A chromophore is defined as an atom or group of atoms that serve as an unit in light absorption.[76] Meanwhile we will use this word to name in general molecular/supramolecular systems.

photochemistry there are 5 distinct approaches (see items 1-5 above), allowing design molecular/supramolecular systems of different origin: organic, inorganic.

In the present work molecular and supramolecular systems were studied under visible and UV excitation, designed using different approaches (see the listed items in italics). In particular we will be interested in studying photophysical processes of the mentioned systems.

1.2.2 General Remarks

Classical chemistry has always been interested in properties of substance[1] and also their changes. Chemistry fixes this property change as a discreet transition from one state into another (luminescence *ON* – luminescence *OFF*, other properties: reactivity, aggregation, etc.). But anyway property or properties change happens due to the electrons clouds reorganisation under external or internal forces, after which nuclear displacement causes change in geometry of molecular system. Because of the great complexity of the studied systems in this work, it is in many cases technically difficult to delve into the processes, which are happening and effecting the properties change of whole system or its sub-system.

A chemist should always consider the system as whole, and when he manages to reveal internal processes of system and uses them explain its properties, it only reinforces his belief in the possibility of chemistry to design systems with desirable final properties.

Substances for a physicist is often the arena in which the process of interest is happening, and he appeals to different substances, only if the observed phenomenon occurs in them in different ways to understand it more thoroughly. Physics, while studying the system differentiates its processes, but not the properties, as does chemistry. It cannot be said that physics is not interested in the initial and final properties of the system, but the process takes a central place in physics, as a phenomenon of the system. For physics, it is important that the object of study was *"simple"*, to be able to not only separate all the processes occurring in it, but also to describe them using methods available to us and find relationships between them.

A molecular system is not the best option for physics as objects of study. But an extremely important feature of man-made systems studied in this work helps to limit complexity of molecular systems. All of then are based on the chemist's *idea*, the *idea* about the future properties of have not yet made system. The *idea* limits the set of properties and processes that need to be studied to be able to confirm the correctness of an *idea*.

Proof that either *ideas* work or not allows us to reduce physics and chemistry to a single point of study. Each of science solves its own problems exploring the object of study. Physics revises, clarifies and confirms the known laws, and the researcher can find sometimes by luck some deviations from[2] them; chemistry searches for possibilities to get new properties from known chemical families for substances or it looks after new principles allowing to obtain desirable properties in new substances mimicking or not natural world.

Reducing the complexity of the molecular system as the research object, leads to a remarkable observation: chemistry overrides physics pointing it to an area of study for *idea* confirmation, actually turning it into a *"servant"*. So it looks at first glance, in fact chemistry is in the petitioner, without physics it is difficult to confirm or refute either, if the idea works or not using only chemical methods.

We would also like to draw attention to the incompatibility of time expanses of chemists and physicists. Often to explore the physics of the system physicists needs a few days or weeks, but for chemist to create a system sometimes it takes months or even years. But even in the case when chemist's **ideas** does not work, it does not make a physicist a *"judge"*. That only strengthens close relationship between people and sciences.

In the previous subsection we have demonstrated that chemistry cannot be part of physics.

[1] But the main goal of chemistry is to study chemical properties and their changes.

[2] Many glorious discoveries were made by accident and even mistake.

But the reader may ask: "Why can the studied systems not be attributed to the objects of study to such a science as physical chemistry[1]? "

Objects of study for physical chemistry are any systems in which any chemical transformations can occur. Physical chemistry studies changes occurring in these systems, accompanied by a transition in the chemical forms of movement in different physical forms of motion - thermal, radiant, electrical, etc. Thus, physical chemistry does not study chemical processes alone, but in close connection with the accompanying physical phenomena – release (or absorption) of heat, radiation energy, the flow of electric current, etc.

We can conclude that the present study will be subject to the logic of *physical chemistry*, where physical methods are used to study chemical systems.

We won't delve deeper into the problems of the philosophy of science, into the difference between research objects and tasks for physics, chemistry and physical chemistry, and their perception of the world which is distant from the other aspects of the thesis research topic.

1.3 Properties and processes of excited states

We discussed earlier that systems studied in this work are photo-activated (RET, REET, PET, Photoisomerization). It simply means that system should be excited from its ground state to some electronic excited state, because only upon being in the excited state the system could be active from the point of displaying useful property. At room temperature thermal energy is not adequate to significantly populate electronically excited states.

Here we would like to spent some time to discuss such terms as *state* and the term *excited state*.

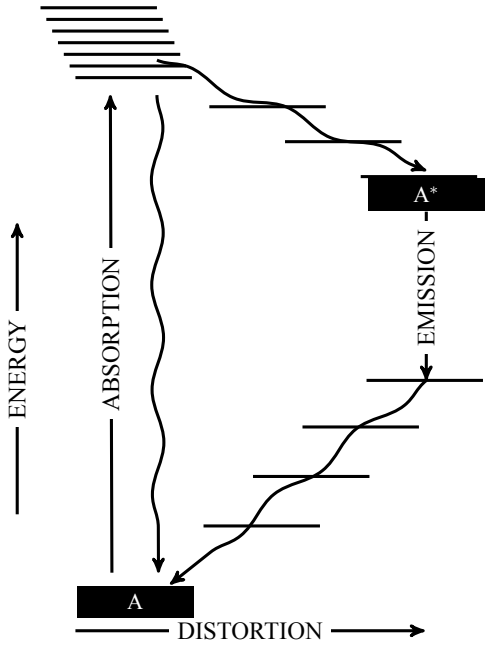

Figure 1.1. Energy versus distortion diagram [79].

The work of Adamson[79] we will helpful in the discussion.

The word *state* has two different usages in science. To the spectroscopist, the state of a molecule is defined by quantum numbers. He will use term designations and thus speak of the $^2P_{1/2}$ state of the sodium atom or the $^3\Sigma_g^-$ state of O_2. In the case of coordination compounds, examples would be the $^4T_{2g}$ and ^2E_g ligand field states of Cr(III). When we assign the various absorption maxima in the UV-vis spectrum of a coordination compound, we are proposing specific state-to-state electronic transitions. Thus the first major absorption band for $Cr(NH_3)_6^{3+}$ is assigned as the $^4A_{2g} \rightarrow {}^2T_{2g}$ transition. To the spectroscopist, then, an excited state has different electronic (and rotational and vibrational) quantum numbers than does the ground state.[79]

The word *state* has a rather different meaning in thermodynamics. When we speak of, say, HCl gas at standard conditions, we mean a collection of molecules with a certain average molar energy, entropy, free energy, etc. This is not a single spectroscopic state. Rather, we have a Boltzmann distribution of quantum states. This collection or ensemble has average properties the above thermodynamic ones, and many others, such as density, index of refraction, absorption

[1]The name of this science was introduced by Russian scientist M. V. Lomonosov in 1752–1753, who also formulated its object and tasks of investigation.

spectrum, etc. The usual standard state of aqueous $Cr(NH_3)_6^{3+}$ refers to a condition of unit activity under 1 atm pressure and at 25°C. A collection of ions in this state has certain average bond lengths and angles; it has thermodynamic properties; it has chemical reactivity described by one or more rate constants, each having temperature dependence and corresponding activation energy.[79]

Excited states could have different meaning in case of molecular and supramolecular systems. Let take spectroscopic ground state A, and a first electronic excited state A^*, illustrated in Figure 1.1. A^* will, usually, have different bond lengths and angles than system in state A.

When light is absorbed by species A, a population of A^* states is produced, and we expect the transition to be a "vertical" one, that is, electronic rearrangement occurs but no appreciable nuclear motion. Transitions occur in about 10^{-15} s,[1] a time too short for significant displacement of nuclei. The consequence is that A^* molecules are not produced in their equilibrium geometry and should therefore be highly vibrationally excited. This collections of molecules is called Franck-Condon collection or Franck-Condon state (A^*_{FC}).[79]

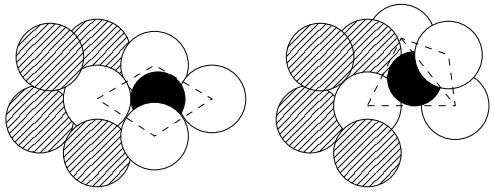

Figure 1.2. Solvent cage effect in excited state thermal equilibration [79].

Assuming that complex A has a square planar geometry, while the equilibrium geometry of A^* is tetrahedral. A newly formed A^* complex cannot immediately relax to tetrahedral geometry, solvent molecules have to rearrange themselves around (Figure 1.2); new solvation sphere must be established. As an estimate, it should take roughly about 200 vibrational periods or about 1 ps for a solvent molecule to make diffusional jump from one position to another. The A^* complex is formed in the ground state geometry in a solvent cage that delays its relaxation to the equilibrium geometry. One could expect the collection of molecules A^*_{FC} to make a succession of configurational adjustments before settling down into an equilibrium Boltzmann distribution of vibrational states. The whole process may take about 10 ps. Thermally equilibrated A^* is a thermodynamic state; it represents an ensemble of A^* molecules that is at ambient temperature with respect to vibrations (a solvated molecule really does not have translation or free rotation).[79]

A representation of molecular electronic state energy levels, with singlet and triplet states in separate columns, is referred to as the Perrin-Jablonski diagram (Figure 1.3). Often, vibrational sublevels are shown schematically as well. Radiative transitions from one level to another are indicated by straight arrows and non-radiative ones by wavy arrows. Most often, the levels correspond to vibrationally relaxed electronic states, i. e. to an equilibrium geometry of each individual state. Sometimes, an effort is made to show the state energies at two or more geometries, and as this representation becomes more elaborate, the diagram gradually turns into a drawing of a slice through potential energy surfaces (Figure 1.4).

Thermally equilibrated excited states have a molar energy, entropy, and free energy and hence standard redox potentials. They have a definite structure, chemical reactivity, absorption spectrum, etc. Chemically speaking, a thermally equilibrated excited state is an isomer of the ground state. As is true for ground state species, the properties of thermally equilibrated excited states are independent of how they are prepared.[79]

After the thermally equilibrated excited state is formed (usually S_1[2]) through internal conversion (Figure 1.3) other processes could be observed, leading the system to ground state relaxation

[1] The velocity of an electron making one complete circuit in a Bohr orbit is $\sim 10^{16}$ Å/sec. Thus, an electron may move on the order of 10 Å in 10^{-15} sec. Since 10 Å is the order if size of many commonly encountered groups of atoms (chromophores) responsible for absorption of light, we deduce that the timescales of photon interaction and electron are of the same order of magnitude.[76]

[2] Kasha's rule, for most photochemical reactions we need consider only the lowest excited singlet state (S_1) or the lowest triplet state T_1.[80]

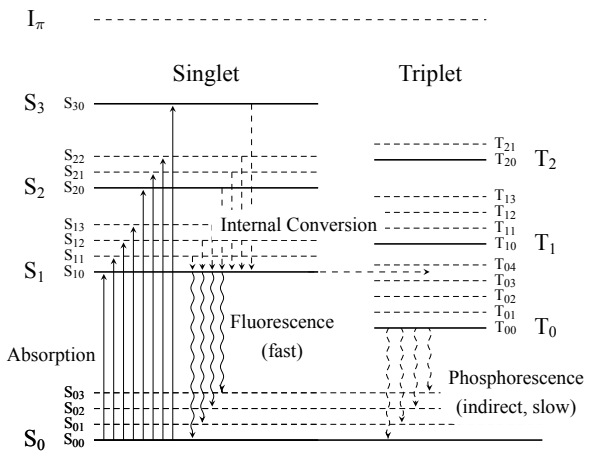

Figure 1.3. One possible form of a Perrin-Jablonski diagram, where I_π – ionisation level, T – triplet and S – singlet state.

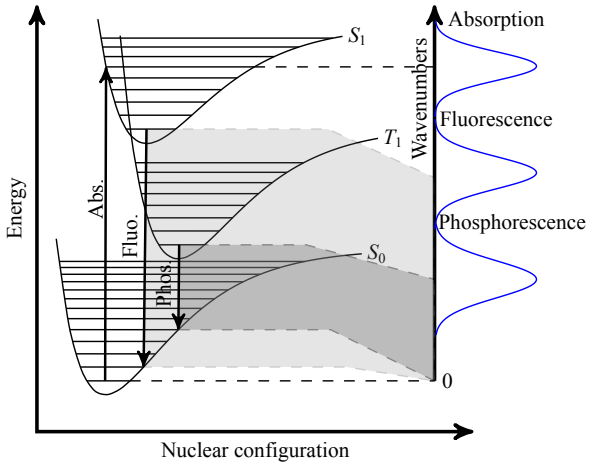

Figure 1.4. The relationship of observed radiative transitions to potential energy curves (schematic) [28].

(Figure 1.5) with significantly different rates (Table 1.2). For example molecules in the S_1 state can also undergo a spin conversion to the first triplet state T_1 (Figure 1.3). Emission from T_1 is termed phosphorescence, and is generally shifted to longer wavelengths (lower energy) relative to the fluorescence. Conversion of S_1 to T_1 is called intersystem crossing. Transition from T_1 to the singlet ground state is forbidden, and as a result the rate constants for triplet emission are several orders of magnitude smaller than those for fluorescence. Molecules containing heavy atoms such as bromine and iodine are frequently phosphorescent. The heavy atoms facilitate intersystem crossing and thus enhance phosphorescence quantum yields.[81]

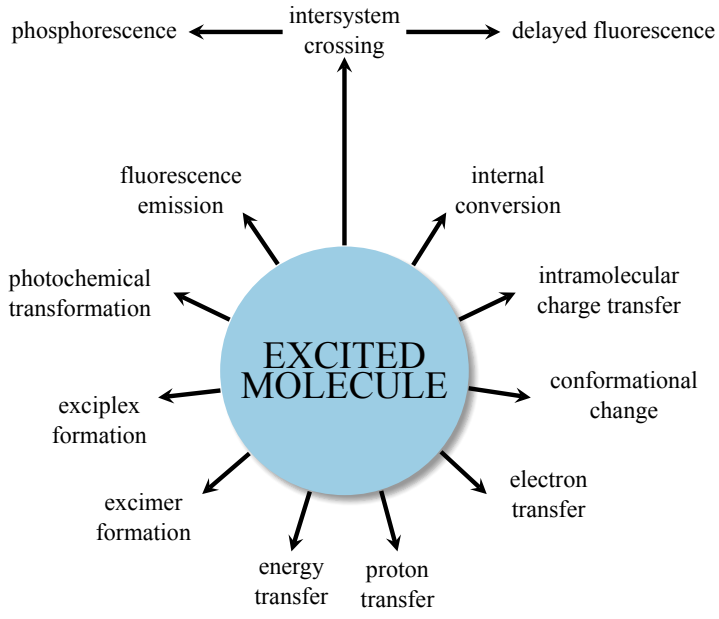

Figure 1.5. Possible de-excitation pathways of excited molecules [82].

Talking about molecular and supramolecular systems one should always consider any electronic transitions from one state to another according to the molecular orbital theory.

In chemistry, Molecular Orbital (MO) theory is a method for determining molecular structure in which electrons are not assigned to individual bonds between atoms, but are treated as moving under the influence of the nuclei in the whole molecule.[83] Electrons are shared among individual atoms in a molecule to form covalent chemical bonds. Single, double and triple bonds can form between carbons atoms in a molecule.

MO theory, proposed in the early twentieth century in 1928 by Robert S. Mulliken and Friedrich Hund, revolutionized the study of bonding by approximating the positions of bonded electrons – the molecular orbitals as Linear Combinations of Atomic Orbitals (LCAO). MO theory applies the wavelike behaviour of electrons as predicted by quantum mechanics, in that electrons no longer deterministically are given defined coordinates, but rather are given probable locations accord-

ing to the mathematical wave functions defining all the possible positions of the electrons. These wave functions, or electron eigenstates, quantitatively describe the atomic orbital basis in which an electron can temporarily reside. Molecular orbitals result from the mixing of these atomic orbitals. In this theory, each molecule has a set of molecular orbitals, in which it is assumed that the molecular orbital wave function ψ_j can be written as a simple weighted sum of the n constituent atomic orbitals χ_i, according to the following equation:

$$\psi_j = \sum_{i=1}^{n} c_{ij}\chi_i \tag{1.1}$$

The interaction between two atomic or molecular orbitals will form two new orbitals. One new orbital is antibonding orbital which has the higher energy than the original molecule orbital. The other new orbital is the bonding orbital which is lower in energy than the initial one.

Table 1.2. Time regime for photophysical processes and associated transitions.

Process	Transition	Timescale, s
Light Absorption (Excitation)	$S_n \longleftarrow S_0$	$\sim 10^{-15}$ (instantaneous)
Internal Conversion	$S_n \longrightarrow S_1$	10^{-14} to 10^{-11}
Vibrational Relaxation	$S_n^* \longrightarrow S_n$	10^{-12} to 10^{-10}
Intersystem Crossing	$S_1 \longrightarrow T_1$	10^{-11} to 10^{-6}
Fluorescence	$S_1 \longrightarrow S_0$	10^{-9} to 10^{-6}
Phosphorescence	$T_1 \longrightarrow S_0$	10^{-3} to 100
Non-Radiative Decay	$S_1 \longrightarrow S_0$	10^{-7} to 10^{-5}
	$T_1 \longrightarrow S_0$	10^{-3} to 100

The stabilization of the bonding molecular orbital and destabilization of the antibonding orbitals can increase when the overlap of two orbitals increases.[84]. In molecular interactions, two very important orbitals can be identified: the Highest Occupied Molecular Orbital (HOMO) and the Lowest Unoccupied Molecular Orbital (LUMO). The HOMO-LUMO concept (namely interaction between these two orbitals in photoreactions and other photoactivated reactions) is often used in photochemistry to understand photoprocesses happening in the systems.

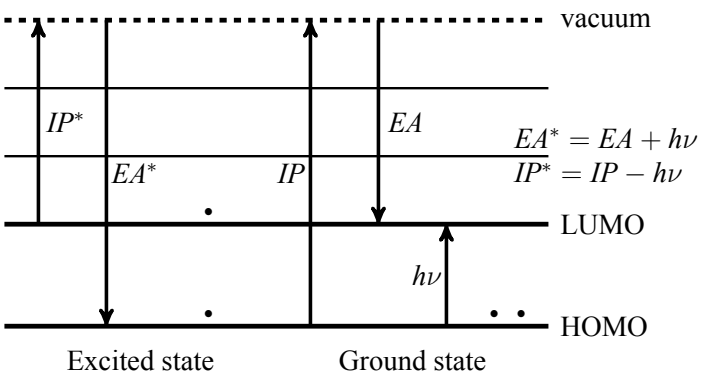

Figure 1.6. Relationships between HOMO, LUMO, EA, IP [76].

Chemical activity of molecules results from the behaviour of valence electrons, and the highest occupied (HO) orbital often determines the lowest-energy electronic pathways available for reaction. We may associate $-IP_1$ (ionisation potential) with energy of HO orbital. The energy of lowest unoccupied (LU) orbital in the ground state could be identify with the molecule's electron affinity (EA). The knowledge of IP_1 and electronic excitation energies will help to locate the energies of orbitals and to establish an qualitative energetic disposition of a molecules's LU and HO orbitals (Figure 1.6).[76]

Together with the Perrin-Jablonski state diagram of molecular orbitals of a chromophore is of enormous importance in understanding of photophysical processes. The state diagram relates

energies of the lowest excited singlet state and the lowest triplet of a molecule to the energy of the ground state of the molecule. The state diagram is only concerned with energies relative to the ground state, since these energy differences represent the maximum electronic energy available for processes such as energy transfer and energy storage in intermediates. The state energy diagram provides a general and systematic structure for the analysis of the molecular photophysics (radiative and radiationless processes that correspond to electronic transitions between states displayed in the energy diagram).[76]

After of act of excitation, the electron density starts to reorganize its spatial density. This process happens in several femtoseconds and for many cases can be described as instantaneous process. The spatial electron density reorganisation causes changes in molecular properties: strength of bonds change (Acidic properties for 2-naphthol at ground state $pK_a(S_0)=9$ and at excited singlet state $pK_a(S_1)=3$), the dipole moment can change greatly. Immediately after excitation, the system locates in so called Franck-Condon state. In quantum mechanics, the classical concept of the precise position of nuclei in space and associated motion is replaced by the concept of a nuclear or *vibrational wave function* χ, which "codes" the nuclear configuration and momentum but is not as restrictive in confining the nuclear configurations to the regions of space bound by the classical potential-energy curves. In classical mechanics we considered that electronic transitions require a similar nuclear configuration and momentum in the initial and final states at the instant of transition. In quantum mechanics the requirement becomes the *net positive overlap* of the wave functions in the initial and final states at the instant of transition. This overlap is give by the *Franck-Condon integral* $<\chi_i|\chi_f>$. The probability of any electronic transition is directly related to the square of the vibrational overlap integral, i. e., $<\chi_i|\chi_f>^2$, which is called Franck-Condon factor. The Franck-Condon overlap integral $<\chi_i|\chi_f>$ is analogous to the electronic overlap integral $<\psi_i|\psi_f>$, i. e., poor overlap means weak interactions and slow transitions rates.[76]

Consider Figure 1.7, which is a schematic representation of the quantum mechanical basis of the Franck-Condon principle for radiative transitions. Absorption is assumed to initiate from the $v=0$ level of ψ^0. The most likely radiative transition from $v=0$ of ψ^0 to a vibrational level of ψ^* will correspond to he transition for which ψ_0 and ψ_i^* is maximal. As shown, this corresponds to the $v=0$ to $v=4$ transition. Other transitions from $v=0$ to vibrational levels of ψ^* will occur, but with lower probability, as shown. A possible resulting absorption spectrum is shown.[76]

The same general ideas could be applied to radiative transitions from excited-state to ground state (emission), except the overlap should be calculated between χ_0 of ψ^* an the various vibrational levels of ψ^0. Overlaps between ψ^* and ψ^0 will cause radiationless transitions, such systems do not show emission.

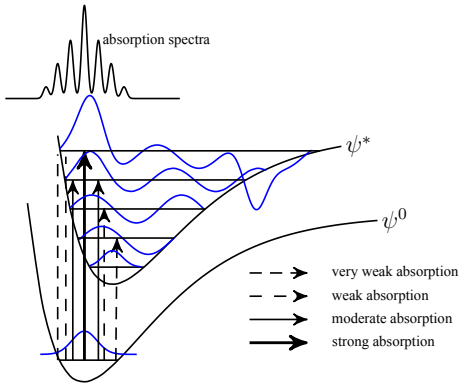

Figure 1.7. Quantum mechanical interpretation of the Franck-Condon principle [76].

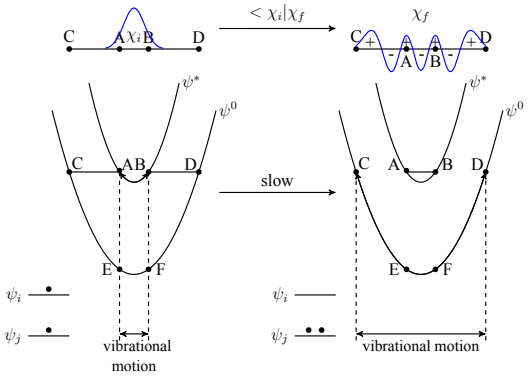

Figure 1.8. Visualization of the quantum mechanical basis for a slow rate of radiationless transitions [76].

Consider Figure 1.8, suppose a molecule starts off on an excited surface ψ^* and during its zero-point motion it makes the trajectory from A to B on the surface. Classically, a "jump" to the

lower surface will require an abrupt change in geometry (i. e., a horizontal "jump" from $B \rightarrow D$ or $A \rightarrow C$) or an abrupt change in kinetic energy (a "vertical" jump from $A \rightarrow E$ or $B \rightarrow F$). The net result of either jump is that the vibration of the molecule will abruptly change from a placid, low-energy vibration between points A and B to a violent, high-energy vibration between points C and D. Both the position and momentum characteristics if the vibration have suffered drastic change. Electrons resist drastic changes in orbital movements or spatial location; nuclei resist drastic changes in their vibrational motion of spatial geometries. Visually, the wave function χ_i (representing initial excited state ψ^*) is different in form (positive everywhere, no node) from that of ψ^0 (highly oscillatory).[76]

The vertical jump from ψ^* to ψ^0 may be thought of as one for which a rate-limiting electron perturbation occurs first and *promotes* the transition from ψ^* to ψ^0. Nuclear motion is now suddenly controlled by the ψ^0 surface rather that ψ^* and *acceptor* vibrations must now be found to soak up the excess potential energy associated with the jump. The horizontal jump may be regarded as one for which a rate-limiting nuclear geometry perturbation occurs first and *promotes* the transition from geometry $A \rightarrow C$ or $B \rightarrow D$. Electronic motion then suddenly switches from that of ψ^* to that of ψ^0. The vibration which brings ψ^* from $A \rightarrow C$ or $B \rightarrow D$ may also act as an acceptor of the excess energy. The horizontal jump is related to quantum mechanical "tunelling", and can be interpreted as being due to the very small overlap of χ_i and χ_f outside the regions of the classical potential-energy surfaces.[76] If the initial and final potential surfaces cross, the overlapping integral for wave functions will be greater that zero $\int \chi_i \chi_f > 0$, and so radiationless transition will be highly favourable, depending on value of overlapping integral.

It was shown by Einstein in 1916, that deexcitation of electron excited state by spontaneous emission[1] is governed by:

$$\frac{\delta N(t)}{\delta t} = -A_{21} N(t),$$

where where A_{21} is the rate of spontaneous emission. In the rate-equation A_{21} is a proportionality constant for this particular transition in this particular light source. The constant is referred to as the Einstein A coefficient, and has units s^{-1}. The above equation can be solved to give:

$$N(t) = N(0) e^{-A_{21} t} = N(0) e^{-k_{rad} t},$$

where $N(0)$ is the initial number of light sources in the excited state, t is the time and k_{rad} is the radiative decay rate of the transition. The number of excited states N thus decays exponentially with time, similar to radioactive decay. After one lifetime, the number of excited states decays to 36 % of its original value ($\frac{1}{e}$-time). The radiative decay rate k_{rad} is inversely proportional to the lifetime τ_{21}:

$$A_{21} = k_{21} = \frac{1}{\tau_{21}}.$$

In the rate-equation above, it is assumed that decay of the number of excited states N only occurs under emission of light. In this case one speaks of full radiative decay and this means that the quantum efficiency is 100 %. Besides radiative decay, which occurs under the emission of light, there is a second decay mechanism; non-radiative decay. To determine the total decay rate k_{tot}, radiative and non-radiative rates should be summed:

$$k_{tot} = k_{rad} + k_{nrad},$$

where k_{tot} is the total decay rate, k_{rad} is the radiative decay rate and k_{nrad} the non-radiative decay rate. The QY is defined as the fraction of emission processes in which emission of light is involved:

$$QY = \frac{k_{rad}}{k_{nrad} + k_{rad}}.$$

[1] Electron spontaneously goes from excited state to ground state emitting photon with energy $h\nu = E_{exc} - E_0$.

In non-radiative relaxation, the energy is released as phonons, more commonly known as heat. Non-radiative relaxation occurs when the energy difference between the levels is very small, and these typically occur on a much faster timescale than radiative transitions.

1.4 Fundamental concepts of electronic energy and electron transfer

Both processes as energy and electron transfers are closely related. Combination of these processes govern metabolism in living organisms: photosynthesis in plants, respiration in animals and information transfer in living cells as well many other examples.[85]

1.4.1 Electronic energy transfer

Excited states posses excessive amount of energy which they can exchange with another non-excited chromophore:

$$D^* + A \longrightarrow D + A^*$$

The Electronic Energy Transfer (EET) could occur in radiative or non-radiative manner.[82] In the first case the spontaneously emitted photon could be absorbed by another chromophore if emission and absorption spectra of donor and acceptor chromophores are overlapping. The energy transfer in a non-radiative manner could obey to two different mechanisms (Figure 1.9):

1. Förster mechanism or long range dipole-dipole (resonant) interaction mechanism;
2. Dexter mechanism or electron-exchange mechanism.

EET could happens between singlet states, between triplet states, as well as between singlet and triplet states, which is the rarest case. The energy transfer is one of deexcitation pathways of excited state (Figure 1.5).

Förster mechanism

Theodor Förster, discovered process of Resonance Energy Transfer (RET) or as it is called nowadays Förster Resonance Energy Transfer (FRET) in 1946 and developed theory.[86] In this case energy transfer occurs without the appearance of a photon and is the result of long range dipole-dipole interactions between the donor and acceptor. The term RET is preferred because the process does not involve the appearance of a photon. The rate of energy transfer depends upon the extent of spectral overlap of the emission spectrum of the donor with the absorption spectrum of the acceptor, the quantum yield of the donor, the relative orientation of the donor and acceptor transition dipoles, and the distance between the donor and acceptor molecules.[81] The distance dependence of RET allows to study of complex biomolecular structures and dynamics, it provides information about distances on the order of 10 to 100 Å[1] and is thus suitable for investigating spatial relationships of interest in chemistry and biochemistry.[88] The RET is widely represented in nature in light-harvesting complexes among the different photosynthetic species. This complexes consist of proteins and photosynthetic pigments and surround a photosynthetic reaction centre transferring energy, attained from photons absorbed by the pigment, toward the reaction centre by RET.

The rate of energy transfer from a donor to an acceptor $k_{ET}(r)$ is given by:

$$k_{ET}(r) = \frac{1}{\tau_D}\left(\frac{R_0}{r}\right)^6,$$

[1] It is beeing called *spectroscopic ruler* [87]

where τ_D – is the decay time of the donor in the absence of acceptor, R_0 – is the Förster distance, and r – is the donor-to acceptor distance. Hence, the rate of transfer is equal to the decay rate of the donor ($1/\tau_D$) when the D-to-A distance (r) is equal to the Förster distance (R_0), and the transfer efficiency is 50 %. At this distance ($r=R_0$) the donor emission would be decreased to half its intensity in the absence of acceptors. R_0, which can be determined from spectroscopic data, is given by:

$$R_0{}^6 = \frac{9\Phi_0(\ln 10)\kappa^2 J}{128\pi^5\eta^4 N_A},$$

where Φ_0 – is the luminescence QY of the donor in the absence of the acceptor, κ^2 is the dipole orientation factor, n is the refractive index of the medium, N_A is Avogadro's number, and J is the spectral overlap integral calculated as:

$$J = \int f_{\mathrm{D}}(\lambda)\epsilon_{\mathrm{A}}(\lambda)\lambda^4 d\lambda,$$

where f_D is the normalized donor emission spectrum, and ε_A is the acceptor molar extinction coefficient. The orientation factor κ is given by:

$$\kappa = \hat{\mu}_A \cdot \hat{\mu}_D - 3(\hat{\mu}_D \cdot \hat{R})(\hat{\mu}_A \cdot \hat{R}),$$

where $\hat{\mu}_i$ denotes the normalized transition dipole moment of the respective luminophore and $\hat{R}$ denotes the normalized inter-fluorophore displacement. $\kappa^2 = 2/3$ is often assumed for isotropic solution. The sixth power dependence explains why resonance energy transfer is most sensitive to the donor–acceptor distance when this distance is comparable to the Förster critical radius.

Dexter mechanism

Dexter energy transfer is sometimes called short-range, collisional or exchange energy transfer which is a non-radiative process with electron exchange. Dexter Energy transfer although similar to Förster energy transfer, differs greatly in length scale and underlying mechanism. In contrast to the inverse sixth power dependence on distance for the dipole–dipole mechanism, an exponential dependence is to be expected from the exchange mechanism. The rate constant for transfer can be written as:

$$k_{ET} = \frac{2\pi}{h} K J \exp(-2r/L),$$

where J is the integral overlap: $J = \int_0^\infty I_D(\lambda)\varepsilon_A(\lambda)d\lambda$, with the normalization condition $\int_0^\infty I_D(\lambda)d\lambda = 1$ and $\int_0^\infty \varepsilon(\lambda)d\lambda = 1$, where L is the effective average Bohr radius of the excited and unexcited states of the donor and acceptor ($0.7 - 6$ Å, average value 1.5 Å [89]), $\varepsilon_A(\lambda)$ – is absorption spectra of acceptor, $I_D(\lambda)$ – is emission spectra of donor, K – experimental factor.

The difference between Förster and Dexter mechanism include: 1) Dexter mechanism involves the overlap of orbitals so that electrons can occupy the partner molecular orbitals. 2) The reaction rate constant of Dexter energy transfer sharply decreases as a function of the distance between D and A and the distance is generally smaller than 10 Å. 3) The Dexter mechanism can be applied to produce the triplet state of some molecules of interest. 4) The special case of exchange-triplet-triplet annihilation-can "push" the electron to upper singlet states by exchanging the electrons of two triplet molecules.

1.4.2 Electron transfer

The electron transfer process is the cornerstone of life, governing metabolism: cell respiration, photosynthesis; as well as information transfer in organisms. The most well known electron

transfer is the electron transfer between metal ions in solutions in reductive-oxidation reactions, which pupils study in middle school. Thus kind of electron transfer process lies very far from our topic of discussion. We are, primarily interested in systems showing so called Photoinduced Electron Transfer (PET).

The phenomenon has attracted the interest of chemists from many fields. For organic chemistry the PET has uncovered novel pathways for the synthesis of organic molecules.[40] Inorganic chemists have applied PET to development of solar energy storage and conversion systems, utilizing transition metal complexes.[2, 32] It also helps to molecular biologists in investigating photosynthesis and electron-transport in biological systems PET.[90]

In PET, an electron migrates between a photoexcited and ground-state species (Figure 1.9). According to this concept, PET can be classified as an quenching pathway. In fact, like quenching by energy transfer, PET may involve a dynamic interaction between a photoexcited state and neighbouring ground-state species: D and A are the conventional designations of a donor and acceptor. In electron transfer, the excited state, identified by the star, can be an electron donor or acceptor; in energy transfer, the excited state is exclusively an energy donor. Energy transfer can operate by a dipole-dipole (Coulomb) mechanism involving the mutual interaction of electrons. Since mutual contact between the reactants is not required, the dipole-dipole mechanism can be operative over large distances, sometimes greater than $50\,\text{Å}$. Energy transfer by electron exchange, however, requires a closer approach of the reactants to allow for the mutual exchange of electrons. In this respect, energy transfer by electron exchange is similar to electron transfer. On the other hand, efficient energy transfer requires that the excited-state energy of D exceeds that of A. In electron transfer, the energetics are dictated by the redox potentials of D and A, as well as the energy of the excited state.[37]The overall pathway in PET can be summarized as shown in:

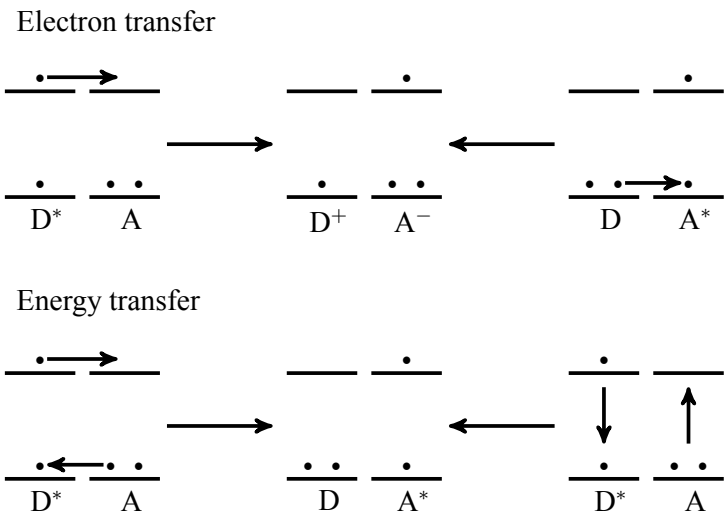

Figure 1.9. Scheme of electron and energy transfer.

$$D^m + A^n \xrightarrow{h\nu} D^{m*} + A^n \rightarrow D^{m+1} + A^{n-1} \leftarrow D^m + A^{n*} \xleftarrow{h\nu} D^m + A^n,$$

the reactants may be neutral (m, $n = 0$) or charged species (m, $n \neq 0$).

The property describing the binding force of an electron to a nucleus is the Ionization Potential (IP), which is the energy required to remove an electron from an atom or molecule in the gas phase. The Electron Affinity (EA), is the energy released when an electron combines with an atom or molecule. On the basis of these definitions, electron transfer is feasible when the electron affinity exceeds the ionization potential:

$$\Delta E = IP - EA,$$

where ΔE is the change in energy accompanying the electron transfer.

When a molecule absorbs a photon, its ionization potential may decrease and its electron affinity may increase:

$$IP^* = IP - E_{00}$$

and

$$EA^* = EA + E_{00},$$

where E_{00} is the zero-zero electronic energy of an excited-state. For the case, where the excited state is an electron donor:

$$\Delta E = IP^* - EA = IP - EA - E_{00}. \tag{1.2}$$

Similarly, when the excited state accepts an electron, we obtain:

$$\Delta E = IP - EA^* = IP - EA - E_{00}. \tag{1.3}$$

The magnitudes of IP and EA are dictated by the ordering of the HOMO and LUMO orbitals (Koopman's theorem, Figure 1.10). On this basis, electrons in low-energy orbitals, e. g. those residing in σ-bonds, are not as easily abstracted as electrons in non-bonding n-orbitals or those occupying higher energy orbitals. Similarly, positive "holes" in low-energy orbitals accept electrons more readily than vacant higher energy orbitals.

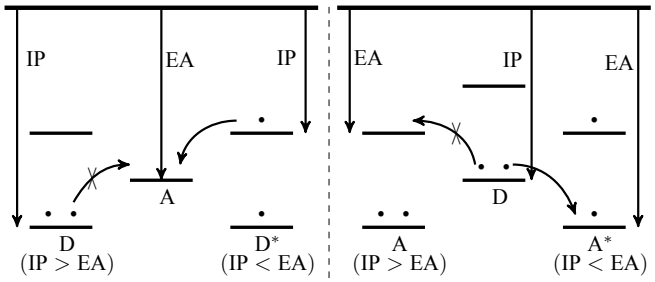

Figure 1.10. The feasibility of PET is dictated by relative energies of donor and acceptor electrons. In this simpified orbital figure, the electrons occupying orbitals can be transferred to other orbitals depending on their IP and EA [37].

Equations 1.2 and 1.3 are intended only to test the feasibility of PET for a given pair of donor and acceptor molecules in the gas phase. Because these equations do not account for electrostatic effects due to ion pairing or solvation energies, they cannot be applied with much confidence to PET in solution or solid environments where significant solvation and Coulomb interactions may take place. To derive more precise thermodynamic expressions, we need to consider the molecular structures of the reactants, their charges, their mobilities, the distances separating the reactants, and the polar nature of the environment.[37]

The seminal work of Marcus[1] and Hush has had a significant impact on the development of PET. The main concepts are clearly presented in works of Kavarnos.[37, 91] The theory includes numerous topics. For us the most important will be consider the concept of a potential energy surface description of photosensitized electron transfer process.

The initial nuclear geometry of the reactant state undergoes reorganization to the transition state prior to electron transfer. The energy of the transition state, $\Delta G^{\#}_{el}$, is gained by intermolecular collisions, in order to satisfy conservation of energy and momentum (Figure 1.11). As an electron jumps from one reactant to the other, the reaction "switches" from the reactant to product surface at the intersection point, which consists of two isoenergetic electronic configurations with one distorted nuclear geometry. The probability of electron transfer at the intersection point is controlled by the electron interaction between reactant and product states. The rate of electron transfer:

$$k_{el} = \mathbf{k} \exp\left(\frac{-\Delta G^{\#}_{el}}{k_B T}\right), \tag{1.4}$$

where **k** is a constant which reflects the electronic barrier of the reaction and $G^{\#}_{el}$ is defined:

$$\Delta G^{\#}_{el} = \frac{\lambda}{4}\left(\frac{\lambda + \Delta G_{el}}{\lambda}\right)^2, \tag{1.5}$$

[1] The Nobel Prize in Chemistry 1992 was awarded to Rudolph A. Marcus "for his contributions to the theory of electron transfer reactions in chemical systems".

and λ:

$$\lambda = \lambda_v + \lambda_s$$

λ is the total reorganizational energy; λ_v the inner-sphere barrier, is the reorganizational energy due to vibrations within the reactants (v = vibrational); and λ_s, the outer-sphere barrier, is the reorganizational energy within the surrounding solvent molecules (s = solvent). ΔG_{el} is the free-change energy at the separation distance, d_{cc}.

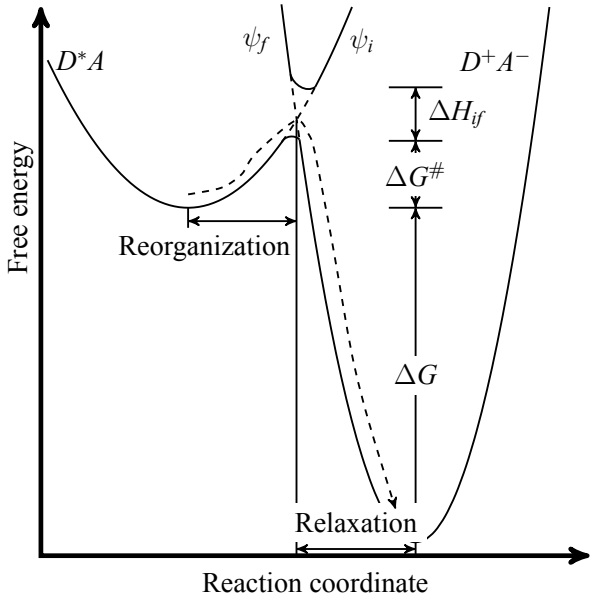

Figure 1.11. A potential energy surface description of PET. $\Delta G^{\#}$ is the activation barrier for electron transfer. H_{if} is the electronic coupling matrix between initial and final energy surfaces. Classical theories of ET apply to situations where $\Delta G^{\#} \gg H_{if}$. ΔG – free energy difference between reactant and product states [91].

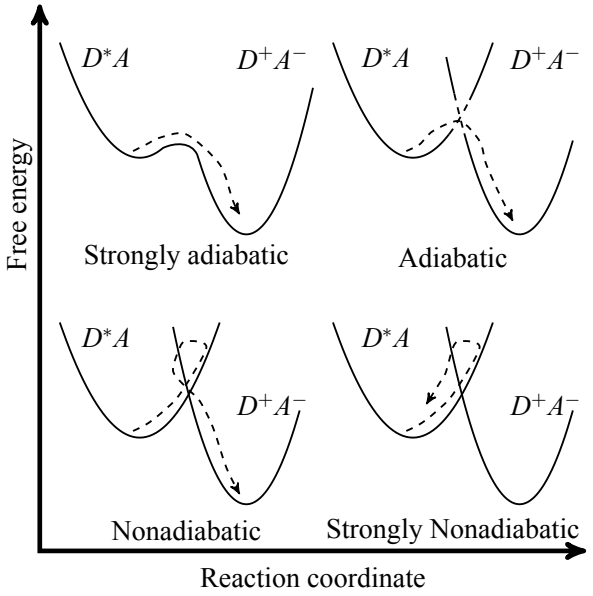

Figure 1.12. Potential energy surface descriptions for adiabatic and nonadiabatic electron transfer. Classical theories of ET are applicable to systems which fall somewhere between adiabatic and nonadiabatic, i. e. $\Delta G^{\#} \gg H_{if}$ [91].

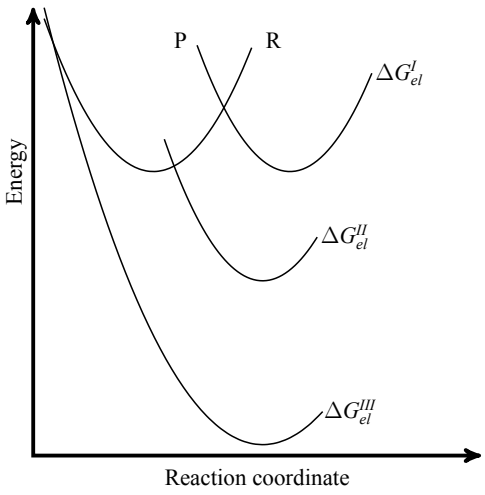

Figure 1.13. Plot of the free energy G versus the reaction coordinate, for reactants (R) and products (P), for three different values of ΔG_{el} [92].

λ is thus related to the entire nuclear reorganization of an electron-transfer reaction. These nuclear barriers, which precede the actual electron transfer, involve bond-length changes within the reactants, and reorientation of the surrounding solvent dipoles.

At the transition state, electron transfer takes place rapidly. During this brief moment, the nuclear geometry of the transition state remains fixed (the Franck-Condon principle). Following electron transfer, nuclear relaxation to the equilibrated successor state takes place. The products then separate from the successor state into the bulk of the solution. The probability of electron transfer at the intersection point is controlled by the electron interaction between reactant and product states. The magnitude of this interaction or "mixing" is given by the electronic coupling matrix, H_{if}, and results in a splitting of the energy surface. At one extreme, if a large electronic energy barrier separates the passage of the electron between the donor and acceptor orbitals, electronic interaction is vanishingly small, i. e., $H_{if} = 0$: the probability of electron transfer is

small, **k** in eq. 1.4 approaches zero, since the reaction surfaces do not cross.[92]

If and when electron transfer occurs, it is defined as nonadiabatic, and the reaction coordinate proceeds abruptly from one surface to the other (Figure 1.12). At large electron interaction energies, the reaction passes smoothly from the reactant to the product surface (Figure 1.12). The rate approaches a value of $\sim 10^{13}\,\mathrm{s}^{-1}$, which is the unimolecular rate of electron transfer within a transition state. In the strong interaction limit, **k** is approximately unity, and the reaction is defined as adiabatic. The electronic interaction can become so large in some cases that the two electronic intermediates in the transition state merge into one short-lived resonance stabilized state with a lifetime of $\sim 10^{-15}$ s. In this strongly adiabatic limit, the rate of charge transfer approaches a maximum $10^{15} - 10^{16}\,\mathrm{s}^{-1}$). Under these circumstances, classical theories of electron transfer break down, since they do not apply to systems where the interaction energy is so large that the transition state is a resonance stabilized complex.[92]

Equation 1.5 predicts a parabolic relationship between the driving force and the activation energy in electron transfer. This relationship, one of the remarkable predictions of Marcus theory and one which runs counter to our intuition at first glance, suggests that the rate of electron transfer should decrease at large negative values of ΔG_{el}. According to eq. 1.5, the rate should maximize at $\Delta G_{el} \simeq \lambda$. Successively making ΔG_{el} more negative (Figure 1.13), by lowering the products' G curve vertically relative to the reactant curve, decreases the free energy barrier $\Delta G^{\#}_{el}$ (given by the intersection of the reactants' and products' curves): that barrier is seen in Figure 1.13 to vanish at some ΔG_{el} and then to increase again.[92]

1.5 Main concepts of time-resolved spectroscopy

In this research molecular/supramolecular systems were studied using steady-state and time-resolved spectroscopies in UV-visible regions. The peculiarity of optical spectroscopy comparing to other types of spectroscopies is that most structurally organized matter (higher than atoms) reacts with a resonant electromagnetic fields in the optical frequency range. Therefore, optical spectroscopy is currently used widely to obtain information on the substance. Interaction of matter with electromagnetic radiation in the frequency range happens due to the interaction of the electrons (electron density) and radiation, as it was discussed earlier.

Time-resolved spectroscopy studies dynamic processes in materials or chemical compounds by means of spectroscopic techniques. Most often, processes are studied after sample excitation, but in principle, the technique can be applied to any process that leads to a change in properties of a substance. Advancement in the field of quantum electronics, non-linear optics and laser physics, achieved by the end of the XX$^{\text{th}}$ century, yielded light pulses with a time of a few femtoseconds (1 fs = 10^{-15} s). Such pulse widths corresponds to only a few periods of light field oscillation and are limited in the visible frequency range. Femtosecond laser pulses allowed for the first time to observe in real time the dynamics of fast elementary molecular processes and get snapshots of molecules and groups of atoms in various stages of chemical reactions. Temporal resolution provided by femtosecond laser pulses is sufficient for the study of any, even the most rapid processes of molecular dynamics as short as several 10^{-15} s.

After short laser pulse excites electron system of sample, registering the relaxation of it to the ground state is the basis of time-resolved spectroscopy, which is achieved in different ways. Conventionally, all the great variety of methods [93] can be divided into two groups:

– time-resolved absorption spectroscopy;
– time-resolved emission spectroscopy.

A time-resolved spectrum is a collection of measurements performed at different (distinct) times and wavelengths. Three measurement sequences can be distinguished [94]:

1. Measurements can be performed simultaneously at a great number of wavelengths and at a certain time delay with respect to the exciting pulse, called time-gated spectrum. For Tran-

sient Absorption Spectroscopy (TRABS), a time-gated spectrum is sensitive to baseline fluctuations.
2. At a particular wavelength a decay trace is measured as a function of time with respect to the exciting pulse. A collection of such decay traces measured at different wavelengths constitutes a time-resolved spectrum.
3. Simultaneous detection of decay traces at a great number of wavelengths, providing high resolution in both dimensions, is possible with a (synchroscan) streak camera in combination with a spectrograph.

1.5.1 Time-resolved absorption spectroscopy

Time-resolved absorption spectroscopy allows observation of the dynamic changes in the properties of the system after its excitation, provided that:
- Excited state is populated sufficiently;
- Ground-state population is decreased measurably;
- Fate of excited states probed by absorption measurements;
- Probe pulse is relatively easy to tune;
- Even "dark" excited states can be seen by $S_n \leftarrow S_1$ absorption.
- Global picture of the involved components can be obtained;
- Very good temporal resolution and signal-to-noise is possible.

During relaxation process of the excited electron system, the system runs through a number of excited states which is accompanied by a decrease or increase in the absorption coefficient in the different regions of the electromagnetic spectrum (for molecular systems as a rule, the optical range ($390-780$ nm), near-ultraviolet ($300-400$ nm), middle ultraviolet ($200-300$ nm) and near-infrared ($800-1400$ nm) ranges[1]. By following the changes of absorption spectrum at different time-delays after exciting the system the two-dimensional map (Figure 1.15) of absorption could be built. The absorption signal is calculated as follows:

$$\Delta O.D.(t,\lambda) = -\log \frac{I(t,\lambda)}{I_0(t,\lambda)},$$

where I – intensity of transmitted light after excitation at given time-delay (t) and wavelength (λ), I_0 – intensity of transmitted light before excitation pulse,

The absorption maps could contain two types of signals:
- Positive:
  Excited state absorption of singlet $S_{n+1} \leftarrow S_n$ or triplet states $T_{n+1} \leftarrow T_n$ (log – function is negative, so after excitation less light of probe is passing through in this particular spectral region);
- Negative:
  - Ground State Bleaching (GSB) (log – function is positive, so after excitation more light of probe is passing through in this particular spectral region)
  - Stimulated Emission – the emission of electromagnetic radiation in the form of photons of a given frequency, triggered by photons of the same frequency[2].

Very often it happens that the system has several excited states, having absorption spectra, located close to each other, thus overlapping (Figure 1.14), sometime it provides the experimentalist with too much information, making it difficult to interpret photophysical processes. Even for the two-state system to determine the true absorption spectra and their dynamics is a complex task. One should solve the inverse problem without knowledge of the relaxation rates and the

[1] Typically, unsaturated organic molecules in ground state possess several absorption bands in the "photochemical" region, $200-700$ nm, saturated organic compounds are generally "transparent" in this region.

[2] http://www.thefreedictionary.com/stimulated+emission

absorption coefficients of each level. In cases of strong overlaps, data should be analysed along with the data provided by time-resolved emission spectroscopy.

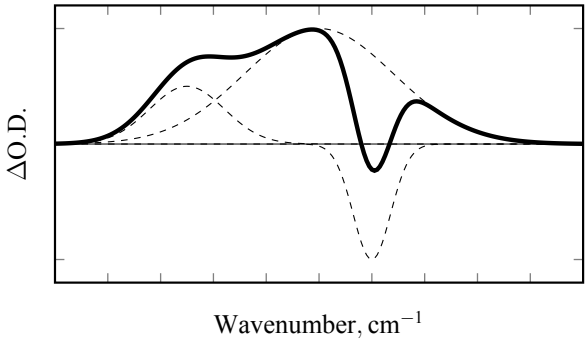

Figure 1.14. Simulation of spectral overlap between two positive and one negative signals.

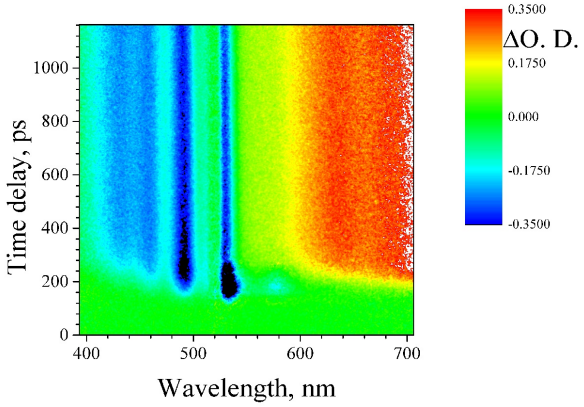

Figure 1.15. Example of time-resolved 2D transient absorption map.

1.5.2 Time-resolved emission spectroscopy

Luminescence: fluorescence and phosphorescence give information not only about the molecule itself, but also its environment. Steady-state measurements lose some information on dynamic processes such as isomerisation, solvation, anisotropy dynamics, etc.

In the case of emission spectroscopy radiative relaxation processes of the electronic system are studied. But since there are practically no molecular systems wherever radiative relaxation was 100 % efficient, the Quantum Yield (QY) of radiative relaxation pathways should be known.

1.6 Experimental

1.6.1 Important experimental factors for time-resolved spectroscopy

There can be different types of experimental organization of time-resolved experiments: strong pulse, weak probe; strong pump- strong probe; several pumps, etc. In this work we used classical scheme of multi-coloured Transient Absorption Spectroscopy (TRABS) with intense *Pump* and weak *Probe* pulses and emission spectroscopy with intense *Pump*.

There are several important factors for time-resolved spectroscopy, that should be mentioned:

1. ***Intense and short*** **pump** ***pulse.***

”+” – advantages:

- Fast excitation provides temporally “clean” start of process.
- High intensity of the light causes non-linear effects, that can be used for excitation and probing.

”–” drawbacks:

- Broad spectrum gives lack of spectral selectivity.
- Non-linearity may induce complications in the dynamics in areas of interest.
- Artefacts (Raman-scattering of solvent): - may complicate early timescale dynamics.

How strong should the *pump* pulse be?

The pump intensity depends in what regime one is working at: linear or non-linear absorption.

- The excitation pump should cause absorption saturation, but at the same time it should not cause overheating, that could damage the solvent and compound of interest.

– In non-linear absorption the pump should be intense enough to cause multi-photon absorption.

2. ***Weak and short* probe *pulse with broad Spectrum*[1].**

"+" – advantages:

– Fast probing allows to make a fine time grid for accurate resolving of the dynamics.
– Broad probe spectrum allows observation of different photochemical processes in one experiment.

"–" – drawbacks:

– Broad spectrum gives lack of spectral selectivity.
– Non-linearity may induce the probe-induced dynamics[2].

How weak should the Probe be?

The intensity of the Probe pulse should fulfill these requirements:

– Additional ΔA amplitude induced by Probe itself has to be smaller than the noise level needed to resolve Pump-induced changes.
– It should be easily achievable in the absorption region with relatively identical intensity in the whole spectra.

3. ***Temporal resolution.***

a. Direct Temporal Resolution:

– Absorption: Flash-photolysis – fast detector and fast oscilloscope.
– Fluorescence: Time-Correlated Single Photon Counting (TCSPC).
– Streak camera detection.

A streak camera operates (Figure 1.16) by transforming the temporal profile of a light pulse into a spatial profile on a detector, by causing a time-varying deflection of the light across the width of the detector. In particular, a light pulse enters the instrument through a narrow slit along one direction. It then gets deflected in the perpendicular direction so that photons that arrive first hit the detector at a different position compared to photons that arrive later. The resulting image forms a "streak" of light, from which the duration, and other temporal properties, of the light pulse can be inferred. Usually, in order to record periodic phenomena, a streak camera needs to be triggered accordingly, similarly to an oscilloscope.

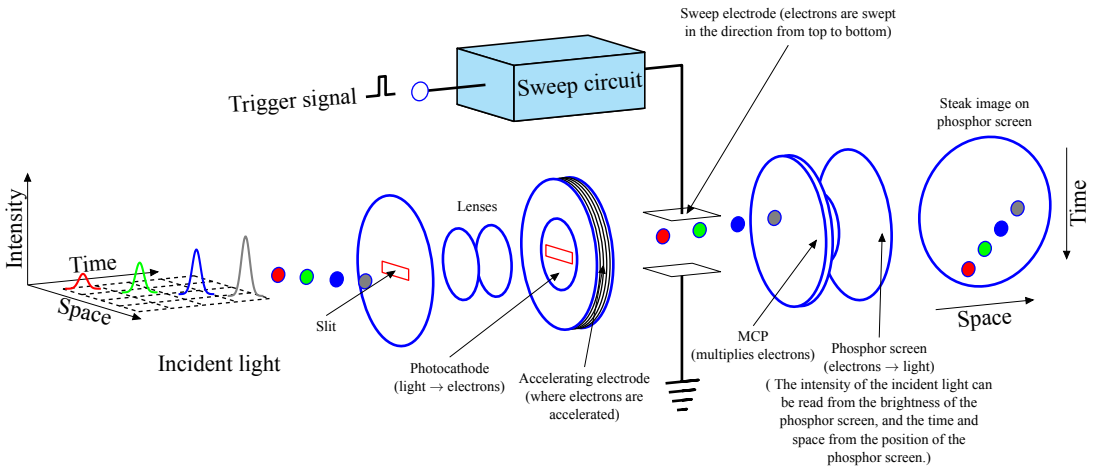

Figure 1.16. Principle scheme of a conventional streak camera (http://www.physics.cit.ie).

The time resolution is the main characteristic of streak camera devices. At present, the fastest streak camera, FESCA-200 (Hamamatsu) has time resolution 200 fs. A range

[1] By other words – white light source.
[2] In case of intense probe pulses.

of devices is available from different manufacturers with the time resolution of about one picosecond. It hardly is a surprise, that the higher time resolution means a much higher cost. Therefore, slower, $10-20$ ps, but cheaper streak cameras are probably a reasonable compromise between the time resolution and the price.
It should be noted that the time resolution is not the only important characteristic to be considered when selecting a streak camera for spectroscopy applications. Another important temporal specification of the camera is the trigger jitter. If the signal is not strong and the averaging of few shots is unavoidable, the trigger jitter will determine the final time resolution of the measurements. Then the time resolution can hardly be better than 1 ps, since the trigger signals the "normal" electric signal and is subjected to all the speed limitations of the electronic devices.[93]

b. Pump-Probe Correlated Temporal Resolution.
   - Strong *pump* and weak *probe* (transient absorption, transient gating);
   - Strong *pump* and strong *probe* (multi-photon ionization, Raman, etc.);
   - Strong *pump* and strong *gate* (fluorescence up-conversion, optical Kerr effect);
   - Coherent methods.

c. Temporal resolution from data analysis.

4. ***Spectral resolution and detection efficiency.*** Spectral resolution is determined by spectral resolution of the detector. Detection quantum efficiency (ratio of the photons creating a photo-response, e. g. generating electron, to the total number of the incident photons), sensitivity, dark count rate and etc. are determined by working characteristics of photodetectors.

- Streak camera resolution is determined by spectral resolution of spectrograph, the width of its slits, size of the detector and stability of electronics. Thus the Streak camera measures photon flux indirectly, by converting it into the flux of electrons using photo-cathode. Spectral sensitivity of any photo-cathode is extremely non-linear on the red side of the spectrum. That is why spectral information which is obtained from Streak camera measurements should be corrected. Typically one may expect to find devices working in $200-700$ nm (bialkali photo-cathode) $200-850$ nm (photo-cathode type S-20) and $200-950$ nm (S-25) ranges. Naturally, the devices with longer red wavelength range have higher dark current.
- Time-Correlated Single Photon Counting (TCSPC) techniques show spectral sensitivity, which is highly depend on spectral sensitivity of spectrograph and detectors they are using. But because photon counting detectors use photo-cathodes for their work, on the red side of the spectra sensitivity is rather weak.
- There are very many sources and types of noise, also three types are the most common for measurements in the optical spectroscopy applications [93], which are:
  - Quantum noise (or photon noise, or shot noise, or Poisson noise). Let us assume that the light source has a constant emission rate, however, the experimentally available value is the number of photons measured in a limited time interval, which is the random value by its nature. This type of noise cannot be eliminated when dealing with quantum objects (but in some applications can be reduced to negligible level). This type of noise can also be found in electric circuit with low current values, when the discrete nature of current carriers (electrons)prevails thermal noise.
  - Thermal noise (or Johnson noise) has actually the same origin as quantum noise but at low frequency limit. At temperatures above absolute zero the space is filled by thermal radiation, which has a quantum nature, i. e., it fluctuates. When applied to electric circuits this noise is called Johnson noise.
  - $1/f$ noise – generation-recombination noise has a spectral density proportional to the inverse of the frequency (which has given the name to this type of noise). Usually it dominates in measurements which take a long time. These measurements are said to below frequency measurements. Depending on the measuring technique and devices used,

the frequency limit for the $1/f$ noise domination can be from 10 Hz (0.1 s in time domain) or smaller.

5. ***Data analysis and modelling.***

– Data analysis is highly important for unveiling processes happening in the system. There is a lot of methods allowing to correct baseline [95], allowing to extract lifetimes distribution from complex luminescence decays using for example method of maximum entropy [96, 97], different deconvolution techniques of signal and Instrument Response Function (IRF) [98–100] and etc.

New twist of time-resolved spectroscopy [101, 102] raised in last decade and spread in many different areas of physics and chemistry so called multidimensional coherent spectroscopy:

– By a first pulse prepare a particular state;
– By the second pulse induce some dynamics in this state;
– By a Probe pulse (strong or weak) resolve the dynamics in this new state.

1.6.2 Steady-state spectroscopy

1.6.2.1 Absorption spectra

The electromagnetic radiation can be absorbed by electron system of molecule, causing electron transitions between different electronic energy states in the molecule. At different wavelength of incident light there is a different degree of absorption. At room temperature organic molecules are normally in their electronic ground states S_0, and measurement of an absorption spectrum provides information about transitions from S_0 to electronicly excited states. The law of Beer-Lambert-Bouguer links absorption (A_λ[1]) and intensity of incident and transmitted light in this form:

$$A_\lambda = \log_{10} \frac{I_0}{I} = \varepsilon \cdot c \cdot l,$$

where c is concentration [mol$\cdot$l^{-1}], ε_λ [l$\cdot$mol$^{-1}\cdot$cm^{-1}] is molar extinction coefficient at wavelength λ [nm] and l [cm] is the optical pathlength of the sample. All absorption spectra in this work were recorded on a spectrophotometer Cary 5G UV-Vis-NIR (Varian) using 10, 2 and 1 mm synthetic quartz (Suprasil) quartz cells .

1.6.2.2 Emission spectra

In order to observe emission spectra of organic molecules, first their excited electronic states need to be populated. This is achieved by light absorption, the obtained emission is referred to as **photo**luminescence. The measurement can be performed in a continuous mode of excitation (steady state photoluminescence) or with pulsed excitation (pulsed photoluminescence). Since both the wavelength of the exciting light and that of the detected emitted light can be varied, photoluminescence is intrinsically a two-dimensional spectroscopic technique, but the full two-dimensional spectra are rarely measured. A spectrum showing the dependence on the frequency (or wavelength) of the emitted light is referred to as an emission spectrum, and a spectrum showing the dependence on the frequency (or wavelength) of the exciting light of constant intensity is called the excitation spectrum.[81]

Luminescence: fluorescence and phosphorescence at varied temperatures ($77-295$ K) spectra were recorded on a Fluorolog-3 (Jobin Yvon) spectrophotometer with iHR-320 spectrograph (range $150-1500$, nm with grating 1200 gr/mm, blazed at 500 nm) and photomultipliers from Hamamatsu Photonics: R928 (range $185-900$ nm) and R2658 (range $185-1100$ nm). Usually,

[1] In spectroscopy, the absorbance A (also called optical density – O. D.).

the excitation wavelength was chosen to correspond to the maximum of the molecule absorption band. The correction of the emission spectrum was performed with respect to the spectral sensitivity of detector and excitation source stability.

Quantum yield is the number of emitted photons relative to the number of absorbed photons. The fluorescence quantum yield is the ratio of the number of photons emitted to the number absorbed. The rate constants k_r and k_{nr} both depopulate the excited state. The fraction of luminophores that decay through emission, and hence the quantum yield, is given as:

$$\Phi = \frac{k_r}{k_r + k_{nr}}$$

Quantum yields of molecular systems (for optical diluted solutions) were determined versus standards of known quantum yield:

$$\Phi_x = \Phi_s \cdot \left(\frac{I_x}{I_s}\right) \cdot \left(\frac{F_S}{F_x}\right) \cdot \left(\frac{\eta_x}{\eta_s}\right)^2,$$

where the I_s are the integrated emission intensities of the standard and sample solutions under identical conditions; F means fraction of light absorbed; Φ_s is the quantum yield of the standard and η denotes refractive index of medium [103]; or using integrating sphere (Labsphere optical Spectralon integrating sphere: diameter of 100 mm, which provide a reflectance $>99\%$ over $400-1500$ nm range).

1.6.3 Time-resolved spectroscopy

1.6.3.1 Principle schemes

In this work three different set-ups were used to measure time-resolved absorption spectra or time-resolved luminescence spectra, decays in different time ranges (Figure 1.17): sub-pico (Figure 1.18), sub-nanosecond (Figure 1.19) and microsecond, sub-millisecond and millisecond (Figure 1.20).

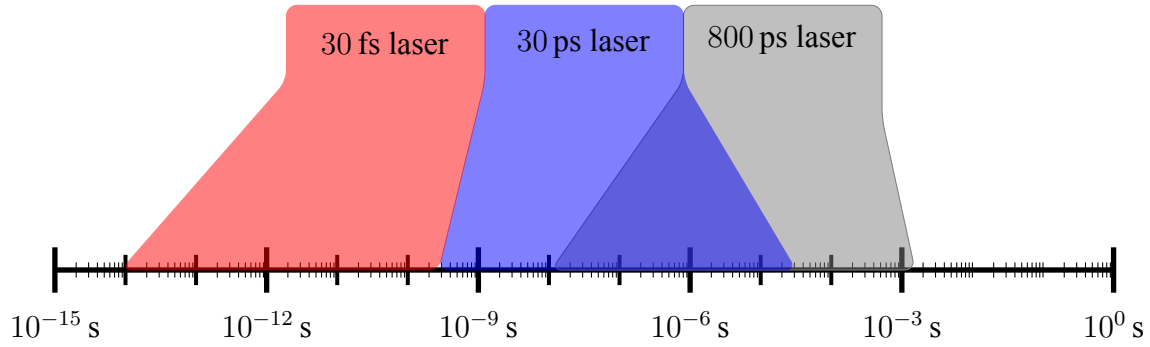

Figure 1.17. Time-scales of different experimental set-ups, used in the work.

1.6.3.2 Sub-picosecond

Measurements were performed simultaneously at a number of wavelengths (spectral width 600 nm) and at a certain time delay with respect to the exciting pulse (time–gated spectrum). A collection of such time–gated spectra at different time delays constitutes a time-resolved spectrum.

The experiment was based on a femtosecond 1 kHz Ti:Sapphire system producing 30 fs, 0.8 mJ laser pulses centred at 800 nm (Femtopower Compact Pro) coupled with optical parametric generator (Light Conversion Topas C) and frequency mixers was used to excite samples at the maximum of the ground state absorption band. White light continuum ($360-1000$ nm)

pulses generated in a 2 mm D_2O cell were used as the probe. The variable delay time between excitation and probe pulses was obtained using a delay line with 0.66 fs resolution. The solutions were placed in 2 mm pathlength circulating cell. White light signal and reference spectra were recorded using a two-channel fibre spectrometer (Avantes Avaspec-2048-2). A home written acquisition and experiment control program in LabVIEW made it possible to record transient spectra with an average error less than 10^{-3} of O. D.[1] for all wavelengths. The temporal resolution of the set-up was better than 50 fs. A temporal chirp of probe pulse was corrected by a computer program with respect to a Lorenzian fit of a Kerr signal generated in a 0.2 mm glass plate used in a place of sample.

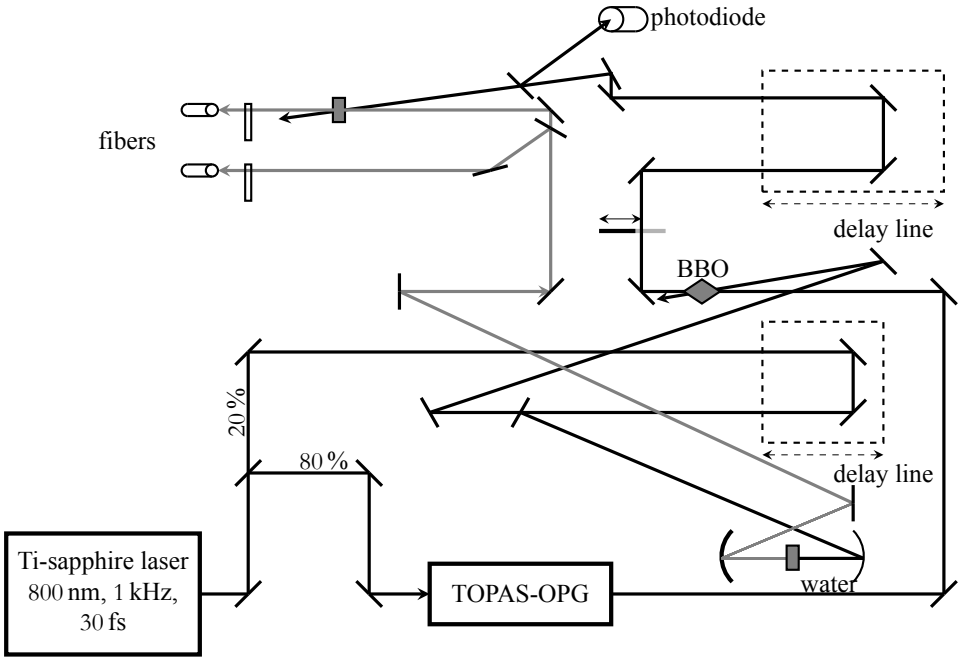

Figure 1.18. Scheme of sub-picosecond laser set-up; OPG – optical parametric generator; BBO – barium borate crystal.

1.6.3.3 Sub-nanosecond set-up

Detection of decay traces at a number of wavelengths (spectral width 300 nm) simultaneously, providing high resolution in both dimensions, is possible with a streak camera in combination with a spectrograph.[104]

The picosecond transient absorption set-up was built as follows (Figure 1.19). The frequency-tripled Nd:YAG amplified laser system (30 ps, 30 mJ @1064 nm, 20 Hz, Ekspla model PL 2143) output was used to pump an optical parametric generator (Ekspla model PG 401) producing tunable excitation pulses in the range $410 - 2300$ nm. The residual fundamental laser radiation was focused in a high pressure Xe filled breakdown cell where a white light pulse for sample probing was produced for nanosecond timescale measurements. For longer scales (micro- and milliseconds), the white light probe was obtained using an ensemble of light emitting diodes (Roithner Lasertechnik, from 365 to 710 nm) working in flash mode in a multi-furcated fiber-optic cable (8-cores, Avantes). All light signals were analysed by a spectrograph (Princeton Instruments Acton model SP2300) coupled with a high dynamic range streak camera (Hamamatsu Photonics C7700). Accumulated sequences (sample emission, probe without and with excitation) of pulses were recorded and treated by *HPDTA* (Hamamatsu Photonics) software to produce two-dimensional maps (wavelength vs delay) of transient absorption intensity in the range $300 - 800$ nm. Typical measurement error was better than 10^{-3} O. D.

[1] A time–gated spectrum is very sensitive to baseline fluctuations.

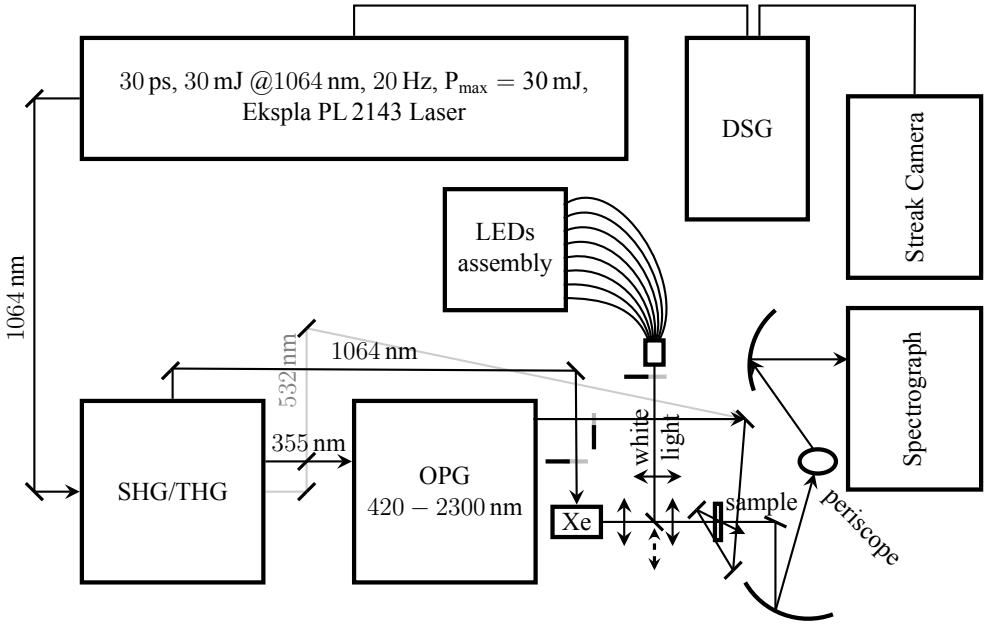

Figure 1.19. Scheme for sub-nanosecond laser set-up; SHG/THG – second/third harmonic generator, OPG – optical parametric generator, LED – light emitting diode, DSG – digital signal generator.

1.6.3.4 Micro- and millisecond set-up

The scheme of micro- – millisecond set-up is presented on Figure 1.20. It was built on commercially available spectrofluorometer Fluorolog-3 (Jobin-Yvon) (see subsection 1.6.2.2, 23 p). In order to measure long time luminescence up to several milliseconds (5 ns–20 ms) Multi-Channel Scaling (MSC) technique was used. We used Picolo-AOT MOPa Nd:YVO laser with 800 ps (Innolas laser, Germany) with variable frequency (10 – 5000 Hz) as excitation source, allowing us have 266 nm, 355 nm, 532 nm and 1064 nm excitation wavelength with high output power, up to 200 mW. The photon counts from photomultiplier detectors (see 23 p.) were send to fast counting card P7879 100ps/10GHz Time off flag/Multiscaler (Comtex GmBH, Germany), allowing to work at high frequency rate up to 10 GHz.

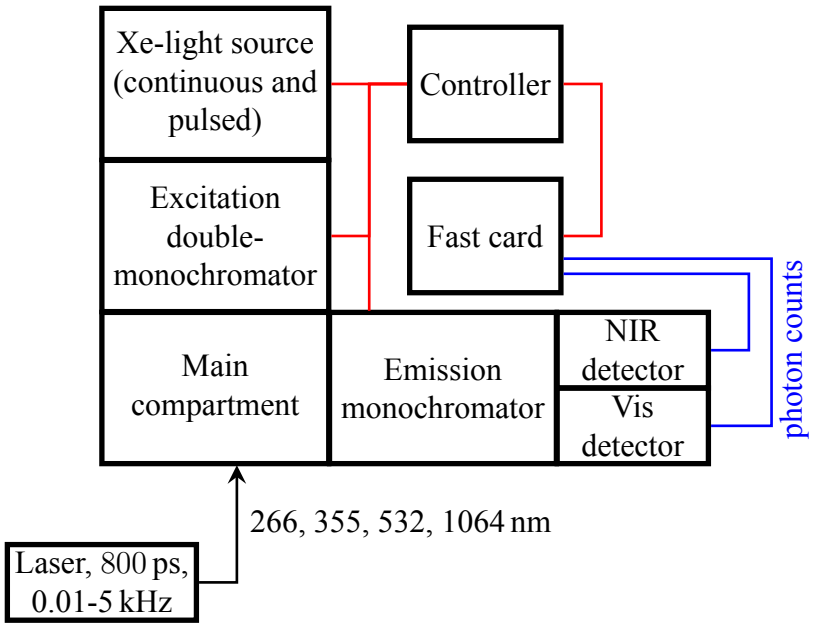

Figure 1.20. Scheme for nanosecond laser set-up.

1.6.3.5 Transient absorption spectroscopy

In our work we used stroboscopic pump-probe experiment. Transient absorption spectrum was measured as follows: short pump pulse promoted the molecular system into transient (excited) state which possessed a specific absorption spectrum. The absorption of a sample was measured with a white light probe pulse. In order to obtain the temporal resolution of the excited states absorption of the system, a time delay between pump pulse and probe pulse was varied. The transient absorption signal of the sample was determined by the ratio of the probe light transmitted through the sample with and without excitation for each delay between pump and probe pulses and for each wavelength, and was defined as:

– Femtosecond set-up (Figure 1.18, see p. 25)

$$\Delta O.D.(t,\lambda) = -\log\frac{I(t,\lambda)-Background(t,\lambda)}{I_0(t,\lambda)-Background(t,\lambda)} = \begin{array}{c} \\ \lambda_0 \\ \lambda_j \\ \dots \\ \lambda_k \end{array} \begin{array}{c} \begin{array}{cccc} t_0 & t_i & \dots & t_n \end{array} \\ \begin{pmatrix} a_{\lambda_0 t_0} & a_{\lambda_0 t_i} & \dots & a_{\lambda_0 t_n} \\ a_{\lambda_j t_0} & a_{\lambda_j t_i} & \dots & a_{\lambda_0 t_j} \\ \dots & \dots & \dots & \dots \\ a_{\lambda_k t_0} & a_{\lambda_k t_i} & \dots & a_{\lambda_0 t_k} \end{pmatrix} \end{array}, \tag{1.6}$$

where I – intensity of transmitted light after excitation at given time-delay (t) and wavelength (λ), I_0 – intensity of transmitted light before excitation pulse, $Background$ – intensity of background.

– Picosecond set-up (Figure 1.19, see p. 26)

$$\Delta O.D.(t,\lambda) = -\log\frac{I(t,\lambda)-Emission(t,\lambda)}{I_0(t,\lambda)-Background(t,\lambda)} = \begin{array}{c} \\ \lambda_0 \\ \lambda_j \\ \dots \\ \lambda_k \end{array} \begin{array}{c} \begin{array}{cccc} t_0 & t_i & \dots & t_n \end{array} \\ \begin{pmatrix} a_{\lambda_0 t_0} & a_{\lambda_0 t_i} & \dots & a_{\lambda_0 t_n} \\ a_{\lambda_j t_0} & a_{\lambda_j t_i} & \dots & a_{\lambda_0 t_j} \\ \dots & \dots & \dots & \dots \\ a_{\lambda_k t_0} & a_{\lambda_k t_i} & \dots & a_{\lambda_0 t_k} \end{pmatrix} \end{array}, \tag{1.7}$$

where I – intensity of transmitted light with excitation pump and wavelength (λ), I_0 – intensity of transmitted light without excitation pulse, $Backrground$ – intensity of background, $Emission$ – intensity of luminescence[1].

1.6.3.6 Time-resolved luminescence spectroscopy

The set-ups were used for luminescence spectroscopy: fluorescence and phosphorescence are shown in Figures 1.19 and 1.20). The samples were excited by laser impulse, emitted light was collected by optical system of set-ups and guided to detector (Streak-camera or R928).

1.6.3.7 Anisotropy

Upon excitation with polarized light the emission from many samples is also polarized. The extent of polarization of the emission is described in terms of the anisotropy r (eq. 1.8). Samples exhibiting non zero anisotropies display polarized emission. The origin of anisotropy comes from existence of transition moments for absorption and emission that lie along specific directions within the fluorophore structure. In homogeneous solution the ground-state fluorophores are all randomly oriented. When exposed to polarized light, those fluorophores that have their absorption transition moments oriented along the electric vector of the incident light are preferentially excited.[81]

[1] Registration of luminescence intensity allows to suppress negative signals in transient maps, coming as rudiment of luminescence and observe stimulated emission. It is especially important in timescales, comparable to lifetimes of luminescence of luminophores (usually nanoseconds and longer)

The emission can become depolarized by a number of processes. All chromophores have transition moments that occur along a specific direction in the molecular axis. Rotational diffusion changes the direction of the transition moments from the axis of excited state being one of common cause of depolarization. Anisotropy measurements reveal the average angular displacement of the fluorophore that occurs between absorption and subsequent emission of a photon. For small fluorophores in low-viscosity solutions the rate of rotational diffusion is typically faster than the rate of emission. Under these conditions the emission is depolarized and the anisotropy close to zero.[81]

The measurement of fluorescence anisotropy is illustrated in Figure 1.21. For most experiments the sample is excited with vertically polarized light. The electric vector of the excitation light is oriented parallel to the vertical or z-axis. The intensity of the emission is measured through a polarizer. When the emission polariser is oriented parallel ($\|$) to the direction of the polarized excitation the observed intensity is called $I_{\|}$. Likewise, when the polarizer is perpendicular ($\perp$) to the excitation the intensity is called $I_{\perp}$. These intensity values are used to calculate the time-dependent anisotropy [81]:

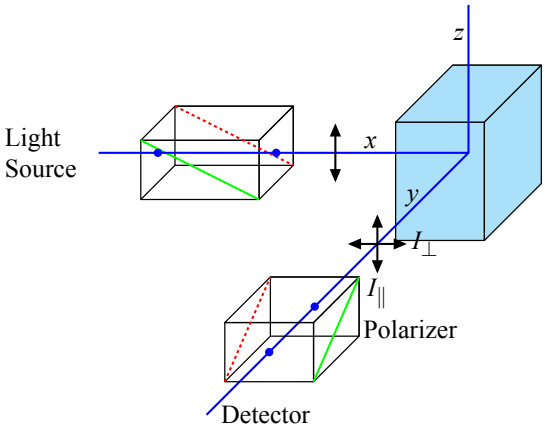

Figure 1.21. Schematic diagram for measurement of fluorescence anisotropy [81].

$$r(t)=\frac{I_{\|}(t)-I_{\perp}(t)}{I_{\|}(t)+2I_{\perp}(t)} \qquad (1.8)$$

The anisotropy is a dimensionless quantity that is independent of the total intensity of the sample. This is because the difference $I_{\|}(t)-I_{\perp}(t)$ is normalized by the total intensity, which is $I_T=I_{\|}(t)+2I_{\perp}(t)$. The anisotropy is an intensity ratiometric measurement. In the absence of artefacts the anisotropy is independent of the fluorophore concentration.[81]

1.6.4 Data analysis

To unravel the processes underlying the observable spectroscopic changes, which result in overwhelming amounts of data, a model-based analysis of the measurements is mandatory. From an analysis perspective, two problems can be distinguished:

a) when a parametrized model of the observations is available, the parameters have to be estimated in a statistically reasonable way; *b*) when only a class of models is known, in addition the "best" model also needs to be determined. Most often such a model consists of a kinetic scheme containing transitions between states.

Different types (see subsection 1.5, p. 18) of measurements require different preprocessing (e. g. baseline correction) and differ in their noise statistics. The resolution of the measurements is determined by a number of instrumental characteristics and by the stochastic nature of the measurements. Time resolution is limited by both the width of the exciting laser pulse and the width of the detector response, wavelength resolution is determined by the characteristics of the spectrograph used [94]:

– Instrument Response Function (IRF). Usually the system is excited by a short laser pulse of a certain energy. The convolution of the shape of this exciting pulse and the detector response is called the IRF. The IRF limits the fastest response observable in the experiment. With pumpprobe spectroscopy the IRF is given by the convolution of pump and probe pulses. Ideally the IRF width should be shorter than the shortest timescale under study. This is impossible when studying ultrafast phenomena. On a (sub)-picosecond timescale, the shape of the IRF as well as its timing precision become important.

– Stochastic. The stochastic of spectroscopic measurements originate from photon properties. Single photon timing fluorescence measurements constitute a counting process which obeys a Poisson distribution, where the variance is equal to the mean and all observations are independent. In contrast, the stochastic properties of the other types of measurements are much more uncertain. The observations are assumed to contain additive normally distributed noise. In general these observations are also assumed to be statistically independent, which seems justified because the measurements are performed sequentially. There is one exception: with time gated spectra a whole spectrum is observed simultaneously, and in principle the responses measured at different wavelengths could be statistically dependent with (unknown) covariance matrix Σ (independent of time).

1.6.4.1 Main principles of data analysis

The data analysis principles are based on two pillars [94]:

1. Homogeneity. The common assumption is that the properties of the system studied are homogeneous, which means that a discrete set of parameters describes the whole system.
2. Separability. The spectroscopic properties of a mixture of components are a superposition of the spectroscopic properties of the components weighted by their concentration. With absorption this is known as the Beer–Lambert law. Thus, the noise-free, time-resolved spectrum $\Psi(t,\lambda)$ is a superposition of the contributions of then n_{comp} different components: $\Psi(t,\lambda) = \sum_{l=1}^{n_{comp}} c_l(t)\varepsilon_l(\lambda)$, where $c_l(t)$ and $\varepsilon_l(\lambda)$ denote, respectively, the concentration and spectrum of component l.

Measurement of Ψ poses the inverse problem: how the spectroscopic and kinetic (dynamic) properties of the components can be recovered from the data. In practice various problems can arise: first, the number of components present in the system may be unknown. Second, in general neither the concentration profiles $c_l(t)$ nor the spectra $\varepsilon_l(\lambda)$ are known. However, the experimentalist usually has a priori knowledge about which shapes of concentration profiles or spectra are realistic. This amounts to common statements regarding continuity, non-negativity, monomodality, etc.

Two main approaches could be identified from big variety of data analysis methods:

– Global analysis. Without a priori knowledge about a detailed kinetic model, the first step is to fit the data with a sufficient number of exponential decays and their amplitudes.[105] This number can be larger than the number of spectrally different components present.
– Target analysis. When a priori knowledge about a detailed kinetic model is known a linear time-invariant compartmental model [106] can be used. In contrast to global analysis, a specific kinetic model is tested, this is often termed target analysis. The aim here is to describe the real concentrations of the components. Note that global analysis is equivalent to a number of non-interacting, parallel decaying compartments.

In this work both concepts for data fitting were used. In fact in most cases, from general considerations or from the literature system' behaviour could be anticipated[1]. In this case we used target analysis, in most cases it was or two parallel deexcitation pathways from excited state ("parallel" fitting by two exponents), or deexcitation through intermediate state ("serial" fitting by two exponents). In cases without heterogeneity in system' properties we used Kohlrausch decay function (stretched exponent), see section 1.3, p. 125.

1.6.4.2 Developed software

During working on thesis problems the special software was developed for data treatment in LabVIEW 2012 system-design platform and development environment. The functionality

[1]The chemists' *idea* of how the system should work was kept in mind and it allowed us to to predict some photophysical properties of the system in advance.

of this software is represented on Figure 1.22 and description of software could be found in Appendix 1.2.

The all data treatment in this work was preformed using this home-made software. Algorithms for data fitting was tested on standard molecules: $[Ru(bpy)_3]Cl_2$, fluorescein, etc.

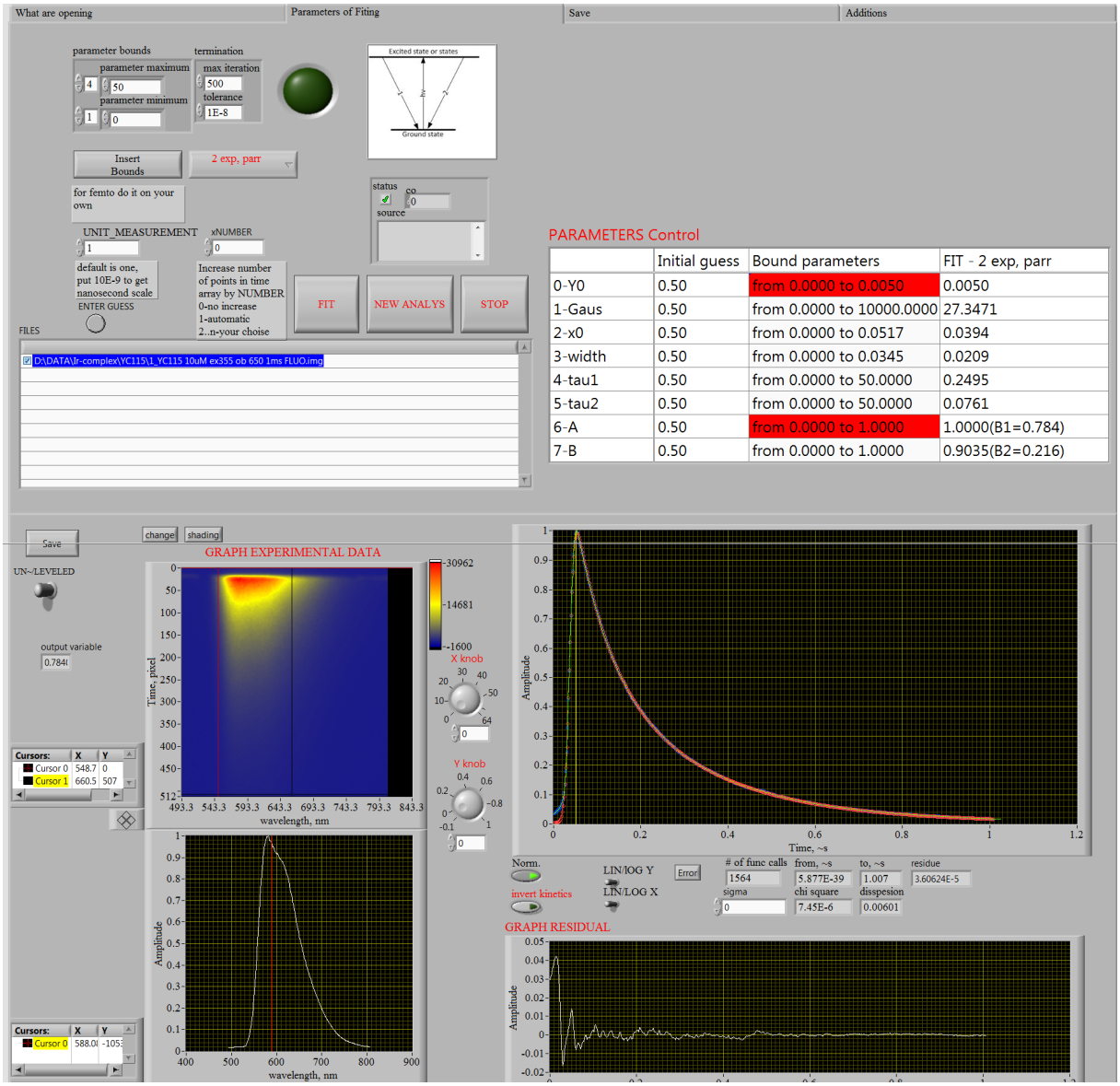

Figure 1.22. The print screen of the main working window of developed software “DATA-FIT”.

Chapter 2

Reversible electronic energy transfer in inorganic supramolecular systems

2.1 Introduction

The management of energy after light absorption act occurred is of fundamental importance for the development of efficient optoelectronic devices [3, 4], charge separation and energy storage as chemical energy. The natural photosynthetic systems are an excellent example where a structurally complex multiporphyrin architecture can absorb light energy, transfer it in an unidirectional fashion to drive a charge transfer process at a distant site, ultimately transforming light energy into chemical energy *via* multi-electron processes.

Recent research efforts in the artificial photosynthesis [107, 108] are largely deals with developing multichromophoric antenna [109–111] systems efficiently absorbing light energy and transferring it in an unidirectional fashion to a specific site following a downhill energy gradient. Close to 100 % efficiency in energy transfer can now be obtained. With regards to temporary energy storage, it was recently shown that in multicomponent molecule-based systems, reversible energy processes can be used [5, 6] to temporarily store electronic excitation energy at one site in multicomponent supramolecular systems, before efficiently tunnelling the energy back to a specific (e. g. emissive) site, in literature this process is often referred as reversible energy transfer. In our group [5–8] we prefer to use Reversible Electronic Energy Transfer (REET).

Studies on REET have been carried since sixties.[112–114] Bäckström [112, 113] and Sandros [114] described the theoretical and experimental results for systems in which energy transfer could be reversible. They found that reverse energy transfer may have to be taken into account when the difference in energy of the donor and acceptor excited states is less than about $2000\,\mathrm{cm}^{-1}$. In an extreme case, Sandros [114] observed back energy transfer from pyrene (E_T=16930 cm^{-1}) to the nominal donor, biacetyl (E_T=19700 cm^{-1}) even though it is endothermic by almost $3000\,\mathrm{cm}^{-1}$ and has a rate constant five orders of magnitude smaller than that for energy transfer from biacetyl to pyrene.[115]

Nordin and Strong [116] emphasized the importance of the relative donor and acceptor excited state lifetimes on reversible energy transfer. They analyzed the transient kinetics for various lifetimes and energy separations of the excited states in terms of a single donor lifetime, representing the best fit to the calculated decay curves.

The REET between different chromophores, following light absorption, leads to a new set of parameters which characterize the system with respect to the constituent chromophores. As such, these species can be considered supramolecular photoactive systems. Besides luminescence quantum yields and emission wavelengths, a key property of photoactive compounds concerns luminescence lifetimes. In certain cases, long-lived luminescence can be obtained that lends a greater flexibility and scope to the applications which could be realized, particularly when considering bimolecular processes: for example, sensors whose long-lived luminescence can be measured after the prompt residual background fluorescence has decayed. This strategy can be employed to obtain a pure optical signal from the molecular probe in time-gated measurements, either directly as oxygen sensors (due to energy transfer to ground-state diatomic oxygen) or after coupling with an appropriate receptor to give a more general strategy towards optical molecular signalling systems.[6]

In 1992 Ford and Rodgers suggested a new strategy [11] to increase emission lifetime of Ru(II) polypyridine complexes by using REET concept. This strategy was based on coupling a Ru(II) polypyridine emitter with an organic chromophore having its lowest-lying and long-lived triplet state close in energy to the triplet ^{3}MLCT emitting state of the metal-based chromophore. In the presence of suitable kinetic and thermodynamic parameters, the triplet state of the organic chromophore could act as an excited-state storage element, leading to a prolongation of the ^{3}MLCT emission, a case related to the "delayed fluorescence" of some organic species.[5]

From an energetic perspective, in order for reversible interchromophore (e. g. from chromophore A to chromophore B) energy transfer to take place, as opposed to unidirectional energy transfer, the lowest-lying excited states of the two chromophores should be thermally accessible

from one another (Figure 2.1). The energy difference (ΔE) between these close-lying states should typically be no higher than a few kcal/mol ($\sim$0.1 eV) to make REET efficient at room temperature. As the energy gap between the two states increases, the rate of back energy transfer value diminishes until back energy transfer becomes uncompetitive with other processes, and REET is no longer possible. If the energy difference between the low-lying interacting states is low enough to permit efficient repopulation of the emissive states and energy transfer rates are much faster than the deexcitation pathways, then the QY of the bichromophoric system will be comparable to that of the parent. Energies of many parent constituent chromophores, and hence ΔE can be obtained through various reference works or estimated from spectroscopic data, e. g. highest energy emission feature from low temperature (77 K) phosphorescence measurements to obtain triplet energy levels.[2]

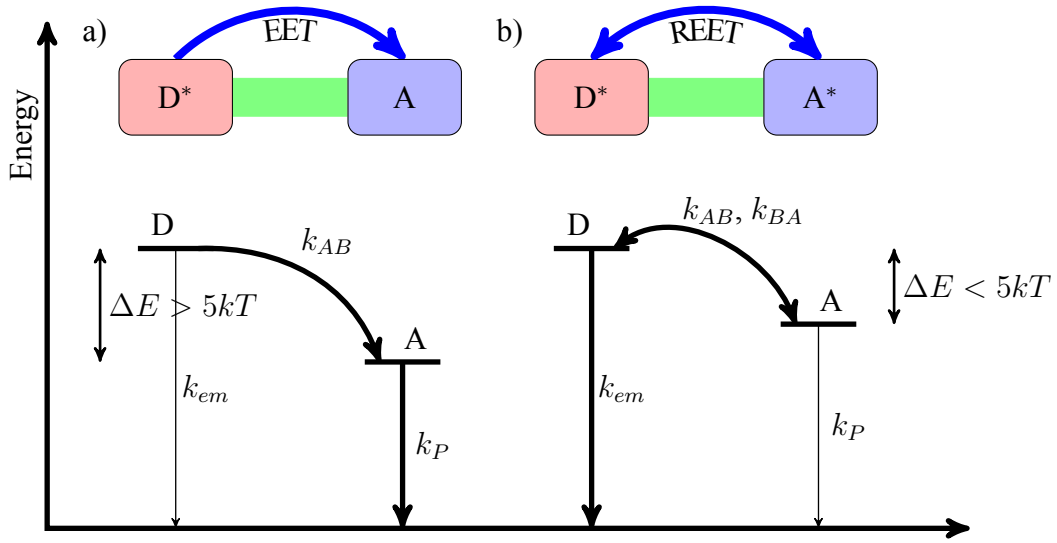

Figure 2.1. Schematic representation of bichromophoric complexes and pertinent excited states in molecular design "chromophore A–spacer–chromophore B". a) Unidirectional electronic energy transfer (rate k_{AB}) to organic moiety with energetically unmatched chromophores; b) reversible electronic energy transfer between energetically close-lying excited-states [2].

We will be especially interested in the REET concept. In this chapter we will show some applications using this approach:

1. For Ru(II)-polypyridine complex the emission lifetime increase of 16-times, reaching 42μs without diminishing QY was shown.
2. For Ir(III)-cyclometalated complex the emission lifetime increase of 52-times, reaching 430μs without diminishing QY was shown.
3. The dynamic control of the efficiency of REET in host-guest complexes, based on host double-helix foldamer and guest thread molecule, showing REET.

2.2 Long-lived luminescence Ru-complex

The results presented in this section were published in *Chemical Communications* "Ruthenium(II) complexes based on tridentate polypyridine ligands that feature long-lived room-temperature luminescence".[7][1]

2.2.1 Introduction

Transition metal polypyridine complexes in general, and ruthenium in particular, have been widely studied to better understand and harness their visible absorption, redox and photochemical processes [19], for application in the general areas of photosensitizers, dyes, sensors, LEDs, catalysts as well as nanotechnology.[20–23] Ligand modification is central in determining many of the key excited-state properties of the complexes, emission is mostly crucial, namely quantum efficiency and luminescence decay rates. Polypyridine ligands generally bind in a bidentate or tridentate fashion, offering complexes with different coordination geometries and properties. Indeed, tridentate ligands can offer access to complexes in 1D-linear geometries in molecular rods and wires, but the luminescence properties are typically hampered by thermally accessible Metal Centered (MC) states which serve to diminish luminescence.[19] As an illustration, while $Ru(bpy)_3^{2+}$ (bpy = 2,2'-bipyridine) has a quantum yield of 0.059 and luminescence lifetime 890 ns in degassed CH_3CN, the terpyridine analogue $[Ru(terpy)_2]^{2+}$ (terpy = 2,2';6',2"-terpyridine) has much lower corresponding values of 10^{-5} and 0.25 ns.[28]

2.2.2 The $[Ru(bpy)_3]^{2+}$ prototype

For better understanding of the general properties of Ru(II) polypyridine complexes, it is convenient to refer to the prototype complex: $[Ru(bpy)_3]^{2+}$.

$[Ru(bpy)_3]^{2+}$ is a chiral molecule, which has two different stereoisomers: Λ- and Δ (Figure 2.2). The general photophysical properties, which are discussed below, do not differ for Λ- and Δ stereoisomers.

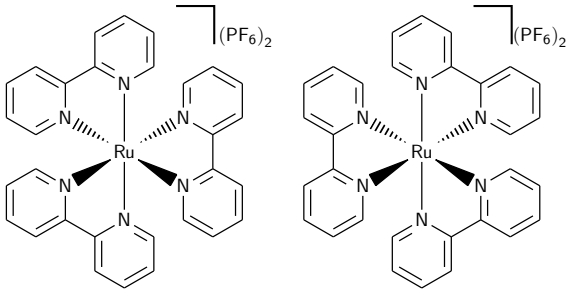

Λ-stereoisomer Δ-stereoisomer

Figure 2.2. Stereoisomers of $[Ru(bpy)_3]^{2+}$.

Ru^{2+} has a d^6 electronic configuration and the polypyridine ligands are usually colourless molecules possessing σ donor orbitals localized on the nitrogen atoms and π and π^* acceptor orbitals more or less delocalized on aromatic rings. Following a single-configuration one-electron description of the excited state in octahedral symmetry (Figure 2.3), promotion of an electron from a π_M orbital to the π_L^* ligand orbitals gives rise to Metal-to-Ligand Charge Transfer (MLCT) excited states, whereas promotion of an electron from π_M to σ_M^* orbitals gives rise to Metal Centered (MC) excited states. Ligand Centered (LC) excited states can be obtained by promoting an electron from π_L to π_L^*. All these excited states may have formal singlet or triplet multiplicity, although spin-orbit coupling causes large singlet-triplet mixing, particularly in MC and MLCT states.[19]

According to Kasha's rule, only the lowest excited state and the upper states that can be populated on the basis of the Boltzmann equilibrium distribution may play a role in determining the photochemical and photophysical properties. The MC excited states of d^6 octahedral complexes are strongly displaced with respect to the ground-state geometry along metal–ligand vibration

[1] http://dx.doi.org/10.1039/C3CC45387A

coordinates.[79, 117] When the lowest excited state is MC, it undergoes fast radiationless deactivation to the ground state and/or ligand dissociation reactions (Figure 2.4)

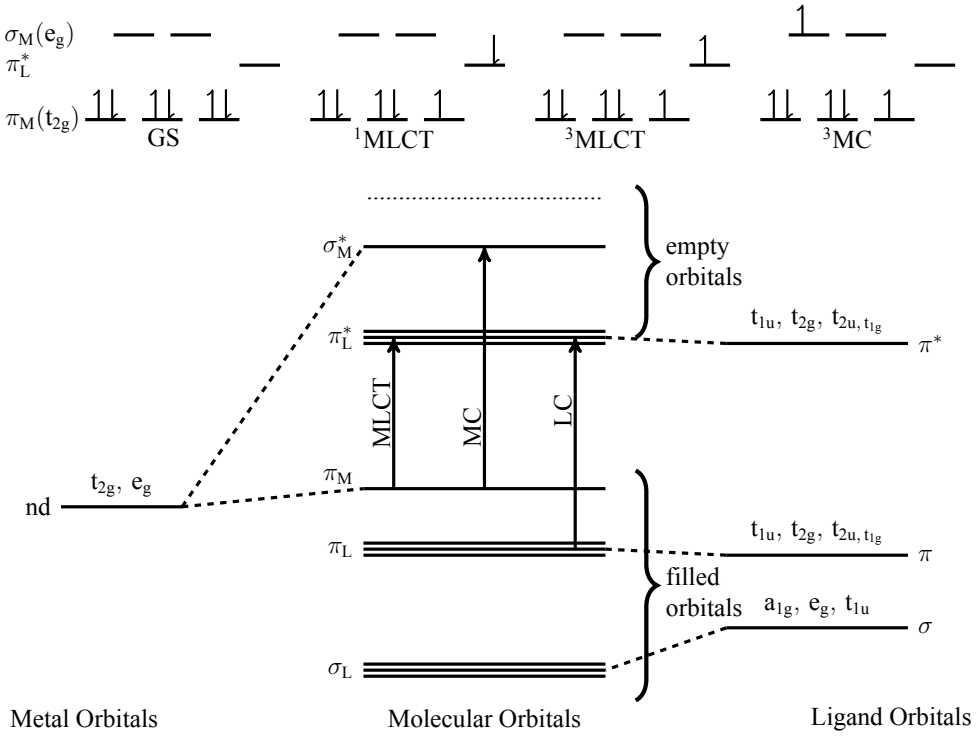

Figure 2.3. Orbital diagram for the electronic ground state and the most relevant excited states for $Ru(bpy)_3^{2+}$ [118].

As a consequence, at room temperature the excited state lifetime is very short, no luminescence emission can be observed [119], and very rarely bimolecular (or supramolecular) reactions can take place. LC and MLCT excited states are usually not strongly displaced compared to the ground state geometry.

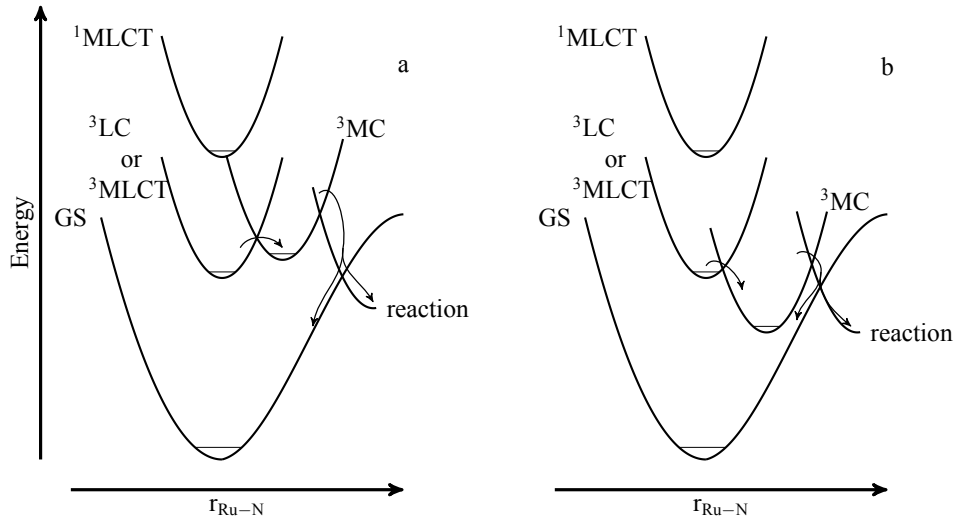

Figure 2.4. Potential well diagrams for limiting cases involving relative energies of the ^{3}MC and ^{3}MLCT for Ru(II) polypyridil complexes. (a) The ^{3}MLCT is the LEES and (b) the ^{3}MC is the LEES [118].

Thus, when the lowest excited state is LC or MLCT (Figure 2.4) it does not undergo fast radiationless decay to the ground state and luminescence can usually be observed. The radiative deactivation rate constant is somewhat higher for ^{3}MLCT than for ^{3}LC because of the larger spin–orbit coupling effect. For this reason, the ^{3}LC excited states are longer lived at low tem-

perature in a rigid matrix and the ^{3}MLCT excited states are more likely to exhibit luminescence at room temperature in fluid solution.[19]

The excited-state properties of a complex are related to the energy ordering of its low-energy excited states and, particularly, to the orbital nature of its lowest excited state. The energy positions of the MC, MLCT, and LC excited states depend on the ligand field strength, the redox properties of metal and ligands, and intrinsic properties of the ligands, respectively.[120–122] Thus, in a series of complexes of the same metal ion, the energy ordering of the various excited states, and particularly the orbital nature of the lowest excited state, can be controlled by the choice of suitable ligands.[120–123] It is therefore possible to design complexes having, at least to a certain degree, desired properties.[19]

2.2.3 The $[Ru(terpy)_2]^{2+}$ prototype

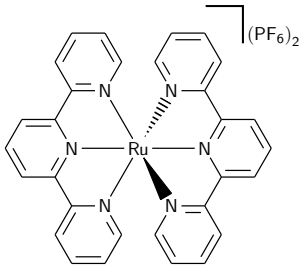

Figure 2.5. Structure of $[Ru(terpy)_2]^{2+}$.

An important family of Ru(II) polypyridine complexes is that based on tridentate ligands, with $[Ru(terpy)_2]^{2+}$ (Figure 2.5) as a prototype (terpy = 2,2';6',2"-terpyridine). The absorption, emission, and redox properties of $[Ru(terpy)_2]^{2+}$ are similar to those of $[Ru(bpy)_3]^{2+}$, except that $[Ru(terpy)_2]^{2+}$ is essentially nonluminescent at room temperature, with a lifetime of the ^{3}MLCT state in degassed acetonitrile at room temperature of about 250 ps, compared with a value of about 1 μs exhibited by $[Ru(bpy)_3]^{2+}$ under the same conditions. Such a short excited-state lifetime is very disappointing, as $[Ru(terpy)_2]^{2+}$ has some advantage over $[Ru(bpy)_3]^{2+}$ from a structural point of view. Whereas $[Ru(bpy)_3]^{2+}$ can exist as a mixture of Λ- and Δ isomers (Figures 2.2), and the isomer problem can become even more complicated for polynuclear species based on "asymmetric" bidentate ligands such as 2,3-bis(2'-pyridyl)pyrazine (2,3-dpp), $[Ru(bpy)_3]^{2+}$ is achiral. Moreover, by taking advantage of parasubstituents on the central pyridine of the terpy ligand, $[Ru(terpy)_2]^{2+}$ can give rise to supramolecular architectures perfectly characterized from a structural viewpoint, in particular to multinuclear one-dimensional ("wire"-like) species. The reason for the poor photophysical properties of Ru(II) complexes with tridentate polypyridine ligands at room temperature, compared to Ru(II) species with bidentate chelating polypyridine, stems from the bite angle of the tridentate ligand that leads to a weaker ligand field strength and thus to lower-energy MC states as compared to Ru(II) complexes of bpy. The thermally activated process from the potentially emitting ^{3}MLCT state to the higher-lying ^{3}MC state is therefore more efficient in $[Ru(terpy)_2]^{2+}$ and its derivatives and leads to fast deactivation of the excited state by nonradiative processes, although terpy-type Ru(II) complexes are inherently more photostable than bpy-type ones because of a stronger chelating effect.[19]

The several reviews and papers are devoted to photophysical properties of Ru-complexes.[10, 19, 118, 120, 124] But now in the interest of brevity we will move to the discussion of our approach which allowed us to achieve significant improvements of polypyridine Ru(II)-complex emission properties.

2.2.4 Approaches for Ru(II) complexes emission properties improvement

Much attention has therefore been focused on the design and synthesis of new Ru(II) complexes with improved emission properties (extended lifetimes and high QY). All different approaches of such improvements are based on different strategies of defavouring thermally-activated loss. These strategies include the use of [26]: *1*) electron accepting and/or donating substituents [25] (by increasing the energy gap between ^{3}MC and ^{3}MLCT states on lowering

emissive ^{3}MLCT level, as a result of incorporating highly electron poor tpy-like ligands [24]), *2*) ligands with extended π-systems, *3*) cyclometalating or incorporating other strong σ-donor ligands, and *4*) bichromophoric systems [13].

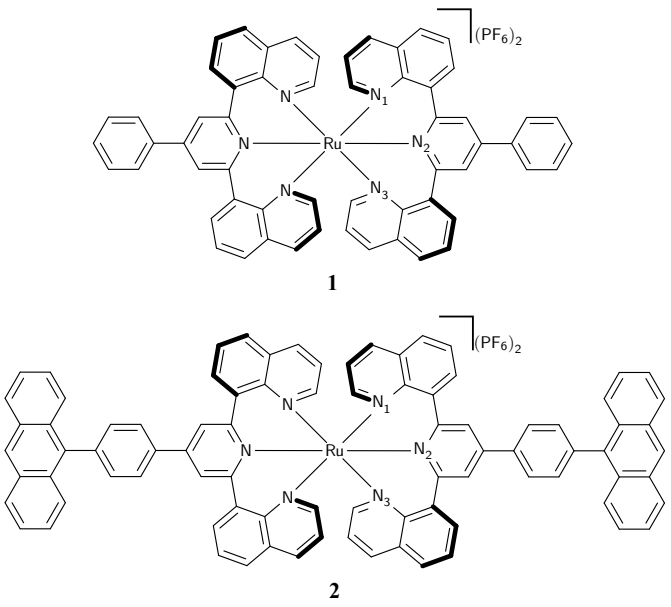

Figure 2.6. Anthracene-free **1** and appended **2** complexes.

In a different approach, a significant breakthrough was achieved by replacing the two external pyridine moieties of terpy with quinolines, giving more emissive tridentante ligand-based octahedral ruthenium complexes whose lifetimes were equally augmented, and whose behaviour can be rationalized by calculations.[26, 27] It was shown that bite angle $N_1 - Ru - N_3$ was $178°$. The ^{3}MC states are less efficiently populated, because they are significantly spatially displaced compared to the ^{3}MLCT states.[125]

Herein we studied Ru(II) complex a product of a straightforward structural modification[1] of the latter type of complex (see model complex **1**, Figure 2.6), involving the judicious integration of an auxiliary matched chromophore, with the goal of giving access to a much longer-lived luminescent complex, while retaining a similar emission quantum yield. This modification could in principle broaden the scope of functions in multicomponent artificial arrays by changing excited-state properties, including luminescence lifetime.

The auxiliary chromophore was anticipated to exert the desired role if specific energetic and kinetic parameters are respected, namely that the newly-introduced triplet level has a slow inherent deexcitation and is quasi-isoenergetic with the emissive ^{3}MLCT state. This would permit REET with the organic subunit acting as an energy reservoir and emission emanating from the metallic sub-unit with a nett luminescence lifetime increase.

Anthracene was anticipated to be an appropriate candidate to act as an energy reservoir (E_T= 1.8 eV; τ_{phos} = 3.3 ms) [28], see prototype **2** in Figure 2.6. Equally this would add to the rather limited known number of matched chromophore pairs.[5, 6, 10, 11, 14–17, 124, 129, 130]

2.2.5 Experimental

All spectroscopic measurements were carried in degassed (freeze-pump-thaw cycles) CH_3CN to eliminate singlet oxygen generation, forming in reaction between ^{3}MLCT and triplet state of dioxygen, dissolved in solvent. For TRABS experiments the 8×10^{-5} M solutions, for time-resolved emission and steady-state measurements 10^{-5} M, respectively were used.

[1]Both model ligand **1** and **2** (Figure 2.6) were prepared from a common intermediate, 4-(4-bromophenyl)-2,6-di(quinolin-8-yl)pyridine.[126] Ligand **1** was prepared by a palladium-catalysed hydro-dehalogenation.[127] Molecule **2** was prepared through a Suzuki coupling reaction, on coupling with the pinacol ester of 9-anthryl boronic acid, with an yield of 34 %. Complex formation was achieved on reacting **1** or **2** with $Ru(DMSO)_4Cl_2$ in hot ethylene glycol under microwave irradiation, yielding the desired complexes **1** and **2**, respectively. While three distinct stereoisomers are possible (mer, cis, fac, and trans, fac), the thermodynamically favourable mer-form can be predominantly formed on heating at 200 °C.[128] Anion metathesis reactions and column chromatography afforded the pure complexes as hexafluorophosphate salts.

2.2.6 Results and discussion

2.2.6.1 Steady-state spectroscopy

Electronic absorption spectra (Figure 2.7) are dominated by ligand-based absorption bands in the UV region and similar MLCT absorption in the visible for both **1** and **2**.

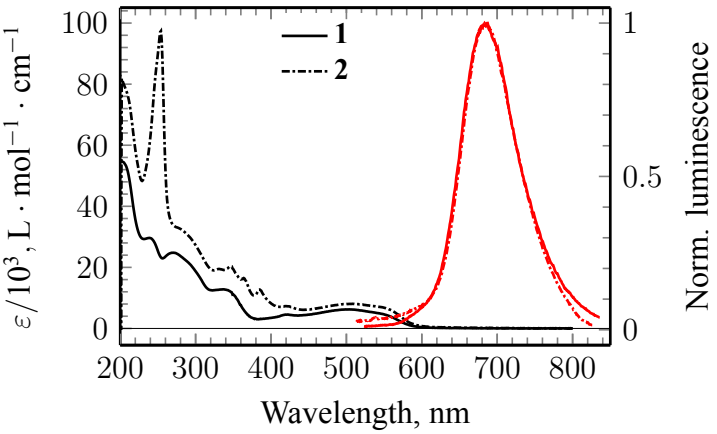

Figure 2.7. Electronic absorption spectra and emission spectra (λ_{exc}=465 nm) of **1** and **2** in CH_3CN.

An additional anthracene absorption band is also observed, which retains its vibronic fine structure implying only weak ground-state coupling between the adjacent chromophores, suggesting an approach to orthoganality of the π-systems, as a result of steric constraints including peri-proton interactions. Consequently, each chromophore is anticipated to retain its own specific properties in the ensemble.

Steady-state luminescence shows ^{3}MLCT-based red emission[1] (Figure 2.7) for both **1** and **2** ($\lambda_{em.max}$= 686 nm) with similar emission QY (Table 2.1) in CH_3CN (Φ_{em}=0.0013).

Table 2.1. Photophysical properties of Ru(II) complexes: **1** and **2** in CH_3CN.

complex	$\lambda_{em.max}$, nm[a]	Φ_{air}[b]	Φ_{degas}[c]	τ, μs[d]	K_{eq}[f]
1	686	2.2×10^{-3}	1.3×10^{-2}	2.7 ± 0.3	–
2	686	4×10^{-4}	9.5×1.3^{-2}	75×10^{-6}[e]; 42 ± 2	15.2 ± 2

[a] Recorded on streak camera and uncorrected.
[b] Luminescence QY in air-equilibrated CH_3CN solution *cf.* $[Ru(bpy)_3]^{2+}$ in H_2O (bpy = 2,2'–bipyridine).
[c] Luminescence QY in degassed CH_3CN solution *cf.* $[Ru(bpy)_3]^{2+}$ in H_2O.
[d] ^{3}MLCT luminescence lifetime in dilute degassed CH_3CN.
[e] Determined *via* transient absorption spectroscopy in degassed CH_3CN.
[f] Excited-state equilibrium constant.

However, a more pronounced oxygen sensitivity is observed in **2** *vs* **1**. While the latter molecule shows a low Φ_{deoxy}/Φ_{oxy} ratio of 5.8, conversely a much higher value of 33 is obtained with **2**, which is consistent with a much longer excited-state lifetime.

2.2.6.2 Time-resolved emission and absorption spectroscopy

Time-resolved spectroscopies on the sub-picosecond to microsecond regimes give supplementary information on the nature of the excited molecule and excited-state processes in the supramolecule. An emission lifetime of 2.7 μs was obtained for deagassed **1**, which is similar to the previously reported tolyl analogue.[128] However, a luminescence lifetime which is over an order of magnitude longer 36 μs was measured for a micromolar solution of **2** (Figure 2.8), which is conducive with the enhanced oxygen sensitivity. Extrapolating to infinite dilution gave an apparent deexcitation rate of 24400 s^{-1} or lifetime of 42 μs, 16-times longer than the unelaborated chromophore (Figure 2.9).

[1] Phosphorescence.

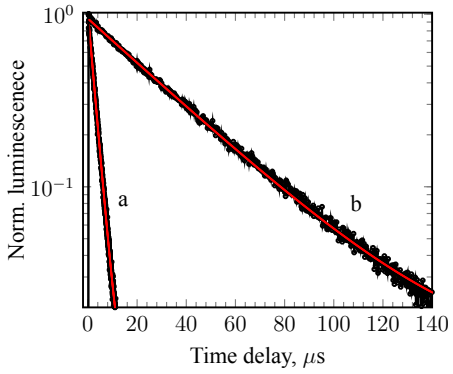

Figure 2.8. Luminescence decay at 686 nm of dilute **1** (a) and **2** (b) in CH_3CN (λ_{exc}=465 nm).

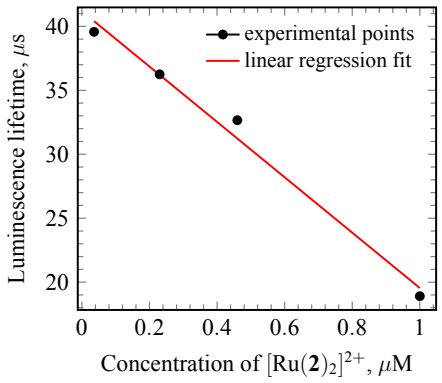

Figure 2.9. Concentration dependence of luminescence lifetime of **2** in CH_3CN (λ_{exc}=465 nm).

While emission data gives information on the ultimate fate of the excited molecule, transient absorption spectroscopy elucidates the management of energy by the excited molecule prior to emission and origin of this large lifetime enhancement. Excitation of **2**, either directly into the MLCT absorption band at 465 nm or predominantly in the anthracene-centred band at 355 nm rapidly led to a similar scenario with the population of the anthracene triplet, denoted by a characteristic $T_n \leftarrow T_1$ absorption at 430 nm (Figure 2.11). The kinetics of deexcitation of this organic triplet band exactly parallels those of the red emission. This behaviour is attributed to a dynamic excited-state equilibrium involving the two chromophores confirming that the excited states on the adjacent chromophores may be considered quasi-isoenergetic, thus permitting rapid and REET. With a similar quantum yield being obtained for both **1** and **2** this implies the energy shuttling in **2** is essentially quantitative.

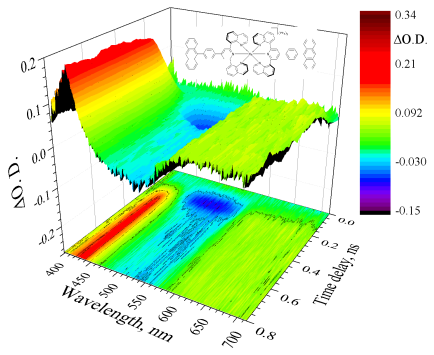

Figure 2.10. TRABS map of **2** showing equilibration of REET in CH_3CN (λ_{exc}=355 nm).

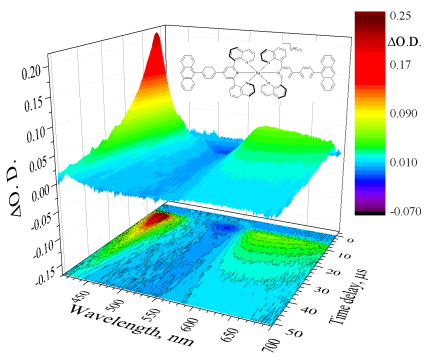

Figure 2.11. TRABS map showing deexcitation of the equilibrated **2** in CH_3CN (λ_{exc}=355 nm).

2.2.6.3 Dynamic excited-state equilibrium

To gain further insight into the energies of the pertinent states, low temperature phosphorescence measurements were undertaken with both **1** and **2** (Figure 2.12). At 77 K, slightly blue-shifted MLCT emission ($\lambda_{em.max}$=672 nm) could be observed from **2** with respect to room temperature, while in the bichromophoric complex the emission of **2** was located further to the red ($\lambda_{em.max}$=712 nm) and attributed to a slightly lower-lying anthracene emission, with only a small energy difference between high energy emission features. While such a small value cannot be measured directly without significant error, kinetic analysis (see later in this section) allows determination of the energy gap at 420 cm^{-1}, which is consistent with reversible interchromophore electronic energy transfer at room temperature.

The establishment of a dynamic excited-state equilibrium from the non-equilibrated initial excited state can be observed directly, in real-time, by picosecond transient absorption spectroscopy (Figure 2.10). Indeed, the rise time of the anthracene triplet absorption signature (Figure 2.14) is measured to be 75 ps. This value gives the rate of establishment of equilibrium (k=13.3×10^9 s^{-1}) and is equal to the sum of forward k_f and back energy k_b transfer processes.[11] The relative k_f and k_b values can be determined by direct observation based on transient absorption signatures.

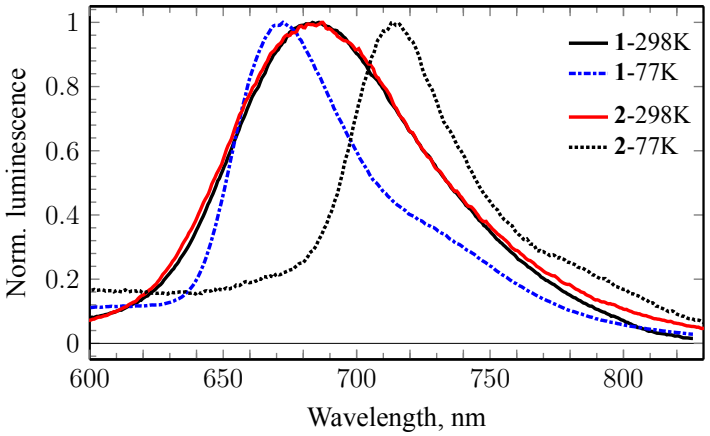

Figure 2.12. Emission spectra of **1** and **2** in CH_3CN at 298 and 77 K (λ_{exc}=465 nm).

Knowledge of the relaxation rates for individual states as well, as the system relaxation rate allows calculation of K_{eq}; where α is the fraction of energy located on ^{3}Anth state; while $1-\alpha$ is the fraction of energy located on the ^{3}MLCT state.

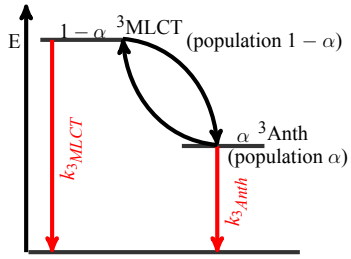

$$\begin{cases} k_{obs}=(1-\alpha)\cdot k_{^3\mathrm{MLCT}}+\alpha\cdot k_{^3\mathrm{Anth}}=23800\,\mathrm{s}^{-1} \\ K_{eq}=\dfrac{[^3\mathrm{Anth}]}{[^3\mathrm{MCLT}]}=\dfrac{\alpha}{1-\alpha}\Rightarrow\alpha=0.937;\ K_{eq}=14.8 \end{cases}$$

Knowing K_{eq}, one can calculate the Gibbs free energy (ΔG) for the equilibration process, remembering that:

$$\Delta G^0=-kT\ln K=-8.6\cdot10^{-5}\cdot298\cdot\ln15\cong-0.07\mathrm{eV}^a\cong-560\mathrm{cm}^{-1}.$$

[a] kT at room temparature equals 0.026 eV

The energy gap between triplet states can be estimated from the equation:

$$\Delta G^0=-\Delta E-T\Delta S=-\Delta E-kT\ln2$$

The additional entropy $kT\ln2$ factor (due to degeneracy of anthracene triplet states) constitutes -140cm^{-1} of energy to ΔG, so:

$$\Delta E\cong560\mathrm{cm}^{-1}-140\mathrm{cm}^{-1}\cong420\mathrm{cm}^{-1}\cong0.05\mathrm{eV}.$$

Concerning direct observation, the changes in absorption of the MLCT band at 485 nm (Figure 2.13) denotes the relative populations initially following excitation, as well as the subsequent metastable equilibrated system. This allows determination of the equilibrated population to be largely 94 % in favour of the organic chromophore, and the equilibrium constant, K_{eq} at 15.2±2.

$$K_{eq}=\frac{k_f}{k_b}=\frac{[^3\mathrm{MLCT}]_0}{[^3\mathrm{MLCT}]_{\mathrm{eq}}}-1=15.2\pm2$$

This values agrees well with that determined at 14.8 *via* the aforementioned energy gap method. Consequently k_f and k_b were determined at 1.25×10^{12} s^{-1} and 8.3×10^8 s^{-1}, respectively, as the equilibrium constant, which is governed by kinetics, is a ratio of k_f to k_b (Figure 2.17).

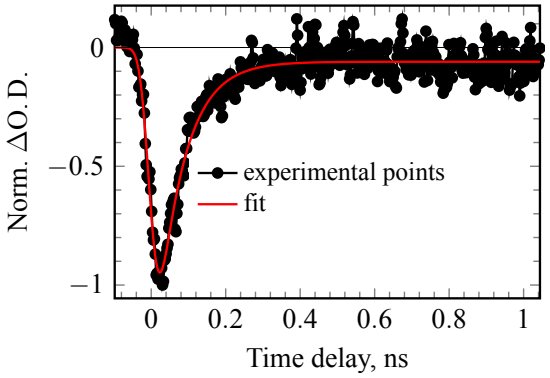

Figure 2.13. TRABS kinetics of ground state bleaching changes for **2** at 485 nm in CH_3CN (λ_{exc}=465 nm).

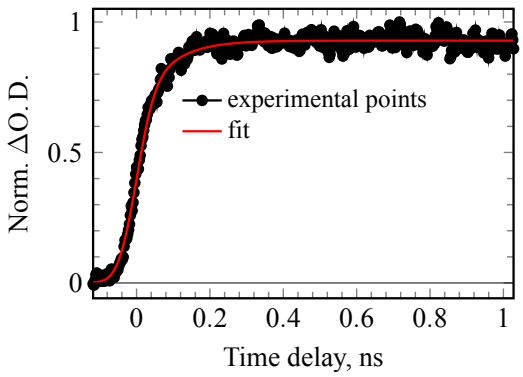

Figure 2.14. TRABS kinetics of anthracene triplet grow-in for **2** at 430 nm in CH_3CN (λ_{exc}=465 nm).

2.2.6.4 Ultrafast absorption spectroscopy

Ultrafast processes of ISC and formal singlet-singlet energy transfer were estimated using femtosecond transient absorption spectroscopy, on exciting the MLCT absorption band or predominantly into the anthracene absorption band, respectively. Based on rapid changes in the spectrum at around 600 nm following visible excitation (λ_{exc}=490 nm) the ^{1}MLCT to ^{3}MLCT intersystem crossing occurred with a time constant of 150 fs (Figure 2.15), which is 2-3 times longer comparing to $[Ru(bpy)_3]^{2+}$ complex having 100 fs [19] or 50 fs [131]. Meanwhile, on exciting anthracene at 370 nm and observing changes in the visible ground-state MLCT absorption band at 530 nm (Figure 2.16), an upper limit for the electronic energy transfer rate from an excited singlet anthracene to lower-lying ^{1}MLCT level could be estimated around 4.2×10^{12} s^{-1}. Indeed, a small amount of direct MLCT excitation and cooling would effectively lower this rate to some extent, while remaining on the same order of magnitude. The ensemble of excited-state processes and rates describing energy transfer, energy distribution at equilibrium and subsequent emission are given in Figure 2.17.

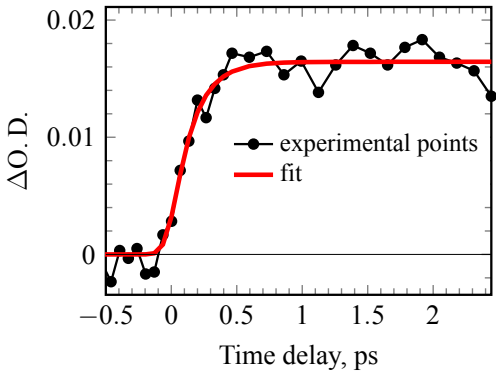

Figure 2.15. Kinetics of increase of absorption at 600 nm from ultrafast TRABS of **2** in CH_3CN (λ_{exc}=465 nm).

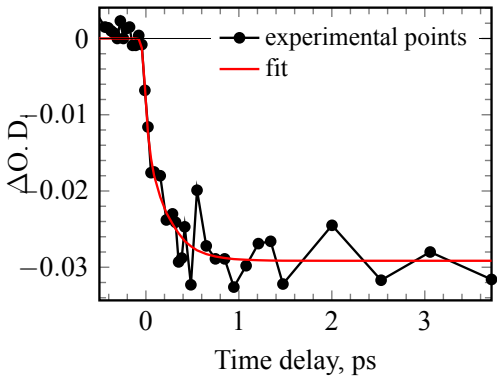

Figure 2.16. Kinetics of ground state bleaching changes at 530 nm from ultrafast TRABS of **2** in CH_3CN (λ_{exc}=370 nm)[1].

2.2.7 Conclusions

Bichromophoric Ru(II) complexes based on tridentate ligands offering an optimised coordination environment combined with an appropriate organic auxiliary are shown to give complexes based on tridentate ligands with unprecedented luminescence lifetimes without affecting

[1] Due principally to fast singlet anthracene to ^{1}MLCT electronic energy transfer (although some direct MLCT excitation cannot be ruled out).

the emission efficiency. Time-resolved spectroscopies show that excited-state equilibration between ^{3}MLCT and ^{3}Anth is reached in less than 300 ps *via* REET with 94 % of energy being stocked on the organic energy reservoir, on average in the microsecond timescale with emission lifetime $\tau_{em} = 42\,\mu$s from the metal-centre. Interestingly this behaviour was instilled in a predetermined fashioned based on a rudimentary knowledge of energies of excited-states and intrinsic deexcitation in respective molecular sub-units. As well as offering the possibility of more efficient photosensitizers, applications in molecule-based light emitting devices, molecular machines and detection are under investigation.

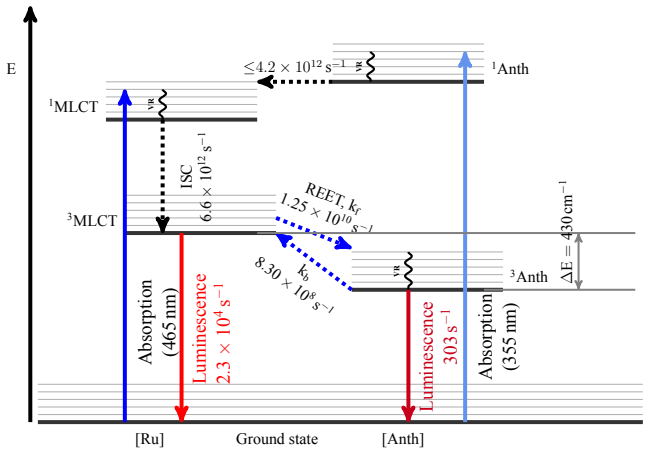

Figure 2.17. Perrin-Jablonski diagram showing pertinent energy levels and kinetics of REET and delayed luminescence of **2**.

2.3 Direct observation of REET involving an Iridium centre

The results presented in this section were published in *Inorganic Chemistry* "Direct Observation of Reversible Electronic Energy Transfer Involving an Iridium Center".[8][1]

2.3.1 Introduction

As it highlighted in the review of Barigelletti [32], the study of Ir(III) complexes has been limited, because the synthesis was difficult to accomplish. Today, we witness an impressive expansion of the literature on the luminescence of Ir(III) complexes. The study of photoinduced processes in Ir(III)-based arrays has been exploited since facile synthetic methods for the preparation of Ir(III)-polyimine complexes became available.[32] But the REET approach has not been applied to the Ir(III)-cyclometallated complexes yet, to the best knowledge of author.

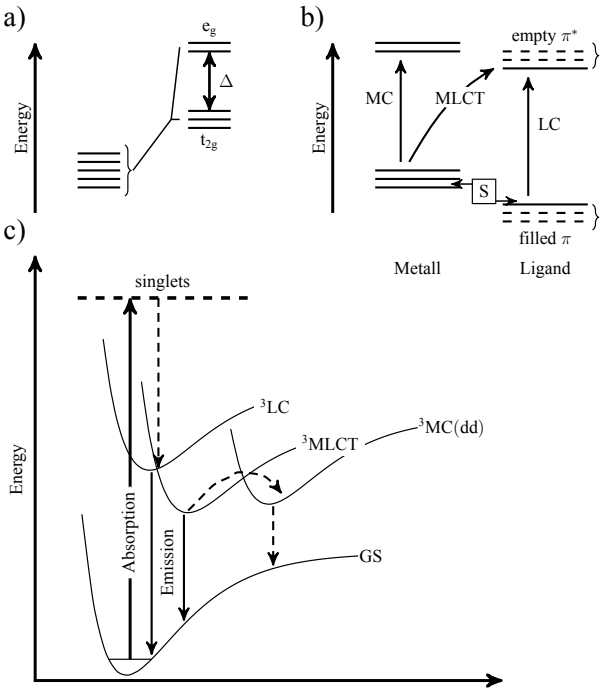

Figure 2.18. a) d-orbitals in an octahedral field; b) orbital description of MC, MLCT, and LC transitions; S is a substituent group capable of exerting electron withdrawing or releasing effects (resulting in stabilization or destabilization, respectively, of the energy level of the filled d and π orbitals); c) electronic transitions involving MC, MLCT, and LC excited states; the MC levels are not emissive [32].

The Ir(III) trication is a $5d^6$ centre and the electronic properties of its polyimine complexes share several features with those of other well-known octahedral complexes of type Fe(II), Ru(II), Os(II), and Re(I) [118], whose metal centres are $3d^6$, $4d^6$, $5d^6$, and $5d^6$, respectively. Figure 2.18 depicts useful orbital and state energy diagrams for electronic transitions taking place in polyimine complexes of such d^6 metal centres. It should be noted that light absorption is associated with electronic transitions from the Ground State (GS) to, mostly, singlet levels of various nature and electronic localization, ligand centred (^{1}LC), metal-centered (^{1}MC), and metal to ligand charge transfer (^{1}MLCT). In addition, ligand to-metal transitions (^{1}LMCT) can in principle be involved. On the contrary, emission is always from triplet levels, ^{3}MLCT or ^{3}LC in nature, which actually include varying amounts of the corresponding singlet.[32]

It is well known that essential properties of transition metal complexes that are intimately linked to the electronic and steric aspects of ligands in the primary coordination sphere include redox properties, light absorption and emission. Additionally, in supramolecule complexes where spatially-distinct chromophores are introduced, the latter may intervene in determining photophysical properties, for example through electron or energy transfer.[9] Concerning emission, quantum yield and luminescence lifetime are important characteristics, which ultimately define applicability in light-emitting and sensing architectures. We and others have previously applied an approach of harnessing REET between energetically-matched chromophore pairs [6, 10, 11] exhibiting complementary kinetic behaviour, in order to enhance the performance of several underperforming luminescent metal complexes based on ruthenium, osmium, copper and rhenium as luminophores and photosensitizing agents.[7, 12–18] Modification of the photophysical properties of cyclometallated iridium complexes are

[1] http://dx.doi.org/10.1021/ic4030712

of particular interest due to their central role in multiple applications requiring highly efficient emission such as electroluminescence, sensing, and bioimaging [29–32], and as well it would add to the rather known limited number of matched chromophore pairs.

We modified[1] a cyclometallated iridium complex (see model complex **3**, Figure 2.19), involving the judicious integration of an auxiliary matched organic chromophore, in order to obtain a much longer-lived luminescent complexes **4** and **5**, while retaining a similar emission quantum yield (Table 2.2). This modification could in principle broaden the scope of functions in multicomponent artificial arrays by changing excited-state properties, including luminescence lifetime and oxygen sensitivity. A key to success was the introduction of a non-conjugated aliphatic spacer between the pyrene group and the adjacent 2,2'-bipyridine, as direct attachment of the pyrene to the ancillary ligand quenches the excited Ir(III)-centre.[33]

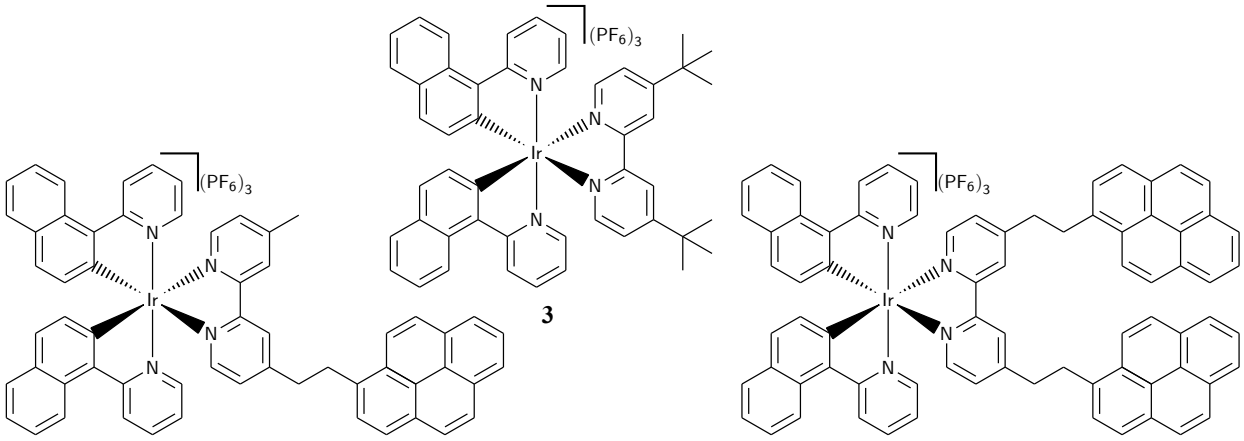

Figure 2.19. Structural formulas of iridium complexes **3**, **4** and **5**.

The auxiliary organic chromophore was anticipated to play the desired role if the newly introduced triplet level was essentially isoenergetic with the emissive ^{3}MLCT state and exhibits slow inherent deexcitation. This would enable reversible intercomponent excited-state energy transfer with the organic subunit acting as an energy reservoir leading to a net luminescence lifetime increase.[6, 7, 10, 11] Based on luminescence data of **3**, vide infra, pyrene was selected as an appropriate candidate to play the desired role ($E_T = 2.09$ eV; $\tau_{phos} = 11$ ms) [28], see prototypes **4** and **5** in Figure 2.19.

2.3.2 Experimental

All spectroscopic measurements were carried in degassed (freeze-pump-thaw cycles) CH_3CN to eliminate singlet oxygen generation, forming in reaction between ^{3}MLCT and triplet state of dioxygen, dissolved in solvent. For TRABS experiments the 8×10^{-5} M solutions, for time-resolved emission and steady-state measurements 10^{-5} M, respectively were used.

2.3.3 Results and discussion

2.3.3.1 Steady-state spectroscopy

The photophysical properties of **3**, **4** and **5** are summarized in Table 2.2. Electronic absorption spectra in acetonitrile at room temperature (Figure 2.20) are dominated by ligand-based absorption bands in the UV region and similar MLCT absorption in the visible for all **3**, **4** and

[1] For more details on synthesis, please refer to article [8].

5 . An additional pyrene absorption band is also observed, which retains its vibronic fine structure implying only weak ground-state coupling between the two chromophores. As such, each chromophore is anticipated to retain its own specific properties in the ensemble.

Table 2.2. Photophysical properties of Ir(III) complexes: **3**, **4** and **5** in CH_3CN.

complex	$\lambda_{em.max}$, nm[a]	Φ_{air}[b]	Φ_{degas}[c]	τ, μs[d]	K_{eq}	τ_{eq}, ns
3	576, 617, 654	4×10^{-3}	10×10^{-2}	8.3 ± 0.3	–	–
4	576, 617, 654	5×10^{-4}	9.5×10^{-2}	225 ± 15	27.8 ± 2	5
5	576, 617, 654	1×10^{-4}	9.6×10^{-2}	430 ± 15	55 ± 2	2.8

[a] The values correspond to maximum of Gaussian peaks, obtained by emission deconvolution (see Figure 2.20).
[b] Luminescence QY in air-equilibrated CH_3CN solution *cf.* $[Ru(bpy)_3]^{2+}$ in H_2O (bpy = 2,2'–bipyridine).
[c] Luminescence QY in degassed CH_3CN solution *cf.* $[Ru(bpy)_3]^{2+}$ in H_2O.
[d] MLCT luminescence lifetime in dilute degassed CH_3CN.

Steady-state luminescence shows ^{3}MLCT-based red emission for both **3**, **4** and **5** ($\lambda_{em.}=576, 617, 654$ nm, Figure 2.20, Table 2.2) with similar emission quantum yields in degassed CH_3CN ($\Phi_{em}=0.1$, Table 2.2). However, a higher oxygen sensitivity is observed in **4** *vs* **3**. While the latter molecule shows a Φ_{degas}/Φ_{air}[1] ratio of 26, a much higher value of 190 is obtained with **4**, which is consistent with a much longer excited-state lifetime of last.

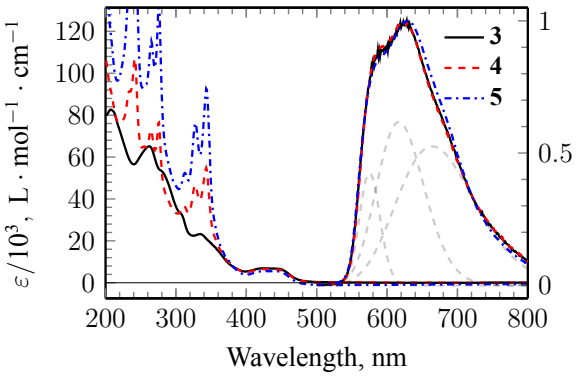

Figure 2.20. Absorption and emission ($\lambda_{exc}=$ 413 nm) spectra of **3**, **4** and **5** in CH_3CN.

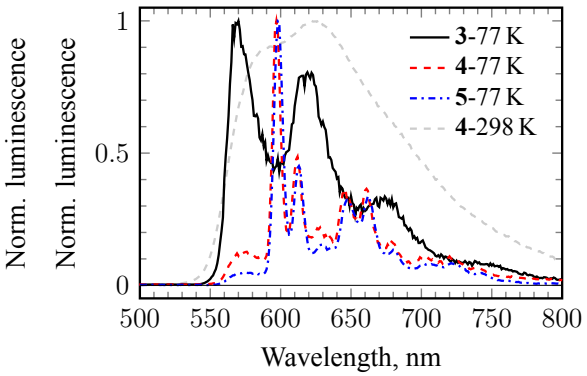

Figure 2.21. Steady-state luminescence of studied samples: **3**, **4** and **5** at 77 K and 298 K (dashed-line) in butyronitrile ($\lambda_{exc}=413$ nm).

Low temperature phosphorescence measurements were undertaken to elucidate the energies of the pertinent states and relative energy levels of **3**, **4** and **5** (Figure 2.21). At 77 K, ^{3}MLCT phosphorescence ($\lambda_{em.max}=572$ nm) could be observed from **1**, while emission of bichromophoric **4** was located further to the red ($\lambda_{em.max}=595$ nm) and is ascribed to pyrene emission.[28, 132] A small energy gap value of ~680 cm^{-1} between high energy emission features can be estimated, assuming similar ^{3}MLCT levels in both complexes (at RT they show similar emission spectra). A small value is consistent with reversible interchromophore electronic energy transfer at room temperature. However, such a small energy gap cannot be measured with precision in this fashion and thus proof of this unusual phenomenon was sought *via* time-resolved spectroscopies.

2.3.3.2 Time-resolved emission and absorption spectroscopy

Time-resolved spectroscopies on the sub-ps to ms regimes give supplementary information on the nature of the excited molecule and a clear insight into excited-state processes in the supramolecules.

[1] For more details on singlet oxygen sensing please see [8].

An emission lifetime of $8.3\,\mu$s was obtained for **3** in degassed CH_3CN solution (Figure 2.22), while a luminescence lifetime that is over 25-times longer ($215 \pm 15\,\mu$s) was measured for a micromolar solution of **4**, $415 \pm 15\,\mu$s for **5**. Extrapolating to infinite dilution gave an apparent deexcitation rate of $4400\,s^{-1}$, or $\tau = 225\,\mu$s for **4** and $430\,\mu$s for **5**, much longer than the parent chromophore.

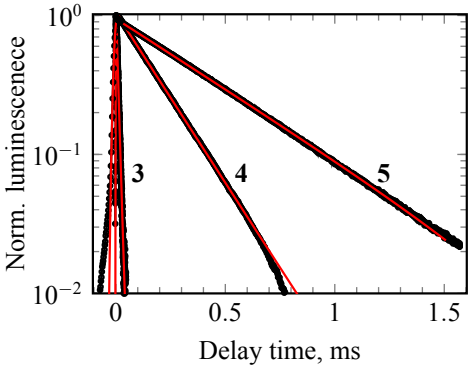

Figure 2.22. Luminescence decay in the 580 – 620 nm range of dilute **3**, **4** and **5** in CH_3CN ($\lambda_{exc} = 465$ nm).

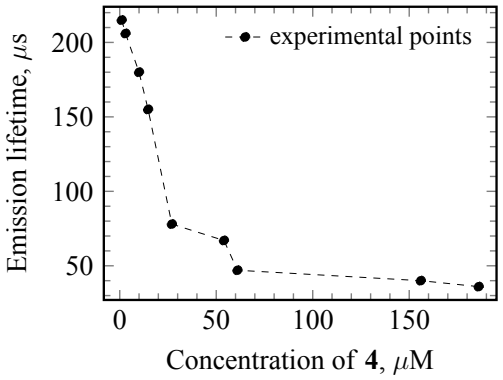

Figure 2.23. Concentration dependence of luminescence lifetime of **4** in CH_3CN ($\lambda_{exc} = 465$ nm).

Complementary transient absorption spectroscopy elucidates the management of energy by the excited molecule prior to emission, and transient absorption signatures for both pyrene and iridium complexes have been described.[7, 13–18, 28] Excitation into the MLCT absorption band of **4**[1] at 465 nm rapidly led to the population of the pyrene triplet, denoted by a characteristic $T_n \leftarrow T_1$ absorption at 410 nm (Figure 2.20). The kinetics of deexcitation of this absorption band exactly parallels those of the emission (Figure 2.25) clearly showing that while energy is principally located on this triplet, it is quantitatively transferred to the metal centre where it is subsequently emitted. This observation implies the presence of quasi-isoenergetic excited states on the adjacent chromophores permitting rapid and REET, leading to a dynamic excited-state equilibrium.

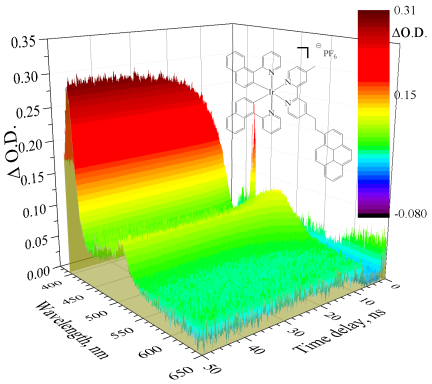

Figure 2.24. TRABS map of **4** showing equilibration of REET in CH_3CN ($\lambda_{exc} = 355$ nm).

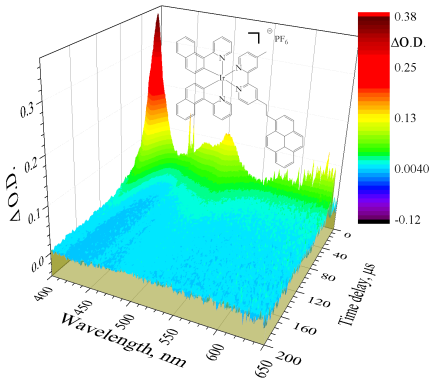

Figure 2.25. TRABS map showing deexcitation of the equilibrated **4** in CH_3CN ($\lambda_{exc} = 355$ nm).

2.3.3.3 Dynamic excited-state equilibrium

The establishment of a dynamic excited-state equilibrium from an initial non-equilibrated excited state can be observed in real time by transient absorption spectroscopy (Figure 2.24), and a 5 ns rise time of the pyrene triplet absorption signature was measured for **4** and 2.8 ns

[1] The same is for sample **5**.

(Figure 2.27) for **5**. This value gives the rate of establishment of equilibrium ($k=2\times10^{8}\,s^{-1}$), and is equal to the sum of forward k_f and back k_b energy transfer processes. The relative k_f and k_b values cannot be determined by direct observation based on transient absorption signatures, because the Ir-centre ground state bleaching signal overlaps with the transient MLCT absorption signal. Along with the excited-state equilibration constant K_{eq}, which describes the distribution of energy between the constituent chromophores, k_f and k_b can be estimated using the inherent deexcitation properties of the constituent chromophores and the observed lifetime decay of **4** ($\tau_2=225\times10^{-6}$ s) and **5** ($\tau_2=430\times10^{-6}$ s), on applying equations 2.1 and 2.2, where ^{3}MLCT and ^{3}Pyr correspond to the time constants for the decays of the iridium moiety and pyrene, respectively; α corresponds to the fraction of excited pyrene-like triplets and $1-\alpha$ corresponds to the fraction of excited MLCT-like triplets in the equilibrated population.

$$\frac{1}{\tau_2}=\alpha\frac{1}{\tau_{Pyr}}+(1-\alpha)\frac{1}{\tau_{MLCT}} \tag{2.1}$$

$$\frac{\alpha}{1-\alpha}=K_{eq}=\frac{k_f}{k_b} \tag{2.2}$$

K_{eq} was thus estimated to be 27.8 ± 2 and 55 ± 2 for **4** and **5**, respectively, which means that the equilibrated population is predominantly 96.5 % in favour of the organic chromophore for **4** and 98.2 % for **5**. Consequently k_f and k_b were determined at 1.9×10^{8} s^{-1} and 6.9×10^{6} s^{-1}, respectively, for **4** and 3.5×10^{8} s^{-1} and 6.4×10^{6} s^{-1} for **5**.

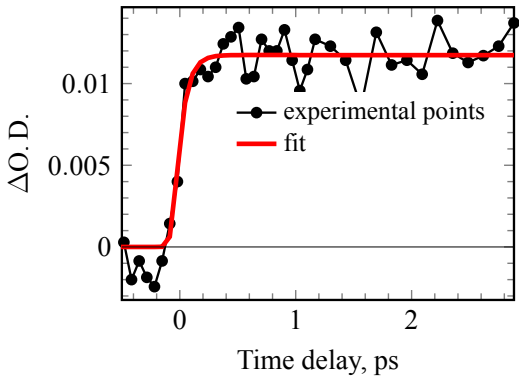

Figure 2.26. TRABS kinetics of ^{3}MLCT grow-in for **4** at 505 nm in CH_3CN ($\lambda_{exc}=465$ nm).

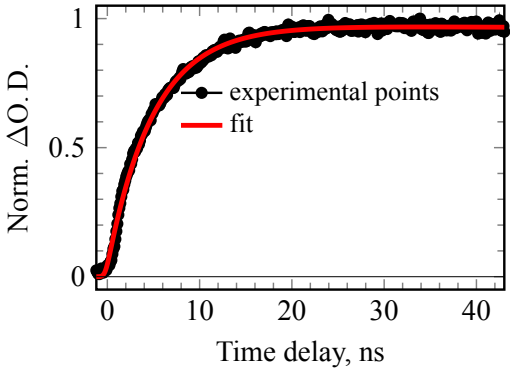

Figure 2.27. TRABS kinetics of pyrene triplet grow in for **4** at 410 nm in CH_3CN ($\lambda_{exc}=465$ nm).

Knowing K_{eq}, one can calculate the Gibbs free energy (ΔG) for the equilibration process:

$$\Delta G_3=-kT\ln K=-8.617\times10^{-5}\cdot298\cdot\ln28\cong-0.085eV\cong-680\text{cm}^{-1}$$

For complex **4** $\Delta E_3\simeq-\Delta G_3$.
For complex **5** the energy gap between triplet states can be estimated from the equation:

$$\Delta G_4=-\Delta E-T\Delta S=-\Delta E-kT\ln2$$
$$\Delta G_4=-kT\ln K=-8.617\times10^{-5}\cdot298\cdot\ln55\cong-0.103\text{eV}\cong-830\text{cm}^{-1}$$

The additional entropy $kT\ln2$ factor (due to degeneracy of pyrene triplet states) adds 140cm^{-1} to ΔG, so:

$$\Delta E_4\cong830\text{cm}^{-1}-140\text{cm}^{-1}\cong690\text{cm}^{-1}\cong0.086\,\text{eV}.$$

2.3.3.4 Ultrafast absorption spectroscopy

The ultrafast ^{1}MLCT to ^{3}MLCT Intersystem Crossing (ISC) rate was estimated using femtosecond transient absorption spectroscopy, on exciting the MLCT absorption band. Based on

rapid changes in the spectrum at around 520 nm the ISC rate was *ca.* $10 \times 10^{12}\,s^{-1}$. This high value corresponds to that previously determined ($14 \times 10^{12}\,s^{-1}$) for related cyclometallated iridium complexes [133, 134], and implies that following excitation, ultrafast intersystem crossing precedes the slower intercomponent energy transfer leading to an excited-state equilibrium (see Figure 2.26). The ensemble of rate constants for pertinent processes are shown in the Perrin-Jablonski diagram in Figure 2.28.

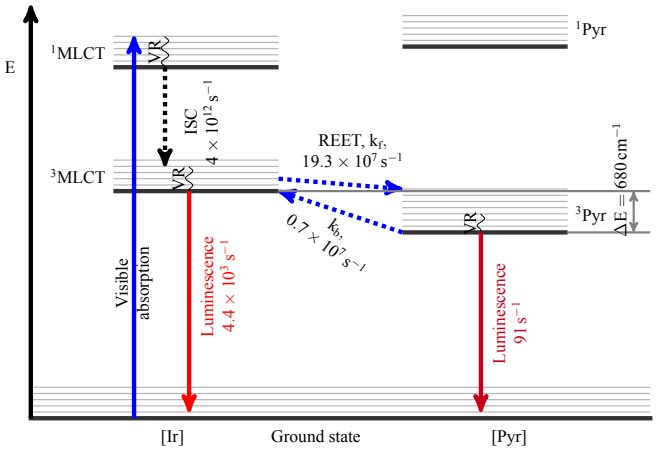

Figure 2.28. Perrin-Jablonski diagram showing pertinent energy levels and kinetics of REET and delayed luminescence of **4**.

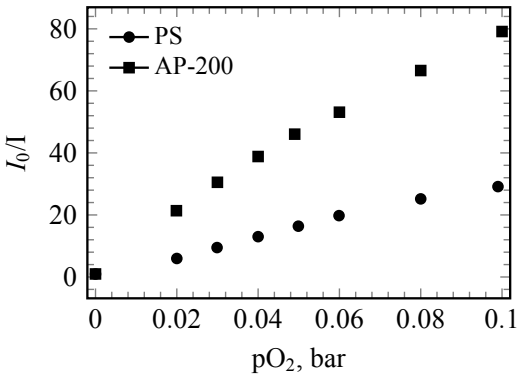

Figure 2.29. Stern−Volmer plot obtained for **4** immobilized in PS and AP-200.

2.3.3.5 Oxygen sensing

Because a long excited-state lifetime is important for efficient oxygen detection using luminescent probes, the oxygen-sensing properties of dye **4** were evaluated in solid hosts through a collaboration with the group of Fernández-Gutiérrez in Granada University, Spain following previously reported methodology measuring emission intensities, in both a polymeric PS 399 membrane and a nanostructured metal oxide matrix (AP200/19).[135] A significantly better performance with AP200/19 compared to PS was observed because of improved oxygen permeability; between 0 and 10 % O_2, the Stern-Volmer constants are 1103 and 294 bar^{-1} for AP200/19 and PS (Figure 2.29), respectively (for more details see [8]). These results make **4** one of the most sensitive iridium-based dye and is highly promising for lifetime-based sensing methods, which are currently being investigated.

2.3.4 Conclusions

Time-resolved spectroscopies conclusively showed for the first time that excited-state equilibration is reached in a bichromophoric cyclometallated Ir(III) complexes after a few nanoseconds *via* REET and subsequent emission of **4** and **5** are delayed τ=225 μs and τ=430 μs, respectively, without compromising the emission quantum yields (Table 2.2). As well as offering an extremely long excited-state lifetime, excellent initial results were obtained for low-concentration oxygen detection.

2.4 REET in helix-rod host-guest complexes

2.4.1 Introduction

Conformationally ordered synthetic oligomers, called foldamers (Figure 2.30), are a class of compounds that have recently attracted attention, and interest in these systems continues unabated, primarily as a result of the fact that they hold considerable promise for potential applications in biomedical sciences. These synthetic oligomers may provide excellent starting points for the elaboration of peptide mimics that could only be designed with difficulty on the basis of small-molecule scaffolds. By means of diverse synthetic tools, the "bottom-up" foldamer approach is also highly useful in engineering new frameworks that can be successfully molded to mimic the structure and functions of biopolymers.[136] The scope and feasibility of this concept is reflected in the exponential growth from its foundation in the early 21st century to the present stage. The recent launch of the heterofoldamer concept has further fuelled activity in this area, essentially because the conformational space that is available for foldamer design can be enormously augmented by developing oligomers that feature a variety of building blocks in the backbone. Despite offering considerable promise because of the enormous structural diversity, a breakthrough in applications of the foldamers in material science, in particular in molecular machines, is yet to be realized.[34]

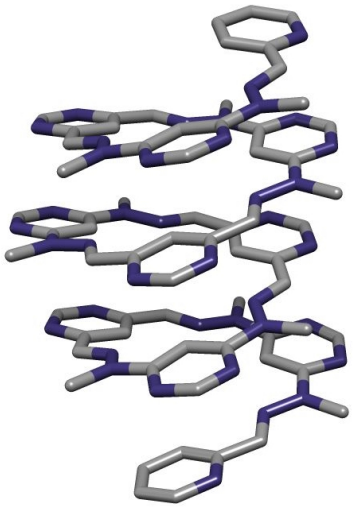

Figure 2.30. Crystal structure of a foldamer reported by Lehn and coworkers [137].

Recently Huc and co-workers [35, 138] reported a finding that clearly indicate that foldamers have a great potential in developing new molecular machines and nanodevices. This idea is valid because foldamers of any desired shape, architecture can be synthesized by using delicate and flexible noncovalent interactions, among which the highly directional hydrogen-bonding interaction assumes prime importance.[136] Huc and coworkers demonstrated that double helical foldamers that are coiled around rod-shaped guest molecules can perform a screw-type motion, which is an unusual phenomenon that is not observed in other molecular machines.[35] These heterofoldamers called foldaxanes by analogy with rotaxanes (i. e. a mechanically-interlocked molecular architecture consisting of a "dumbbell shaped molecule" which is threaded through a "macrocycle"), are able to hybridize into a stable, antiparallel, double-helical architecture by means of a collection of hydrogen-bonding and π-stacking interactions.[34]

We were especially interested in the perspective of combination of the REET approach with double-helix structures, allowing to both form and probe guest-host complexes. The main *idea* of such a supramolecular system is presented in Figure 2.31. The guest-molecule (for the sake of simplicity further we will call it "*thread*") was synthesized to have a luminophore, based on Ru(II)-emitting centre (i. e. $[Ru(bpy)_3]^{2+}$, bpy – 2,2'–bipyridine) attached on one thread terminus and on the other an energy reservoir (pyrene), connected *via* a flexible chain. The flexible connection between the Ru(II)-centre and pyrene chromophore allowed to the molecule to adopt a conformation in solution in such conformation, that energy transfer between them could occur in a reversible way. So REET is *ON*, and the lifetime of emission is elongated. When thread and double-helix are brought into the interaction – the conformation of thread changes to a more rod-like structure decoupling Ru(II)-emitting centre and pyrene chromophore, thus decreasing the possibility for energy transfer to occur. In this case the REET is *OFF*, causing decrease of emission lifetime of supramolecular system.

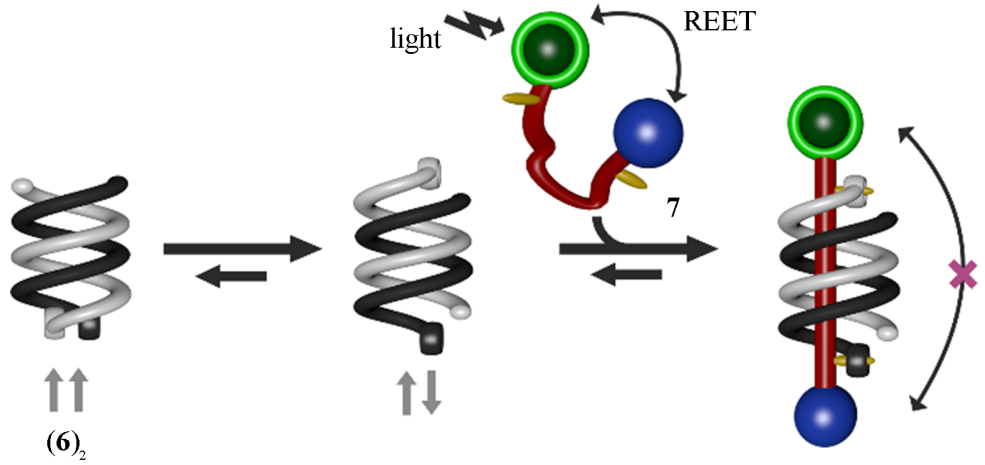

Figure 2.31. Host-guest complex **7**⊂$(\mathbf{6})_2$ formation, demonstrating the REET process; the green ball represent Ru(II)-based organic complex luminophore and blue one a pyrene chromophore. At equilibration an antiparallel $(\mathbf{6})_2$ is predominant.

Such a supramolecular system could be used as a conformational probe offering and alternative to FRET probes [36], and having greater sensitivity for small distances.

Our colleagues, Huc, Ferrand and coworkers [139] showed that rod-shaped guest molecules enter (threading process) the cavity of mono-helical structures very fast, so that it could not be resolved by classical NMR-technique nor as we observed by time-resolved emission spectroscopy measurements using molecule **7** as a guest[1] (Figure 2.32). In the present study we were interested in studying the complexation process between the **7** and $(\mathbf{6})_2$ (Figure 2.32), resulting in formation of the host-guest complex **7**⊂$(\mathbf{6})_2$, occurring much slower compared to single-helix **6** complexation with **7**, thereby allowing us to use spectroscopic measurements to characterize this process of complexation.

2.4.2 Results and discussions

In the present work we used oligomer **6** (Figure 2.32) for single-helix and double-helix $(\mathbf{6})_2$ formation and a guest molecule **7** (Figure 2.32), which was synthesized in Huc's laboratory in Institut Européen de Chimie et Biologie: IECB, Pessac, France. For more details on synthesis and molecules characterization, see PhD thesis (Université de Bordeaux 1) of Gan [140].

2.4.2.1 Steady-state spectroscopy

The electronic absorption spectrum (Figure 2.33) of **7** shows absorption features of both chromophores: Ru(II)-centre MLCT absorption in the visible range, centred around 460 nm and structured pyrene absorption in UV range. Vibronic fine structure of pyrene absorption is not affected by the presence of Ru(II)-centre and bpy ligands, implying only weak ground-state coupling between two chromophores.

By exciting **7** with visible light (λ_{exc}=450 nm) ^{3}MLCT emission of the Ru(II)-centre was observed with a maximum at 630 nm (Figure 2.33), with QY of 0.05 in degassed $CDCl_3$ and 0.062 in degassed CH_3CN, respectively. By exciting **7** with UV light (λ_{exc}=355 nm), emission of pyrene and ^{3}MLCT emission could be observed, showing that after pyrene excitation singlet state the energy could be transferred to ^{1}MLCT state (Figure 2.34), accompanied by fast ISC to the ^{3}MLCT state, which is then detected by its emission[2].

[1] Both methods acquire a relatively long time period to accumulate useful signal, while complexation process is already finished.

[2] The energy transfer from organic chromophore was also observed for Ru(II) and Ir(III) complexes studied before, see sections 2.2 and 2.3.

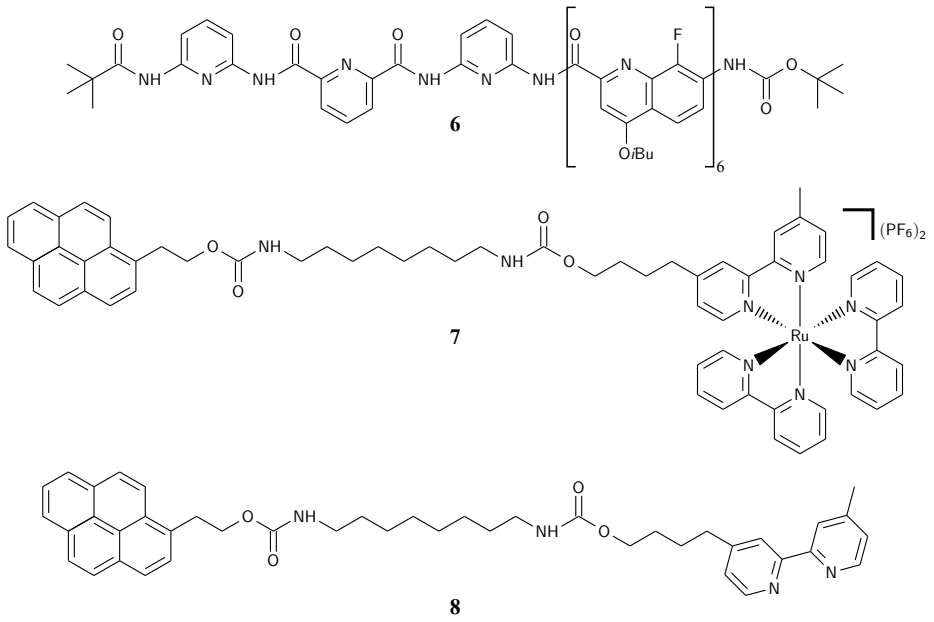

Figure 2.32. Structural formulas of single stranded oligomer **6**, guest-molecule **7**, guest-molecule **8** (without Ru(II)).

2.4.2.2 Time-resolved emission and absorption spectroscopy

Time-resolved emission spectroscopy experiments showed, that **7** ($c \simeq 10^{-4}$M) in degassed $CDCl_3$ solutions showed emission with a lifetime $\tau = 2.5\,\mu$s (Figure 2.37), while analogue complex $[Ru(bpy)_3]^{2+}$ has lifetime $\tau = 0.49\,\mu$s in degassed CH_2Cl_2.[141] The principle cause of emission elongation is anticipated to be the REET process. To determine the rate of REET equilibration time-resolved spectra and time-resolved TRABS were conducted. As it could be seen from the time-resolved emission decay (Figure 2.35) and Ground State Bleaching (GSB) recovery (Figure 2.36), both kinetics are governed by a sum of two exponential functions $A\exp(-k_1 t) + B\exp(-k_2 t)$. The faster component $k_1 > k_2$ corresponds to the energy transfer equilibration process, which takes almost 200 ns to finish with lifetime $\tau_{eq} = 28$ ns or $k_{eq} = 3.5 \times 10^7$ s^{-1}, the longer component describes emission of the system. The rate of equilibration is an order of magnitude lower, comparing to k_{eq} described previously for Ru(II) complex ($\tau_{eq} = 75$ ps) in section 2.2.

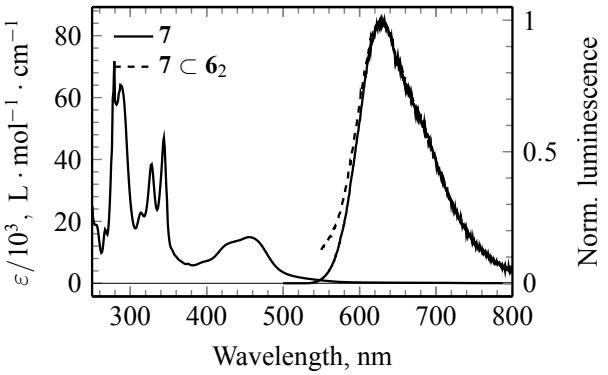

Figure 2.33. Absorption and emission ($\lambda_{exc} =$ 460 nm) spectra of **7** in $CDCl_3$.

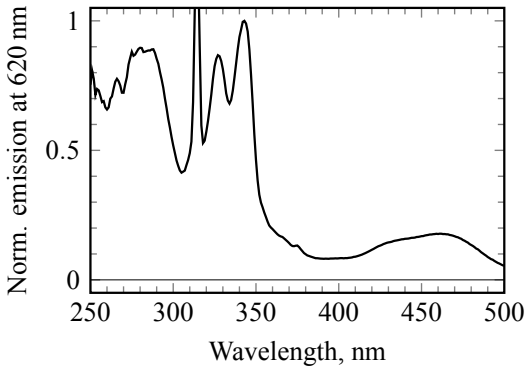

Figure 2.34. Excitation spectra ($\lambda_{ob} = 620$ nm) of **7** in $CDCl_3$.

This slower equilibration rate for **7**-system, comparing to Ru(II)-complex, studied in previous section may be explained by the fact that Ru(II)-centre of thread is attached to a pyrene energy reservoir through a long flexible chain, so Brownian motion is constantly causing an effect on the geometry between two chromophores, thus affecting REET process – slowing it down. The process of equilibration is a dynamic process: energy shuttles forwards and backwards from

^{3}MLCT state to ^{3}Pyr. According to TRABS data ground state bleaching recovery (Figure 2.35) the constant of equilibration equals to $K_{eq}=5\pm1$. The knowledge of equilibration constant K_{eq} allows us to calculate the amount of energy stored on ^{3}MLCT and ^{3}Pyr states, which equals to 16 % and 84 %, respectively. So we can write that at given moment rate of deexcitation of equilibrated **7** equals $k_{em}=\frac{0.16}{500\,\text{ns}}+\frac{0.84}{3000\,\mu\text{s}}=334\times10^3\,\text{s}^{-1}$ or $\tau_{em}=3\,\mu$s, which is in good agreement with experiment. The rate of backwards energy transfer $k_b=\frac{k_{eq}}{K_{eq}+1}=6.0\times10^6\text{s}^{-1}$ while forward energy transfer rate $k_f=3.6\times10^7\text{s}^{-1}$.

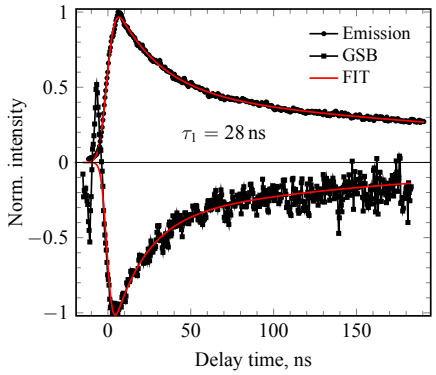

Figure 2.35. Time resolved emission decay of **7** in $CDCl_3$ ($\lambda_{exc}=465$ nm, $\lambda_{ob}=620$ nm) and GSB of **7** (see Figure 2.36).

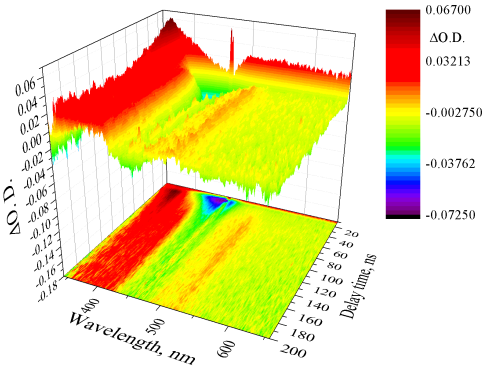

Figure 2.36. 3D TRABS map of **7** in $CDCl_3$ ($\lambda_{exc}=465$ nm).

In the presence of single stranded helix in degassed $CDCl_3$ the emission lifetime of **7** decreases down to $0.7\,\mu$s (Figure 2.38) and the QY drops from 0.05 to 0.023. Presence of $(\mathbf{6})_2$ causes **7** emission lifetime to drop twofold to $\tau\simeq1.1\,\mu$s (Figure 2.40), while the QY is reduced even more significantly 7 times, compared with the single stranded helix case. Such behaviour of emission properties of **7** in the presence of single helix and $(\mathbf{6})_2$ is simply explained by the fact that helix wraps around flexible hydrocarbon chain between Ru(II)-centre and pyrene chromophores, separating them to such distance that REET is not favourable any more. We explain QY decrease by the increased rate of deactivation channel losses, as well as the radiative channel rate is decreased through Ru(II)-complex interaction with single or double helix strands, and concentration dependence should be also taken in account.

By solving the system of equations for free **7** and for host-guest complex case:

$$\begin{cases} k_{em}=k_r+k_{nr} \\ \dfrac{k_r}{k_r+k_{nr}}=QY \end{cases}$$

we could calculate rates for radiative and non-radiative channels of deexcitation of **7** without and with $(\mathbf{6})_2$:

$$\begin{cases} k_r^{free}=k_{em}QY=2\times10^4\text{s}^{-1};k_r^{bound}=0.5\times10^4\text{s}^{-1} \\ k_{nr}^{free}=k_{em}-k_{em}QY=38\times10^4\text{s}^{-1};k_{nr}^{bound}=180\times10^4\text{s}^{-1} \end{cases}$$

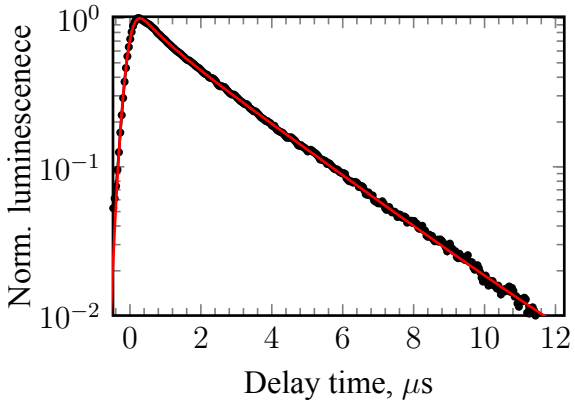

Figure 2.37. Time resolved emission decay of **7** in $CDCl_3$ (λ_{exc}=465 nm, λ_{ob}=620 nm).

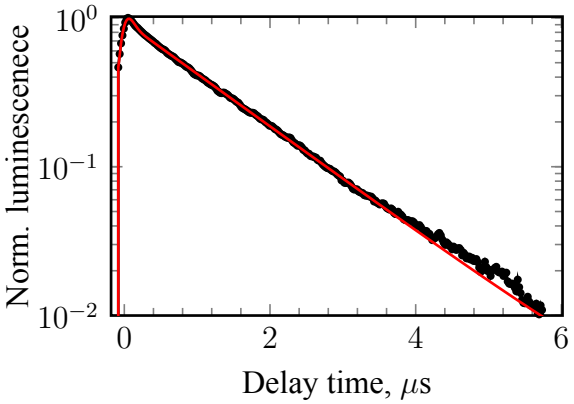

Figure 2.38. Time resolved emission decay of **7** in $CDCl_3$ in the presence of **6** (λ_{exc}=465 nm, λ_{ob}= 620 nm).

The complex formation between **7** and $(\mathbf{6})_2$ was proved by X-ray single crystal diffraction studies[1], and figure 2.39 shows the crystal-structure of **8** incorporated in $(\mathbf{6})_2$ cavity. The distance between pyrene and bpy-ligand equals to 18.5 Å. Thus the rate of energy transfer between D and A governed by Dexter mechanism (see subsection 1.4.1) sharply decreases as a function of the distance between D and A, and usually smallest possible distance between D and A is $\sim$10 Å when energy transfer is still possible. At 18.5 Å between D and A energy transfer cannot occur[2].

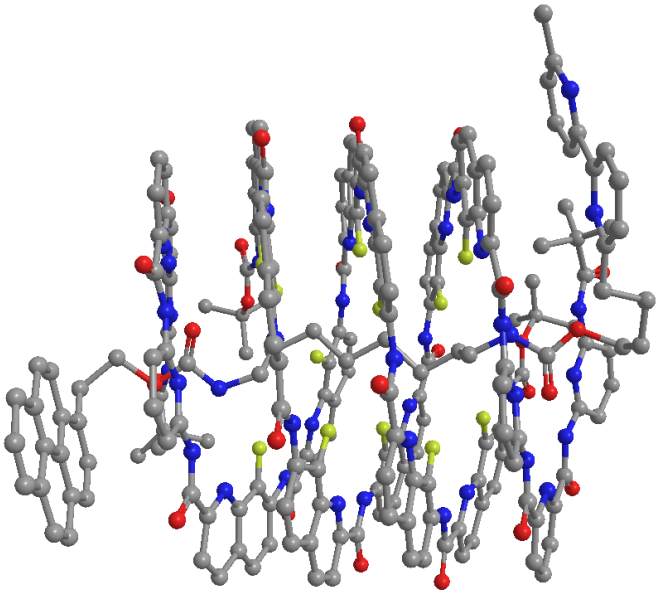

Figure 2.39. Crystal structure of **8** incorporated in $(\mathbf{6})_2$ cavity.

The complexion process of **7** and $(\mathbf{6})_2$ cavity happens slowly, as it was found during preliminary experiments, compared to single stranded helix **6**. Formation of complex $\mathbf{7}\subset(\mathbf{6})_2$ is a dynamic, reversible process and it is dependent on concentrations of reacting reagents and time. The emission lifetime of **7** decreases during its penetration inside of $(\mathbf{6})_2$ cavity. As **7** enters the $(\mathbf{6})_2$ cavity, the distance between luminophore (Ru(II)-centre) and energy reservoir (pyrene) increases, whereas efficiency of REET drops down. By determining the emission lifetime of **7** during complexation process, we were able to calculate its rate.

2.4.2.3 Threading process

Following the threading process was conducted as follows: solutions of **6** and **7** were prepared in $CDCl_3$[3] at 4 mM and 80 μM concentrations, respectively. Double-helix $(\mathbf{6})_2$ was prepared by dimerization of **6**, in advance, one day before the experiment, which was sufficient [140] for separately process of **6** dimerization to be accomplished, resulting $(\mathbf{6})_2$ formation (2 mM). The process of $(\mathbf{6})_2$ formation is dynamic reversible process, the constant of the equilibration is

[1] Crystal growth of **7** with $(\mathbf{6})_2$ was complicated by steric factors, as well as a multitude of diastereoisomers.

[2] According to $k_{Dexter}=\frac{2\pi}{h}KJ\exp(-2r/L)$ (see Dexter mechanism, p. 14), $k_{Dexter}\sim\exp(-37/1.5)\approx 0\,s^{-1}$.

[3] The $CDCl_3$ was purified from trace amounts of protons and water vapour by passing through predried (300 °C) Al_2O_{3basic} 100 μm powder.

equal to $K_{dh}^{353}=10000\,\mathrm{M}^{-1}$ at $353\,\mathrm{K}$[1] [140]. After $24\,\mathrm{h}$, when the process of $(\mathbf{6})_2$ formation is finished and $\sim 95.5\,\%$ of **6** is dimerized:

1. the given quantity of **7** solution was transferred into a spectroscopic quartz;
2. solvent was evaporated and a predetermined volume of $(\mathbf{6})_2$ solution was added into this cell;
3. molecules of **7** were dissolved;
4. obtained solution was frozen at liquid nitrogen temperature ($77\,\mathrm{K}$).

We studied different ratios between **7** and $(\mathbf{6})_2$ in our experiments: 1:6, 1:12, 1:32. Solutions for spectroscopic study were degassed by multiple[2] freeze-pump-thaw cycles and cells were blowtorch sealed. The closed and frozen cell at $77\,\mathrm{K}$ was transferred to the experimental set-up (Figure 1.19).

We used $\lambda_{exc}=460\,\mathrm{nm}$ excitation wavelength and recorded the $400-700\,\mathrm{nm}$ spectral region, where ^{3}MLCT emission lies, with a streak-camera as time-resolved detector. The emission lifetime τ of **7** lies in the range of $1-2.6\,\mu\mathrm{s}$, this fact caused us to work in a $10\,\mu\mathrm{s}$ timescale. The streak-camera in this timescale is triggered by the rising edge of laser pulse train, causing a $\sim 1\,\mu\mathrm{s}$ jitter. To suppress the effect of such a big jitter on the emission decays, we recorded every time-resolved 2D-emission map after every laser excitation pulse ($20\,\mathrm{Hz}$). Jitter-correction was applied to every 2D-map: all 2D-maps were aligned by rising edge of emission, after that the maps were integrated and averaged. The emission decays at $630\,\mathrm{nm}$ were analysed at different times during the complexation process between **7** and $(\mathbf{6})_2$.

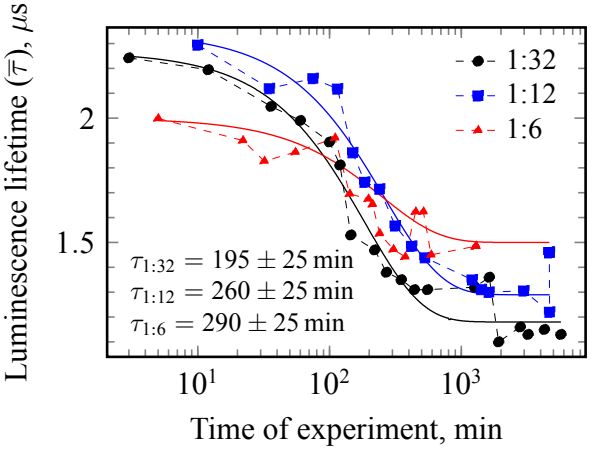

Figure 2.40. Average $\overline{\tau}$ emission lifetime dependence of **7** during formation of **7**$\subset(\mathbf{6})_2$.

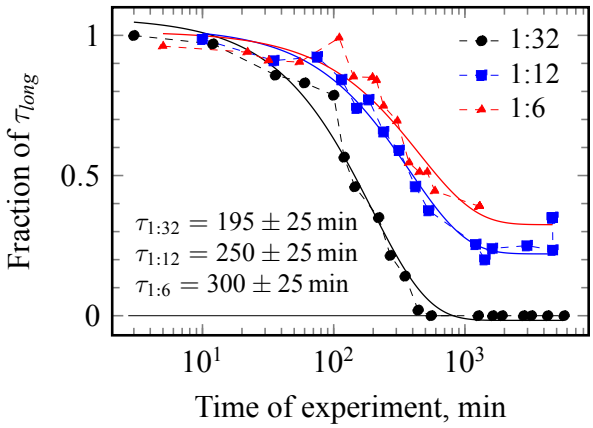

Figure 2.41. Fraction of emission lifetime τ_{long} of **7** during formation of **7**$\subset(\mathbf{6})_2$.

The data analysis merits special consideration. During the experiments there are different species in solution giving rise to emission: $1-\alpha\,\%$ of free **7** and $\alpha\,\%$ of **7**$\subset(\mathbf{6})_2$ complex, which could be at different stages of binding between **7** and $(\mathbf{6})_2$. It also should be taken in account that in solution there is $4.5\,\%$ of undimerized **6**, which can form **7** $\subset$**6** complex. As for free **7**, its emission lifetime is fixed and equals $\sim 2.5\,\mu\mathrm{s}$ in degassed $CDCl_3$, depending on concentration and the bound **7** lifetime has an unknown distribution. The latter is a main obstacle in data treatment of such dynamic systems. As we have mentioned above our goal in these experiments was to determine the rate of the complexation process forming **7**$\subset(\mathbf{6})_2$, which can be achieved by determination of the fraction of bound **7**, tracked using emission lifetime dependence *vs* time of experiment. In our work, instead of using distributions (which would not allow in a simple form to realize the rate of complexation) for emission lifetime of bound **7**, emission decays were treated using a sum of two exponents $A\exp(-t/\tau_{short})+B\exp(-t/\tau_{long})$, where τ_{long} stands for

[1] At room temperature binding constant $K_{dh}^{293}\simeq 66000\,\mathrm{M}^{-1}$, calculated assuming that $\Delta G_{dh}^{293}\simeq G_{dh}^{353}$.

[2] At least three times. Note: After three times of freeze-pump-thaw cycles the solvent volume reduction was minimal $\sim 5\,\%$.

lifetime of unbound **7** and τ_{short} for bound **7** in the **7**⊂$(\mathbf{6})_2$ complex[1]. This replacement allowed us to observe with acceptable error, the fraction of growth for **7**⊂$(\mathbf{6})_2$ during the experiment. Another more simplified way to treat data is to fit emission decays curves using one exponent (vide infra). During the threading process, as the fraction of **7**⊂$(\mathbf{6})_2$ grows, the rate of emission increases, so by treating emission decays with one exponent, a general trend could be observed in obtained dependency $\tau = f(time)$, allowing to tell whether the complexation process has several characteristic time constants or only one and determine values for them.

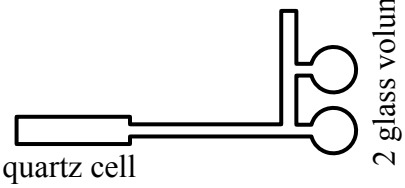

Figure 2.42. Special, 2-volumes spectroscopic cell.

Figure 2.40 demonstrates luminescence lifetime dependence as a function of time during complexation process between **7** and $(\mathbf{6})_2$ as averaged value $\overline{\tau} = \frac{A \cdot \tau_{short} + B \cdot \tau_{long}}{A+B}$, where τ_{long} was fixed during the fitting procedure. The changes of fraction of τ_{long} during the experiment represents change of fraction of non-bound **7** during the experiment (Figure 2.41), which decreases. As the Figure 2.40 shows: the higher is relative concentration of **7**, the longer will be the emission lifetime after the complexation process is completed. For the system with concentration ratios 1:32 the lifetime reaches 1.1 μs, 1:12 – 1.3 μs, 1:6 – 1.5 μs. Remembering that the binding constant for **7**⊂$(\mathbf{6})_2$ equals to 1700 M^{-1} [140], which is a relatively low value. Only ∼78 % of **7** is bound in the **7**⊂$(\mathbf{6})_2$ complex for all ratios studied in the experiments. So differences in lifetimes could be understood if the interactions between pyrene and Ru(II)-centre of different **7** molecules would be taken in account. At higher concentration of **7** there are more possibility pf REET to occur between two different **7** molecules. This interpretation could also explain why we are observing such dependencies in fraction change of τ_{long} (Figure 2.41).

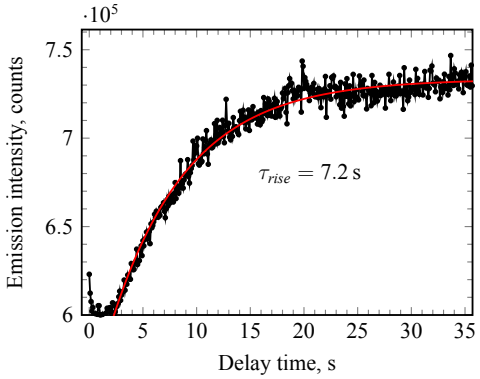

Figure 2.43. Changes in emission intensity of **7** during decomplexation process of **7**⊂$(\mathbf{6})_2$ system (λ_{exc}=465 nm, λ_{ob}=620 nm).

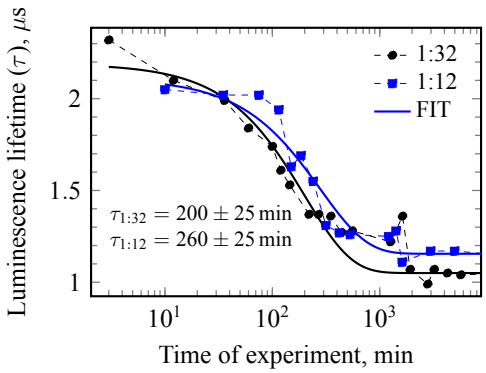

Figure 2.44. Single τ emission lifetime dependence of **7** during formation of **7**⊂$(\mathbf{6})_2$ (λ_{exc}=465 nm, λ_{ob}=620 nm).

The rates of complexation of **7** and $(\mathbf{6})_2$ at different ratios between **7** and $(\mathbf{6})_2$ were determined by fitting the experimental curves with mono-exponential function. The lifetimes determined from averaged luminescence lifetime $\overline{\tau}$ and from fraction of "long" lifetime of **7** are very similar and equal $\tau_{1:32}$=195±25 min; $\tau_{1:12}$=250±25 min; $\tau_{1:6}$=290±50 min.

Treating experimental data of emission lifetime as a function of complexation time $\tau = f(t)$ using monoexponential fit $A\exp(-kt)$ give similar results (Figure 2.44), compared to biexponential fits (Figure 2.40). The rates of complexation process between **7** and $(\mathbf{6})_2$ determined from Figure 2.44 are very similar ($\tau_{1:32}$=200±25 min; $\tau_{1:12}$=280±25 min) to rates determined from bi-exponential treatment of experimental data.

[1]Note: Fast preequilibration process (τ=28 ns) of REET in **7** is not considered in emission analysis.

2.4.2.4 Dethreading process

It was found that the decomplexation (dethreading) process upon high dilution happens much faster than the complexation process. It was not possible to resolve this process by measuring emission lifetimes at different time of de-threading process. But taking in account that QY of **7** is lower, when it is in the **7**⊂$(\mathbf{6})_2$ complex, we were able to record the growth of emission intensity during the time of dethreading, by exciting **7**⊂$(\mathbf{6})_2$ complex with visible light $\lambda_{exc}=465$ nm using single photon-counting detection (Figure 2.43). The experiment was conducted as follows:

1. **7**⊂$(\mathbf{6})_2$ complex formation was completed in non-degassed $CDCl_3$ solution as described before.
2. The solution of **7**⊂$(\mathbf{6})_2$, as well as pure $CDCl_3$ was degassed using freeze-pump-thaw cycles in the same custom made glass cell (Figure 2.42), being stored in two different parts of the cell, so they cannot mix during degassing procedure.
3. Then $CDCl_3$ (20-times excess) was poured into to the solution of **7**⊂$(\mathbf{6})_2$ to start the decomplexation process.

During the decomplexation of **7**⊂$(\mathbf{6})_2$ two processes are happening simultaneously: *1)* **7**⊂$(\mathbf{6})_2$ →**7** +$(\mathbf{6})_2$ and *2)* $(\mathbf{6})_2$ →2**6** , because the values of binding constants for $(\mathbf{6})_2$ formation $K_{dh}=66000\,\mathrm{M}^{-1}$ and **7**⊂$(\mathbf{6})_2$ $K_{th}=1700\,\mathrm{M}^{-1}$, resulting an almost complete decomplexation of **7**⊂$(\mathbf{6})_2$ and $(\mathbf{6})_2$. The rate of decomplexation was determined to be equal $k_{decom}=1.4\times10^{-1}\,\mathrm{s}^{-1}$.

2.4.3 Conclusions

By using time-resolved spectroscopies it was shown, that in helix-rod host-guest complexes, showing REET the efficiency of REET process can be controlled by the degree of complexation between a host double-helix foldamer and a guest thread molecule. The rates of complexation were determined for different ratios between double-helix and thread, and rate of decomplexation was estimated. The observed experimental results attest to the possibility of using this approach as a new basis for designing new conformation/distance probes.

2.5 Chapter Summary

Several applications of the Reversible Electronic Energy Transfer (REET) approach to modify photophysical properties in bichromophoric supramolecular systems were discussed. The REET approach was used to dramatically enhance emission lifetimes of Ru(II) complexes based on tridentate ligands and cyclometallated Ir(III) complexes, respectively, without diminishing QY. Modulation of photophysical properties of these chromophores can be pertinent for applications in gas sensors and electroluminescence devices. A new approach of using REET in the perspective of probing conformation/distance was proposed: to control the efficiency of the REET in the process by the degree of complexation, exemplified between a host double-helix foldamer and guest thread molecule.

Bichromophoric Ru(II) complexes based on tridentate ligands offering an optimised coordination environment combined with an appropriate organic auxiliary are shown to give complexes based on tridentate ligands with unprecedented luminescence lifetimes without affecting the emission efficiency. Time-resolved spectroscopies show that excited-state equilibration is reached in less than 100 ps *via* REET with 94 % of energy being stocked on the organic energy reservoir, on average in the microsecond timescale with emission lifetime $\tau_{em}=42\,\mu$s from the metal-centre. Interestingly this behaviour was instilled in a predetermined fashioned based on a rudimentary knowledge of energies of excited-states and intrinsic deexcitation in respective molecular sub-units. As well as offering the possibility of more efficient photosensitizers, applications in molecule-based light emitting devices, molecular machines and detection are under investigation.

Time-resolved spectroscopies conclusively showed for the first time that excited-state equilibration is reached in a bichromophoric cyclometallated Ir(III) complexes after a few nanoseconds *via* REET and subsequent emission of **4** and **5** are delayed $\tau=225\,\mu$s and $\tau=430\,\mu$s, respectively, without compromising the emission QYs. As well as offering an extremely long excited-state lifetime, excellent initial results were obtained for low-concentration oxygen detection.

By using time-resolved spectroscopies it was shown, that in helix-rod host-guest complexes, showing REET the efficiency of REET process can be controlled by the degree of complexation between a host double-helix foldamer and a guest thread molecule. The rates of complexation were determined for different ratios between double-helix and thread, and rate of decomplexation was estimated. The observed experimental results attest to the possibility of using this approach as a new basis for designing new conformation/distance probes.

Chapter 3

Photoinduced energy and electron transfer in supramolecular systems

3.1 Introduction

Transfer of excitation energy in natural systems is a fundamental process for example: light harvesting, cell respiration, photosynthesis, propagation of information, where the energy should be transferred from a specific cite (e. g. light absorption by antennas, energy release *via* an oxidation process, etc.) to another site where useful work should be done.

For a long period of time, since Förster described Resonance Energy Transfer (RET) in 1948 scientists are exploring this process along with electron transfer (where electron acts as a carrier of excessive energy) in an attempt to mimic natural processes such as artificial photosynthesis, applying it to effective energy storage. One of the best known examples is water reduction for hydrogen gas generation using different catalysts [142–144] or photocatalytic water treatment [145]. One fundamental aspect in artificial photosynthesis development is obtaining effective photoinduced charge-transfer processes, allowing to separate charge over long distances with a slow charge recovery rate. In particular, the spatial organization of the individual molecules within the photosynthetic unit imposed by the surrounding protein matrix enables the formation of a charge separated state with extraordinarily long lifetimes. In order to understand and mimic these biological photophysical processes, artificial model systems have been designed in which the distance dependence for charge separation and charge recombination reactions is studied in donor-bridge-acceptor molecules.[138]

In the section 3.2 we report on the investigation of photoinduced charge-transfer processes between an electron donor, an Oligo(p-phenylene vinylene) (OPV) and an electron acceptor, a Perylene Bisimide (PB) connected through helical aromatic oligoquinoline amide-based foldamer bridge, showing fast charge-separation and slow charge-recovery rates.

Electronic Energy Transfer (EET) and Förster Resonance Energy Transfer (FRET) as it is well known has become widely used in all applications of fluorescence imaging and probing, including medical diagnostics, DNA analysis and etc. The widespread use of EET is used due to the favourable distances for energy transfer, which are typically the size of a protein or the thickness of a cell membrane. One of the most common application of EET is the distances to measure between two sites on a macromolecule.[81] The other very promising application of EET or FRET process is its usage in fluorescence probe development where excitation energy could be transferred from light harvesting antenna to emissive site in the presence of stimulus (pH, ion presence and etc.)

We report (section 3.3) the photophysical investigation of novel lanthanide-based luminescent probe for time-gated *in situ* detection of Cu(I) ion, being modulated by the antenna effect through cation/π interactions, based on the process of energy transfer between energetically adapted light harvesting antenna and emitter.

3.2 Photoinduced electron transfer in helical aromatic oligoamide foldamers

3.2.1 Introduction

One of the remarkable achievements of photochemistry has been the recognition that certain molecules on photoexcitation become powerful electron donors or acceptors.[37] This phenomenon known as photoinduced electron-transfer[1]. The nature of how charge is propagated through molecules, molecular systems and materials is the basis of molecular electronics as well as being of fundamental importance in the design of organic photovoltaic devices and light emitting diodes, and in understanding the functioning of photosynthetic reaction centres. The charge transfer process challenge our understanding of fundamental charge dynamics in molecular systems. Numerous investigations during many decades were carried out on this question, frequently using two redox centres: donor and acceptor covalently bound to the bridge structure that is under investigation, forming donor-bridge-acceptor systems.[38–40]

Many artificial model systems have been designed in which the distance dependence for charge separation and charge recombination processes are studied.[40–44] In these examples, the chromophores are either placed on top (cofacial) or next to each other (collinear). As a consequence of the rigidity of these bridges, in all cofacial and collinear positions, the chromophore position is fixed and the distance between the chromophores through space is similar as the distance through the bridge. The bridge groups can be generally classified into three categories, σ-systems, cofacial π-systems, of which DNA is the most studied, and linear π-systems. Depending on the properties of the bridge and the way the chromophores are attached to the bridge, charge transfer may proceed *via* a superexchange[38, 45] or a charge hopping mechanism.[44–46]

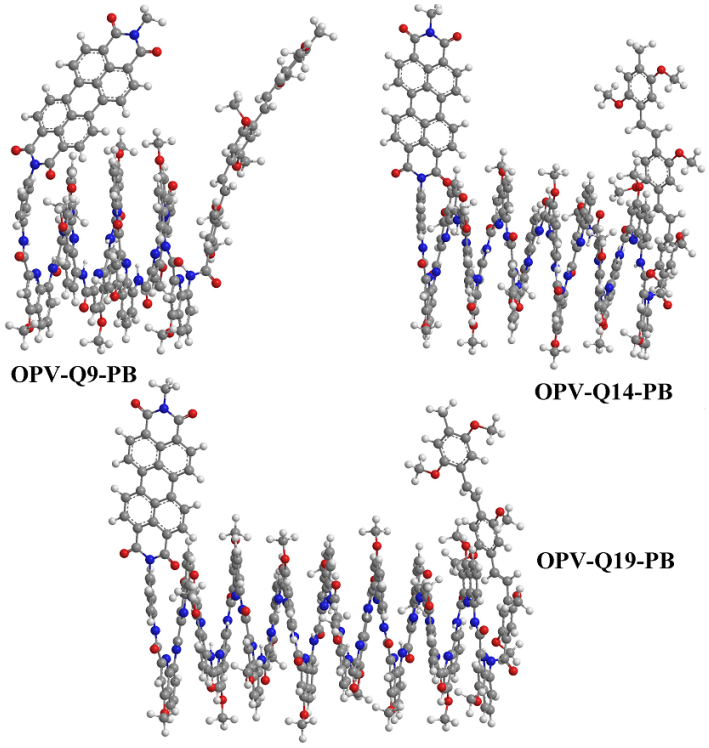

Figure 3.1. Structures of studied samples: **OPV-Q9-PB**, **OPV-Q14-PB**, **OPV-Q19-PB** (MOPAC, PM7 calculations).

According to the superexchange model based on perturbation theory, bridge orbitals are involved in virtual states contributing to the electronic coupling between donor and acceptor subunits.[45] In the hopping mechanism the electron is located at the bridge for a short period of time during which the charge transfer occurs.[45] The effectiveness of the bridge to mediate the charge transfer process is expressed in the attenuation factor β. Typical attenuation factors found are $\beta = 0.6 - 1.2\,\text{Å}^{-1}$ for hydrocarbon bridges, $\beta = 0.32 - 0.66\,\text{Å}^{-1}$ for conjugated polyphenylenes, $\beta = 0.04 - 0.2\,\text{Å}^{-1}$ for polyenes and $\beta = 0.04 - 0.17\,\text{Å}^{-1}$ for polyynes. A lower attenuation factor indicates that the bridges can more effectively mediate the charge transfer reaction. The use of bridges to spatially organize chromophores in an intermedi-

[1] Sometimes researcher call it charge-transfer.

ate situation where the chromophores are positioned in both a cofacial and a colinear arrangement has rarely been explored. Examples include the investigation of chromophores with constrained molecular assemblies or connected at ortho, meta, or para positions by rigid aromatic molecular linkers. In both cases the chromophores are held at a relatively short distance from each other by non-helical bridges. These studies revealed that the effect of chromophore orientation on the charge transfer process, if any, depends highly on the system at hand. One hurdle in studying the effect of chromophore positioning in both a cofacial and collinear arrangement lies in the difficulty in achieving large distances between the electron donor and acceptor and to simultaneously be able to control and tune their relative orientations.[40]

In the group of collaborator Dr. Huc[1], helical foldamers possessing stable and predictable conformations were used as a bridge in donor-bridge-acceptor structures [40], where the helicity of the bridge was used as a scaffold to organize chromophores in space.

Here, we will continue work, started by Huc and coworkers in 2009 [40], concerned characterization of a helical aromatic oligoquinoline amide-based foldamers acting as a helical bridge between an electron donor, oligo(p-phenylene vinylene) (OPV), and an electron acceptor, perylene bisimide (PB). The charge transfer couple (OPV-PB) was selected since the photophysics of the individual compounds and the charge transfer pair have been thoroughly studied.[47–53]

The oligoquinoline amide foldamers feature remarkably high structural robustness and predictability in a variety of apolar, polar, and protic solvents and in the solid state as determined *via* NMR and single-crystal X-ray diffraction studies. These beneficial properties are expected to enable the exact positioning of the chromophores in order to vary and control not only the distance between the donor and the acceptor, but also their relative orientation in space. As a result of the helicity of the foldamers the distance between the chromophores either through space or through bridge is different. For this reason it is likely that the charge transfer pathways will depend on the foldamer that is studied. In 2009 Huc and coworkers synthesized four different foldamers sequences ranging from dimer to nonamer, for which a photophysics was studied.[40]

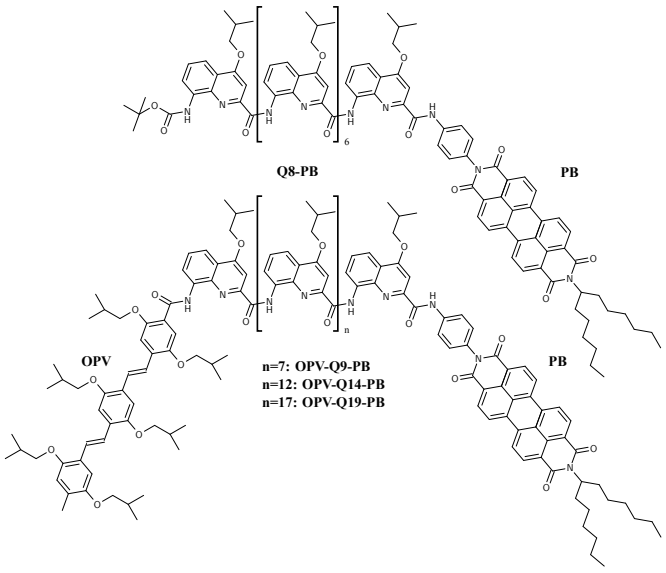

Figure 3.2. Structural formulas of studied samples: **Q8-PB**, **OPV-Q9-PB**, **OPV-Q14-PB**, **OPV-Q19-PB**.

Herein we will be working on longer oligoquinoline amide foldamers (see Figure 3.1), containing nine, fourteen and nineteen quinoline units in the bridge (Figure 3.2), connecting electron donor (OPV) and acceptor (PB). The length of foldamer bridges were chosen in a such manner, that donor and acceptor sites would be orientated to each other in a cofacial way. The distance between donor and acceptor through bridge d_{bridge} was estimated as: 69, 108 and 145 Å, respectively for 9-mer (4 full turns of helix), 14-mer (6 turns) and 19 mer (8 turns); through space at d_{DA}: 14, 21 and 28 Å, respectively, according to previously published data [40].

[1] Institut Européen de Chimie et Biologie

3.2.2 Experimental

In this research we studied 4 samples (see Figures 3.2) by means of ultrafast and sub-nanosecond time-resolved emission and absorption spectroscopies: **Q8-PB**[1], **OPV-Q9-PB**, **OPV-Q14-PB**, **OPV-Q19-PB**.

The studies were carried out in 3 different solvents with different dielectric permeability:

1. Toluene (C_7H_8, $\varepsilon = 2.3$);
2. Chloroform ($CHCl_3$, $\varepsilon = 4.8$);
3. Dichloromethane (CH_2Cl_2, $\varepsilon = 8.9$).

Temperature dependences of electron transfer rate were studied for **OPV-Q9-PB**, **OPV-Q14-PB** and **OPV-Q19-PB** in CH_2Cl_2 in the temperature range from 173 to 303 K. For these measurements the liquid nitrogen Cryostat 77 K OptistatDN2 (Oxford instruments) was used. The all studied samples were treated in non-degassed solutions, which were degassed by freeze-pump-thaw cycles or by Ar gas (high purity, 99.9998 %) bubbling through solutions. The degassing procedure was necessary, as it was found in the preliminary studies **OPV-Q14-PB** and **OPV-Q19-PB** samples that showed fast photodegradation under excitation in oxygen containing solvents, due to the extremely long lifetime of PB triplet state. The **Q8-PB** and **OPV-Q9-PB** samples did not show fast photodegradation in air-equilibrated solutions, so it was possible to use them during several measurements even in non-degassed solutions. For TRABS experiments the 10^{-5} M solutions, for time-resolved emission and steady-state measurements 2×10^{-6} M, respectively were used.

3.2.3 Results and discussions

3.2.3.1 Steady-state spectroscopy

The UV-vis absorption spectra of all studied samples are shown in Figure 3.4 and can be roughly divided into three regions: a quinoline part (300 – 400 nm), an OPV part (350 – 450 nm), and a PB part (450 – 550 nm), according to the spectra of the individual chromophores in $CHCl_3$ (Figure 3.3). The quinoline part of the spectra shows a progressive increase in molar absorption coefficient upon elongation of the foldamer bridge as a result of the increase in quinoline content. The OPV and PB part only show small fluctuations in molar absorption coefficient that are likely caused by changes in electronic structure and environment, as also observed by ^{1}H NMR [40].

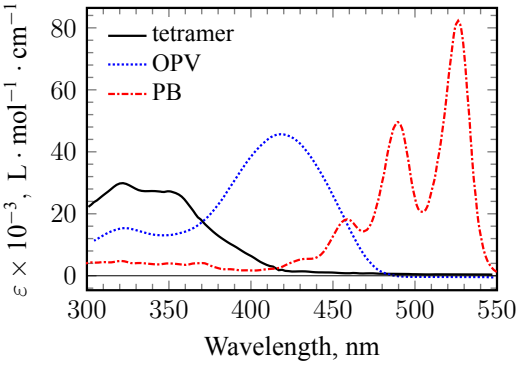

Figure 3.3. UV-vis absorption spectra of individual chromophores OPV, PB and bridge tetramer [40].

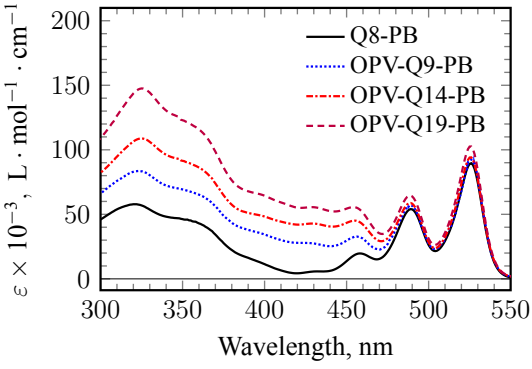

Figure 3.4. UV-vis absorption spectra of studied samples: **Q8-PB**, **OPV-Q9-PB**, **OPV-Q14-PB**, **OPV-Q19-PB**.

The structure and spectral positions of the vibronic bands of the PB are similar for all samples and are characteristic for the dissolved chromophore. Even at high concentration (5.0×10^{-4} M) the absorption spectrum displays these characteristic vibronic bands and therefore ensures that

[1] Number n (Q_n) means number of quinolines units in the sample.

further photophysical measurements are not hampered by aggregation phenomena.[40] Decreasing solvent polarity by using toluene instead of chloroform did not affect the shape of the absorption spectra or the position of the absorption maxima of the foldamers.[40]

The PB emission QY are represented in the Table 3.1, recorded in different solvents using fluorescein water solution (0.1 M NaOH) as a reference. Irrespective of excitation wavelength and solvent, the QY of fluorescence for PB are strongly quenched. Excitation spectra recorded at the residual emission band of the PB (576 nm) show contributions of all chromophores, revealing that both the quinoline foldamer and the OPV chromophore contribute to an energy transfer reaction to the PB (Figure 3.5). The fluorescence and excitation spectra of PB (**OPV-Q19-PB**) presented in Figure 3.5 are characteristic for all studied samples.

Table 3.1. PB emission QY for all studied samples: **Q8-PB**, **OPV-Q9-PB**, **OPV-Q14-PB**, **OPV-Q19-PB** in toluene, $CHCl_3$ and CH_2Cl_2.

Sample	toluene, %	$CHCl_3$, %	CH_2Cl_2, %
Q8-PB-Ar[a]	3.6	0.7	3.1
Q8-PB-air[b]	3.6	0.6	0.6
OPV-Q9-PB-Ar	1.86	0.45	0.6
OPV-Q14-PB-Ar	1.32	0.44	0.6
OPV-Q19-PB-Ar	0.8	0.48	0.6

* λ_{exc}=490 nm; fluorescein (0.1 M NaOH) water solution was used as a reference

[a] Argon-equilibrated solutions;

[b] Air-equilibrated solutions;

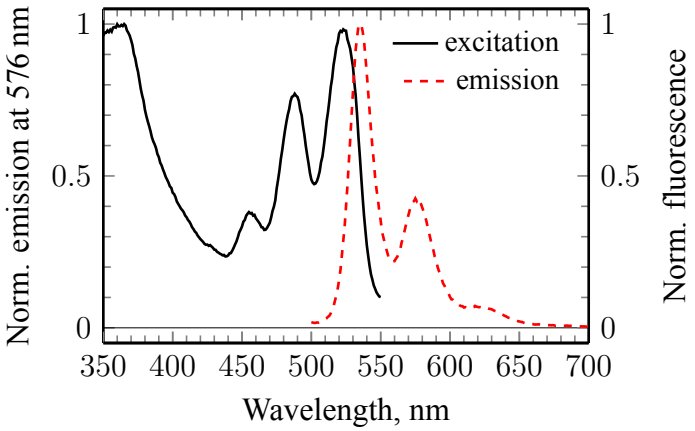

Figure 3.5. Excitation (λ_{ob}=576 nm) and emission (λ_{exc}=490 nm) spectra of **OPV-Q19-PB** in CH_2Cl_2.

3.2.3.2 Time-resolved spectroscopies

Before starting discussion of experimental results it would be useful to consider a simplified Perrin-Jablonski diagram (see Figure 3.6), showing the general concept of electron transfer of studied systems, based on previous results[40], where the longest studied foldamer system was **OPV-Q9-PB** and proved by the new experimental data.

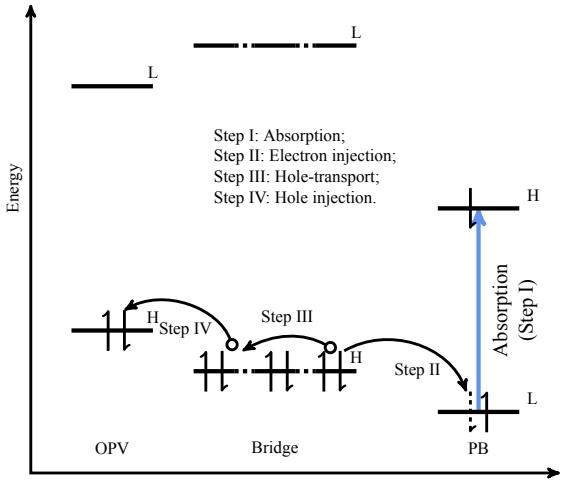

Figure 3.6. Simplified Perrin-Jablonski diagram of OPV-Q_n-PB systems.

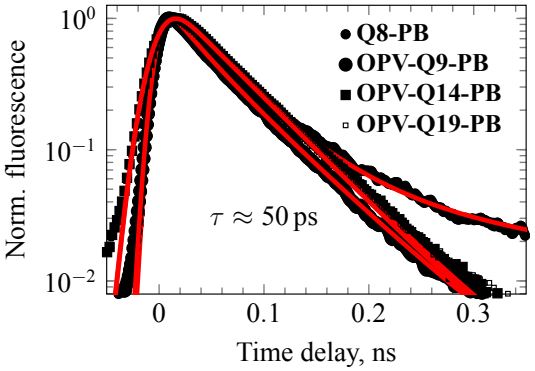

Figure 3.7. Fluorescence decay of all studied samples in $CHCl_3$ (λ_{exc}=490 nm, λ_{ob}=550 nm).

Fluorescence quenching

Considering the case of electron acceptor PB, direct excitation can be achieved with $\lambda_{exc}=$ 490 nm (Figure 3.6). Being excited to its singlet state, radiative relaxation of this state to the ground state with high emission QY=0.99 [40, 146] is expected, and with fluorescence decay lifetime of τ=4.2 ns [40, 146]. But instead of this behaviour, as it can be seen from Figure 3.7, emission of acceptor PB is highly quenched (150-times, Table 3.1) by a fast process observed for all samples. In the case of longer bridge samples **OPV-Q14-PB** and **OPV-Q19-PB** (Figure 3.7) slight increase in emission lifetimes is observed for $CHCl_3$ and CH_2Cl_2 solvent (Table 3.2). But still in the case of more polar solvents: $CHCl_3$ and CH_2Cl_2, comparing to toluene, emission lifetimes of PB for all studied samples are much alike (within the error of measurements ±10 ps). On the other hand, the emission lifetimes of PB in toluene for different samples differ greatly (for explanations see below Figure 3.14).

Such behaviour could be explained by an electron transfer process either from the quinoline unit or OPV electron donor site to a PB single-occupied ground state, thus forming either OPV-Q_n^+-$PB^{\bullet-}$ or $OPV^{\bullet+}$-Q_n-$PB^{\bullet-}$, respectively. But the fact that similar fluorescence quenching is observed in the case of **Q8-PB** sample (Figure 3.7), leads us to believe, that the fluorescence quenching of all samples occurs due to electron transfer from HOMO state of the foldamer bridge unit quinoline to a single-occupied ground state of PB (Step I, Figure 3.6). By this act two radicals are being formed: cation-radical of the quinoline unit and anion-radical of $PB^{\bullet-}$. Then the electron of the electron donor OPV ground state should be transferred to a quinoline cation-radical. In this way formation of charge separated state $OPV^{\bullet+}$-Q_n-$PB^{\bullet-}$ will be accomplished.

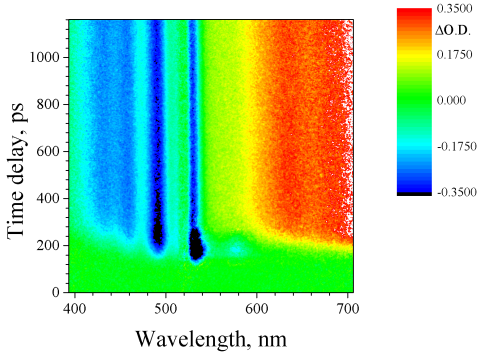

Figure 3.8. TRABS map of **OPV-Q9-PB** in $CHCl_3$ (λ_{exc}=532 nm, timescale 1 ns).

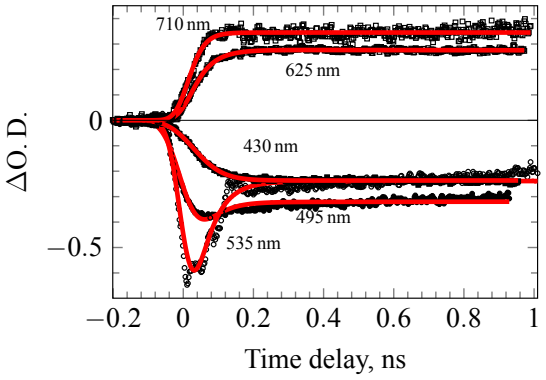

Figure 3.9. TRABS signals for **OPV-Q9-PB** in $CHCl_3$ (λ_{exc}=532 nm, timescale 1 ns).

The rates of electron transfer from the quinoline scaffold to the ground state PB, determined from fluorescence quenching rates, as measured by time-resolved emission spectroscopy (streak-camera detection) are presented in Table 3.2, p. 70.

In order to prove that electron transfer from a quinoline to the PB site is responsible for the observed fluorescence quenching of PB emission, photoinduced absorption spectroscopy was employed. Through this technique, the rates of charge separation and charge recombination were measured.

TRABS spectroscopy measurements

In Figures 3.10 and 3.8 the TRABS maps of **Q8-PB** and **OPV-Q9-PB** ($\lambda_{exc}=532$ nm) are represented, respectively.

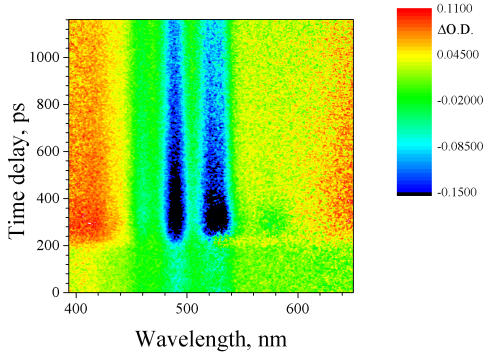

Figure 3.10. TRABS map of **Q8-PB** in $CHCl_3$ ($\lambda_{exc}=532$ nm, timescale 1 ns).

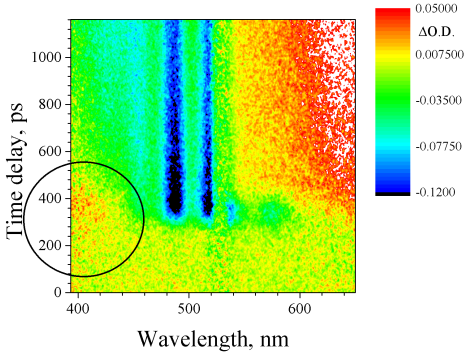

Figure 3.11. TRABS map of **OPV-Q19-PB** in $CHCl_3$ ($\lambda_{exc}=532$ nm, timescale 1 ns).

Immediately after excitation **OPV-Q9-PB** in $CHCl_3$ (Figure 3.8) Ground State Bleaching (GSB) of electron acceptor PB appears at the wavelength of ground state absorption, 490 nm and 530 nm, along with another negative band, associated to stimulated emission at 535 nm, which rapidly recovers with the lifetime $\tau=50$ ps (Figure 3.9), which was found to be in good agreement with time-resolved fluorescence measurements. The GSB of electron donor (OPV) site (negative band, centred at 430 nm, which slightly overlaps with negative bands, determined as GSB of PB) and band, centred at 625 nm (cation-radical $OPV^{\bullet+}$ absorption) appears in parallel with anion-radical $PB^{\bullet-}$ band growth with time constant of 67 ps[1].

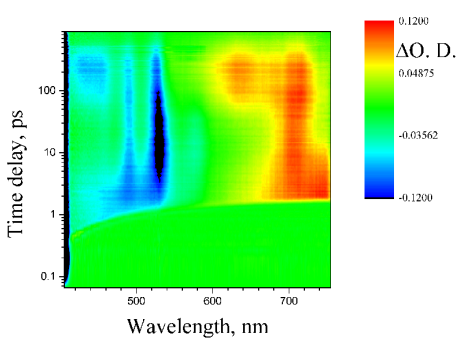

Figure 3.12. TRABS map of **OPV-Q9-PB** in $CHCl_3$ ($\lambda_{exc}=400$ nm, timescale 1 ns).

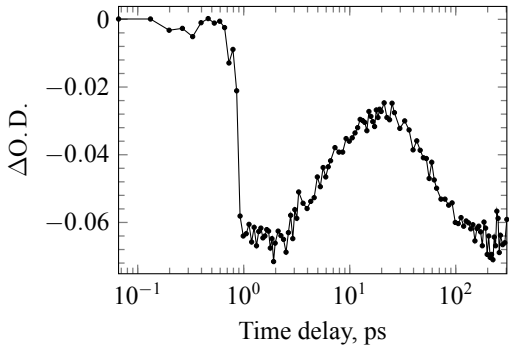

Figure 3.13. GSB signal of **OPV-Q9-PB** at 430 nm (see Figure 3.12).

The TRABS map of **Q8-PB** shows a band in near-UV region, at 400 nm (Figure 3.10), representing absorption of a quinoline-cation radical, formed after electron transfer from a quinoline

[1]Cation-radical $OPV^{\bullet+}$ absorption bands overlaps with anion-radical $PB^{\bullet-}$ absorption band, as observed in [147].

HOMO state to single-occupied ground state of PB. According to [148] the cation radical absorption spectra in CH_3CN has an intense band at 320 nm, and a weaker band at 410 nm, which we observe in TRABS data. The same absorption band of $Q^{\cdot+}$ can be observed for **OPV-Q14-PB** and **OPV-Q19-PB** (Figure 3.11) in $CHCl_3$, which demonstrate slower rates of OPV GSB appearance (OPV oxidation) with 170 ps and 520 ps lifetimes, respectively. At near UV region at ∼400 nm the quinoline cation absorption band is clearly seen, which rapidly disappears. In the case of **OPV-Q14-PB** this band can be barely seen. The absorption band of $Q^{\cdot+}$ in the case if **OPV-Q9-PB** in $CHCl_3$ cannot be observed, because fluorescence quenching rate and rate of OPV GSB are assumed to be similar.

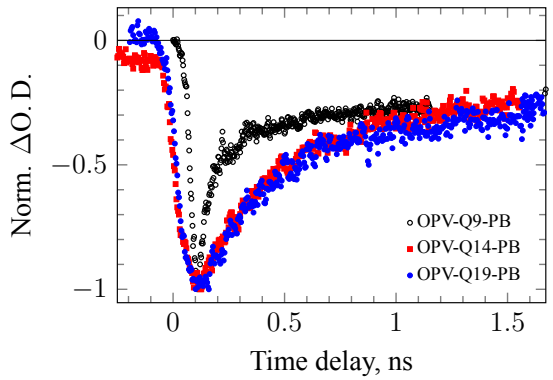

Figure 3.14. Signals of GSB for all studied samples in toluene (λ_{exc}=532 nm, λ_{ob}=490 nm).

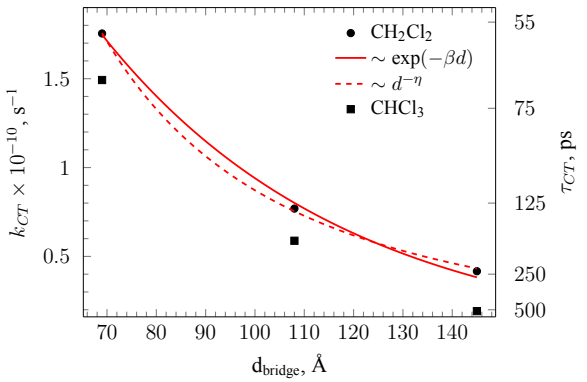

Figure 3.15. Dependence of OPV oxidation rate on distance, determined from TRABS data (CH_2Cl_2, $CHCl_3$; RT).

The rates of electron transfer, determined by means of TRABS are presented in Table 3.2, p. 70, for all studied samples in different solvents.

Referring to the data of fluorescence decays in toluene for all samples, it could be seen (Table 3.2) that fluorescence decays are biexponential. In Figure 3.14 the signals of PB ground state bleaching, recorded at 490 nm after 532 nm excitation are represented. 70 % of GSB signals intensities are recovered during few hundreds of ps for all studied samples with rates similar to calculated from time-resolved fluorescence decays (see Figure 3.9), what is not observed for samples in $CHCl_3$ and CH_2Cl_2 (Table 3.2). It could be explained that in toluene two different conformations of foldamers bridges are presented with a ratio of 30:70 approximately. In the case of the conformer with a smaller relative fraction (30 %) the electron transfer from a quinoline unit to PB could occur, but it seems that it could not in the conformation with higher fraction (70 %). In other words after excitation of PB, only 30 % of all excited PB molecules will form anion-radical $PB^{\bullet-}$, other 70 % will relax to the ground state.

The set of TRABS data confirm our assumptions about the mechanism of electron transport between electron donor (OPV) and acceptor (OPV) through the foldamer bridge. After electron acceptor excitation (PB) the first step is the oxidation of the bridge unit (or hole injection into bridge); after that the hole is transferred to the electron donor site (OPV) by random hopping between energetically degenerate[1] modular quinoline units, where it is irreversibly trapped by the electron donor. This mechanism is at least true for long foldamers samples **OPV-Q14-PB** and **OPV-Q19-PB**, which are not expected to have electronic coupling through the bridging foldamer between donor and acceptor, as it was observed for shorter foldamers bridges in [40]. Therefore, one cannot deny the possibility of superexchange mechanism for shorter foldamers samples. Additionally, there could be a superexchange between bridge and OPV site. According to a superexchange model for electron transfer through modular bridges the exponential

[1] It could also be expected that quinoline units are not energetically degenerate, and there is a slope in energy from the OPV site to the PB site, explained by possible conjugation between single quinoline units, which is confirmed by preliminary quantum mechanics calculations (MOPAC, PM7).

fall off of electron transfer rate constant with donor–acceptor distance should be observed: $k_{CT}=C\exp(-\beta d)$.[38, 45] Remarkable low attenuation factor β was obtained using the distance through bridge ($\beta_{CS}=0.02$ Å^{-1}, Figure 3.15).

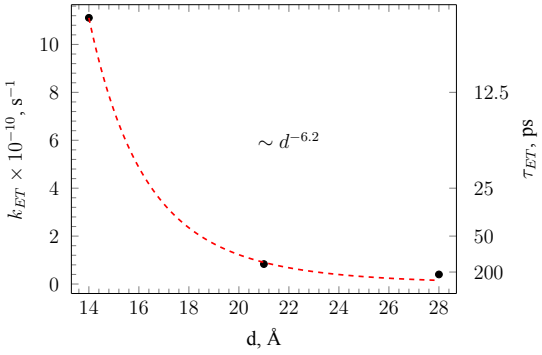

Figure 3.16. Energy transfer rate dependence on distance between OPV and PB through space ($\lambda_{exc}=400$ nm, $CHCl_3$; RT).

Depending on the length of the foldamer bridge, the rate of OPV GSB appearance (OPV oxidation) decreases (Figure 3.15). In injection–hopping–trapping mechanism of electron transfer, a weak distance dependence of electron transfer rate is expected, of type, $k_{CT}\sim n^{-\eta}$, where $\eta\approx1-2$.[45] The η was determined to be 1.9 (Figure 3.15), according to experimental data. As n it the *no.* of hopping steps over similar repeating units (quinolines), this value is related to distance d between donor and acceptor. As it could be seen from the Figure 3.15 the fit to experimental data with hyperbola is better, compared to an exponential fit, which could mean that we are observing hopping of the hole through the bridge. In order to understand whether there is hole delocalization in the quinoline bridge or hole transport through the bridge is governed by hopping mechanism, longer foldamers should be studied.

Energy transfer between OPV and PB

As we mentioned before (Figure 3.5) OPV site could play a role of light-harvesting antenna. This can be exemplified considering the **OPV-Q9-PB** sample. By exciting the **OPV-Q9-PB** sample with $\lambda_{exc}=400$ nm, namely donor (OPV) site of the system. Firstly, energy transfer with the rate 10^{11} s^{-1} occurs between donor and acceptor parts of the system; secondly, after excitation of the acceptor PB the electron transfer, as described above occurs. This process was tracked by femtosecond time-resolved absorption spectroscopy (Figure 3.12). As it can be seen from Figure 3.13, showing OPV site GSB signal evolution at 430 nm, after the excitation pulse arrives the drop in ground state absorption of OPV is observed; after the recovery of GSB is observed, explained by an EET process, occurring between OPV and PB; the recovery of OPV GSB is replaced by a decrease, which is explained by an electron transfer process. The energy transfer rates were determined for all studied samples in $CHCl_3$. As shown in Figure 3.16, energy transfer rate dependence on the distance between OPV energy donor and PB energy acceptor is subject to Förster law $k_{ET}\sim\frac{1}{d_{DA}^6}$, what proves that foldamers are rigid structures.

Electron recombination rates

The charge separated state OPV$^+$-Q$_n$-PB$^-$ formation rates for all studied samples lie in the range of $\sim10^{10}$ s^{-1}. The charge recombination (reduction of OPV$^{\bullet+}$ and oxidation of PB$^{\bullet-}$) happens much more slower. The TRABS map in Figure 3.17 for **OPV-Q9-PB** in $CHCl_3$ is represented, which shows that the anion-radical of PB (absorption band at ~720 nm) and cation-radical OPV (absorption band at ~625 nm) are relaxing with the same lifetime of 180 ns (Figure 3.19). In more polar CH_2Cl_2 solvent, this relaxation lifetime equals 450 ns and in less polar toluene is 13 ns, thus the stabilization energy of CSS is smaller in toluene compared to more polar solvents. Anion-radical PB$^{\bullet-}$ relaxation is accompanied by triplet state formation of PB, which is characterized by intense absorption, centred at ~500 nm, slightly shifted from 510 nm, observed in [53].

The triplet state of PB relaxation occurs in much longer timescale – hundreds μs (Figure 3.18) with lifetime of $\tau>340$ μs for **OPV-Q9-PB** and $\tau>420$ μs for **OPV-Q19-PB** (Figure 3.20,

Table 3.2). According to TRABS data, $PB^{\bullet-}$ in the case of **OPV-Q14-PB** and **OPV-Q19-PB** relaxes more slowly, compared to **OPV-Q9-PB**. As it can be seen from the Figure 3.20 the absorption band of $OPV^{\bullet+}$ and $PB^{\bullet-}$, at $\sim$625 nm and $\sim$720 nm, respectively, are observed even after >80 μs after excitation pulse, thus in **OPV-Q9-PB** case (Figure 3.18) only PB triplet state could be detected in this time range. This demonstrates an outstanding long OPV^{+}-Q_n-PB^{-} time of charge separation in the case of **OPV-Q14-PB** and **OPV-Q19-PB** in $CHCl_3$.

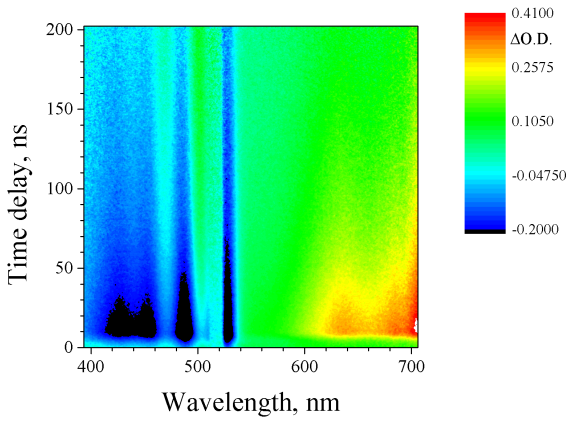

Figure 3.17. TRABS map of **OPV-Q9-PB** in $CHCl_3$ (λ_{exc}=532 nm, timescale 200 ns).

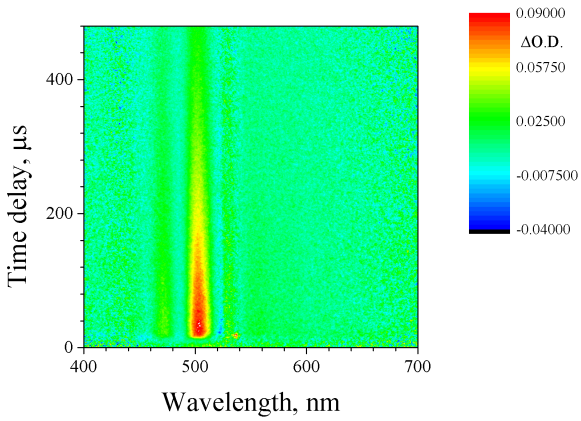

Figure 3.18. TRABS map of **OPV-Q9-PB** in $CHCl_3$ (λ_{exc}=532 nm, timescale 500 μs).

Recombination from a singlet charge-separated state to a local triplet excited state can only occur if one of the electrons inverts its spin. Two mechanisms are known to describe the formation of triplet states from singlet charge separated states; radical pair and spin-orbit intersystem crossing.[40, 149] In radical pair intersystem crossing the spins in the singlet charge-separated state dephase and evolve into the triplet charge-separated state, followed by a charge recombination to a local triplet excited state (in this case that of the PB). In spin-orbit intersystem crossing, charge recombination from the singlet charge-separated state to the local triplet excited state occurs in one step involving a change in orbital magnetic momentum that is needed for the spin flip. However, at this point we are unable to distinguish between the radical pair and spin-orbit intersystem crossing mechanism.

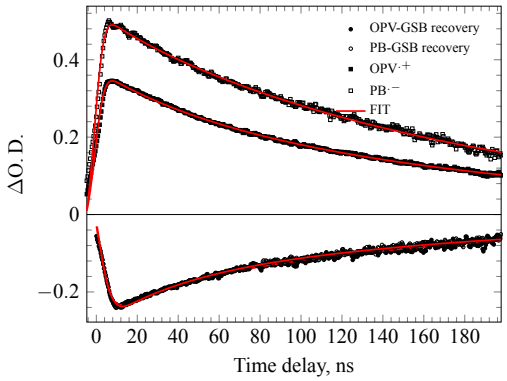

Figure 3.19. TRABS signals of **OPV-Q9-PB** in $CHCl_3$ (λ_{exc}=532 nm, timescale 200 ns).

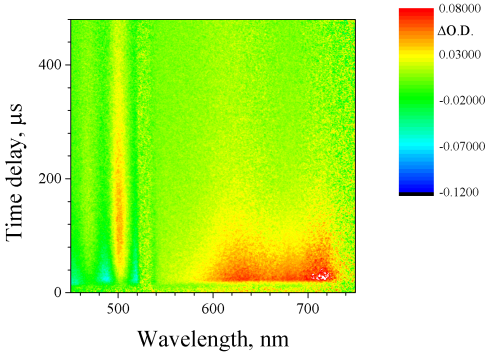

Figure 3.20. TRABS signals for **OPV-Q19-PB** in $CHCl_3$ (λ_{exc}=532 nm, timescale 500 μs).

3.2.3.3 Temperature dependence of charge separation rate

In order to study the electron transfer process in more depth, TRABS and time-resolved fluorescence measurements were performed on varying temperature from 300 to 180 K. The

Table 3.2. Fluorescence decays, electron and energy transfer rates of **Q8-PB**, **OPV-Q9-PB**, **OPV-Q14-PB**, **OPV-Q19-PB** in toluene, $CHCl_3$, CH_2Cl_2.

Sample	Solvent (ε)	τ_{fluo}, ps	$\tau_{\text{OPV oxid}}$, ps	τ_{CR}, μs	$\tau_{Triplet}$, μs	τ_{ET}, ps
Q8-PB	$CHCl_3$ (4.8)	65	–	0.0012	~75	–
	CH_2Cl_2 (8.9)	68	–	0.001	~75	–
OPV-Q9-PB	toluene (2.3)	162(26 %), 137(74 %)	140	0.013	–	–
	$CHCl_3$ (4.8)	46	67	0.18	350	10
	CH_2Cl_2 (8.9)	60	57	0.450	–	–
OPV-Q14-PB	toluene (2.3)	170(31 %), 370(69 %)	350	>50	>80	–
	$CHCl_3$ (4.8)	55	170	>80	>360	120
	CH_2Cl_2 (8.9)	51	130	>80	–	–
OPV-Q19-PB	toluene (2.3)	130(34 %), 600(66 %)	780	>50	>80	–
	$CHCl_3$ (4.8)	56	520	>80	>420	250
	CH_2Cl_2 (8.9)	61	240	>80	–	–

fluorescence quenching rate and appearance of GSB of electron donor (OPV) rate in CH_2Cl_2 temperature dependencies were considered. To analyse the temperature dependencies of the electron transfer rates, the semiclassical Marcus equation in the nonadiabatic limit was used:

$$k_{CT} = \frac{2\pi}{h} V_{eff}^2 \sqrt{\frac{1}{4\pi\lambda k_B T}} \exp\left(\frac{-\Delta G^{\#}}{k_B T}\right), \tag{3.1}$$

where V_{eff} – is electronic coupling matrix element; $\Delta G^{\#} = (\lambda + \Delta G_{RP})^2/4\lambda$, ΔG_{RP} – is the free energy change of radical ion pair formation, and λ is the reorganization energy. Because these experiments are performed in $CHCl_3$, a low polarity solvent, and the chromophores are large, λ was assumed to be dominated by inner-sphere reorganization.[38] Use of equation 3.1 in the adiabatic limit (no T dependence in the prefactor) yields a worse fit. Employing a functional form of equation 3.1, $k_{CT} = AT^{-1/2} \cdot \exp(-E_A/k_B T)$, we plot $1/T$ versus $k_{CT}T^{1/2}$ on a logarithmic plot for **OPV-Q9-PB**, **OPV-Q14-PB** and **OPV-Q19-PB** (Figures 3.21, 3.22). The parameters E_A and A can be easily extracted from the slope and intercept, respectively, which are summarized in Table 3.3.

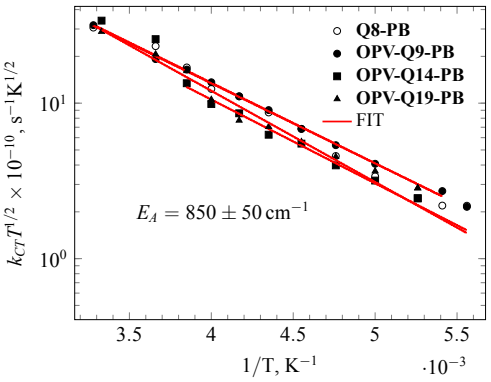

Figure 3.21. Temperature dependence of PB fluorescence quenching rates for **OPV-Q9-PB**, **OPV-Q14-PB**, **OPV-Q19-PB** in CH_2Cl_2.

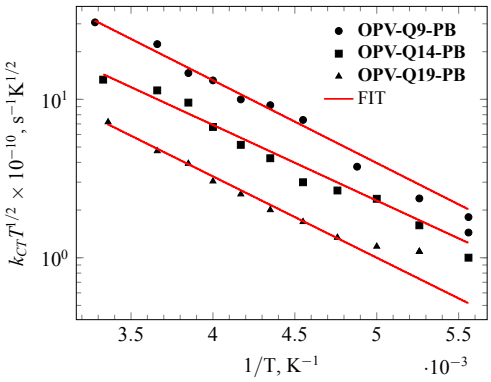

Figure 3.22. Temperature dependence of GSB of OPV appearance rates for **OPV-Q9-PB**, **OPV-Q14-PB**, **OPV-Q19-PB** in CH_2Cl_2.

The temperature dependence of fluorescence quenching and OPV GSB appearance rates

Table 3.3. Parameters of equation 3.1 extracted from a fit of the data in Figures 3.21, 3.22.

Sample	Parameters from fluorescence quenching		Parameters from OPV oxidation	
	E_A, cm^{-1}	$A \times 10^{12}$, s^{-1}	E_A, cm^{-1}	$A \times 10^{12}$, s^{-1}
OPV-Q9-PB	860 ± 50	1.5 ± 0.4	830 ± 50	1.6 ± 0.3
OPV-Q14-PB	930 ± 50	2.5 ± 0.7	780 ± 50	0.6 ± 0.2
OPV-Q19-PB	860 ± 50	1.5 ± 0.1	810 ± 50	0.4 ± 0.1

show very similar trends for all studied samples. All temperature dependencies (Figures 3.21, 3.22) could be described by one energy of activation, E_A. The determined energies of activation (E_A) for different processes (fluorescence quenching and OPV oxidation) are similar within the error of measurements ($50\,cm^{-1}$), which appears to represent the same process, which affects the electron transfer rates for different samples.

The values of fluorescence quenching rates for all studied samples are similar in the whole temperature range, which is in good agreement with fact, that fluorescence is quenched by electron transfer from a quinoline unit to single-occupied ground state of excited acceptor site (PB).

As it can be seen from Figure 3.22, the represented temperature dependencies of OPV oxidation rate are displaced in parallel from lower values to higher ones when the sample bridge length decreases. This can be easily understood from the perspective of hole transfer through the quinoline-based bridge towards the OPV site (directly or reversible hopping between energetically degenerate quinoline units), before being trapped by the OPV site. The longer the bridge – the longer the time it takes for the hole to reach the OPV site, the smaller rate of OPV GSB appearance (OPV oxidation).

3.2.4 Conclusions

Time-resolved characterization of charge separation between electron donor (OPV) and acceptor (PB) in the sub-nanosecond timescale through an oligoquinoline bridge in foldamers of increasing oligomeric length (9, 14, 19 units) was carried out in solvents with different polarity: toluene, $CHCl_3$, CH_2Cl_2. The general mechanism of electron transfer in such systems was proposed, consisting of 4 separate steps: acceptor excitation, hole injection from a quinoline unit HOMO state to single-occupied ground state of electron acceptor; after that hole is transferred to electron donor site by random, reversible hopping between energetically degenerate modular quinoline units, where it is irreversibly trapped by the electron donor. An outstanding long lifetime of OPV^+-Q_n-PB^- state $\tau_{CSS} > 80\,\mu s$ in CH_2Cl_2 was observed. It was also demonstrated that in the studied OPV-Q_n-PB systems, the electron donor OPV site could play the role of light-harvesting antenna. Excited OPV could transfer excitation energy to PB site through dipole-dipole interaction, which is reflected in $1/d_{DA}^6$ energy transfer rate dependence on distance between OPV and PB.

3.3 Lanthanide-based luminescent probes for time-gated *in situ* detection of Cu(I) ion

3.3.1 Introduction

Life on Earth has evolved harnessing a complex mixture of organic and inorganic compounds. Organic molecules such as amino acids, carbohydrates and nucleotides form the backbone of proteins and genetic material and are fundamental components of macromolecules are enzymatically synthesized and ultimately degraded in the environment. Inorganic elements, such as ions of copper, iron, zinc and other, once extracted from the Earth's crust, are neither created nor destroyed and therefore their homeostatic regulation is under strict control.[150]

Metal ions play an essential role in normal human physiology since at least one third of all proteins are thought to require a metal ion co-factor for their functioning. Copper is a vital trace nutrient that is required for a broad range of biological processes, including mitochondrial respiration, bone metabolism, wound healing, connective tissue formation, and the mobilization and uptake of iron.[54] Due to the redox properties of copper(I/II), almost half of the known copper proteins are oxidoreductases, or in other words electron transfer proteins. The other half are proteins involved in the homoeostasis and storage of copper ions to avoid appearance of free copper in the cell, which catalyses the Fenton reaction and produces reactive oxygen species.

Indeed all the metal ions required for cell functioning are essential but could be very toxic at elevated concentration. Misregulation of zinc and copper concentrations in the cell are observed in many pathologies, such as neurodegenerative disorders: Alzheimer, Parkinson. For a better understanding of the role of metals ions in diseased and healthy cells, tools are required to image these metal ions *in vitro* and *in vivo*. Compared to zinc and iron, the average concentration of cellular copper is approximately one order of magnitude lower. For example, a single mouse fibroblast cell contains only between 3 and 5 femtogram of total amount of copper. This quantity falls below the detection limit of standard elemental speciation techniques, such as inductively coupled plasma mass -spectrometry or atomic emission spectroscopy. In contrast, synthetic fluorescent probes offer sufficient sensitivity and thus have found widespread applications for the *in situ* detection of a broad range of metal ions in the cells. Compared to non-redox active metal ions such as Mg^{2+}, Ca^{2+}, or Zn^{2+}, the design of fluorescent probes for the detection of Cu^{+} ions is challenging due to interfering quenching pathways.[56]

The ideal *in situ* fluorescence probe must fulfill several criteria:

- *selectivity* towards a specific metal;
- *specificity* (no interference with other metals or the media);
- *high binding constant* for a targeted metal;
- be able to penetrate a cell membrane;
- *biocompatibility*;
- show *proportional and pronounced turn* ON response to metal concentration;
- *ratiometric and/or fluorescence lifetime* detection;
- *visible/NIR* excitation and NIR emission.

There are only a few Cu^{+} specific probes in the literature, which suffer from several drawbacks, due to their organic nature. The main drawbacks are poor water solubility, excitation and emission spectra are in the UV-visible range, where the absorption and autofluorescence of biological media are strong and should be considered.[55]

To design a luminescent Cu^{+} probe, which binds copper selectively and avoids problems of solubility, the group of Sénèque[1] was inspired by copper protein CusF, involved in copper and silver resistance in *Escherichia coli* (Figure 3.23).[56] The CusF protein binds Cu^{+} ion

[1]Laboratoire de Chimie et Biologie des Métaux, equipe Physicochimie des Métaux en Biologie, Institut de Recherches en Technologies et Sciences pour le Vivant (iRTSV), Grenoble, France

in a loop with two methionines, one histidine and one tryptophan (Figure 3.23) by a cation-π interactions.[57] These interactions modify the electronic properties of the tryptophan, so its absorption is red-shifted and fluorescence is quenched due to Intersystem Crossing (ISC) from the singlet state to the triplet state of tryptophan.

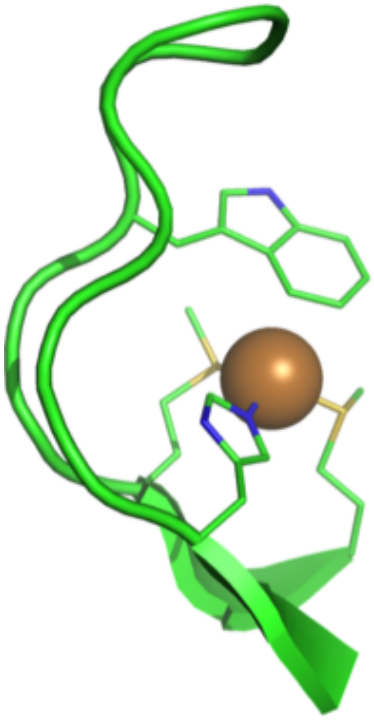

Figure 3.23. Cu^{+} binding site of the protein CusF.

The peptide probe, called **CC9Tb** (Figure 3.24) was synthesized. The protein sequence was homologous to the CusF [56] protein (Figure 3.23), amino-acids which bind Cu^{+} (M47, M49, and H36) were conserved, only the tryptophan (W44) was sometimes replaced by a methionine. A D-proline and a methylalanine (Aib) were added to make a cyclic peptide and induce the formation of β-hairpin to make probe more rigid.

In order to realize a luminescent turn *OFF-ON* Cu^{+} ion probe, the emissive Tb^{3+} ion was incorporated in the peptide near the tryptophan light antenna. It is known that energy from the triplet state of tryptophan ($E_{T_1} = 24600\,\mathrm{cm}^{-1}$ [58]) could be transferred to $^5D_4$ state of the Tb^{3+} ($E = 20500\,\mathrm{cm}^{-1}$; Figure 3.29), which relaxes to the ground state by emitting light (Figure 3.25). Without Cu^{+} ion the main mechanism of excited state relaxation of the probe is fluorescence of tryptophan. On interaction with the Cu^{+} ion, the fluorescence of tryptophan is quenched, as the tryptophan triplet state is populated by ISC from singlet state of tryptophan (ISC efficiency is enhanced due to cation-π interactions[59]), resulting in more efficient energy transfer to the Tb^{3+} ion, and thus more luminescence of Tb^{3+} is observed – fluorescence is turned *ON* (Figure 3.26).

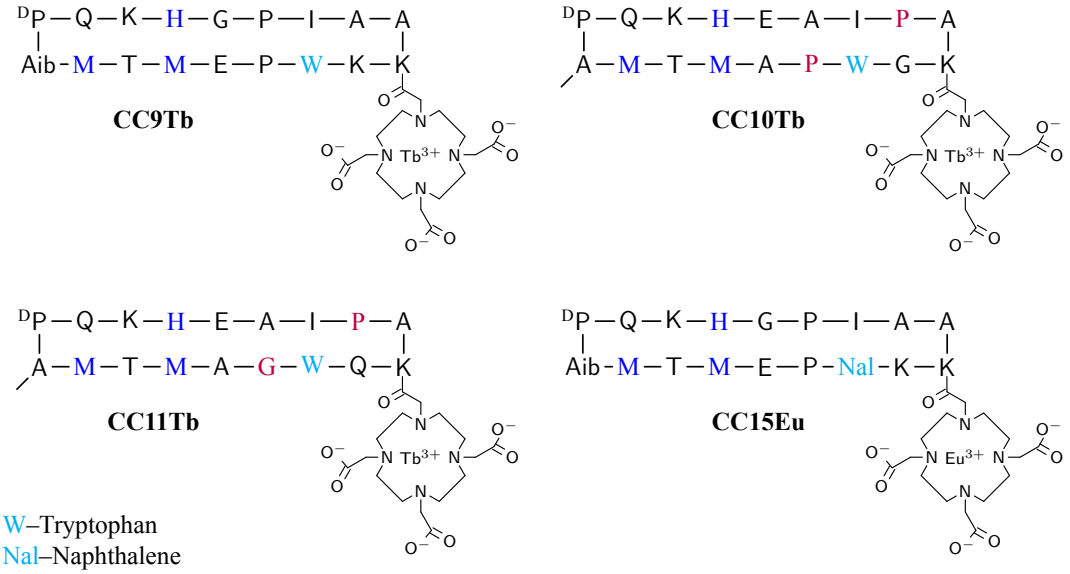

Figure 3.24. Sequence of the peptides: **CC9Tb**, **CC10Tb**, **CC11Tb** and **CC15Eu**, based on CusF protein.

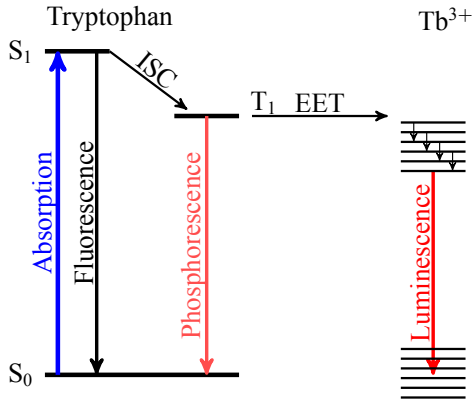

Figure 3.25. Simplified Perrin-Jablonski diagram of **CC9Tb** probe.

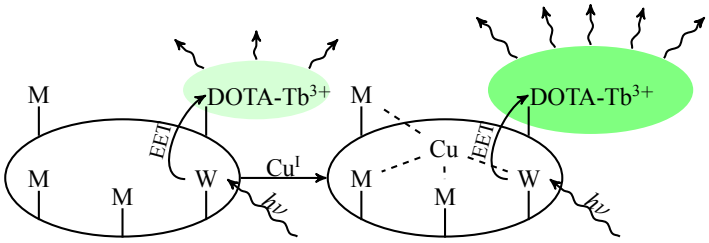

Figure 3.26. Scheme of the Cu(I) probe working principle.

Two other peptides **CC10Tb** and **CC11Tb** (Figure 3.24) were synthesized to study the influence of the prolines on the folding. For more details of metal sites modelling of peptide probes refer to works of our collaborators [151–153].

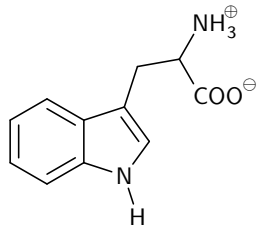

Figure 3.27. Structural formula of tryptophan.

Tryptophan[1] (see Figure 3.27) is the main fluorophore within proteins and can acts as an efficient photosensitizer, so all Cu^+ ion probes **CC9Tb**, **CC10Tb** and **CC11Tb** performed efficiently (see subsection 3.3.3). Analysis of photophysical processes occurring in tryptophan is hampered due to the fact, that fluorescence decay of tryptophan instead of being mono-exponential is governed by a bi exponential law. During 40 years much research was performed to explain and understand the behaviour of fluorescence emission of tryptophan in different conditions. It was shown, that QY of emission and lifetime of emission are dependent on solvent polarity, its rigidity, pH and etc.[154–158] The typical luminescence lifetimes for tryptophan are $0.4-0.5$ ns and $2-4$ ns in water and methanol solutions [158]. The QY of L-tryptophan in water solutions equals to 0.12 [154], 0.14 [156] at pH$=7$.

Figure 3.28 shows typical absorption spectra of L-tryptophan and its fluorescence emission spectrum at RT in water with PBS buffer at pH$=7$. The tryptophan absorption spectra has two main bands of absorption centred at 280 nm and 288.5 nm [159], which is explained by formation of two different dipole moments at singlet excited state of tryptophan. The fluorescence emission of tryptophan is centred at 340 nm. The replacement of tryptophan by naphthalene, which has a monoexponential fluorescence decay would afford a simplified model to understand photophysical process governing fluorescence turn *ON* of Cu^+ probes. For that reason the **CC15Eu** probe (Figure 3.24) was synthesized. The Eu^{3+} ion was used as luminophore instead of Tb^{3+} ion (Figure 3.29), be-

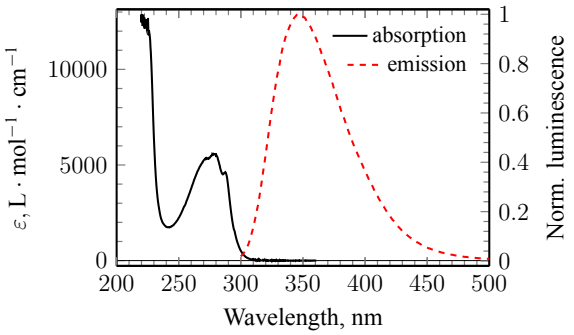

Figure 3.28. L-tryptophan UV-vis electronic absorption and emission spectra in water ($\lambda_{exc}=$ 280 nm, PBS buffer at pH$=7$).

[1]Tryptophan is an α-aromatic amino acid, one of the 22 naturally occurring amino acids and is an essential amino acid in the human diet. It exists in two optical isomeric forms – L, D and in the form of the racemate (DL). In our work we used L-tryptophan, for the sake of brevity, we use the designation *tryptophan* throughout instead of L-tryptophan.

cause it is better energetically matched to the naphthalene triplet state ($E_T = 22000\,\mathrm{cm}^{-1}$ [28]).

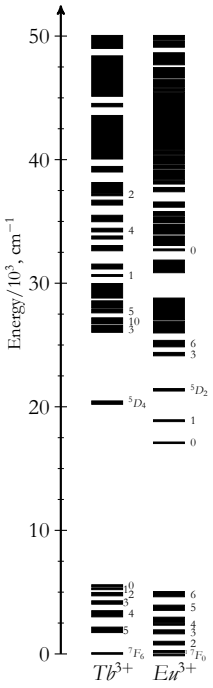

Figure 3.29. Energy level diagram for La^{3+} ions doped in a low-symmetry crystal, LaF_3 [160].

Choice of the lanthanide ions: Tb^{3+} and Eu^{3+} as luminophores in the studied probes **CC9Tb**, **CC10Tb**, **CC11Tb**, **CC15Eu** is very useful in *in vivo* studies, because these lanthanide ions emit in the red and NIR optical regions, so emission could easily pass through the different cell organelles and its membrane. Also the millisecond emission of lanthanide ions can overcome problems of background fluorescence, by applying a time-gated mode of signal acquisition. The organic compound fluorescence is simply being cut by applying the electronic time gate and lanthanide ions emission (phosphorescence) is thus recorded without any contamination. Lanthanide ions are widely used in *in vitro* and *in vivo* imaging [161, 162] often due to the possibility of using an energy transfer mechanism for turning *ON* lanthanide ion emission [163].

We would like to point out, that despite the fact that probes were designed for Cu^+ recognition and they show high metal-ion selectivity (see below), they also show the same response to Ag^+ ions, which can be ignored *in vivo* studies, because Ag^+ ion is not an essential trace element for cellular processes. For photophysical studies it was very convenient to have two different stimulae (two ions Cu^+ and Ag^+) to get the same system response (emission turn *ON*), which allowed us to propose the mechanism of emission turn *ON* for these peptidic Cu^+ probes. On the other hand, the probe **CC15Eu** showed an extremely interesting result. The probe responded to Ag^+ ion presence, but not to Cu^+ ion, which to the best of our knowledge is the first probe, which is sensitive to Ag^+, but not to Cu^+.

3.3.2 Experimental

During the study: QYs of phosphorescence and fluorescence, time-resolved evolution of emissions: phosphorescence of tryptophan, naphthalene and lanthanide metal ions (Tb^{3+} and Eu^{3+}), fluorescence of tryptophan and naphthalene were measured for these Cu^+ probe samples:

- **CC9Tb**:
  - **CC9Tb**
  - **CC9Tb-Ag**
  - **CC9Tb-Cu**
  - **CC9La**
  - **CC9La-Ag**
  - **CC9La-Cu**
- **CC10Tb**:
  - **CC10Tb**
  - **CC10Tb-Ag**
  - **CC10Tb-Cu**
  - **CC10La**
  - **CC10La-Ag**
  - **CC10La-Cu**
- **CC11Tb**:
  - **CC11Tb**
  - **CC11Tb-Ag**
  - **CC11Tb-Cu**
- **CC15Eu**
  - **CC15Eu-Ag**
  - **CC15Eu-Cu**

The use of La^{3+} ions instead of Tb^{3+} in several cases was dictated by the need of measuring clear tryptophan phosphorescence emission spectrum, which overlaps with the Tb^{3+} phosphorescence emission spectrum. As there is no energy transfer from the triplet state of tryptophan to La^{3+} ion[1], no metal emission would contaminate the spectrum of tryptophan phosphorescence.

All samples were prepared in water with 10 mM buffer HEPES (pH=7.5) at concentrations that gave sufficient absorption at the wavelength of excitation ($\lambda_{exc}=280$ nm, for time-resolved emission spectroscopy $\lambda_{exc}=266$ nm) of *circa.* 0.12, $\sim 20\,\mu$M (see Figure 3.31). The metal salts

[1] La^{3+} electronic configuration corresponds to the [Xe]-shell.

were stored as solutions of $AgClO_4$ and $CuSO_4$ in water. All metal salts were added into the solutions of probes in air-equilibrated conditions and after that solutions were degassed by multiple freeze-pump-thaw cycles to prevent singlet oxygen generation in the solution, by oxygen reacting with the triplet state of tryptophan after exciting the system. Because Cu^+ ion is not stable in non-degassed solutions and it can be easily oxidized, the Cu^+ was generated *in situ* from Cu^{2+} reacting with hydroxylamine [164]:

$$2NH_2OH + 4Cu^{2+} \rightarrow N_2O + H_2O + 4Cu^+ + 4H^+$$

The hydroxylamine was added to the spectroscopic cell immediately before the degassing procedure.

3.3.3 Results and discussion

3.3.3.1 Cation-π interaction

The studied copper probes bind Cu^+ ion through cation-π interactions as in CusF probe [56], which affects the indole ring of tryptophan.[59] To confirm the presence of cation-π interactions in the presence of Cu^+ and Ag^+ ions, the absorption and fluorescence spectra were recorded for studied Cu^+ probes.

Figures 3.30 and 3.31 show the characteristic electronic absorption spectra of **CC9Tb** probe in the absence and presence of Cu^+ and Ag^+ ions, respectively.

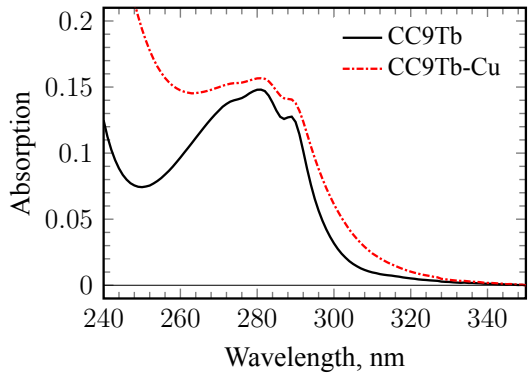

Figure 3.30. Electronic absorption spectra of **CC9Tb** and **CC9Tb-Cu**.

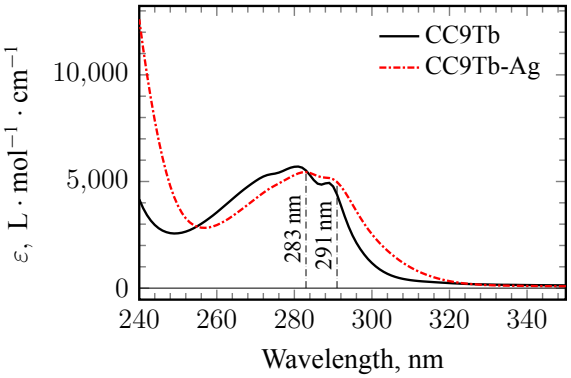

Figure 3.31. Electronic absorption spectra of **CC9Tb** and **CC9Tb-Ag**.

The absorption maximum for **CC9Tb** probe is centred at 280 nm and the probe emits at 350 nm (Figures 3.30, 3.33), corresponding to absorption and emission spectra of tryptophan (Figure 3.28). In presence of Cu^+-ions, the absorption band is red-shifted (4 nm at full-width half maximum) and the fluorescence is quenched (by 76 %, see Tables 3.4, 3.6). These facts testify that photophysical properties of tryptophan are affected by the presence of Cu^+, ascribed to the cation-π interaction. The **CC15Eu** probe (Figure 3.32) in the presence of Cu^+ ion shows similar behaviour, described for **CC9Tb**. As it can be seen from Figure 3.32 the absorption spectra of **CC15Eu** probe experiences a 3 nm red-shift at the half height of absorption band in the presence Cu^+ ion, and the naphthalene fluorescence is quenched.

The presence of Ag^+ ions causes a similar influence (Figure 3.31, see Tables 3.4, 3.6) on probes **CC9Tb**, **CC10Tb**, **CC11Tb** and **CC15Eu** compared to Cu^+ ion.

A Circular Dichroism (CD) titration of **CC9Tb** with Cu^+ performed in the Sénèque laboratory shows a decrease of the negative band at 200 nm indicating folding of the peptide (Figures 3.34, 3.35)[1]. The increased band at 225 nm could be explained due to the folding of the peptide or the cation-π interaction. In 2008, Takeuchi and coworkers [165] showed that the

[1]The presented data is obtained in the group of our collaborator Sénèque.

cation-π interactions could be observed on a CD spectra. They used a peptide of 10 amino-acids which was able to bind Cu^{2+} in a square-planar environment with a tryptophan in the axial position. They observed a band on CD spectra at 223 nm after Cu^{2+} ions were added, which they assigned to cation-π interactions between Cu^{2+} and tryptophan.

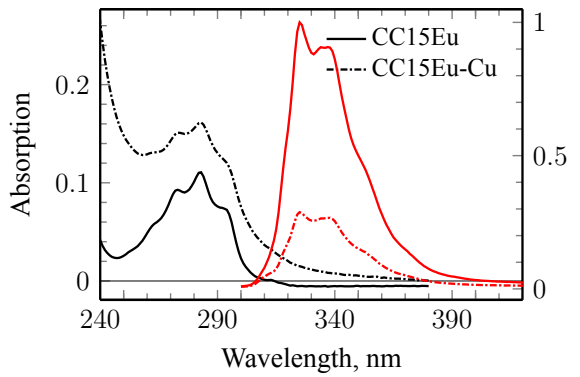

Figure 3.32. Electronic absorption and emission spectra of **CC15Eu** and **CC15Eu-Cu**.

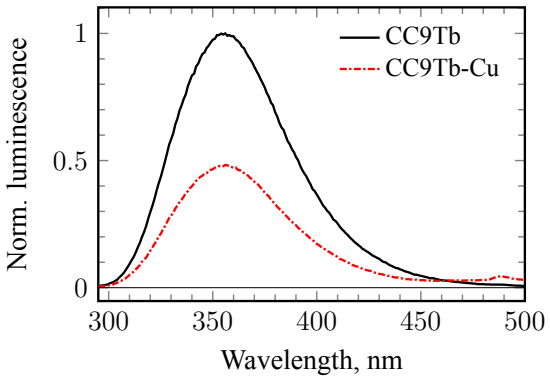

Figure 3.33. Emission spectra of **CC9Tb** and **CC9Tb-Cu** (λ_{exc}=280 nm).

As show in Table 3.4, cation-π interactions in Cu^{+} are strongest in the CusF protein case, where tryptophan fluorescence is 100 % quenched [166] and largest absorption shift of 10 nm is observed, among all studied probes. The weaker cation-π interactions for studied Cu^{+} probes could be explained by higher flexibility of the probe protein backbone, compared to CusF protein. Indeed, NMR studies confirmed that there could be at least two different conformations of the **CC9Tb** probe.

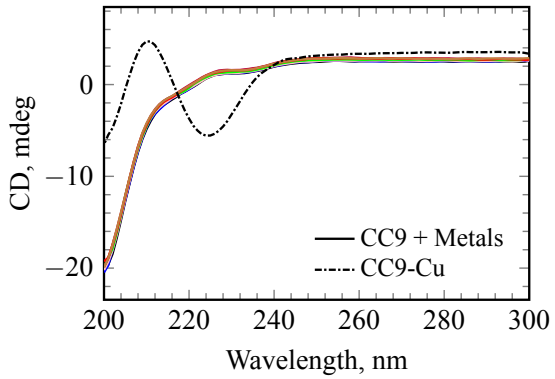

Figure 3.34. CD spectra of **CC9Tb** probe upon Cu^{+} titration.

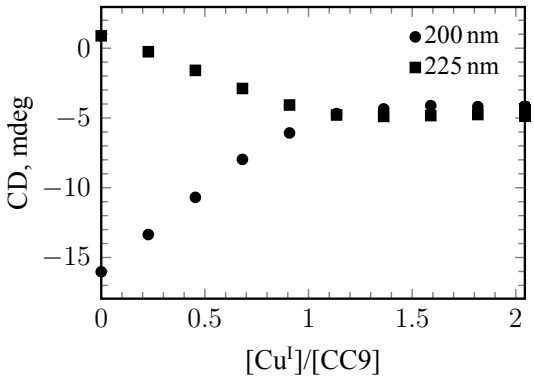

Figure 3.35. CD signal changes at 200 nm and 225 nm for **CC9Tb** upon Cu^{+} titration.

Table 3.4. Consequences of the cation-π interactions of **CC9Tb**, **CC10Tb**, **CC11Tb**, **CC15Eu** probes and CusF protein [166] with Cu^{+} and Ag^{+} ions.

	CC9Tb	**CC10Tb**	**CC11Tb**	**CC15Eu**	**CusF**
UV-vis $\Delta\lambda_{Cu}$, nm	4.5	5	4	3	10
UV-vis $\Delta\lambda_{Ag}$, nm	4	4	3	2	–
Fluorescence quenching (Cu^{+}-case)[a], %	76	73	55	86	100
Fluorescence quenching (Ag^{+}-case)[a], %	60	65	45	50	–

[a] Calculated from emission QY measurements (see Table 3.6).

The Ag^{+} ion shows less strong cation-π interactions with probes, compared to the Cu^{+} ion, which is expressed by smaller values for UV-vis absorption spectra shift at the half-height of the absorption band, as well as less pronounced tryptophan fluorescence quenching.

3.3.3.2 Emission spectroscopy

The **CC9Tb** Cu^+ probe demonstrates a pronounced turn *ON* of luminescence in the presence of Cu^+ ions. The addition of one equivalent of Cu^+ to **CC9Tb** gives an increase of *circa.* 60 times of Tb^{3+} luminescence intensity (Figure 3.36, or 4-times emission QY increase). Only one copper ion can be bound per one **CC9Tb** probe, which was confirmed by mass-spectrometry. The increase of Tb^{3+} luminescence (λ_{exc}=266 nm) is more pronounced for **CC9Tb** probe, compared to **CC10Tb** and **CC11Tb** probes (see Table 3.6). The QY of Tb^{3+} luminescence – phosphorescence for different probes with one equivalent of Cu^+ was determined at 0.043, 0.040, 0.021, respectively for **CC9Tb**, **CC10Tb** and **CC11Tb** probes. More intense cation-π interactions between Cu^+-ion and probe in case of **CC10Tb** and **CC11Tb** do not provide an increase in Tb^{3+} luminescence.

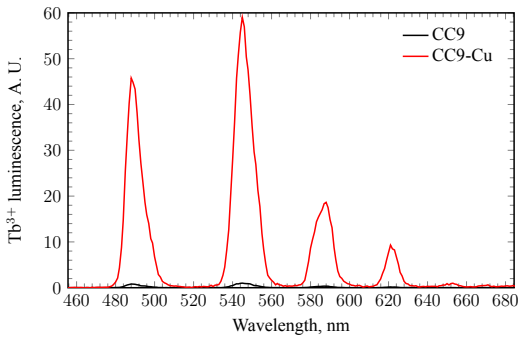

Figure 3.36. Tb^{3+} emission of the probe **CC9Tb** when Cu^+ ion is added (λ_{exc}=310 nm).

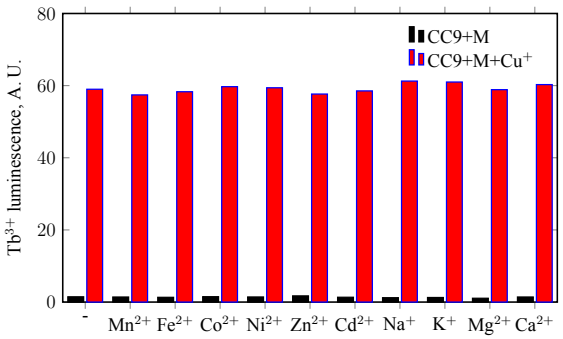

Figure 3.37. Tb^{3+} emission of the probe **CC9Tb** in presence of d-group metals (8 mM), alkali metals (10 mM) and alkaline-earth metals 100 mM (λ_{exc}= 310 nm).

Table 3.5. Number of water molecules coordinated to Tb^{3+} in **CC9Tb** and **CC9Tb-Cu** samples.

	τ_{D_2O}, ms	τ_{H_2O},[a] ms	q(Parker)
CC9Tb	3.60	1.7	1.3 ± 0.20
CC9Tb-Cu	3.45	1.7	1.2 ± 0.20

[a] See Table 3.8

The heavy atom effect of the Cu^+ ion causes an increase of the ISC from the singlet state to the triplet state of tryptophan, but it should also increase rate of tryptophan the triplet state depopulation to the ground state. Indeed, in the presence of Ag^+ ions the luminescence of Tb^{3+} is increased even further for the **CC11Tb** probe (see Table 3.6), but the cation-π interaction is less strong for tryptophan and the Ag^+ ion, compared to the Cu^+ ion. This means that ISC process is more efficient in Cu^+ case than in Ag^+ case, but these Cu^+ ion interacts more strongly with tryptophan so the energy level of its triplet state decreases more substantially than in the Ag^+ case, which causes a more rapid deexcitation of tryptophan triplet state (see Table 3.8, p. 84).

An important and unexpected result was obtained for the **CC15Eu** probe: in the presence of Ag^+ ion it showed an increase of Eu^{3+} emission (Figure 3.39, Table 3.6), but not in the Cu^+ ion case. The emission QY was 0.027 and 0.003, respectively, or 7-fold intensity enhancement (or 3-fold emission QY enhancement) for Ag^+ ion case was observed and no-enhancement was observed for the Cu^+ ion case. It is a promising result, since to the best of our knowledge there are currently no examples in the literature of luminescent molecular probes, which can distinguish between Ag^+ and Cu^+ ions.

We would like to point out, that the naphthalene fluorescence in **CC15Eu** is quenched more efficiently in the Cu^+ ion case, compared to the Ag^+ ion case, meaning that in the Cu^+ case there is more efficient ISC from the singlet state of naphthalene to its triplet state. But despite

this fact no Eu^{3+} luminescence increase is observed for **CC15Eu** probe. We will discuss this behaviour further together with time-resolved emission spectroscopy data.

The increase of the Tb^{3+} emission QY could arise from different phenomena: more Tb^{3+} excited states could be populated due to more efficient ISC in tryptophan and thus more energy could be transferred from triplet state of tryptophan to Tb^{3+} $^5D_4$ state, or the rates of non-radiative deexcitation of Tb^{3+} could be reduced due to the coordination sphere changes as a result of Cu^+ or Ag^+ complexation with the probe. In particular, water molecules are known to deactivate lanthanide ions efficiently. The number of water molecules ($q=5(k_{H_2O}-k_{D_2O}-0.06)$) coordinated to the terbium ion [168] in **CC9Tb** and **CC9Tb-Cu** does not change, in each case there was only one water molecule (Table 3.5). As the lifetime of Tb^{3+} phosphorescence almost does not change for the sample with copper **CC9Tb-Cu**, compared to free probe **CC9Tb** (Table 3.5, Table 3.8, p. 84), which means that Cu^+ ion addition to **CC9Tb** probe does not change properties of the Tb^{3+} ion. This statement is also true for other probes as well, the emission lifetimes did not change in the presence of neither Cu^+ nor Ag^+ cations. Thus the presence of Cu^+ or Ag^+ ions does not change deactivation pathways, nor the primary coordination sphere of Tb^{3+} or Eu^{3+} ions.

Table 3.6. Quantum yields of studied samples: **CC9La**, **CC9Tb**, **CC10Tb**, **CC11Tb**, **CC15Eu** (λ_{exc}=280 nm).

Sample	$QY_{degas.phos.} \pm 0.005$[a]	$QY_{degas.fluo.} \pm 0.005$[b]
CC9Tb	0.011	0.084
CC9Tb-Ag	0.042	0.035
CC9Tb-Cu	0.043	0.020
CC9La	–	0.082
CC9La-Ag	–	0.050
CC9La-Cu	–	0.035
CC10Tb	0.017	0.124
CC10Tb-Ag	0.048	0.043
CC10Tb-Cu	0.040	0.033
CC10La	–	0.078
CC10La-Ag	–	0.011
CC10La-Cu	–	0.019
CC11Tb	0.012	0.104
CC11Tb-Ag	0.033	0.066
CC11Tb-Cu	0.021	0.049
CC15Eu	0.009	0.028
CC15Eu-Ag	0.027	0.012
CC15Eu-Cu	0.003	0.004

[a] Phosphorescence QY in degassed H_2O in spectral region 500–800 nm *cf.* $[Ru(bpy)_3]^{2+}$ in H_2O (bpy = 2,2'–bipyridine) [103], λ_{exc}=280 nm.
[b] Fluorescence QY in degassed H_2O solution *cf.* L-tryptophan in air-equilibrated solution H_2O [167], λ_{exc}=280 nm.

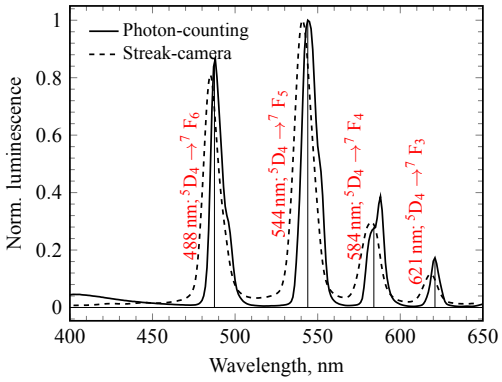

Figure 3.38. Steady-state phosphorescence spectra of **CC9Tb-Ag** (λ_{exc}=280 nm).

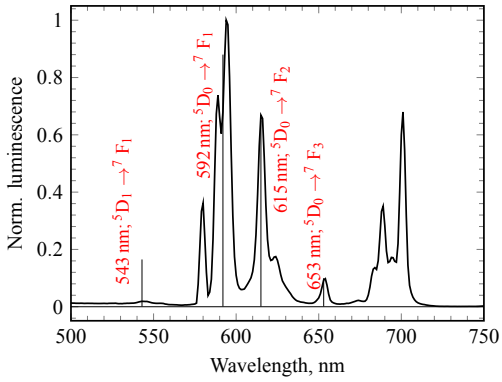

Figure 3.39. Steady-state phosphorescence spectra of **CC15Eu-Ag** (λ_{exc}=280 nm).

The studied probes demonstrate very good metal ion selectivity in water solution, as it can be seen from the Figure 3.37 where no enhancement of Tb^{3+} luminescence of **CC9Tb** probe is observed with alkali, alkaline-earth metals without presence of Cu^{+} ions, but addition of 1.5 equivalent of Cu^{+} causes 60-fold increase of luminescence emission.

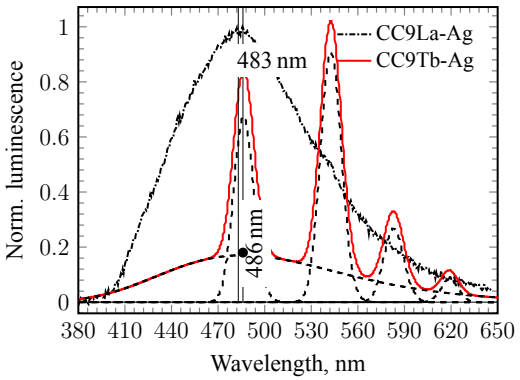

Figure 3.40. Phosphorescence spectra of **CC9La-Ag** and **CC9Tb-Ag** recorded on streak-camera ($\lambda_{exc}=266$ nm, gated-mode, time-window 200 μs, integration time 10 μs).

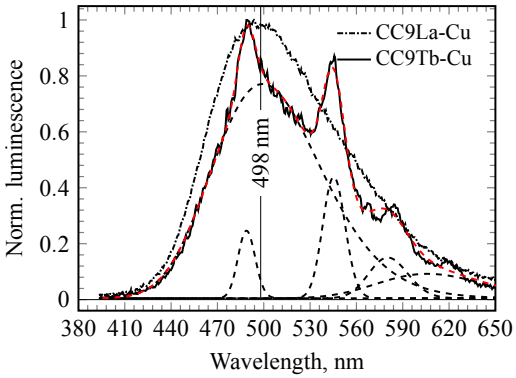

Figure 3.41. Phosphorescence spectrum of **CC9La-Cu** and **CC9Tb-Cu** recorded on streak-camera ($\lambda_{exc}=266$ nm, gated-mode, time-window 200 μs, integration time 20 μs).

The luminescence spectrum of **CC9Tb-Ag** is represented in Figure 3.38, which is characteristic for the studied family of Tb^{3+}-based Cu^{+} probes **CC9Tb**, **CC10Tb** and **CC11Tb**. It demonstrates highly structured [169] Tb^{3+} ion phosphorescence emission. As show in the figure, the spectrum obtained on streak-camera (1 ms timescale integration) demonstrates a small hypsochromic shift, which is explained by the fact, that there is no spectral sensitivity correction for the photo-cathode used in the streak-camera, while a spectral sensitivity correction function was applied to photon-counting detector during measurements. This fact should be taken in account, because all following spectra, demonstrating phosphorescence of tryptophan were measured on a streak-camera with time-gated mode.

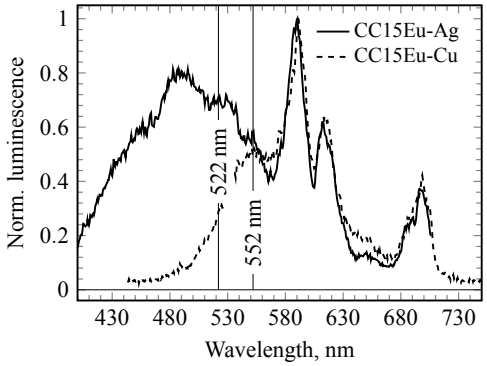

Figure 3.42. Phosphorescence spectra of **CC15Eu-Ag** and **CC15Eu-Cu** recorded on streak-camera ($\lambda_{exc}=266$ nm, gated-mode, time-window 200 μs, integration time 50 μs)

Table 3.7. The positions of phosphorescence maxima for tryptophan and naphthalene in **CC9Tb**, **CC10Tb**, **CC11Tb** and **CC15Eu** probes with Ag^{+} and Cu^{+} ions.

		CC9Tb	**CC10Tb**	**CC11Tb**	**CC15Eu**
Tb, Eu	Ag	486 nm	488 nm	488 nm	480, 522 nm
	Cu	498 nm	502 nm	504 nm	552 nm
La	Ag	–	475 nm	–	–
	Cu	495 nm	504 nm	–	–

The maxima positions are determined by fitting the spectra using Gaussian functions in energy scale.

On figure 3.39 luminescence spectrum of **CC15Eu-Ag** is represented, demonstrating highly structured Eu^{3+} ion phosphorescence emission.

On figure 3.40 luminescence spectra of **CC9La-Ag**, demonstrating tryptophan phosphorescence emission ($\lambda_{max}=483$ nm) and **CC9Tb-Ag** emission are represented. To determine maximum of tryptophan phosphorescence emission in **CC9Tb-Ag** the deconvolution technique was

used[1], thus emission of Tb^{3+} ion overlaps with tryptophan phosphorescence. The maximum was estimated at 486 nm, and the maximum of tryptophan phosphorescence emission in the Cu^{+} ion case (figure 3.41) was estimated at 498 nm, while tryptophan phosphorescence emission in the case of sample **CC9La-Cu** had a maximum position at 495 nm.

The position of phosphorescence maxima for tryptophan and naphthalene in samples **CC9Tb**, **CC10Tb**, **CC11Tb** and **CC15Eu** probes with Ag^{+} and Cu^{+} ions are presented in Table 3.7. According to [58] the maximum of tryptophan emission at 1.2 K lies at 407 nm, corresponding to a tryptophan triplet state energy of 24600 cm^{-1}. The peptide sequence and cation-π interactions causes changes in the tryptophan triplet state energy level. The maximum of tryptophan phosphorescence emission is shifted further to the red (Table 3.7). The presence of Ag^{+} ion causes less change in tryptophan triplet level energy, than the Cu^{+} ion. This is particularly clear, for the **CC15Eu** probe (Figure 3.42, Table 3.7). In this case, the energy difference of naphthalene triplet states in the Ag^{+} case and the Cu^{+} case differ by $\sim$1100 cm^{-1} (Table 3.7), calculated as difference between maximum of naphthalene phosphorescence.

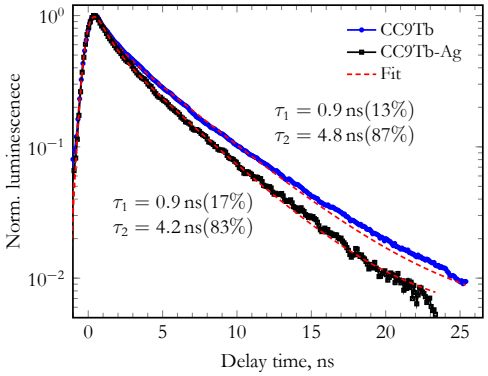

Figure 3.43. Fluorescence decays for **CC9Tb-Ag** and **CC9Tb** (λ_{exc}=266 nm, λ_{ob}=345 – 380 nm).

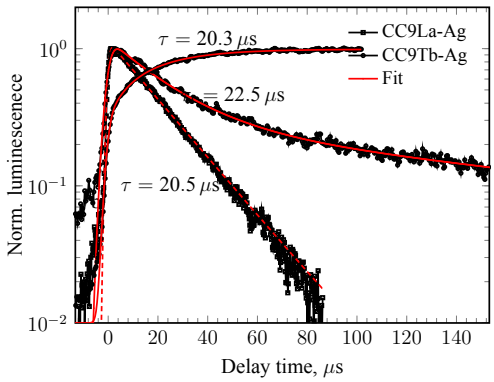

Figure 3.44. Tryptophan and Tb^{3+} phosphorescence decays for **CC9Tb-Ag** ($^5D_4 \rightarrow ^7F_5$) on 200 μs timescale (streak-camera, gated-mode, λ_{exc}=266 nm, λ_{ob}^{Trp}=435 nm, λ_{ob}^{Tb}=540 nm).

The real energy levels of tryptophan and naphthalene triplet state in the presence of Ag^{+} and Cu^{+} ions could be estimated from the blue side rising of tryptophan and naphthalene phosphorescence spectrum, but this method could give only a rough estimations. For correct determination of tryptophan and naphthalene triplet levels the low temperature emission measurements should be performed, which are associated with number of problems:

- the water solutions of probes at 77 K do not form an optically transparent glass;
- the excitation of tryptophan lies in the far UV, namely λ_{exc}=266 nm, so special quartz for sample cuvette should ideally be used to avoid intense fluorescence, originating from glass surface defects.

As mentioned above tryptophan fluorescence has a bi-exponential decay (Figure 3.43), thus determination of fluorescence quenching percentage, rate of ISC from fluorescence decay lifetimes changes is a difficult task. Values of fluorescence decay, constants as well as their weights (Table 3.8, p. 84) are changing in opposing directions: one is growing, the other is decreasing.

In the case of a naphthalene (**CC15Eu** probe), which has a mono-exponential decay the analysis of the fluorescence decay is much easier. The lifetime of naphthalene fluorescence equals to 20 ns. In the presence of Ag^{+} ions, 50 % of naphthalene singlet states relax with 10 ns lifetime, which corresponds to a 10^8 s^{-1} ISC rate. A 50 % value is in a good agreement with steady-state QY measurements (Table 3.6).

Tryptophan phosphorescence decays with a lifetime of 20.5 μs in the presence of Ag^{+} ions (Figure 3.44) for probe **CC9La-Ag**. The same rates are observed for sample **CC9Tb-Ag**,

[1]The emission signal was fitted with with 5 Gaussian-functions, while x-axis was represented in energy scale.

namely the rise of Tb^{3+} phosphorescence and tryptophan phosphorescence decay measured at the very edge, so the decay is less contaminated with Tb^{3+} emission, originated from intense $^5D_4 \rightarrow {}^7F_6$ Tb^{3+} emission. The rise of Tb^{3+} phosphorescence occurs due to energy transfer from triplet state of tryptophan to the $^5D_4$ state.

In the case of Cu^+ ion, the lifetimes of phosphorescence decays for probes are shorter $\tau = 17 \pm 2\,\mu$s (Figure 3.45), which can be explained by that fact, that Cu^+ ion participates in stronger interactions with tryptophan causing increases of deexcitation pathways of the tryptophan triplet state. The phosphorescence of Tb^{3+} and tryptophan in the case of the Cu^+ ion (Figure 3.41) overlaps, so to obtain the rise of Tb^{3+} emission the data should be extracted from the mixed emission spectra. The lifetime of Tb^{3+} emission is much longer than the lifetime of tryptophan phosphorescence emission, so by tracking the 490 nm emission band of Tb^{3+}, taking into account the amount of tryptophan phosphorescence emission at its maximum, 498 nm, the relative quantity of Tb^{3+} emission could be estimated. Consequently it, the absolute value could be calculated. In this way the rising Tb^{3+} emission was constructed (Figure 3.45).

Tb^{3+} emission decay lifetimes are not affected by the presence of Ag^+, Cu^+ ions or by peptide probe composition, which is also true for the Eu^{3+} containing probe **CC15Eu** (see Table 3.8, p. 84).

All time-resolved data analysis: the lifetimes of fluorescence and phosphorescence decays, growth of Tb^{3+} and Eu^{3+} emissions are listed in the Table 3.8).

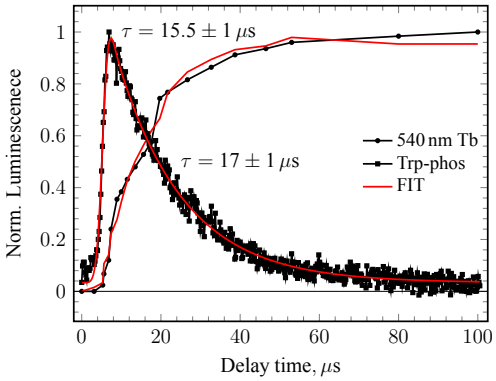

Figure 3.45. Emission for **CC9Tb-Cu** on μs timescale (streak-camera, $\lambda_{exc} = 266$ nm, $\lambda_{ob} = 540$ nm).

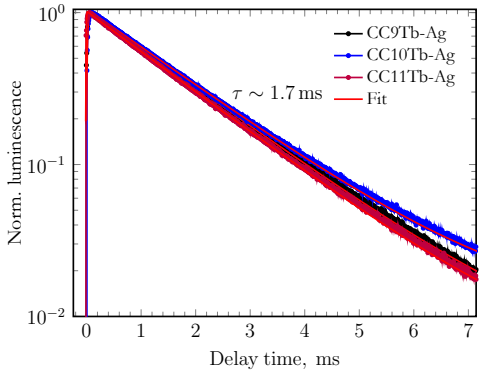

Figure 3.46. Tb emission for **CC9Tb-Ag**, **CC10Tb-Ag**, **CC11Tb-Ag** ($^5D_4 \rightarrow {}^7F_5$, Multichannel Scaling, λ_{exc}=266 nm, λ_{ob}=540 nm).

3.3.3.3 Mechanism

To discuss the general mechanism of emission turn *ON* of studied Cu^+ probes **CC9Tb**, **CC10Tb**, **CC11Tb** and **CC15Eu** it would be useful to consider a simplified Perrin-Jablonski diagram presented on Figure 3.47, built according to experimental data.

The conducted experiments confirmed our assumptions concerning luminescence turn *ON* for studied Cu^+ probes in the presence of Cu^+ and Ag^+ ions, i. e. the presence of cations Ag^+ or Cu^+ causes an increase of tryptophan ISC process effectiveness [170]. Concomitantly the energy level of tryptophan triplet state is decreased, due to cation-π interactions. From our estimations, the triplet level of tryptophan in the case of the Ag^+ ion in Tb^{3+}-based probes is located near the original triplet state, at $\sim$24600 cm^{-1}. In the Cu^+ ion case the level decreases in energy down to $\sim$23000 cm^{-1}. In the case of **CC15Eu** probe the naphthalene triplet levels are located near $\sim$21700 cm^{-1} and $\sim$20600 cm^{-1}, for Ag^+ and Cu^+ ions cases, respectively.

The level $^5D_4$ of the Tb^{3+} ion is located at least 2600 cm^{-1} below the tryptophan triplet state. The excess energy of the tryptophan triplet could be transferred to $^5D_4$ state by means of energy transfer mechanism, but cannot return back to the tryptophan triplet state. As reported

in [171], if the triplet state of an aromatic hydrocarbon lies higher than $1800\,cm^{-1}$ the reversible electronic energy transfer is almost completely hindered between triplet state and lanthanide ion.

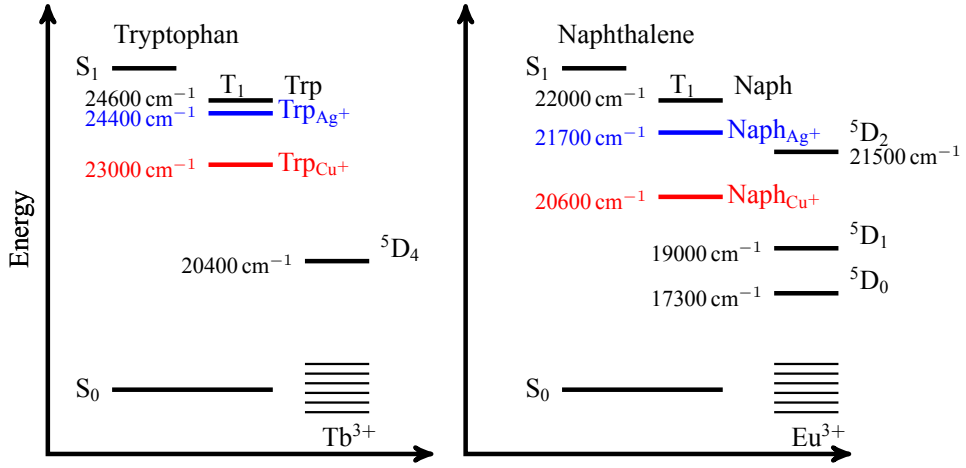

Figure 3.47. Simplified Perrin-Jablonski diagram of studied Cu^+ probes **CC9Tb**, **CC10Tb**, **CC11Tb** and **CC15Eu** in the presence of Cu^+ and Ag^+ ions.

In the case of **CC15Eu** probe with Cu^+ Figure 3.47 the position of naphthalene triplet states are close to $\sim 20600\,cm^{-1}$, which is $1600\,cm^{-1}$ (or even smaller, more accurate measurements at low temperatures should be performed) higher than $^5D_1$ state of Eu^{3+} ion. In this case reversible energy transfer is allowed, which could explain that in the presence of the Cu^+ ion no enhancement of Eu^{3+} emission of the **CC15Eu** probe is observed, while naphthalene fluorescence is quenched.

The energy in principle could be transferred from naphthalene triplet states to the $^5D_1$ state of Eu^{3+} ion, being mostly dissipated through non-radiative relaxation channels (emission QY of $^5D_1 \rightarrow {}^7F_0$ in water is low [172]). The transition $^5D_1 \rightarrow {}^5D_0$ [173] of Eu^{3+} ion, which in theory could give rise to $^5D_0$ state emission, is formally forbidden due to the triangle selection rule, but should occur due to J-mixing [174] with high efficiency 0.5 [172], but it seems that it does not happen.

In the case of Ag^+ for **CC15Eu**, the energy from the naphthalene triplet could be transferred to the $^5D_2$ state ($\tau = 4.5\,\mu s$), which relaxes down *via* multiphonon relaxation ($\tau \approx 40\,\mu s$) to an emissive $^5D_0$ state and emission of the probe is turned *ON*.

3.3.4 Conclusion

The photophysical processes of novel Tb^{3+} and Eu^{3+}-based probes for *in situ* Cu^+ ion detection mimicking the CusF peptide structure were studied. Tb^{3+}-based probes showed pronounced turn *ON* emission of the lanthanide luminophore in the presence of the Cu^+ and Ag^+ ions. The Eu^{3+}-based probe showed a response only to the Ag^+ ion, which is a promising result, thus far to our knowledge in the literature there are no *in situ* probes described that can distinguish between the Ag^+ and Cu^+ ions. Steady-state and time-resolved spectroscopies showed that in the presence of the aforementioned cations the Intersystem Crossing (ISC) from singlet state to triplet state for the light harvesting antenna of the probe (tryptophan for Tb^{3+}-based and naphthalene for Eu^{3+}-based probes) increased, due to cation-π interactions between organic aromatic hydrocarbon chromophores and the Ag^+ and Cu^+ ions. The cation-π interactions caused triplet level energy decrease for tryptophan and naphthalene to varying degrees in Cu^+ (bigger shift) and Ag^+ (smaller shift) cases. The general mechanism, based on photophysical experimental data, was proposed to explain lanthanide luminescence turn *ON* in the presence of Ag^+ and Cu^+ ions. An explanation for Eu^{3+}-based probe selectivity to Ag^+, compared to Cu^+ ions was offered.

Table 3.8. The lifetimes of luminescence kinetics of studied samples: **CC9La**, **CC9Tb**, **CC10Tb**, **CC11Tb**, **CC15Eu** (λ_{exc}=266 nm).

#	Sample	τ_1, ns	τ_2, ns	%$_1$	%$_2$	ion	scale
1	**CC9Tb**	0.9	4.8	13%	87%	–	ns
2	**CC10Tb**	1.0	5.0	10%	90%		
3	**CC11Tb**	0.9	4.3	9%	91%		
4	**CC15Eu**	20.0 ns					
5	**CC9Tb-Ag**	0.9	4.2	17%	83%	Ag^+	
6	**CC10Tb-Ag**	1.1	4.6	18%	82%		
7	**CC11Tb-Ag**	1.1	4.1	13%	87%		
8	**CC15Eu-Ag**	10	23.5	47%	53%		
9	**CC9Tb-Cu**	$\overline{0.7}$[a]	$\overline{3.9}$	$\overline{0.16}$	$\overline{0.85}$	Cu^+	
10	**CC10Tb-Cu**	$\overline{0.7}$	$\overline{4.1}$	$\overline{0.17}$	$\overline{0.83}$		
11	**CC11Tb-Cu**	$\overline{0.7}$	$\overline{3.8}$	$\overline{0.12}$	$\overline{0.88}$		
12	**CC15Eu-Cu**	$\overline{7.6}$	$\overline{21.5}$	$\overline{0.39}$	$\overline{0.61}$		
#	Sample	$\tau_{\text{rising}} \pm 2$, μs		$\tau_{\text{decay}} \pm 2$, μs		ion	scale
13	**CC9Tb**	23		–		–	μs
14	**CC10Tb**	17		–			
15	**CC11Tb**	19		–			
16	**CC15Eu**	52		–			
17	**CC9Tb-Ag**	18		19		Ag^+	
18	**CC10Tb-Ag**	22		18			
19	**CC11Tb-Ag**	23		23			
20	**CC15Eu-Ag**	42		4.5			
21	**CC9La-Ag**	–		20 ± 0.5			
22	**CC9Tb-Cu**	$\overline{16.3}$		$\overline{15.5}$		Cu^+	
23	**CC10Tb-Cu**	$\overline{14.3}$		$\overline{12.8}$			
24	**CC11Tb-Cu**	$\overline{15.0}$		$\overline{14.1}$			
25	**CC15Eu-Cu**	$\overline{22.3}$		$\overline{22.7}$			
26	**CC9La-Cu**	–		17.5 ± 0.5			
#	Sample	$\tau_{Me^{3+}}$ μs[c]				ion	scale
27	**CC9Tb**	1.6				–	ms
28	**CC10Tb**	1.7					
29	**CC11Tb**	1.6					
30	**CC15Eu**	0.6					
31	**CC9Tb-Ag**	1.7				Ag^+	
32	**CC10Tb-Ag**	1.7					
33	**CC11Tb-Ag**	1.7					
34	**CC15Eu-Ag**	0.6					
35	**CC9Tb-Cu**	1.8				Cu^+	
36	**CC10Tb-Cu**	1.7					
37	**CC11Tb-Cu**	1.6					
38	**CC15Eu-Cu**	0.6					

[a] The line over number means that value is averaged.

3.4 Chapter Summary

Several photoinduced electron and energy transfer processes were considered in the chapter. Time-resolved characterization of charge separation between electron donor (OPV) and acceptor (PB) in the sub-nanosecond timescale through an oligoquinoline bridge in foldamers of increasing oligomeric length (9, 14, 19 units) was carried out in solvents with different polarity: toluene, $CHCl_3$, CH_2Cl_2. The general mechanism of electron transfer in such systems was proposed, consisting of 4 separate steps: acceptor excitation, hole injection from quinoline unit HOMO state to single-occupied HOMO state of electron acceptor; after that hole is transferred to electron donor site by random, reversible hopping between energetically degenerate modular quinoline units, where it is irreversibly trapped by the electron donor. An outstanding long lifetime of OPV^+-Q_n-PB^- state $\tau_{CSS} > 80\,\mu$s in CH_2Cl_2 was observed. It was also demonstrated that in the studied OPV-Q_n-PB systems, the electron donor OPV site could play the role of light-harvesting antenna, transferring excitation energy to a PB site through a dipole-dipole interaction.

Novel Tb^{3+} and Eu^{3+}-based probes for *in situ* Cu^+ ion detection mimicking the CusF peptide structure were studied. Tb^{3+}-based probes showed pronounced turn *on* emission of the lanthanide luminophore in the presence of Cu^+ and Ag^+ ions. The Eu^{3+}-based probe showed a response only to the Ag^+ ion, which is a promising result, thus far to our knowledge in the literature there are no *in situ* probes described that can distinguish between the Ag^+ and Cu^+ ions. The general mechanism, based on photophysical experimental data, was proposed to explain lanthanide luminescence turn *on* in the presence of the Ag^+ and Cu^+ ions, based on cation-π interactions between organic aromatic hydrocarbon chromophores (tryptophan for Tb^{3+}-based and naphthalene for Eu^{3+}-based probes) and the Ag^+ and Cu^+ ions. An explanation for Eu^{3+}-based probe selectivity to Ag^+, compared to Cu^+ ions was offered.

Chapter 4

Multistate molecular systems

4.1 *OFF-ON* fluorescent nanoparticles for *in vivo* imaging

4.1.1 Introduction

Fluorescence imaging with molecular fluorophores, nowadays often acts as a central tool for the investigation of fundamental biological processes in cells and tissues, offering huge potential for human body imaging coupled to therapeutic procedures.[60, 61] One of the main limitations with fluorescence imaging is the complex problem of distinguishing background emission from a fluorophore emission localized at a specific point of interest. This limits fluorescence imaging to individual time points at which background fluorescence could be minimized. It would be of significant advantage if the fluorescence emission could be modulated from *OFF* state to *ON* state in response to a specific biological event as this would permit imaging of such an event in real time without background interference.[62]

The use of organic fluorophores as *in vitro* probes of dynamic biological and environmental processes is widely used in molecular and cell biology. The recent technological advances in noninvasive small animal fluorescence imaging and the future prospect of routine human fluorescence imaging have given rise to an interest in molecular fluorophores which have emission in the NIR (>700 nm) spectral region.[62, 175]

Our collaborators O'Shea and coworkers in Centre for synthesis and chemical biology, University College Dublin, Ireland reported in their work [62] an approach allowing imaging of the most fundamental of cellular processes, i. e. endocytosis, in real time without background interference. In their work a new NIR *OFF* to *ON* fluorescence switchable nanoparticle architecture was described that is capable of switching its fluorescence *ON* following cellular uptake, but remains switched *OFF* in extracellular environments. This permits continuous real-time imaging of the uptake process as extracellular particles are nonfluorescent.[62]

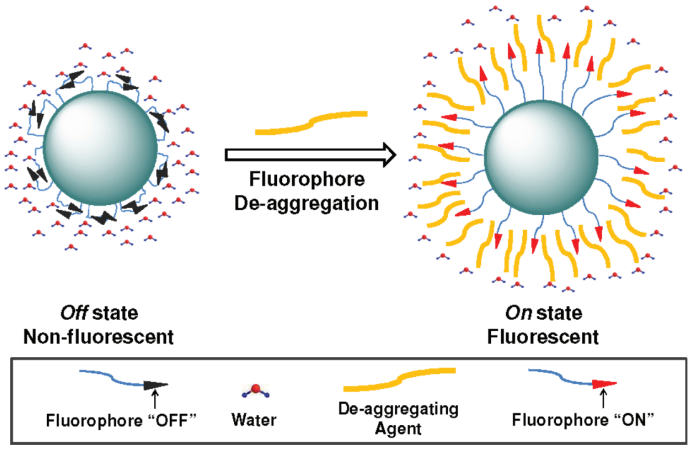

Figure 4.1. Proposed switching mechanism for *OFF-ON* fluorescent nanoconstructs [62].

Fluorophore immobilization on or within particles can yield significant photophysical benefits and is being increasingly investigated for roles in nanomedicine, nanobiotechnology, and fluorescence imaging.[63] Intensive studies are carried out on particle based fluorophores with noncovalently linked dyes on the surface of the polymer particle. In contrast, the development of nanoparticles with surface covalently bound fluorophores is rather limited. A potential advantage of covalently linking the fluorophores at the surface of a particle is that they may be induced to respond to stimuli in the surrounding microenvironment not being shielded by a surrounding particle.[62] The principle of functioning of such *OFF-ON* fluorescent nanometric architectures is presented in Figure 4.1. The surface of nanoparticle (NP) is loaded with NIR hydrophobic fluorophores, being quenched in high polar aqueous media, which defines a particle *OFF*-state. Particle fluorescence can be turned *ON* in aqueous media in response to various surfactants agents. This *OFF-ON* fluorescence responsive behaviour was used in real-time biological imaging in which the cellular uptake of the particles with inclusion within organelles mimics the *OFF-ON* switching obtained with surfactants. The ability of these fluorescence responsive nanoconstructs to allow real-time continuous imaging of their uptake into cells has been demonstrated in a movie

format in the work of O'Shea [62].

In this work we were specially interested in studying the mechanism governing the process of switching *ON* fluorescence of dyes grafted on the poly(styrene-co-methacrylic acid) based NP[1] surface on adding of surfactant (de-aggregating) agents. We studied several systems:

- Model system **NP-P** with pyrene-based[2] moiety (Figure 4.2), grafted on the surface of $d{=}100$ nm of polymeric Nanoparticle (NP).
- Boron-dipyrromethene (BODIPY) based polymeric NPs ($d{=}100$ nm): **NP-B1** and **NP-B2** (Figure 4.4).

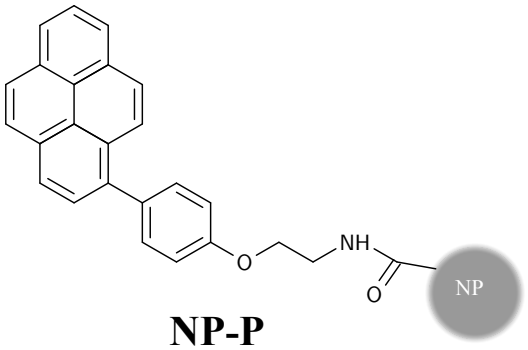

NP-P

Figure 4.2. Structure of pyrene-based monomer unit covalently linked to the polymeric NPs.

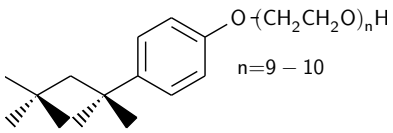

Figure 4.3. Structural formula of Triton X-100 surfactant (de-aggregating) agent.

2

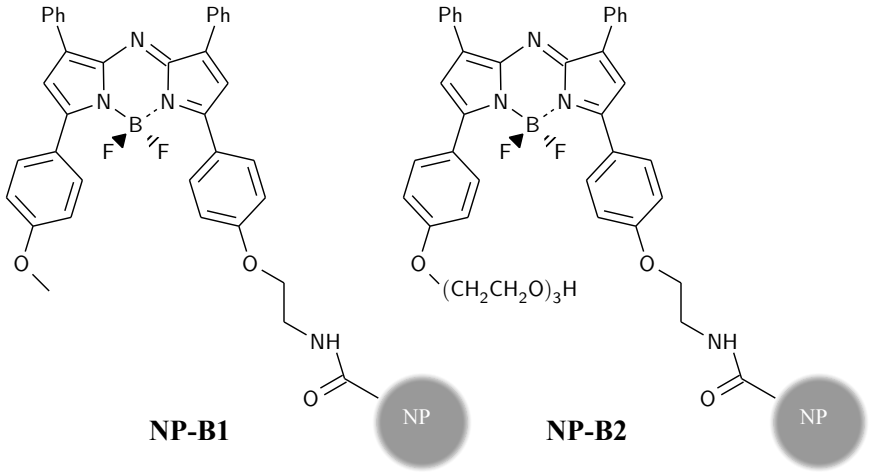

NP-B1 **NP-B2**

Figure 4.4. Structure of aza-BODIPY: **B1** and **B2** coated NPs.

[1]Polystyrene NP with carboxylate surface groups impacted increased solubility to hydrophobic fluorescence probe molecules in polar solvent, such as water.

[2]Pyrene was used as a fluorophore, because of its high emission QY and also because its emission lies in the blue spectral range, which is convenient for *in vitro* studies. Equally, monomer and excimer emission was anticipated, giving further information of chromophore-chromophore interactions. Furthermore FRET between Triton X-100 and pyrene was anticipated to give further information in surfactant-chromophore interaction.

4.1.2 Experimental

All samples were prepared from NP powders by dissolving[1] them in Milli-Q water with Phosphate Buffered Saline (PBS) buffer, pH=7.5 to imitate cellular media. Spectroscopic measurements were done using non-degassed solutions at two main concentrations 0.0025 mg/mL and 0.01 mg/mL. Triton X-100 – a nonionic surfactant that has a hydrophilic polyethylene oxide chain (on average it has 9.5 ethylene oxide units) and an aromatic hydrocarbon lipophilic group (Figure 4.3) was used as a main surfactant (de-aggregating) agent, allowing to turn *ON* fluorescence of NP. Another way to turn *ON* the fluorescence of NP was to introduce them in vesicles, made of phospholipids 1,2-Dioleoyl-sn-Glycero-3-Phosphocholine (DOPC) (prepared *via* rehydration of drop-cast films). The latter method allowed a better mimic of a cellular environment, compared with Triton X-100 surfactant.

4.1.3 Results and discussion

4.1.3.1 Steady-state spectroscopy

Steady state emission spectra for **NP-P** were recorded by varying the concentration from 0.0002 mg/mL up to 0.01 mg/mL. The characteristic pyrene monomer fluorescence centred at 410 nm remained unchanged while a new band at λ_{max}=480 nm, which is characteristic for the pyrene excimer[2] emission appeared (Figure 4.5), arising from excimer formation between two NP, aggregating at high **NP-P** concentration.

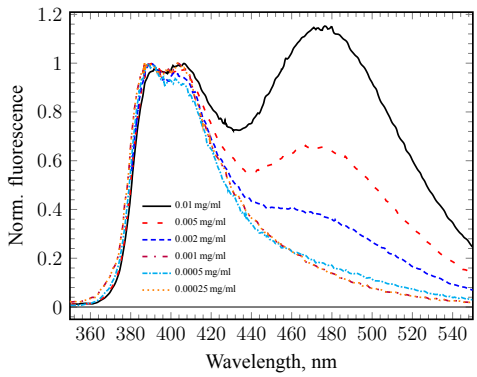

Figure 4.5. Evolution of the emission spectra of **NP-P** in PBS at different concentrations (λ_{exc}= 340 nm).

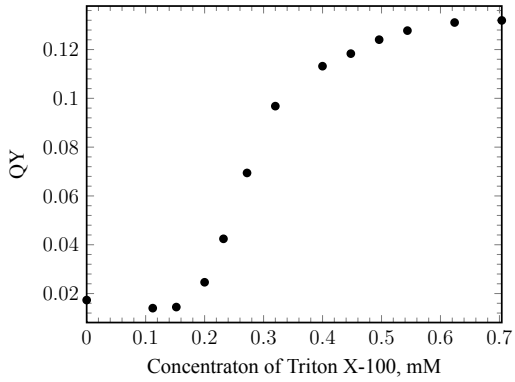

Figure 4.6. Relative fluorescence quantum yield upon addition of **NP-P** in PBS upon addition of Triton X-100 (λ_{exc}=345 nm).

A concentration of **NP-P**, 0.0025 mg/mL, was chosen for luminescence properties studies of pyrene based nanoparticles. At this concentration no emission arising from the excimer was observed and a relatively (*vs.* pyrene in cyclohexane 0.32 [176]) low fluorescence QY was measured (Figure 4.6). Upon titration with Triton X-100, a 4-fold increase of the **NP-P** fluorescence QY was observed. It should be mentioned that relative QY values might be affected by the change of the media polarity upon addition of surfactant to the **NP-P** water based solution.

The solutions of **NP-B1** and **NP-B2** did not show any unexpected behaviour at concentration of 0.01 mg/mL. So this concentration was used for aza-BODIPY based NP systems in order to get stronger fluorescence emission from these samples.

More information about pyrene molecule interaction can be extracted by comparison of the excitation spectra recorded monitoring pyrene monomer and excimer emission wavelengths.

[1]NP did not show any visible precipitation during several months period. Some drift in the size distribution was observed over time. This did not affect the use of the same batch of NP over time as they could be easily redispersed by sonification.

[2]Excimer – is an excited dimer formed by the association of an excited and an unexcited chromophore, which will dissociate in the ground state.

While the excitation spectra of pyrene recorded at monomer (λ_{mon}=410 nm) and excimer (λ_{exc}= 480 nm) emission wavelengths show the same features, upon formation of excimer the two excitation spectra are not superimposable with the excimer one being characterized by a red shift of a few nm.[177] At a relatively low concentration of **NP-P** (0.0025 mg/mL) the excitation spectra were superimposable suggesting the absence of pyrene excimers, while the spectral features where not affected by the addition of small aliquots of surfactant (Figure 4.7).

The absorption and emission spectra of **NP-B1** and **NP-B2** are represented in Figure 4.8. Both aza-BODIPY dyes demonstrate similar absorption spectra with absorption centred at 690 nm and emission maxima lying in the NIR spectral region, centred at 720 nm.

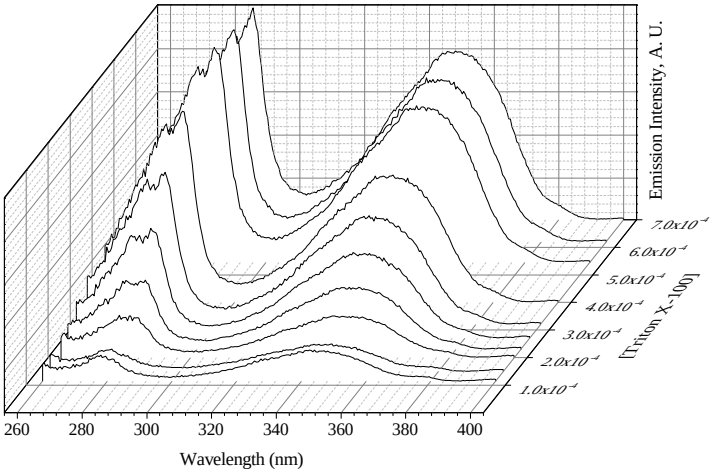

Figure 4.7. Excitation spectra of **NP-P**, 0.0025 mg/mL, in PBS upon addition of Triton-X100 (λ_{ob}=410 nm).

Steady state emission studies performed on **NP-B1** and **NP-B2** samples under physiological condition showed the absolute emission QY[1] increase up to 10-times upon addition of Triton X-100 surfactant[2]. Despite the only difference between **NP-B1** and **NP-B2** is the 3-aryl group in azo-BODIPY fluorophore we observed a different fluorescence response of the two samples upon addition of surfactant Triton X-100 (Figure 4.9) was observed, namely different Triton X-100 concentration thresholds.

Steady state emission spectroscopy allowed us to track responses of **NP-P**, **NP-B1** and **NP-B2**, observed upon Triton X-100 surfactant concentration variations. In order to describe phenomena occurring at the NP surface upon addition of the surfactant molecules, time-resolved emission experiments were performed.

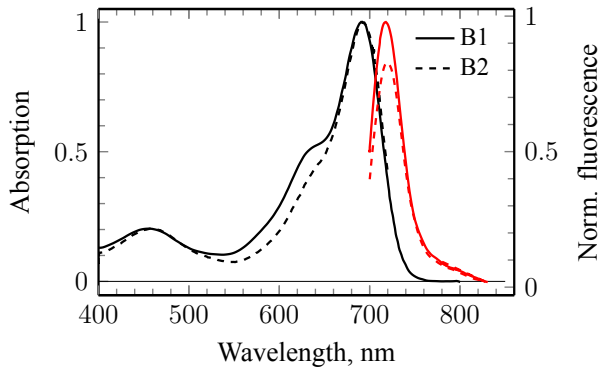

Figure 4.8. Electronic absorption and emission spectra for **B1** and **B2** aza-BODIPY dyes in THF (λ_{exc}=675 nm).

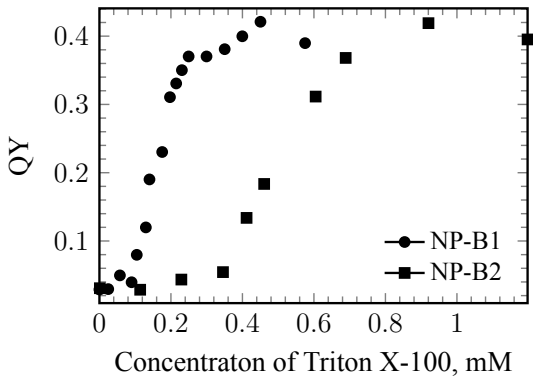

Figure 4.9. Absolute quantum yields for **NP-B1** and **NP-B2**, 0.01 mg/mL, in PBS determined upon addition of Triton X-100 surfactant (λ_{exc}=675 nm).

4.1.3.2 Time-resolved emission spectroscopy

It is assumed that heterogeneity of fluorophore spatial distribution on the surface, surface roughness, defects should have an effect on rates of non-radiative and radiative relaxation pro-

[1]Determined using spectrofluorometer, equipped with integration sphere [178].
[2]Critical Micelle Concentration (CMC) of Triton X-100 is $\sim 2 \times 10^{-4}$ M.

cesses for fluorophores attached to the NP surface. Thus fluorescence decays should consist of a sum of a finite, but large number of exponents with different values of decay lifetimes (or relaxation kinetics could even be described by a non-exponential law), corresponding to different states of fluorophores, characterized by different geometric organization of the medium around them. Several models can be used to extract of rate constant distributions from such fluorescence decays. An exponential series method [179, 180] or maximum entropy method [96, 99, 180] could be used for the determination of the deexcitation rate distributions. Although a simpler method using stretched exponential function fit [181, 182] (see section 1.3) has also been used to describe the interaction occurring between fluorophores and their environment. A stretched exponential function was used by Wong [183] in the case of pyrene covalently linked to spherical silica particles and pyrene covalently linked to spherical aluminium NP [182] fluorescence emission analysis, which allowed determination of emission rate distribution and thus determination of the fluorophore state on the particle surface.

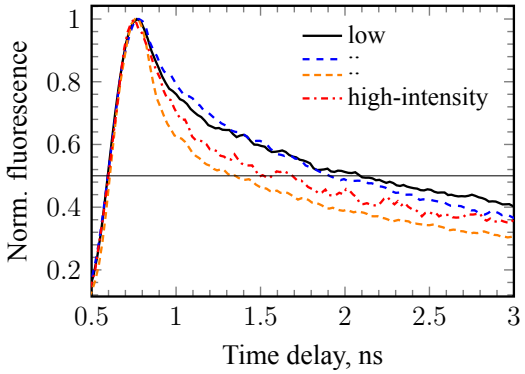

Figure 4.10. Fluorescence decays of **NP-P**, 0.0025 mg/mL, obtained at different intensities of excitation source (λ_{exc}=355 nm, λ_{ob}=410 nm).

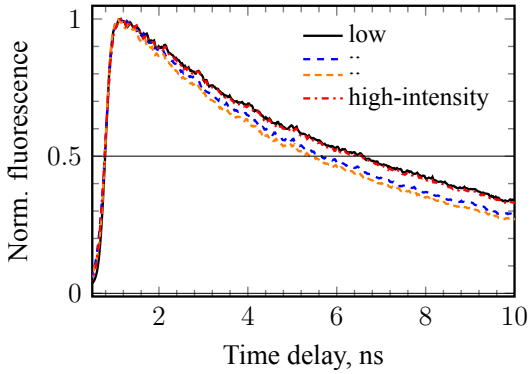

Figure 4.11. Fluorescence decays of **NP-P**, 0.0025 mL/L, obtained at different intensities of excitation source with 9.22×10^{-4} M of Triton X-100 surfactant (λ_{exc}=355 nm, λ_{ob}=410 nm).

The relaxation kinetics of fluorescence obtained at different intensities of excitation source for **NP-P** at concentration 0.0025 mg/mL are represented in Figure 4.10. The higher the intensity of the excitation source – the faster the system relaxes. This could be explained as follows: the surface of the NP is covered by pyrene molecules, at high excitation source intensity several pyrene excited states on one NP could be created, which could migrate on the NP surface through FRET mechanism, before they meet and annihilate (in analogy with surface exciton-exciton annihilation in solid bodies). The presence of Triton X-100 surfactant molecules in the system (Figure 4.11) causes prolongation of pyrene emission, but still pyrene excited state annihilation at higher intensities of excitation source can be seen (Figure 4.11), meaning that Triton X-100 molecules do not efficiently change distance between pyrene units or reduce efficiency of energy transfer between them. Due to these observations, namely intensity dependence of fluorescence rates for the **NP-P** system, we worked at the minimum possible intensity during time-resolved photophysical studies, namely with 0.3 J/cm^2 per pulse.

Figure 4.12 shows the decays of the **NP-P** system (0.0025 mg/mL) emission in the absence and the presence of Triton X-100 surfactant molecules. The emission lifetime of **NP-P** without Triton X-100 has a value of ~20 ns (pyrene in CH_3CN shows a monoexponential emission decay lifetime ~13 ns). At the Triton X-100 concentration $\sim7\times10^{-4}$ M the decay cannot be described by an one exponent decay function. The appropriate fit could be made by fitting this decay with a stretched exponent function $A\exp\left(-(kt)^{\beta}\right)$, with τ=6.30 ns and β=0.66 parameters.

Figure 4.13 demonstrates fluorescence decays for **NP-B1** and **NP-B2**, 0.01 mg/mL, at different Triton X-100 surfactant concentrations. As shown in the figure the samples **NP-B1** and **NP-B2** demonstrate almost monoexponential emission decay at high concentration of Triton

X-100, but at low concentration of Triton X-100 the decays are highly non monoexponential.

All recorded time-resolved emission decays at different concentrations of Triton X-100 surfactant for studied samples **NP-P** (0.01 mg/mL and 0.0025 mg/mL) and **NP-B1** and **NP-B2** were analysed (fitted) using a stretched exponent function.

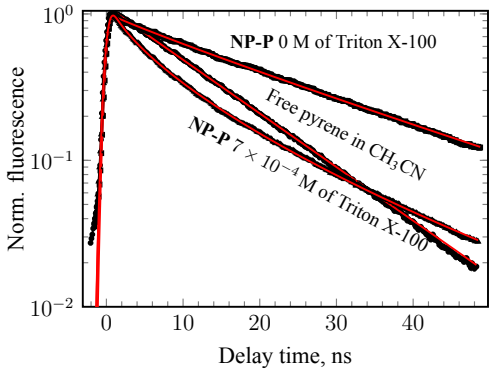

Figure 4.12. Fluorescence kinetics of **NP-P**, 0.0025 mg/mL, at different concentrations of Triton X-100 surfactant (λ_{exc}=355 nm, λ_{ob}=410 nm).

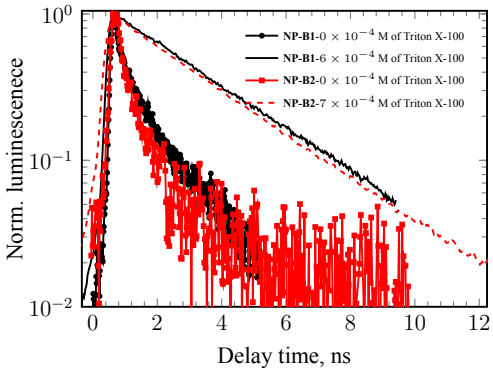

Figure 4.13. Fluorescence kinetics of **NP-B1** and **NP-B2**, 0.01 mg/mL, at different concentrations of Triton X-100 surfactant (λ_{exc}=650 nm, λ_{ob}= 720 nm).

The dependence of τ and β for **NP-P** (0.0025 mg/mL) from Triton X-100 surfactant concentration is illustrated in Figure 4.14. At the CMC $\sim 2 \times 10^{-4}$ M the minimum for parameters τ and β are observed. To explain this, additional parameters should be considered.

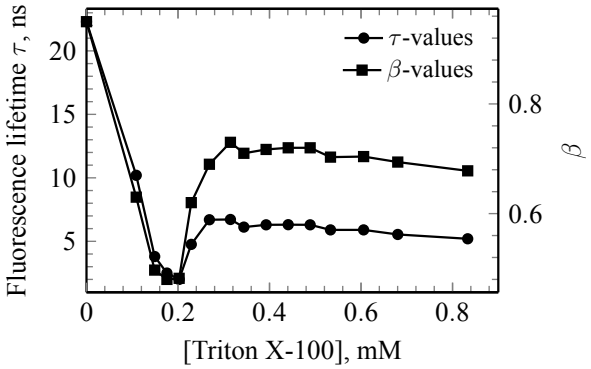

Figure 4.14. The dependency of parameters values τ and β value from Triton X-100 surfactant concentration in **NP-P** solution, 0.0025 mg/mL (λ_{exc}= 355 nm, λ_{ob}=410 nm).

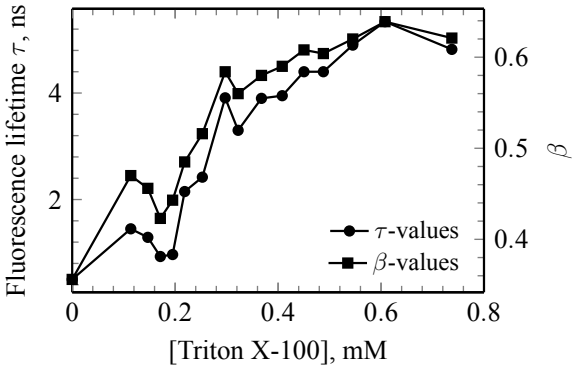

Figure 4.15. The dependency of parameters values τ and β value from Triton X-100 surfactant concentration in **NP-P** solution, 0.01 mg/mL (λ_{exc}= 355 nm, λ_{ob}=410 nm).

At zero concentration of Triton X-100 surfactant, the fluorescence QY of **NP-P** is relatively low, because pyrene units on the surface are almost completely quenched, through interaction with the surface, which is also true for **B1** and **B2** fluorophores. Weak **NP-P** emission with decay lifetime $\tau \simeq 20$ ns could be attributed to "free" pyrene molecules, which do not interact with the surface. Such emission is not observed in case of **NP-P** with a higher concentration of 0.01 mg/mL. At this high concentration of NP as shown previously, NP start to aggregate, causing quenching of "free" pyrene units fluorescence. Presence of Triton X-100 surfactant molecules changes spatial organization of pyrene units, which are attached to the surface of NP (see Figure 4.1). It gives rise to stronger fluorescence emission (QY grows). At CMC $\sim 2 \times 10^{-4}$ M the τ and β reach their minima, which represents a broad lifetime distribution (Figure 4.17, and Figure A.5) of pyrene units emission and as a consequence a greater uncertainty in spatial organization of surface groups. Further increase of Triton X-100 concentration leads to an increase of τ and β, thus lifetime distribution, representing heterogeneity of pyrene

spatial organization, shrinks and its centre moves to lower values, as it can be seen from Figure 4.17, but still spatial organization of pyrene units, which are attached to the NP surface remains heterogeneous.

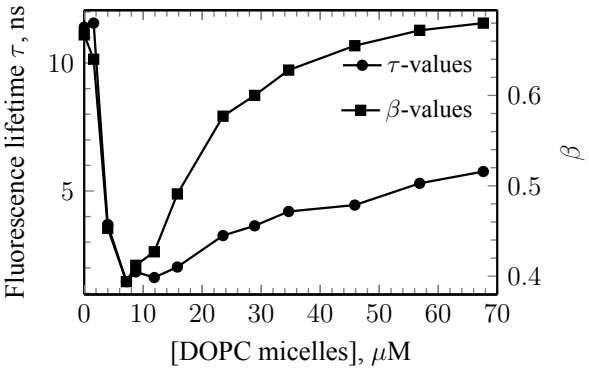

Figure 4.16. The dependency of parameters values τ and β value from DOPC micelles concentration in **NP-P** solution, 0.0025 mg/mL (λ_{exc} = 355 nm, λ_{ob} = 410 nm).

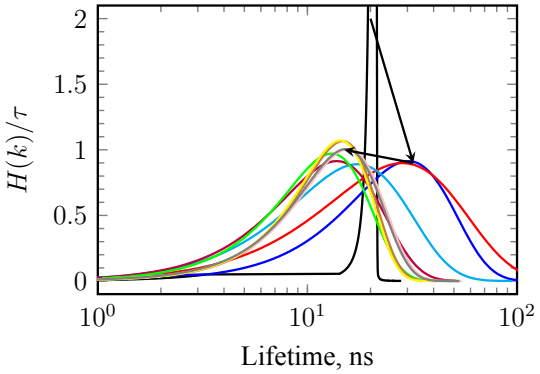

Figure 4.17. Distribution of lifetimes for **NP-P**, 0.0025mg/mL, at different concentration of Triton X-100 surfactant.

NP-P solutions with DOPC micelles show a similar trend (see Figure 4.16) as described above, leading us to the conclusion that different surfactant agents switch *ON* fluorescence of the **NP-P** system similarly.

Although Triton X-100 and DOPC micelles surfactants significantly increase the QY of **NP-P**, the lifetime distribution remains very broad, meaning that there are many different interactions between pyrene units in the system: pyrene-NP surface, pyrene-pyrene, pyrene-surfactant interactions. Additional quenching mechanisms should be considered for **NP-P** systems with high concentrations of NP 0.01mg/mL, namely pyrene excimer formation between different NP. Despite this fact τ and β parameters show very similar trends (Figure 4.15), compared to the **NP-P** system at low concentration 0.0025 mg/mL, which does not show excimer formation.

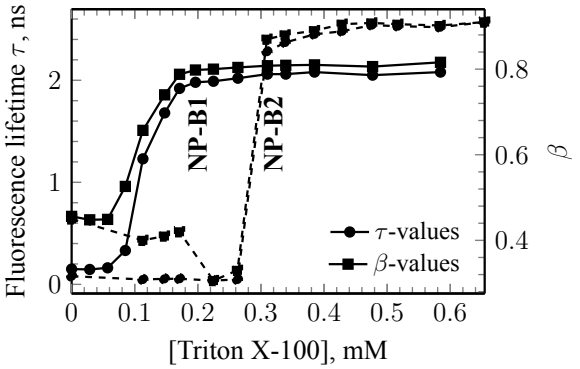

Figure 4.18. The dependency of τ and β parameters values from Triton X-100 concentration in **NP-B1** and **NP-B2** solutions, 0.01 mg/mL (λ_{exc} = 620 nm, λ_{ob} = 660 nm).

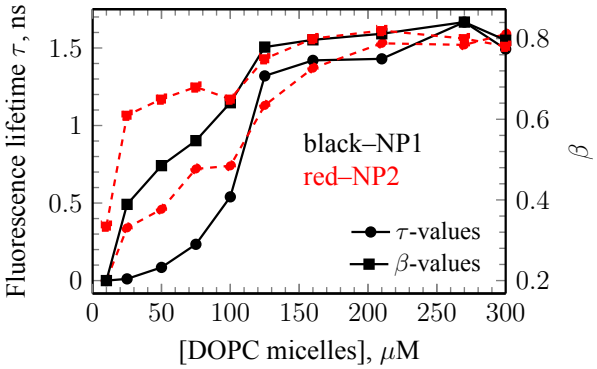

Figure 4.19. The dependency of τ and β parameters values from DOPC micelles concentration in **NP-B1** and **NP-B2** solutions, 0.01 mg/mL (λ_{exc} = 620 nm, λ_{ob} = 660 nm).

NP-B1 and **NP-B2** NPs demonstrate more pronounced dependencies on Triton X-100 surfactant concentration (Figure 4.18). Both systems show abrupt turn *ON* behaviour at 10^{-4} M and 3×10^{-4} M, for **NP-B1** and **NP-B2**, respectively, matching with the thresholds, determined from QY titrations (Figure 4.9). Influence of DOPC micelles on **NP-B1** and **NP-B2** turning *ON* is not so pronounced (Figure 4.19), showing approximately the same thresholds of turning *ON* for both **NP-B1** and **NP-B2** samples. What is important in the case of **NP-B1** and **NP-B2** is that the β parameter almost reaches unity, meaning that almost all aza-BODIPY fluorophores,

attached to the NP surface are in the same conditions. In other words, the spatial organization seems to be homogeneous at concentrations of Triton X-100 of DOPC micelles concentration higher than the thresholds.

The simple model describing the process of switching *ON* fluorescence for all studied systems **NP-P**, **NP-B1** and **NP-B2** could be described as follows: without Triton X-100 surfactant all emission of fluorophore units attached to the surface is quenched; in the presence of Triton X-100, which penetrates between fluorophores units and the NP surface, causing fluorophores units to rise from the surface, results in a decreased efficiency of non-radiative deexcitation, arising through fluorophore-surface interaction, and thus increases emission QY of the NP systems.

4.1.3.3 Time-resolved anisotropy

In order to study molecular dynamics of fluorophores, attached to the surface of NP and consider the process of turning fluorescence *ON*, time-resolved anisotropy measurements were conducted (see section 1.6.3.7) for pyrene containing NP **NP-P** and aza-BODIPY: **NP-B1** and **NP-B2** with Triton X-100 surfactant at concentrations higher than threshold, as well as without it. As shown in Figure 4.20, anisotropy decay of fluorescence for **NP-P** without Triton X-100 decays with a time constant τ=60 ps, which could be associated with free pyrene molecule rotation. The maximum value of anisotropy equals to 0.17. Upon addition of Triton X-100 surfactant molecules the anisotropy decay lifetime increases up to $\sim$6 ns. This fact could be understood considering that Triton X-100 molecules interact with pyrene units. As we have suggested before: Triton X-100 molecules cause pyrene units to rise from the surface of NP, which turns out to be in more rigid matrix of Triton X-100 surfactant molecules, thus the emission depolarization occurs more slowly.

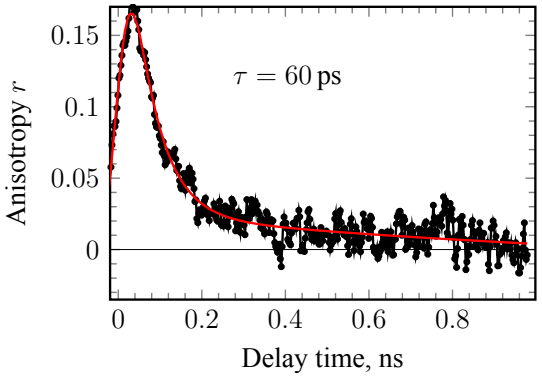

Figure 4.20. Anisotropy relaxation kinetics for **NP-P** (0.0025 mg/mL) without Triton X-100 surfactant (λ_{exc}=355 nm, λ_{ob}=410 nm).

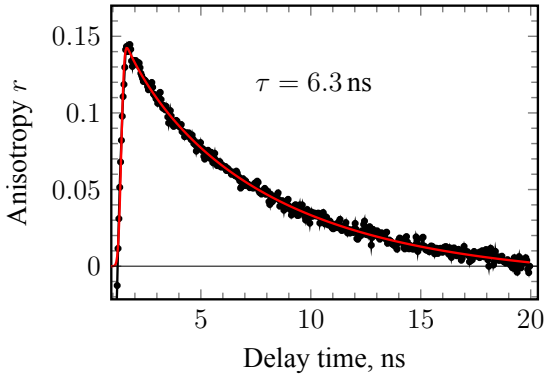

Figure 4.21. Anisotropy relaxation kinetics for **NP-P** (0.0025 mg/mL) with $\sim 7 \times 10^{-4}$ M Triton X-100 surfactant (λ_{exc}=355 nm, λ_{ob}=410 nm).

The effects of a whole NP rotation on anisotropy decay could be neglected, due to the much slower rate of rotation, compared to the rotation of the pyrene unit.

In the case of **NP-B1** and **NP-B2** the anisotropy decay time constants at high concentrations of Triton X-100 equal to $\sim$5 ns, what could be understood as complete fixation of aza-BODIPY molecules, attached to the NP surface from rotational movements around their linkers.

4.1.3.4 Resonance energy transfer

The Resonance Energy Transfer (RET) between Triton X-100 surfactant molecules and pyrene units was studied following λ_{exc}=266 nm excitation (Figure 4.22). The RET process is possible for this pair because the emission spectrum of Triton X-100 molecules overlaps with

the pyrene absorption spectrum (Figure 4.23). As it can be seen from Figure 4.22 the RET efficiently occurs only above the CMC of Triton X-100 surfactant, which is expressed by elongation of fluorescence emission growth. The data analysis was performed according to the scheme showed in Figure 4.24. Both the singlet of Triton X-100 and pyrene states can be excited by the excitation wavelength 266 nm. As we were tracking emission kinetics of pyrene emission, (λ_{ob}=410 nm) which does not intersect with Triton X-100 emission, we did not include the radiative channel for Triton X-100 deexcitation in our scheme, assuming that there is only energy transfer through which deexcitation of S_{Triton} state passes.

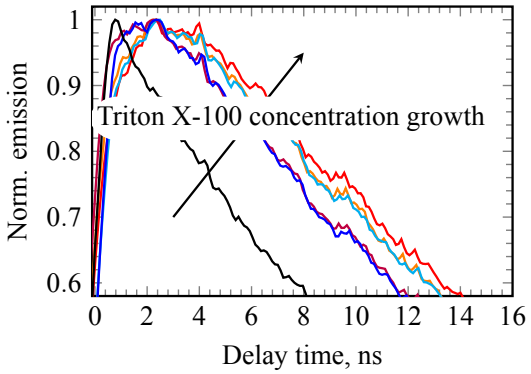

Figure 4.22. Fluorescence kinetics of **NP-P**, 0.0025 mg/mL, at different concentration of Triton X-100 surfactant (λ_{exc}=266 nm, λ_{ob}=410 nm).

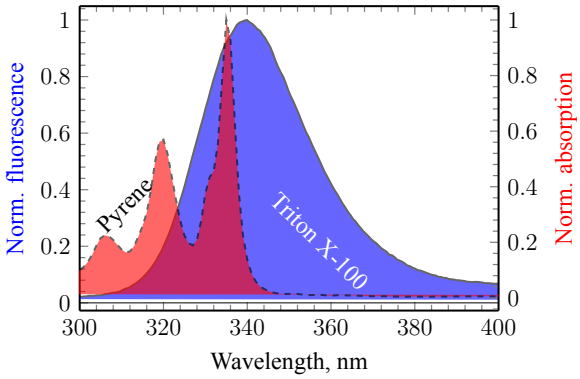

Figure 4.23. Absorption spectra of pyrene and emission spectra of Triton X-100 (λ_{exc}=266 nm).

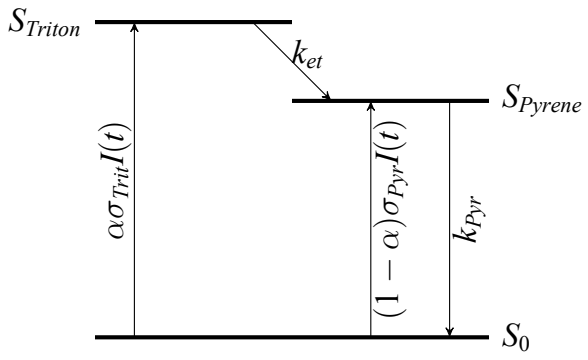

Figure 4.24. Electronic Energy Transfer data treatment scheme.

Figure 4.25 shows the rate of RET (between Triton X-100 and pyrene units) dependence on Triton X-100 surfactant concentration for **NP-P** system (0.0025 mg/mL). Titration of **NP-P** with Triton X-100 causes decrease of RET rate (time-constants changes from 1.1 ns up to 1.65 ns), while simultaneously the rate of emission decay is reduced as well (Figure 4.26), which is expected in accordance with results shown above. This can be explained by a simple consideration of the microenvironment refractive index change. While water is characterized by a the refractive index of 1.33, for Triton X-100 it is equal to 1.493, hence from the Förster theory RET efficiency is defined as:

$$E_{RET}=\frac{k_{RET}}{k_{RET}+k_{fluo}+k_{nr}}=\frac{1}{1+\left(\frac{r}{R_0}\right)^6},$$

where R_0 – the distance at which the energy transfer efficiency is 50 %:

$$R_0^6=\frac{9\Phi_0\ln 10\kappa^2 J}{128\pi^5 n^4 N_A}$$

From the simplest consideration, not including changes of κ^2 or J integral, if refractive index η increases – R_0^6 decreases, so k_{RET} should decrease as well, because $k_{RET}=\frac{1}{\tau_D}\left(\frac{R_0}{R_{DA}}\right)^6$.

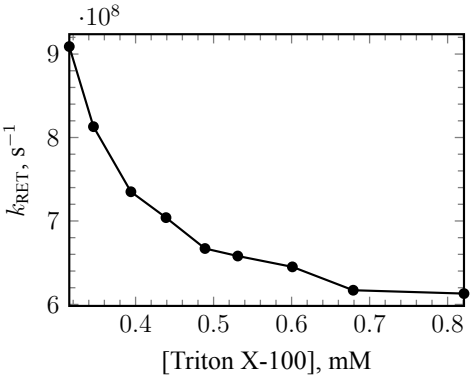

Figure 4.25. Dependency of energy transfer rate from Triton X-100 concentration for **NP-P** (0.0025 mg/mL, λ_{exc}=266 nm, λ_{ob}=410 nm).

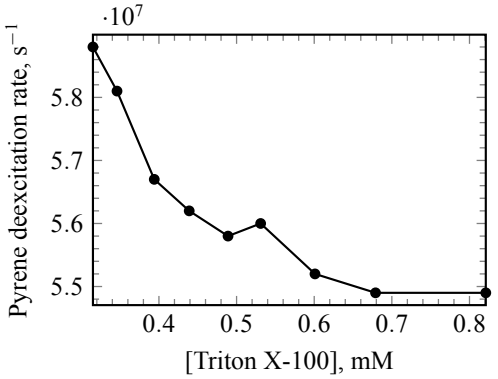

Figure 4.26. Dependency of pyrene emission rate relaxation from Triton X-100 concentration for **NP-P** (0.0025 mg/mL, $\lambda_{exc} = 266$ nm, $\lambda_{ob} = 410$ nm).

It should be mentioned that lifetime of Triton X-100 surfactant fluorescence has a concentration dependence. Changing concentration of Triton X-100 in PBS from 85μM to 860μM affects the lifetime of Triton X-100 emission, centred at 340 nm, changing it from 4.5 to 5.6 ns. It seems that after CMC the lifetime of Triton X-100 fluorescence increases, so in more rigid media (micelles) Triton X-100 fluorescence lifetime becomes longer.

During titration of **NP-P** NP with Triton X-100 at low concentration the emission lifetime of Triton X-100 has value of 5.6 ns, which indicates that Triton X-100 molecules are located in rigid media. All Triton X-100 molecules are physisorbed on the NP surface. At high concentration of Triton X-100 its emission lifetime decreases down to 4.4 ns, due to a RET process. Concerning these data, we could estimate efficiency of RET to be equal to $1 - \frac{4.4}{5.6} \times 100\% = 22\%$. But this efficiency value is very approximate, because we do not know how many Triton X-100 molecules are absorbed on the NP surface and how many are in the water solution.

4.1.4 Conclusions

The study of NIR fluorescent *OFF-ON* probes, based on aza-BODIPY dyes, covalently attached to the surface of NP (poly(styrene-co-methacrylic acid)) with characteristic size of d=100 nm was conducted in water solutions. Equally, the model system with pyrene-like units, covalently attached to the surface of same NP was investigated. It was shown that studied systems demonstrate pronounced responses (fluorescence turning *ON*) to the presence of surfactant (de-aggregating) agents, such as Triton X-100 and DOPC micelles. Due to the outstanding photostability properties [64], emission properties and good response to stimulus these systems could find applications in fluorescence cell imaging. The mechanism of fluorescence turn *ON* was proposed, which consisted in direct impact of surfactant on spatial organization of fluorophores, attached to the surface of NP, causing elimination of non-radiative deexcitation pathways and as a result an increase of fluorescence emission QY, up to 0.13 and 0.4 in the case of pyrene and aza-BODIPY, respectively.

4.2 Fluorescent pH-sensitive NIR aza-BODIPY dye for *in vivo* imaging

4.2.1 Introduction

pH-sensitive fluorescent probes are widely used to test the acidic conditions of a number of cellular compartments. This approach has been applied to *in vivo* imaging of diseases associated with acidity level changes.[65, 184].

As it was shown in [65] there are several mechanisms by which a fluorescent probe can react to a pH change in media. The common approach utilizes enhancement or quenching of fluorescence intensity, that corresponds to the pH close to a probes' pK_a value. However, fluorescence intensity measurements are difficult to quantify in heterogeneous tissue. Thus recorded intensity changes may be due to a concentration gradient instead of difference of pH values in different areas of cell or tissue. Another approach is based on a shift of emission wavelength maximum, which is more reliable and quantitative, but developing NIR fluorescent probes[1] with pH-induced response spectral shift between 700 and 900 nm is a synthetic challenge.[65]

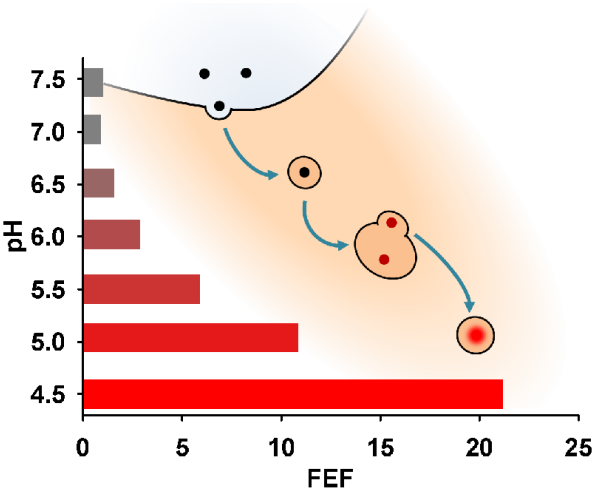

Figure 4.27. Switching mechanism for *OFF-ON* pH sensitive fluorescent probe. FEF – fluorescence enhancement factor.

In contrast to intensity measurements, the fluorescence decay lifetime of a probe has been introduced for *in vivo* optical imaging as a way to overcome the problem of concentration dependence and also enhance contrast and overcome other typical problems: light scattering, sample turbidity, and autofluorescence. Despite the advantages of fluorescence decay lifetime measurements, several limitations hinder the broad usage of the method for *in vivo* imaging. Recently, significant advances in the design of fluorescent environment-sensitive lifetime probes [185–188] high-speed electro-optic instrumentation, and fast postacquisition time have turned fluorescence lifetime *in vivo* imaging into a practical tool.[65]

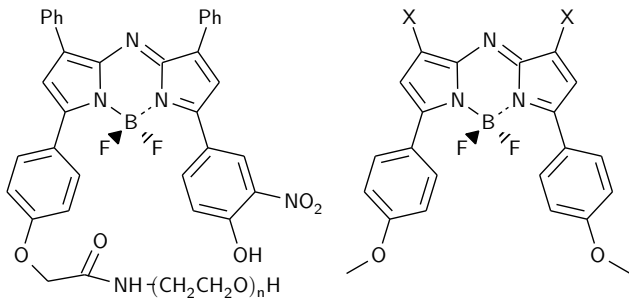

B3 X=Ph – **B4** X=Me – **B5**

Figure 4.28. Structure of **B3** (molecular weight≃ 5630 g/mol), **B4** [64] and **B5** [66].

In order to have fluorescence *OFF-ON* system responding to pH-stimulus (Figure 4.27), dye **B3** (Figure 4.28) was synthesized in the group of our collaborator O'Shea and coworkers in Centre for synthesis and chemical biology, University College Dublin, Ireland. The Polyethylene Glycol (PEG) chain (with average molecular weight of 5000 g/mol) was introduced in order to increase solubility in the water. In future applications the **B3** dye could be immobilized through covalent attachment with the NP, providing a robust and efficient system of *in vivo* fluorescent microscopy similar to the fluorescence *OFF-ON* systems de-

[1]NIR fluorescent probes allow detection in the "optical window" where cells have minimal light absorption.

scribed in section 4.1.

Studied **B3** system has well-proven behaviour as efficient fluorescence pH sensitive probe by collaborators O'Shea and coworkers *in vitro* studies, but photophysical processes of the **B3** system have not been completely elucidated. In this work the main goal was to understand photophysical processes, occurring in **B3** molecules at different pH values after light excitation.

4.2.2 Experimental

All spectroscopic measurements were performed in air-equilibrated, optically dilute[1] water solutions with 0.1 M KCl at RT. pH corrections were done using diluted solutions of HCl and KOH.

4.2.3 Results and discussion

4.2.3.1 Steady-state spectroscopy

B3 demonstrates pronounced fluorescence (switching *ON*) dependence as a function of pH values, represented in Figure 4.29. Fluorescence spectra were recorded at varying pH, starting from pH = 8.5 and acidifying with dilute HCl to pH = 2.2. At low pH < 4 the fluorescence is *ON*, QY[2] is 0.01, at high pH > 6 the fluorescence is *OFF* with a 2.5-times QY drop. The ratio between emission intensities at 710 nm was $\frac{I_{acid}}{I_{basic}} = 80$ (Figure 4.29), so it should be expected, that QY should decrease more, but it is not observed. Such behaviour is explained by the fact that emission band centred at 785 nm shows weak pH dependence, it is increasing when pH is increasing. So this band at 785 nm compensates the drop in emission at 710 nm, so the QY of the system drops down only 2.5-times.

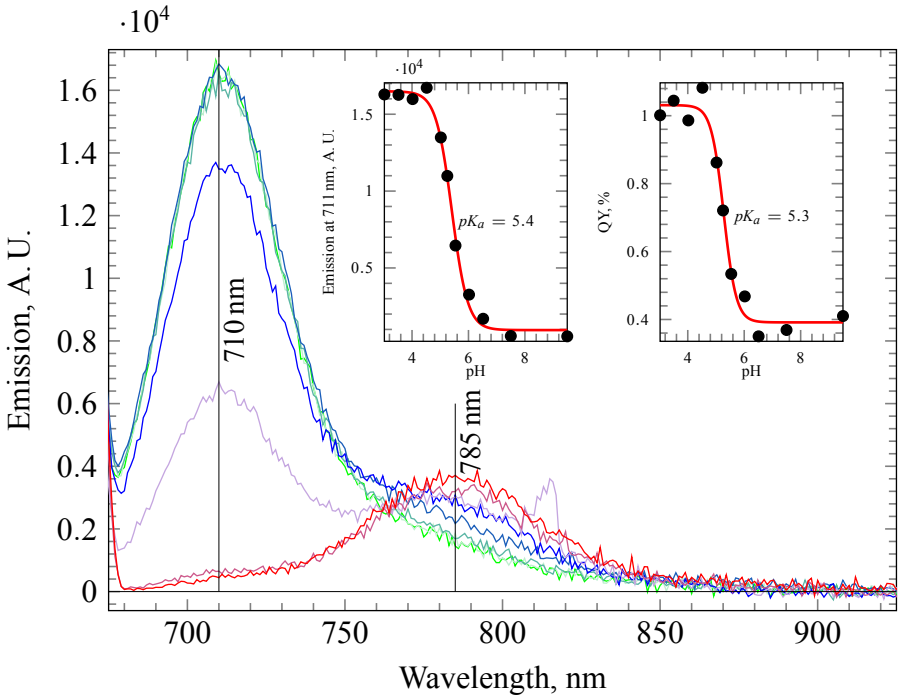

Figure 4.29. Evaluation of **B3** emission spectra at different pH in aqueous solution (0.1 M KCl, $\lambda_{exc} =$ 660 nm).

Despite this fact observed fluorescence pH response is very promising comparable to the behaviour of previously published phenol substituted azadipyrromethene fluorophores.[189, 190]

[1] Absorption at wavelength of excitation did not exceed 0.15, which equals 15 μM concentration for **B3**.

[2] The QY at different pH values was determined *vs* reference **B3** in CH_3CN with QY 0.058, which in turn was determined *vs* **B4** [64] (Figure 4.28) in CH_3CN which has QY 0.35

On top of an achieved effective *ON-OFF* switching mechanism, the estimated apparent pK_a was found to be 5.4, which is, as expected, almost 2 units lower than the corresponding derivative without an orto-NO_2 group (shown by O'Shea group). This behaviour is fundamental for biological studies as it allowed an effective fluorescence quenching at physiological pH and a raise in fluorescence signal in acidic conditions.

Recently the photophysics studies of **B4**-like molecules (Figure 4.28) were published by our group [64]. The QY determined for **B4** molecule in CH_3CN was calculated to be 0.35, which is 35-times higher comparing to **B3** molecule. It could mean, that **B3** molecule has an additional non-radiative deexcitation channel, which we attributed to interactions with polar solvent and NO_2-group, causing excited state energy losses through thermal energy dissipation.

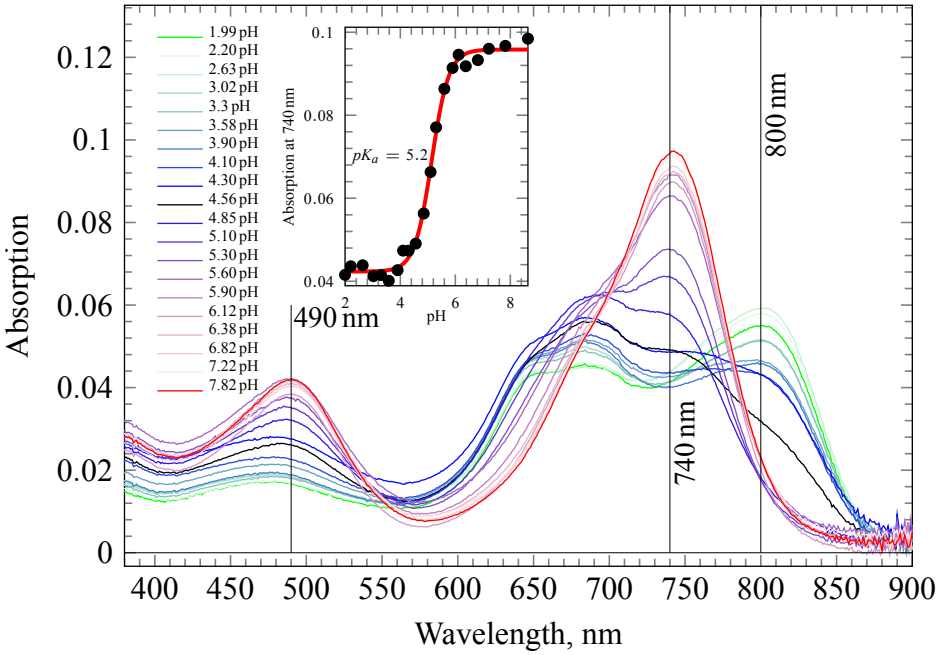

Figure 4.30. Absorption spectra of **B3** at different pH in aqueous solution (0.1 M KCl).

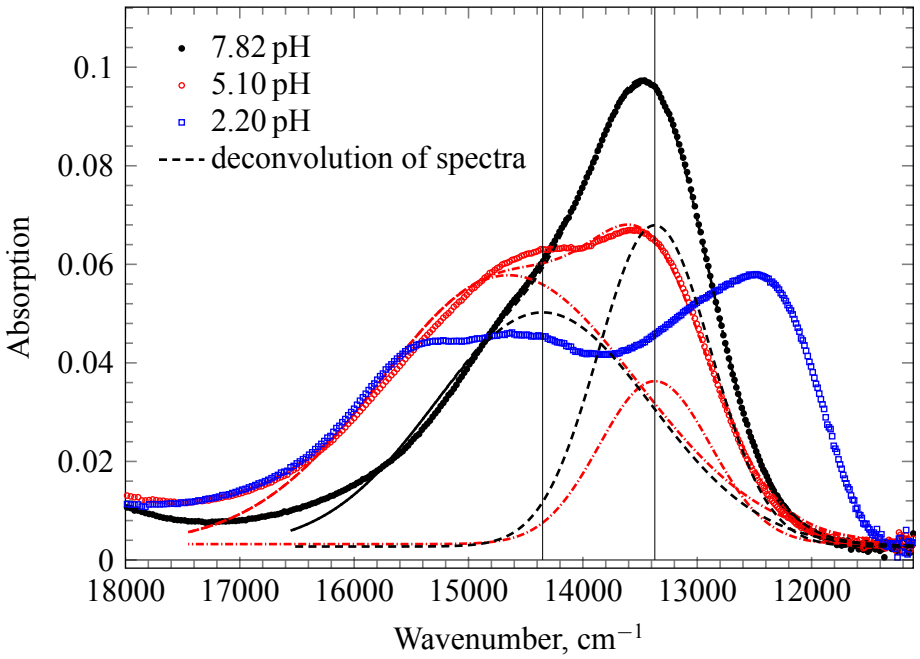

Figure 4.31. Asbsorption spectra of **B3** at different pH in aqueous solution (0.1 M KCl).

UV-pH titration (Figure 4.30) clearly shows that at basic pH there are two components:

deprotonated form of **B3** dominates over protonated form, at acidic pH there are at least 3 components in the solution, that could be detected (Figure 4.31):

1. deprotonated-form;
2. protonated-form;
3. unknown-form.

The studies performed in the O'Shea group in organic solvents with molecule **B3** without PEG chain showed that transition between protonated and deprotonated forms produced in all cases (Toluene, THF, ACN, DMSO) a clear isosbestic point, which was not observed in more polar aqueous solutions, tracked by UV-vis absorption.

4.2.3.2 Time-resolved emission spectroscopy

As shown previously, the fluorescence decay lifetime measurements have become one of the most promising tools for *in vivo* imaging studies. We conducted time-resolved fluorescence measurements (Figure 4.32) at different pH values in order to test the **B3** molecule for its potential application as a fluorescent lifetime pH sensitive probe.

During steady-state emission pH titration **B3** molecules showed reasonably high value 80 of FEF, when the pH value changed from 8 to 3, allowing use of this molecule as a pH sensitive intensity fluorescence probe. Time-resolved emission experiments clearly proved that the **B3** molecule also could be used as a lifetime fluorescence pH probe.

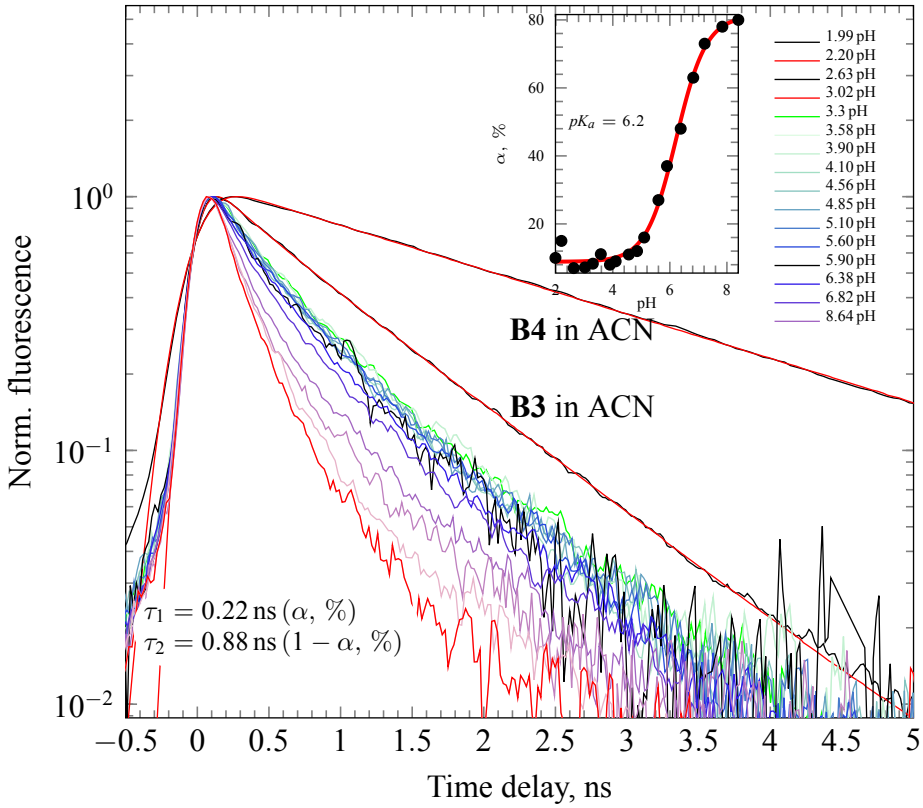

Figure 4.32. Emission decays of **B3** at different pH in water solution (0.1 M KCl, λ_{exc}=650 nm; decay kinetics obtained by integration of whole emission spectra); α – fraction of short-lived component.

As it shown in Figure 4.32, during pH titration from 2 to 8 the quantity of fast relaxation in emission decay kinetics, which was obtained by integration of whole emission spectra grows. The obtained pH dependence of short-lived component fraction α allowed us to built calibrating curve and determine excited state pK_a^*=6.2. The fast relaxation component corresponds to the species, which has emission spectra centred at 785 nm, while the slower decaying component corresponds to the species, that has emission centred at 710 nm. Indeed, steady-state emission

pH titration (Figure 4.29) showed that during pH change from 2 to 8 the relative weight of emission band centred at 785 nm grows, so the short-lived component in emission decay should grow up as well.

The emission lifetime decay for **B3** in CH_3CN equals to 1.2 ns with QY 0.058, while **B4** exhibited a longer lifetime of 2.4 ns with QY 0.35. It should be noted that in CH_3CN the **B3** molecule does not show any evidence of emission band centred at 785 nm.

4.2.3.3 Ultrafast absorption spectroscopy

To understand photophysical processes happening in the **B3** molecule immediately after excitation, femto-second time-resolved absorption spectroscopy measurements at different pH and excitation wavelengths (exciting different species of **B3** molecule) were performed.

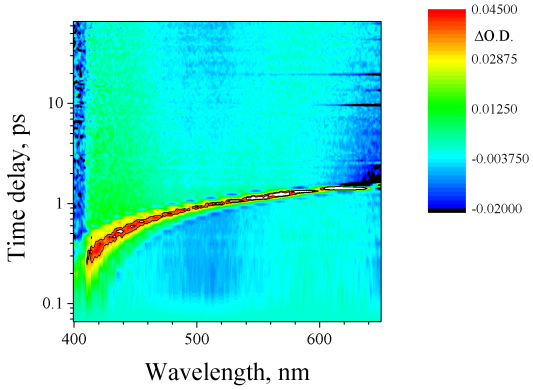

Figure 4.33. TRABS map of **B3** (pH=1.0, λ_{exc}= 800 nm).

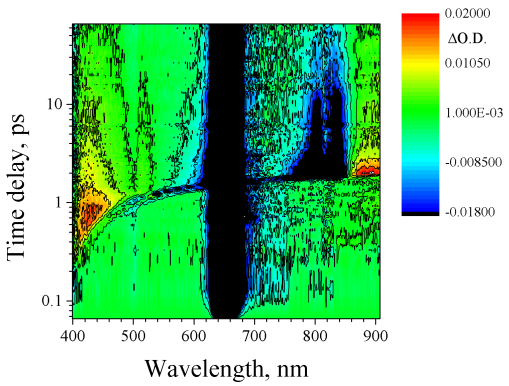

Figure 4.34. TRABS map of **B3** (pH=2.2, λ_{exc}= 650 nm).

A positive signal on TRABS map, presented in the Figure 4.33, at 400−480 nm (Figure 4.33), appearing after 800 nm 50 fs laser pulse at pH=1.0 was attributed to excited singlet state absorption $S_n \leftarrow S_1$ with decay lifetimes calculated to be 11 ps (Figure 4.35). The negative signal centred at 640 nm was ascribed to ground-state bleaching, which reverts to the ground state with the same rate as the $S_n \leftarrow S_1$ band centred at 422 nm.

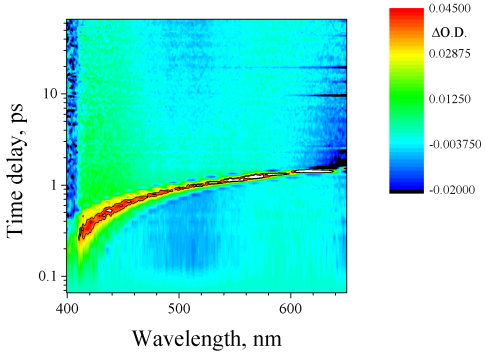

Figure 4.35. TRABS kinetic at 422 nm for **B3** (pH= 1, λ_{exc}=800 nm).

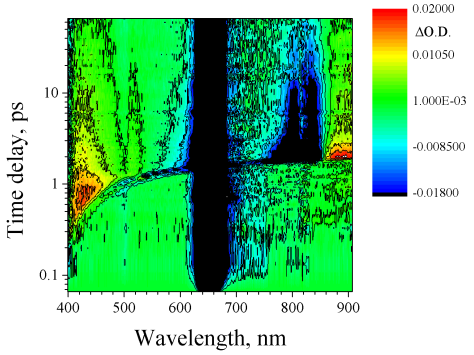

Figure 4.36. TRABS kinetics for **B3** at 422, 800, 895 nm (pH=2.2, λ_{exc}=650 nm).

Excitation of **B3** at pH=2.2 at 650 nm, along with the absorption band at 400−480 nm, gives rise to an absorption band centred at 900 nm (Figure 4.34), which can be attributed to excited singlet state absorption $S_n \leftarrow S_1$, which decays with the lifetime 10 ps (Figure 4.36). Equally, a structured negative signal around 800 nm is detected, which can be explained by stimulated emission, which disappears with the same rate as absorption bands at 422 nm and 900 nm[1].

[1] Intense negative signal at 650 nm is laser excitation.

Other TRABS experiments at pH values 5.2 and 8.5 (Figures 4.37, 4.38, 4.39) show similar behaviour as described above.

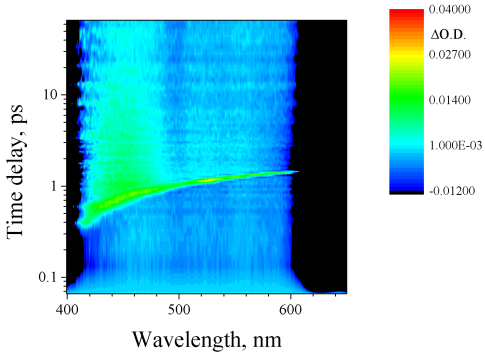

Figure 4.37. TRABS map of **B3** (pH=5.2, λ_{exc}= 650 nm).

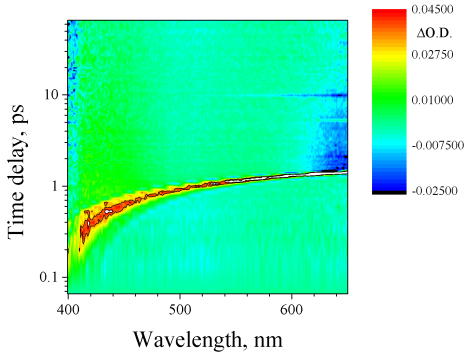

Figure 4.38. TRABS map of **B3** (pH=5.2, λ_{exc}= 800 nm).

Transient absorption maps at pH=1.0 (Figure 4.33) and pH=2.2 (Figure 4.34) with excitation 800 nm and 650 nm, respectively, do not show any evidence of stimulated emission at 710 nm. This fact could be explained by the idea that probably less than 5 %[1] of all excited states, generated by excitation at 650 or 800 nm could reach an a new emissive state, which will appear in TRABS as a negative band of stimulated emission.

The major part of excitation energy rapidly relaxes to another state, which shows fast relaxation to the ground state (τ=10 ps), which can be explained by strong electron acceptor (-M-effect) NO_2-group influence. The electro negative oxygen atoms could form hydrogen bonds with water molecules. The excess of energy located to singlet state of molecule could be dissipated through vibration of these hydrogen bonds.

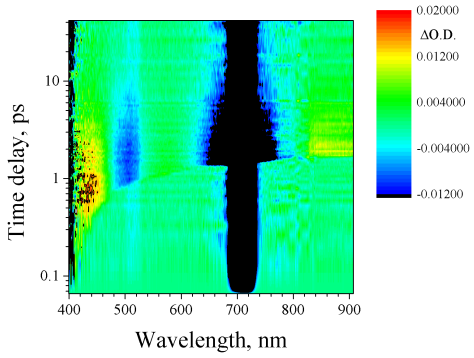

Figure 4.39. TRABS map of **B3** (pH=8.5, λ_{exc}= 710 nm).

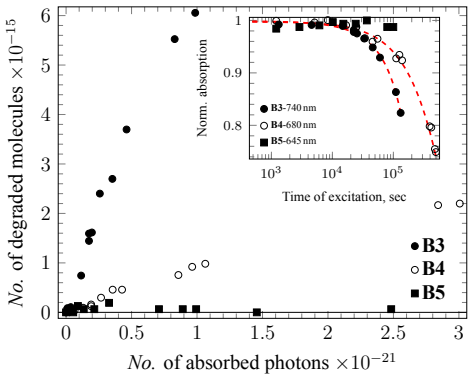

Figure 4.40. Photodegradation of **B3** and **B5** in air-equilibrated CH_3CN (λ_{exc}=630 nm).

The TRABS experiments conducted with **B4** molecule along with other similar molecules in work [64] showed that the excited state relaxes with nanosecond lifetimes, almost 3-order of magnitude difference.

Ultrafast absorption spectroscopy corroborated our assumptions, that in molecule **B3** there is a fast relaxation pathway, which turns out to have a lifetime in the sub-nanosecond range. We can suggest that this state (B) is populated from another excited state (A), initially excited by the laser pulse. The major part of this excited state relaxes down to another state, which gives all observed signals, and a small part of B relaxes to emissive states, which cannot be detected by absorption spectroscopy, but seen to govern the emission properties of the **B3** molecule.

[1] Sensitivity of TRABS is said to be equal ∼5%.

4.2.3.4 Photodegradation studies

The efficiency of the fluorescence probe is not only dependent on its emission properties such as wavelength of emission, which should lie in the NIR optical range window, it should have a long emission decay lifetime, high values of QY, but it also should show low values of photodegradation QY. In biological fluorescence microscopy, studies of low concentration of fluorophores is used along with experiments of long duration, which requires fluorophores to be highly robust.

The experiments on photodegradation QY determination under $633\,\text{nm}$ excitation ($5.6\,\text{mW}$) was conducted in air-equilibrated CH_3CN (Figure 4.40, see section 1.4 for detailed description of method for photodegradation QY determination). The QY of photodegradation for **B3** was determined as 5.4×10^{-6}, which is three orders of magnitude higher, compared to the **B4** ($< 10^{-8}$) [64] molecule and order of magnitude higher compared to **B5** (5.2×10^{-7}). Such behaviour could be explained by fast rates of excited state relaxation specific for **B3**. We anticipate that replacement of the NO_2-group with another strong electro-acceptor group, in which the formation of hydrogen bonds will be hindered by steric factors, for example could improve emissive properties of **B3** molecule: elongate emission decay lifetime and increase emission quantum yield.

4.2.4 Conclusions

The reasonably high FEF value of 80 for **B3** proves that the introduction of the NO_2-group in **B3** fluorophore guaranteed an efficient *OFF* to *ON* switching of the fluorescence signal from physiological to acidic pH. In other words, at a cellular level molecule **B3** would remain non-fluorescent in the extracellular environment and become highly fluorescent upon uptake and localization in acidic cellular compartment (e. g. endosomes and lysosomes). It was proved, that **B3** could be used as lifetime fluorescence pH probe, as well as a pH sensitive intensity fluorescence probe in fluorescence imaging. Studied **B3** molecules demonstrate sub-nanosecond relaxation pathways, which reduces its photostability compared to the **B4** molecule and decreases its emission QY, which could be improved by replacement of NO_2-group with another strong electro-acceptor group, in which the formation of hydrogen bonds will be hindered by steric factors.

4.3 Azobenzene-based systems for calcium ion capture/release

4.3.1 Introduction

A wealth of synthetic macrocyclic receptors have been reported over the last 40 years, which have shown varying affinities to a various guests, notably metal ions.[68] Among these receptors, stimulus-modulated (light, heat, pH, etc.) species where the binding affinity can be modified as a response to a stimulus represents an expanding research area. This is because there are a variety of potential applications in biomimetic nanotechnology, as well as molecular biology, where capture/release of a chemical effector at a certain time is employed to allow elucidation of specific biological pathways. For example cells use a wide variety of chemical messengers for signalling. Ionized calcium (Ca^{2+}) is on of the most important information carriers in the cell.[69] Development of effective chemical structures for Ca^{2+} ion controlled release/capture with high selectivity, speed and stability in live-cell media is a challenge for modern chemistry.[67]

In this context, photoactivated receptors are particularly attractive as light energy can be applied to autonomous molecules in solution with high spatial and temporal resolution.[191] Increasingly popular two photon absorption techniques offer a further possibility to irradiate with NIR light in the so-called therapeutic window, allowing deeper penetration of excitation light to activate deep lying molecules. Reversible photoinduced ion release and uptake imply photochromic receptors, where light switching between two distinct forms has a direct influence on binding. Indeed, a wealth of photochromes have been integrated with different receptors to give access to photocontrolled binding of a range of species. The origin of the binding change happens due to either electronic or steric effects. In the former case, upon switching, electron density is less available to binding sites in one form with respect to the other, with binding constant lowering. For the latter scenario, steric effects come into play when there is a significant geometrical change in the photoactive group between each form of the photochrome, which varies the shape of the receptor and hence suitability to bind a guest species.[67]

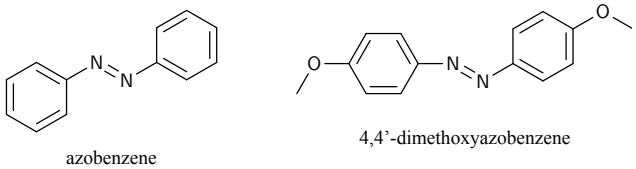

Figure 4.41. Chemical structure of azobenzene and 4,4'-dimethoxyazobenzene.

A popular choice of photochrome is azobenzene (Figure 4.41), which can be efficiently and reversibly switched from the thermally stable elongated trans-form to the more compact cis-form under UV irradiation. The return cis-to-trans transformation can be achieved by visible irradiation or thermally, which takes hours to days at room temperature.

Among different manifestations of azobenzene in supramolecular hosts, one of the most successful implementations was the development of photocrowns where an azobenzene unit was directly incorporated in the macrocyclic host or in "butterfly" variants. However, binding constants are typically low and strategies to increase this parameter would be anticipated to widen the scope of implementation of these photoactive functional molecules. Concerning the photoswitching and photochemistry of these macrocylic azobenzene-containing hosts, the complexing ring imparts differing levels of strain on the azobenzene link, which as a function of size can drastically modify QY, activation energy of cis-to-trans conversion, absorption band intensities, as well as complexation selectivity.[67]

In our group two different systems [67, 70] based on: lariat ether (Figure 4.42) and 1,2-bis(o-aminophenoxy)ethane-N,N,N',N'-tetraacetic acid (BAPTA)[1] (Figure 4.43) with incorporated photochrome azobenzene unit for Ca^{2+}-ion capture/release under light stimulus were designed

[1] 1,2-bis(o-aminophenoxy)ethane-N,N,N',N'-tetraacetic acid (BAPTA) is well known selective Ca^{2+} chelator widely used in biology.

and studied (Figures 4.42 and 4.43).

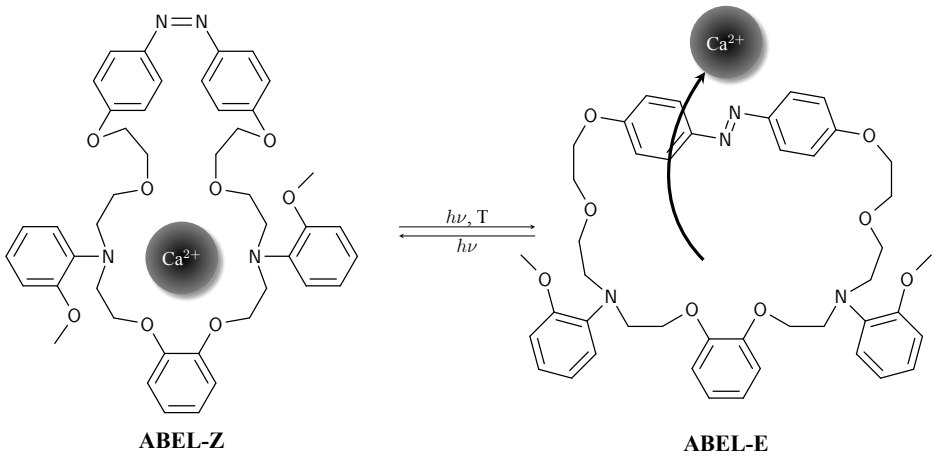

Figure 4.42. Photoswitching of prototype photolariats **ABEL**.

ABEL E-isomers should weakly complex with cations (Figure 4.42), while the Z-isomer is anticipated to be better adapted to complex.

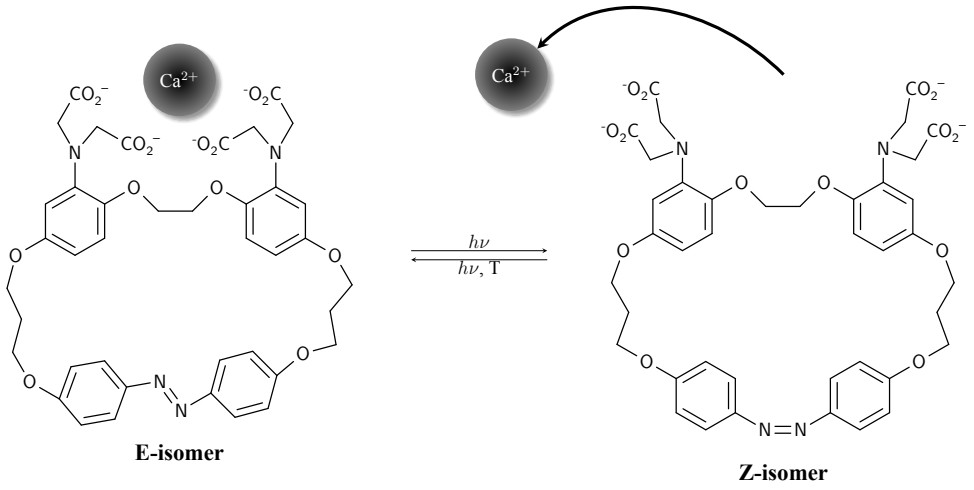

Figure 4.43. Photoswitching of azobenzene-BAPTA.

Azo-BAPTA Z-isomers should weakly complex with cations (Figure 4.43), while the E-isomer is anticipated to be better adapted to complex.

In this work we were primarily interested in the photoisomerization processes of **ABEL** and **azo-BAPTA** in the presence and absence of Ca^{2+} ion[1]. In the presence of Ca^{2+} ion the rates of isomerization may be anticipated to decrease due to host-guest interactions, compared to free **ABEL** and **azo-BAPTA** hosts isomerization rates.

4.3.2 Results of ultrafast time-resolved spectroscopy measurements

Despite the structural simplicity of azobenzene its isomerization process after $\pi - \pi^*$ excitation has quite a complex pathway. The generally accepted relaxation scheme of azobenzene molecules is given in Figure 4.44, based on multiple results of transient absorption experiments and quantum chemical calculations of azobenzene.[192–198] The validity of model was proven experimentally by various groups.[195, 197, 199]

[1] Detailed chemical characterization of studied systems can be found in thesis of Ducrot, Université de Bordeaux I, 2012 [70].

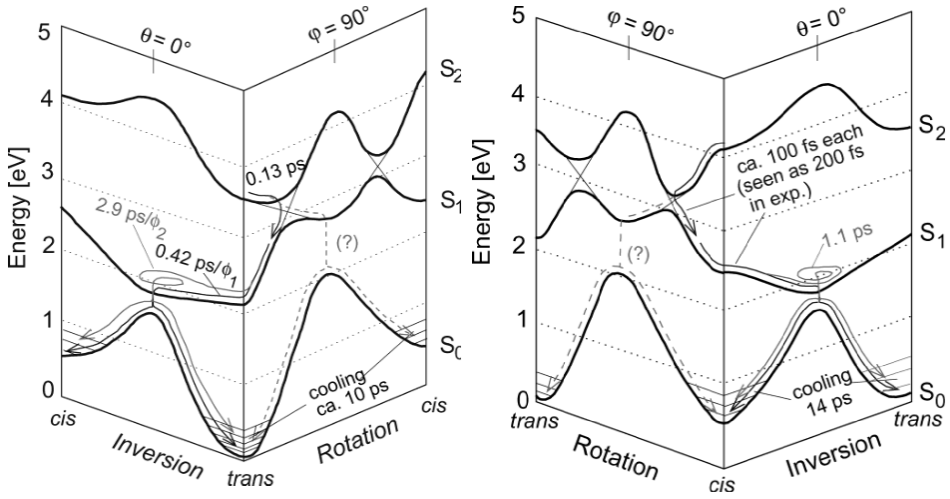

Figure 4.44. Scheme [199] of the Z-E (cis-trans) and E-Z (trans–cis) azobenzene isomerization processes after $\pi - \pi^*$ excitation, based on calculations [200].

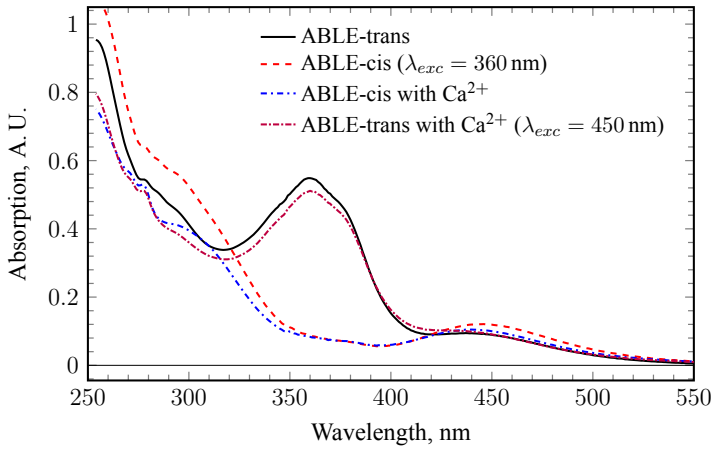

Figure 4.45. Electronic absorption spectra of **ABEL** and its complex with Ca^{2+}-ion.

The trans-cis isomerization process (Figure 4.44) after system $\pi - \pi^*$ excitation, based on [200] calculations, to S_2 state occurs as follows: after excitation the system makes a fast movement along the rotational coordinate toward the S_1 potential energy surface with a time constant of 0.13 ps, which is reached with high excess energy. As can be seen from the slope of the S_1 surface, a further isomerization reaction then proceeds *via* the inversion coordinate to the cis-ground state. Here, a branching takes place, where a larger fraction of the molecules make a direct movement to the conical intersection (0.42 ps, isomerization quantum yield ϕ_1) and fewer molecules follow a diffusive path (2.9 ps, isomerization quantum yield ϕ_2, indicated by the loop). The potential energy landscape shows also the possibility of a branching at the transition point between S_2 and S_1 potential energy surface with a further isomerization along the rotational coordinate.[199]

The cis-trans isomerization process (Figure 4.44) after $\pi - \pi^*$ excitation could be described as follows: the S_2 state is populated and makes a fast movement along the rotational coordinate toward the S_1 potential energy surface, which is reached with high excess energy. The experimental data suggest sequential dynamics $S_2 \leftarrow S_1$ and $S_2 \leftarrow S_0$ with time constants of about 0.1 ps each, not experimentally distinguishable and described with only one time constant of 0.2 ps. On the S_1 potential energy surface, a small part of the molecules take a diffusive pathway toward the trans-ground state (time constant of 1.1 ps, indicated by the loop). The intermolecular cooling process takes place with 14 ps.[199]

The absorption spectra of **ABEL** is presented on Figure 4.45[1]. As the trans-conformation of azobenzene in general is thermodynamically more stable than the cis-conformation, it is anticipated that at equilibrium in the dark the population of **ABEL** will consist of 100 % trans-form. This trans-form is characterised by an absorption band centred at 240 nm, attributed to $\pi - \pi^*$

[1]The absorption spectra of **azo-BAPTA** is similar to **ABEL**, thus its absorption features in UV-vis range is determined by azobenzene absorption bands.

transitions localised on the phenyl groups, a relatively intense band at 360 nm due to symmetry-allowed $\pi-\pi^*$ transitions, which are delocalised through the molecule including the two nitrogen atoms, and a weak band around 450 nm, originating from symmetry forbidden $n-\pi^*$ transitions occurring at the central nitrogen atoms. On irradiation with UV light (360 nm) the azobenzene unit isomerises to the cis-form, where the symmetry-allowed $\pi-\pi^*$ transitions band gets weaker and undergoes a hypsochromic shift. The band ascribed to the forbidden $n-\pi^*$ transition also increases slightly Figure 4.45. The photostationary state consists almost exclusively of the cis-form, as judged from changes in the $350-400$ nm spectral region.

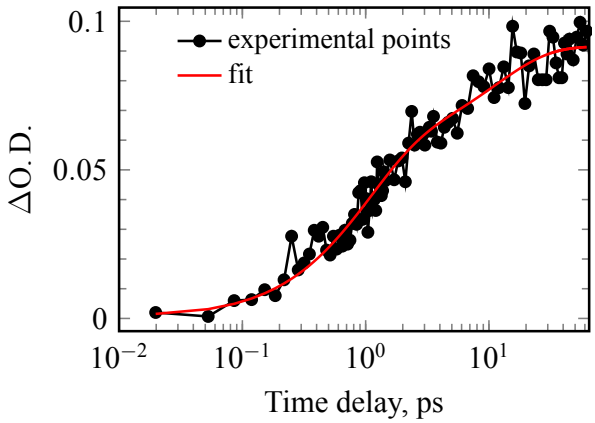

Figure 4.46. TRABS kinetics at 360 nm (Z-E isomerization) of 4,4'-dimethoxyazobenzene in CH_3CN (λ_{exc}=400 nm).

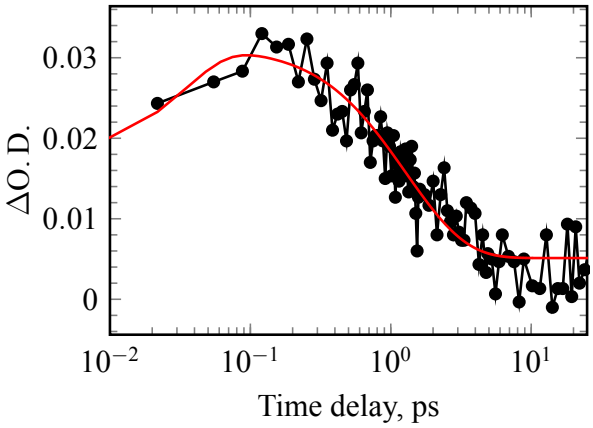

Figure 4.47. TRABS kinetics at 450 nm (E-Z isomerization) of 4,4'-dimethoxyazobenzene in CH_3CN (λ_{exc}=365 nm).

On irradiating the cis-form with visible light (450 nm), the photochemical trans-to-cis form reaction occurs. However, the photostationary state that is attained after a few minutes of irradiation is not completely the trans-form. For **ABEL** the photostationary state is estimated to consist of 80 % of the trans-form. The azobenzene can recover completely to its original cis-form by thermal isomerisation in the dark, showing that no photodegradation had occurred.[67] Addition of Ca^{2+} into solution makes small changes in the initial absorption spectrum. The bands at 450 nm and 300 nm decrease due to the effect of complexation with Ca^{2+}.

4,4'-Dimethoxyazobenzene (Figure 4.41) in CH_3CN was studied using ultrafast TRABS spectroscopy as a model molecule under excitation of 400 nm (Z-E isomerization, Figure 4.46) and 365 nm (E-Z isomerization, Figure 4.47). Z-E isomerization kinetics process in CH_3CN, tracked by the band at 360 nm growth, can be described by three exponent growth lifetimes: 0.8, 2.1, 11.6 ps; the E-Z isomerization process, tracked at 450 nm, is characterized by two exponent decay lifetimes: 0.2 and 2 ps.

Figure 4.48 demonstrates evolution of TRABS signal of **ABEL** with and without Ca^{2+} ions at 370 nm, characterizing the Z-E photoisomerization process, in which Ca^{2+} ion release occurs from the complex **ABEL**-Ca^{2+}. The **ABEL** isomerization process can be described by 3 rising lifetimes 0.15, 1.1, 17.5 ps. Complex **ABEL**-Ca^{2+} does not show any significant difference (0.13, 1.4, 11 ps) in the rate of photoisomerization process. This can be explained by weak binding between host **ABEL** and guest Ca^{2+} ion, what finds its expression in rather low binding constant $\log K = 1.7$ at Z-form and $\log K \simeq 0$ at E-form.

Azo-BAPTA complex with Ca^{2+} (Figure 4.49), which has higher binding constant $\log K \approx 5$ in E-form shows 4-fold slowing down of the photoisomerization rate of azobenzene. For free **azo-BAPTA** the rate of TRABS signal at 460 nm, after exciting E-form of **azo-BAPTA** at 365 nm is expressed by 2 decay lifetimes: 0.2 and 3.5 ps in a H_2O-CH_3OH mixture (*v:v*=1:1), when **azo-BAPTA**-Ca^{2+} complex has these corresponding values: 0.9 and 13.6 ps.

4.3.3 Conclusions

Ultrafast transient absorption measurements of photoisomerization processes of the azobenzene-based (azobenzene-lariat ether, azobenzene-BAPTA) ion release/capture systems were investigated. The rates of the isomerization processes were determined for systems in the presence of Ca^{2+}-ion and without it. It was observed that azobenzene-lariat ether systems did not show any significant difference in the photoisomerization kinetics while binding Ca^{2+} or not. This can be explained by weak binding between host **ABEL** and guest Ca^{2+} ion, what finds its expression in rather low binding constant $\log K = 1.7$ at Z-form and $\log K \simeq 0$ at E-form. Azobenzene-BAPTA complex with Ca^{2+}, which has higher binding constant $\log K \approx 5$ in E-form shows 4-fold retardation of the photoisomerization rate of azobenzene.

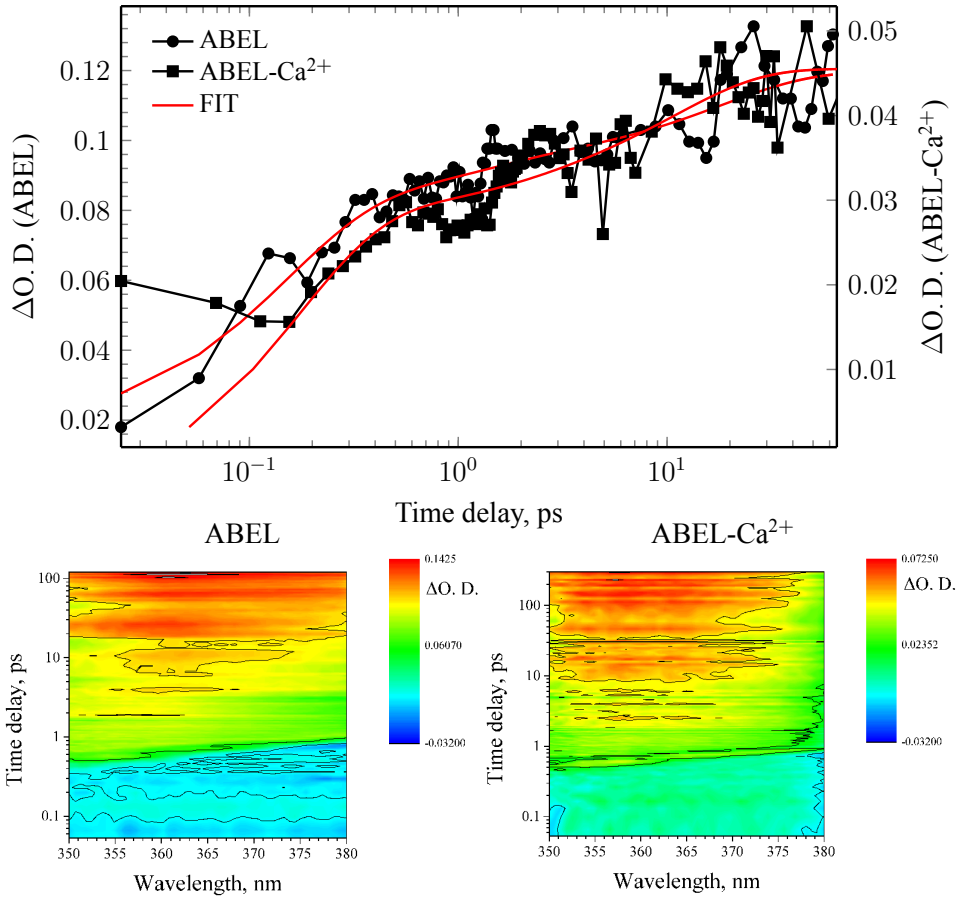

Figure 4.48. TRABS kinetics (Z-E photoreaction) at 370 nm of **ABEL**-lariat ether without (circles) and with (squares) Ca^{2+}-ion in CH_3CN (λ_{exc}=400 nm).

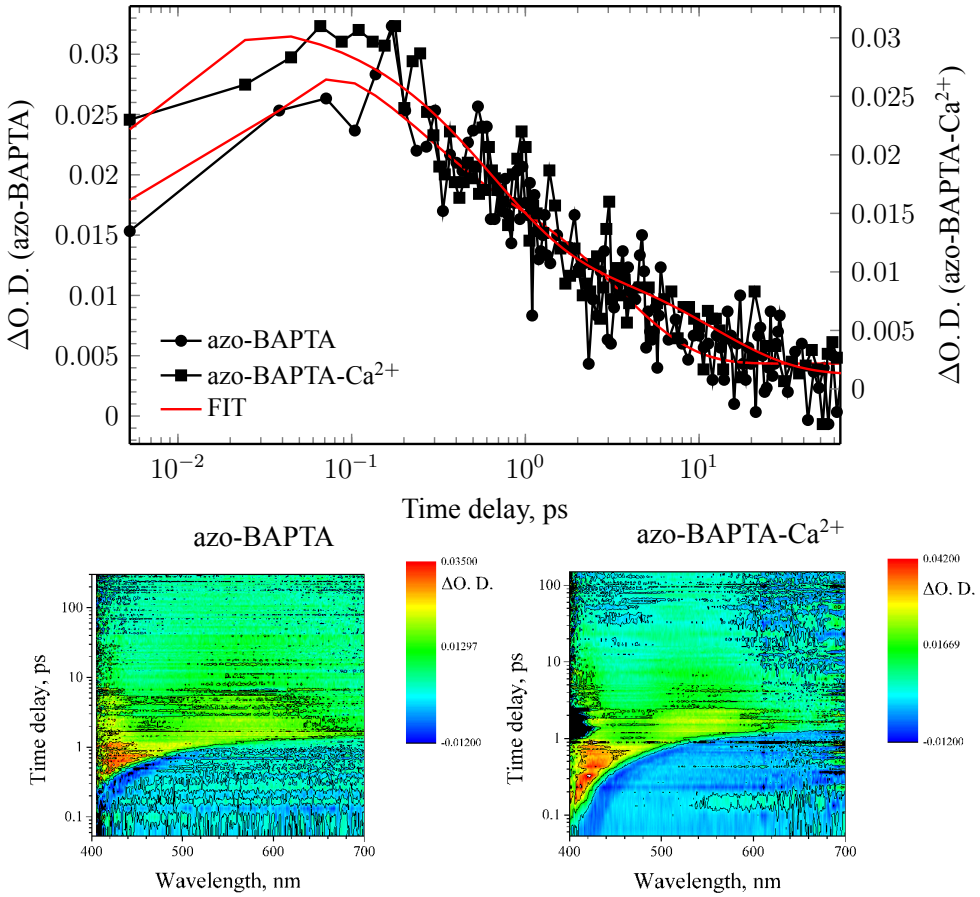

Figure 4.49. TRABS kinetics (E-Z isomerization) at 460 nm of **azo-BAPTA** without Ca^{2+} (circles) and with (squares) in $H_2O - CH_3OH$ mixture (v:v=1:1) (λ_{exc}= 350 nm).

THE JOURNAL OF PHYSICAL CHEMISTRY A

Article

pubs.acs.org/JPCA

Impact of Water on the Cis–Trans Photoisomerization of Hydroxychalcones

Yoann Leydet,*[,†] Pinar Batat,[‡,§] Gediminas Jonusauskas,[§] Sergey Denisov,[‡,§] João Carlos Lima,*[,†] A. Jorge Parola,[†] Nathan D. McClenaghan,[‡] and Fernando Pina[†]

[†]REQUIMTE, Departamento de Química, Faculdade de Ciências e Tecnologia, Universidade Nova de Lisboa, 2829-516 Caparica, Portugal

[‡]Institut des Sciences Moléculaires (ISM), CNRS UMR 5255, and [§]Laboratoire Ondes et Matière d'Aquitaine (LOMA), CNRS UMR 5798, Université de Bordeaux, F-33400 Talence, France

Supporting Information

ABSTRACT: The photochromism of a 2-hydroxychalcone has been studied in CH_3CN and H_2O/CH_3OH (1/1, v/v), as well as in analogous deuterated solvents using steady-state (UV–vis absorption, ^1H and ^{13}C NMR) and time-resolved (ultrafast transient absorption and nanosecond flow flash photolysis) spectroscopies. Whereas the irradiation of *trans*-chalcone (**Ct**) under neutral pH conditions leads to the formation of the same final chromene derivative (**B**) in both media, two distinct photochemical mechanisms are proposed in agreement with thermodynamic and kinetic properties of the chemical reaction network at the ground state. Following light excitation, the first steps are identical in acetonitrile and aqueous solution: the Franck–Condon excited state rapidly populates the *trans*-chalcone singlet excited state ^{1}**Ct*** (LE), which evolves into a twisted state ^{1}**P***. This excited state is directly responsible for the photochemistry in acetonitrile in the nanosecond time scale (16 ns) leading to the formation of *cis*-chalcone (**Cc**) through a simple isomerization process. The resulting *cis*-chalcone evolves into the chromene **B** through a tautomerization process in the ground state (τ = 10 ms). Unlike in acetonitrile, in H_2O/CH_3OH (1/1, v/v), the **P*** state becomes unstable and evolves into a new state attributed to the tautomer ^{1}**Q***. This state directly evolves into **B** in one photochemical step through a consecutive ultrafast tautomerization process followed by electrocyclization. This last case represents a new hypothesis in the photochromism of 2-hydroxychalcone derivatives.

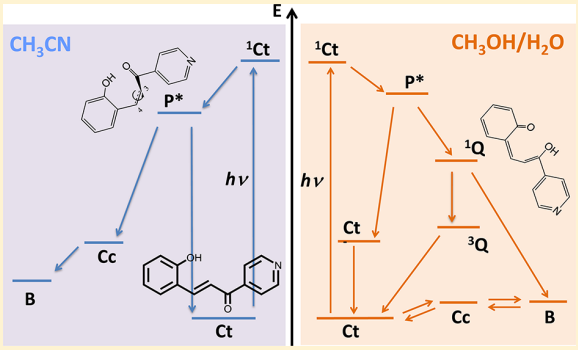

INTRODUCTION

Chalcones constitute an important class of compounds with applications in medical sciences,[1] biotechnology,[2] and photochemistry, because of their photochromism based on a trans–cis isomerization process.[3] Within this family of compounds, the natural 2-hydroxyderivatives are particularly interesting because they can promote the formation of the flavylium cation and the quinoidal base of anthocyanins, a family of pigments responsible for most of the red and blue colors appearing in flowers and fruits.[4] Anthocyanins are involved in a network of chemical reactions including proton transfer, hydration, tautomerization, and cis–trans isomerization.[5] The complexity of this natural network has been reproduced by flavylium salts, synthetic analogues of anthocyanins, leading to efficient and versatile photochromic systems depending on pH and light inputs.[6]

The network of chemical reactions occurring in flavylium compounds is shown in Scheme 1 for 2-phenyl-1-benzopyrylium (structurally, the simplest flavylium). In aqueous solution, at sufficiently acidic pH values (pH < 1), the flavylium cation, AH^+, is the more stable and dominant species. As the pH is increased (pH > 2), the flavylium cation undergoes hydration to give the hemiketal **B** form, which, in turn, can tautomerize to form a *cis*-chalcone (**Cc**). This species can further undergo isomerization to the *trans*-chalcone (**Ct**) form. The system can proceed forward and backward by the action of pH and light and has been used as a "write–lock–read–unlock–erase" molecular switching system[7] and to mimic some elementary properties of neurons.[8] The photoisomerization observed for 2-hydroxychalcone derivatives has been widely studied, revealing a relationship between the quantum yield of isomerization and the chemical structure, viscosity, and polarity of the medium.[6] Despite the apparent simplicity of photochemical processes, the ubiquity of systems displaying such reactions (e.g., olefins, stilbenes, azobenzenes, amides, enols) has led to a large variety of mechanisms accounting for the elementary processes after photoexcitation.[9] Some parallels can be drawn between chalcones[10] and other trans–cis photoisomerization model compounds (such as stilbene)[11] and perhaps even more so with

Received: March 20, 2013
Published: April 23, 2013

Scheme 1. Network of Chemical Reactions in Acidic/Neutral Medium Connecting *trans*-2-Hydroxychalcone (Ct) and 2-Phenyl-1-benzopyrylium (AH^+)

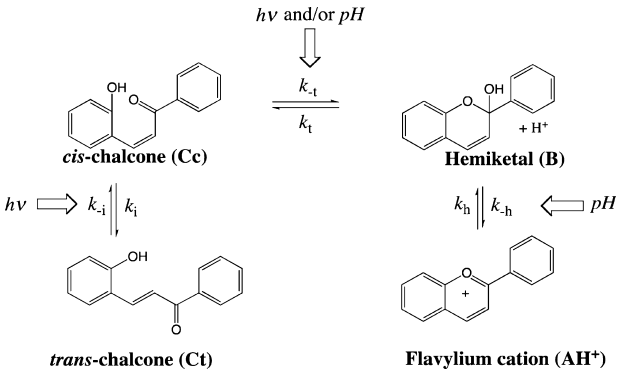

compounds, such as dimethylaminobenzonitrile (DMABN),[12] that contain donor/acceptor substituents across the double bond, which confers charge-transfer character to the first excited state. However, unlike in the aforementioned photochromic families, the photoisomerization reaction represents only one of the several processes taking place in the excited state, and competition between these processes can occur. Other photophysical processes have already been identified, such as the formation of various triplet states, electrocylization, or photoinduced proton transfer especially in aqueous medium.[13] To the best of our knowledge, a comprehensive study including the effect of the solvent on the deactivation pathways of the first excited state and the identification of the first intermediate species after excitation leading to photoisomerization and other competing channels has never been published.

We recently demonstrated that the formation of a flavylium salt can be excluded or limited to extremely acidic conditions when an electron-withdrawing substituent is inserted in the structure of the 2-hydroxychalcone skeleton.[14,15] In this study, the absence of a flavylium cation facilitates not only the attribution of the processes involved in the photophysics of 2-hydroxychalcones but also the determination of the photoproduct of the reaction. We report a detailed study on the photophysics and photochemistry of a 2-hydroxypyridinechalcone (compound **1**, Scheme 2). The aim of this work was to

Scheme 2. Structure and Numbering of Compound 1[a]

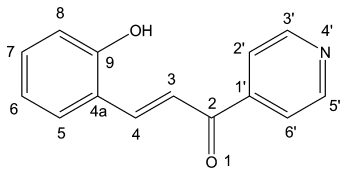

[a]Notation of the flavylium cation instead of the chalcone ions was used to simplify the discussion.

characterize the photochromism of 2-hydroxychalcones, from the formation of the excited state responsible for the isomerization process to the identification of the photoproduct. The solvent dependence of the photochemistry was studied first in an organic solvent (CH_3CN) and then in an aqueous solution under neutral conditions (H_2O/CH_3OH, 1/1, v/v), as well as in the analogous deuterated mixture (D_2O/CD_3OD, 1/1, v/v).

EXPERIMENTAL SECTION

Instrumentation and Measurements. Compound **1** was available from previous studies.[14] Solutions were prepared using Millipore water and spectroscopic-grade methanol and acetonitrile. Electronic absorption spectra were recorded on a Varian-Cary 100 Bio or Shimadzu VC2501-PC spectrophotometer. Photochemical transformations were carried out using a medium-pressure xenon/mercury arc lamp, and the excitation bands (254 and 365 nm) were isolated with interference filters (Oriel). The incident light intensity was measured by ferrioxalate actinometry.[16] NMR spectra at 298.0 K were obtained on a Bruker AMX400 spectrometer operating at 400.13 MHz (^1H) and 100 MHz (^{13}C). Nanosecond laser flash photolysis experiments were run on an LKS.60 laser photolysis spectrometer from Applied Photophysics, using an Applied Photophysics SX20 stopped-flow spectrometer to guarantee that all of the transient signals were reproducibly obtained with fresh solution and to avoid accumulation of photoproducts competing for light excitation.

Picosecond transient absorption spectra were recorded on a setup that was built as follows: A frequency-tripled Nd:YAG amplified laser system (30 ps, 30 mJ at 1064 nm, 20 Hz, Ekspla model PL 2143) output was used to pump an optical parametric generator (Ekspla model PG 401), producing tunable excitation pulses in the range of 410−2300 nm. The residual fundamental laser radiation was focused in a high-pressure Xe-filled breakdown cell where a white-light pulse for sample probing was produced. All light signals were analyzed by a spectrograph (Princeton Instruments Acton model SP2300) coupled with a high-dynamic-range streak camera (Hamamatsu C7700). Accumulated sequences (sample emission, probe without and with excitation) of pulses were recorded and treated with HPDTA (Hamamatsu) software to produce two-dimensional maps (wavelength versus delay) of transient absorption intensity in the range of 300−800 nm. Typical measurement error was better than 10^{-3} of the optical density (OD). Samples were equally studied on the subpicosecond time scale: This experiment was based on a femtosecond 1 kHz Ti:sapphire system producing 30 fs, 0.8 mJ, laser pulses centered at 800 nm (Femtopower Compact Pro) coupled with an optical parametric generator (Light Conversion Topas C) and frequency mixers to excite samples at the maximum of the steady-state absorption band. White-light continuum (360−1000 nm) pulses generated in a 2 mm D_2O cell were used as a probe. A variable delay time between excitation and probe pulses was obtained using a delay line with 0.66 fs resolution. The solutions were placed in a 1 mm circulating cell. White-light signal and reference spectra were recorded using a two-channel fiber spectrometer (Avantes Avaspec-2048-2). A self-written acquisition and experiment control program in LabVIEW enabled the recording of transient spectra with an average error of less than 10^{-3} of the optical density for all wavelengths. The temporal resolution of the setup was better than 50 fs. A temporal chirp of the probe pulse was corrected by a computer program with respect to a Lawrencian fit of a Kerr signal generated in a 0.2 mm glass plate used in place of a sample.

dx.doi.org/10.1021/jp402761j | J. Phys. Chem. A 2013, 117, 4167−4173

RESULTS AND DISCUSSION

Study in Acetonitrile. Irradiation of an equilibrated solution of compound **1** in acetonitrile at 365 nm was followed by UV–vis absorption spectroscopy (Figure 1A). The spectrum of the initial solution (thermally equilibrated) is dominated by a broad band at 350 nm assigned to the absorption of the **Ct** form. This band decreases upon irradiation until a photostationary state is reached, displaying two absorption bands with maxima at 254 and 300 nm. The spectral variations are consistent with the disappearance of **Ct** and concomitant formation of a photoproduct with a global quantum yield of 0.1. The well-defined isosbestic points (246 and 270 nm) support the conclusion that **Ct** is being converted into a single photoproduct.

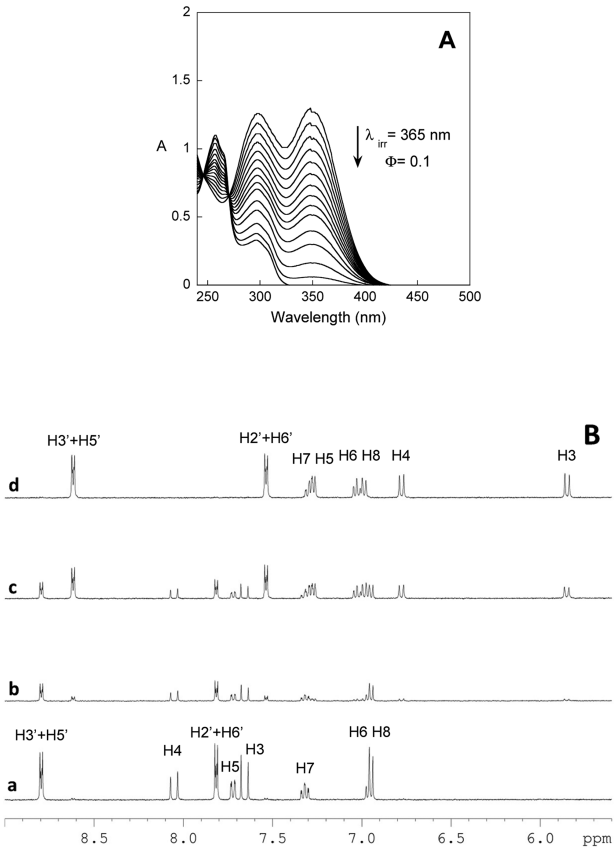

Figure 1. (A) Spectral variations upon continuous irradiation of compound **1** ($C_0 = 1.1 \times 10^{-4}$ M) in acetonitrile at 365 nm ($\Phi = 0.1$). (B) ^{1}H NMR spectra (400 MHz, 300 K) of **1** in CD_3CN (a) at thermal equilibrium (>95% **Ct**, <5% **B**), (b,c) upon irradiation at 365 nm, and (d) after reaching the photostationary state upon irradiation at 365 nm (100% **B**). Proton assignments for **Ct** and **B** given in traces a and d, respectively (according to the numbering of **Ct** in Scheme 2 and assuming the same numbering for **B**).

^{1}H NMR spectra, obtained before, during, and after reaching the photostationary state (traces a–d in Figure 1B), show that the initially (thermally equilibrated) solution comprises two different species, one of which is predominant (>95%). The predominant species displays a large coupling constant between protons H3 (δ = 7.65 ppm) and H4 (δ = 8.04 ppm) [^3J(H3, H4) = 16.0 Hz], typical of the *trans*-chalcone isomer, whereas the minor species (<5%) is characterized by a smaller coupling constant [^3J(H3, H4) = 9.8 Hz] (spectrum a). The initial **Ct** is converted progressively into the minority species, which is also present in the initial solution (spectra b–d). Formation of additional species was not observed during irradiation or at the photostationary state. The nature of the photoproduct was unambiguously confirmed by NMR spectroscopy (HMBC experiments), where the C2 carbon presents a chemical shift in agreement with that of an sp^3 carbon (δ = 97.4 ppm, Figure S1, Supporting Information), which is only present in the hemiketal species, **B**. In contrast to aqueous solutions, for which complete recovery of **Ct** is observed when solutions are allowed to equilibrate in the dark, species **B** is stable in acetonitrile, and only traces of **Ct** can be found even after 3 days. Nevertheless, the photochemistry of **1** in CH_3CN allows it to be described as a photochromic system because the recovery of **Ct** can be achieved upon irradiation of **B** at 254 nm (data not shown).

Ultrafast transient absorption spectroscopy was employed to follow the evolution of the excited *trans*-chalcone. The overall spectral evolution between 400 and 750 nm in CH_3CN following 355 nm excitation is divided into two sequential steps (Figure 2).

Following excitation of **1**, two distinct signals can be observed on a picosecond time scale (Figure 2, left). An initial positive absorption signal, assigned to a locally excited state

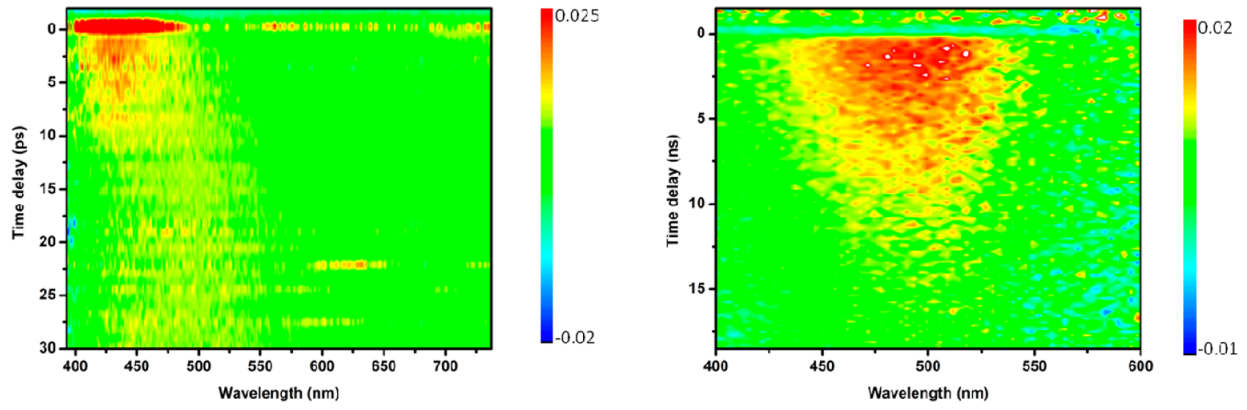

Figure 2. Ultrafast dynamics of **1** in CH_3CN. Transient absorption spectra with time delays of 0–30 ps (left) and 0–20 ns (right). Transient absorption bands were observed between 425 and 550 nm and decayed with a lifetime of 16 ns. Colors correspond to ΔOD values according to the included scales.

dx.doi.org/10.1021/jp402761j | J. Phys. Chem. A 2013, 117, 4167–4173

The Journal of Physical Chemistry A Article

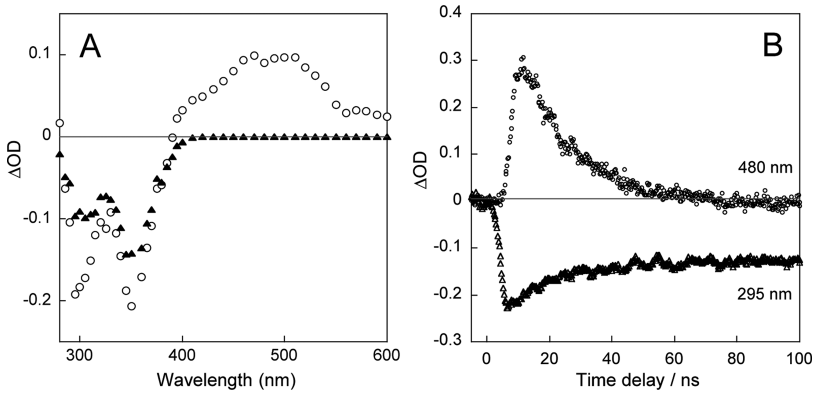

Figure 3. (A) Transient absorption spectra of **1** in CH_3CN obtained by flash photolysis in air-equilibrated solution (○) immediately and (▲) 100 ns after the pulse. (B) Kinetic traces at (○) 480 and (Δ) 295 nm.

(LE) absorbing at 420 nm, appears immediately after the pulse and subsequently relaxes to a second state (**R**), which presents a broad red-shifted band extending between 400 and 550 nm. The LE-state decay time is identical to the formation time of the relaxed state **R** (τ_1 = 2 ps). The spectrum of **R** does not shift further, and the relaxed state decays on the nanosecond time scale (τ_2 = 16 ns) (see Figure 2, right), at the same rate over the whole spectral region, indicating the presence of a single transient species. The absorption of **R** cannot be attributed to any molecule of the network in the ground state (**Cc**, **B**) because such species do not absorb at these wavelengths. Nanosecond flash photolysis (λ_{exc} = 355 nm) was employed to further follow the decay of the relaxed state **R** and characterize its relation with the ground-state photoproduct formation. The time-resolved absorption spectra immediately after the flash and after complete disappearance of **R** (100 ns) are represented between 280 and 600 nm in Figure 3.

Whereas the spectrum recorded immediately after the nanosecond laser pulse is composed of the sum of **Ct** bleaching (negative ΔOD) and transient absorption of **R** (positive ΔOD), the spectrum after 100 ns presents only a negative signal that is stable on the microsecond time scale. The recovery of **Ct** is not complete, in agreement with the photoconversion of *trans*-chalcone into photoproducts. Also, the final spectrum is different from that of pure **Ct**, confirming the presence of a photoproduct absorbing in the same region. The quantum yield for photoproduct formation can be crudely estimated to be 0.5, based on the intensity of the persistent negative signal with respect to the initial intensity, immediately after excitation (see Figure 3b); however, the presence of a photoproduct absorbing in the same region can introduce a significant error in this value.

The pure **R** absorption can be obtained by subtracting the contribution of **Ct** to the initial spectrum (Figure S2, Supporting Information), and the photoproduct can be obtained on subtracting the contribution of **Ct** to the final spectrum (Figure S3, Supporting Information). It can be seen that the spectrum obtained for the photoproduct in this time window corresponds to a photoproduct different from **B** (see Figure S3, Supporting Information), the final product of the irradiation identified by ^{1}H NMR spectroscopy. The photoproduct absorption in this time window resembles the features of the absorption spectrum of the **Cc** isomer (Figure S3, Supporting Information); unfortunately, it is not possible to obtain the spectrum of short-lived **Cc** in acetonitrile, and the comparison must be made with the spectrum of **Cc** in water.[14] For the stated reasons, the photoproduct is attributed to the formation of **Cc** through deactivation of **R** together with **Ct**. On this basis, the most reliable alternative is the attribution of the transient absorption **R** to a twisted excited state **P*** corresponding to a rotation of 90° around the isomerizing double bond, which, in 16 ns, yields both **Cc** and **Ct** with equal relaxation rates, as deduced from the bleaching intensities immediately and 100 ns after excitation (Figure 3b).

This interpretation is complemented by a kinetic analysis performed on the millisecond time scale at 330 nm, showing that the resulting *cis*-chalcone evolves to the chromene **B** through a fast tautomerization process (τ = 10 ms), in agreement with similar kinetics recorded previously[17] for this type of system (Figure S4, Supporting Information).

The thermal stability of the final photoproduct, **B**, in acetonitrile accounts for the absence of **Cc** in the final solution; that is, the **Cc** isomer initially formed from **P*** is completely converted to **B**. The **Cc** species could not be obtained, either thermally or upon irradiation.

Pertinent photophysical events, with kinetic parameters, leading to the formation of **B** are summarized in Scheme 3. Following light excitation, the Franck−Condon excited state rapidly populates the *trans*-chalcone singlet excited state ^{1}**Ct*** (LE), which evolves into the twisted state ^{1}**P***(τ = 2 ps). This

Scheme 3. Jablonski Diagram Showing the Species at Both the Excited and Ground States Intervening in the Photochemistry of Compound 1 (Ct) in CH_3CN Solution

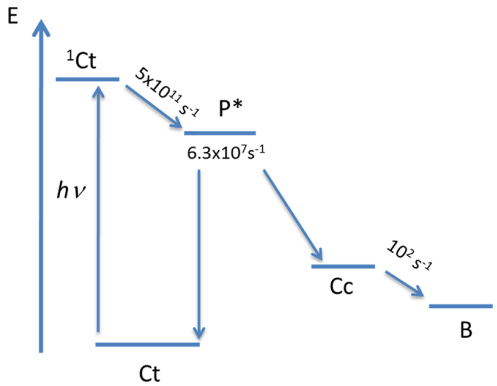

dx.doi.org/10.1021/jp402761j | J. Phys. Chem. A 2013, 117, 4167−4173

The Journal of Physical Chemistry A Article

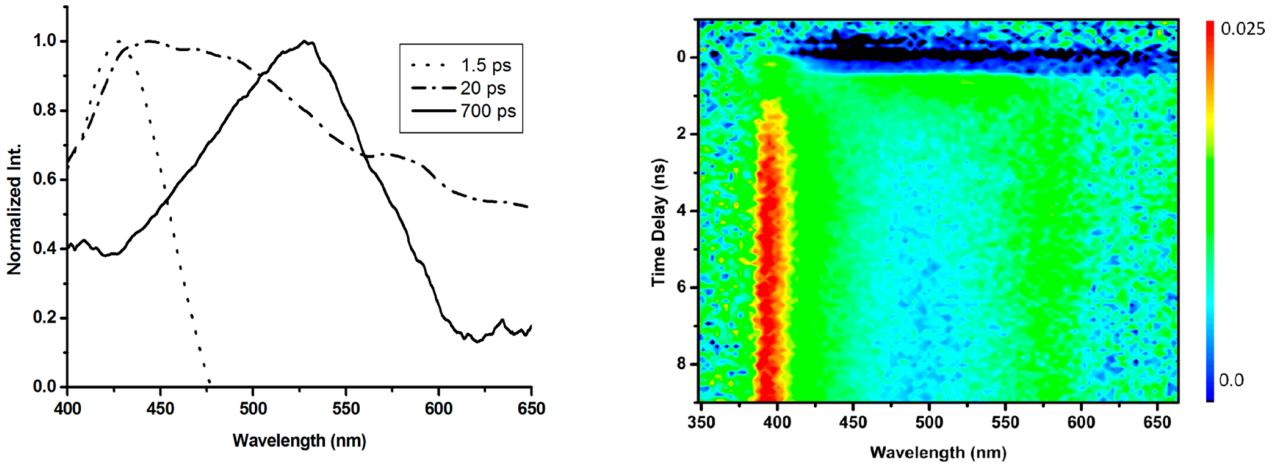

Figure 4. Ultrafast dynamics of **1** in H_2O/CH_3OH at neutral pH. Transient absorption spectra (left) on the picoseond time scale after 1.5, 40, and 700 ps and (right) on the longer nanosecond time scale after 0–9 ns. Colors correspond to ΔOD values according to the included scale.

excited state is responsible for the formation of both **Ct** and **Cc** in the ground state.

The final product observed in the NMR experiment was formed through a tautomerization process in the ground state (τ = 10 ms) with a quantum yield of 0.1 (Figure 1 and Figure S4, Supporting Information).

Photochemistry in H_2O/CH_3OH (1/1, v/v). The photochemistry of **1** in the aqueous medium H_2O/CH_3OH (1/1, v/v) was previously studied.[14] Irradiation of non-equilibrated solutions (100% **Ct**) also leads to the exclusive formation of **B**. The results from pump–probe experiments of **1** in H_2O/CH_3OH (1/1, v/v) solution are presented in Figure 4 for two different temporal scales: picosecond and nanosecond.

An initial positive absorption at 420 nm appeared immediately after the excitation pulse and subsequently relaxed to a second red-shifted broad band in the visible region with a maximum at 480 nm. The initial spectral evolution is similar to that observed in previous experiments in CH_3CN and can be assigned to the formation of the twisted ^{1}**P*** state from ^{1}**Ct*** (LE state) with a lower kinetic rate constant (τ = 5 ps) (Figure S5, Supporting Information). The initial spectra of ^{1}**P*** in the two media are identical. This signature is constant over time in acetonitrile solution, until the disappearance of the twisted excited state after 16 ns.

However, in aqueous solution, the maximum of the broad band further shifts from 480 to 520 nm (Figure 4, left). Unfortunately, the rate of disappearance of the **P*** state could not be obtained because the signal was too weak in the ultrafast experiment, but on the other hand, no shift was observed in the longer-time-scale experiment, meaning that this process is probably faster than 50 ps. The aforementioned stabilization of the $S_n \leftarrow S_1$ transition of the twisted ^{1}**P*** state from 480 to 520 nm (ca. 1600 cm^{-1}), could correspond to water-mediated tautomerization (enolization). We refer to the state absorbing at 520 nm as the **Q*** state.

To confirm the involvement of proton transfer in the formation of the **Q*** state, pump–probe experiments of **1** in D_2O/CD_3OD (1/1, v/v) solution were performed (Figure S6, Supporting Information). In D_2O/CD_3OD, the **P*** state evolves into the **Q*** state after ca. 100 ps, and even though the signal is still too weak in the ultrafast experiment, the spectral evolution can be clearly seen on the longer time scales (see Figure S6, Supporting Information). The decrease in the **Q*** formation rate in the deuterated solvent mixture is a clear indication that proton migration is involved in the **P*** → **Q*** conversion, supporting the hypothesis of water-mediated tautomerization. The **Q*** state, which has a short lifetime (900 ps in H_2O/CH_3OH, 3 ns in D_2O/CD_3OD) evolves into a transient absorption extending over the whole visible region with two different maxima at 395 and 580 nm that does not decay in this time window (Figure 4, right). The kinetic traces collected at 580 nm showed a single-exponential formation with a rate identical to the decay rate of the **Q*** state.

To clarify the subsequent process(es), flash photolysis experiments were performed between 280 and 700 nm (Figure 5).

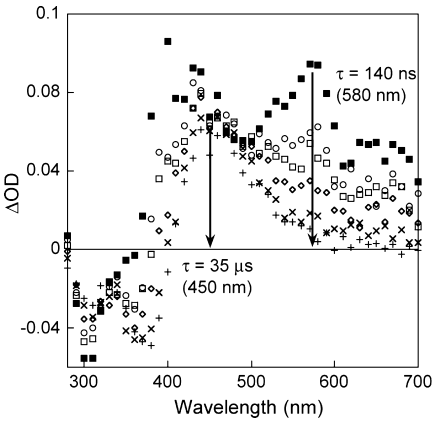

Figure 5. Transient absorption spectra of compound **1** in H_2O/CH_3OH (1/1, v/v) at neutral pH on the nano- to microsecond time scale from 15 ns to 0.9 μs. The evolution of the remaining signal is not shown (τ = 35 μs). (■) 15, (○) 100, (□) 200, (◊) 300, (×) 600, and (+) 900 ns.

The evolution on the nano-/microsecond time scale allowed identification of two different contributions in addition to the negative signal clearly identified as the photobleaching of **Ct**. The previously observed transient at 580 and 395 nm decays according to a single-exponential process with a rate equal to 7.3 × 10^6 s^{-1} (τ = 140 ns), which could be affected by molecular oxygen as expected for a triplet state. After the triplet

dx.doi.org/10.1021/jp402761j | J. Phys. Chem. A 2013, 117, 4167–4173

decayed, the remaining spectrum could be fitted by superimposing the spectra of **Ct** and **Ct**$^-$ (Figure S7, Supporting Information, and Figure 5). **Ct**$^-$ (transient absorbing at 450 nm) further decays as a single exponential with a rate of 2.9×10^4 s^{-1} (τ = 35 μs). The assignment to **Ct**$^-$ is further corroborated by an observed dependence of the decay rate on the pH (and independence of the presence of oxygen). Whereas it is clear that part of the **Ct** recovery is linked to the triplet decay, it is not straightforward, because of the spectral overlap, to elucidate whether **Ct**$^-$ is formed initially from the deprotonation of **Q*** or later from the deprotonation of the triplet state. However, the isotope effect observed in the rate of disappearance of **Q*** (900 ps in H_2O/CH_3OH, 3 ns in D_2O/CD_3OD) is compatible with a deprotonation reaction and, as a consequence, with the formation of **Ct**$^-$ from **Q***. Inspection of Figure 5 shows that the transient corresponding to **Ct**$^-$ does not change during this time scale, which is also compatible with its formation from the deprotonation of the **Q*** state. In fact, the subtraction of **Ct** and **Ct**$^-$ contributions at 2 μs from the transient spectra obtained at successive times (Figure S8, Supporting Information) yields the disappearance of the same spectrum that we assigned to the pure triplet state.

Nevertheless, the final photoproduct (**Cc** or **B**) is produced in a very small amount, either from **Q*** or from the triplet. Also, the photochemical quantum yield in methanol/water (0.02) is much lower than that in acetonitrile (0.1), and this probably implies that formation of **Ct**$^-$ and the triplet compete with the photoproduct formation pathway. From the flash photolysis data, after the disappearance of **Ct**$^-$, only the presence of **Ct** can be observed. To identify the nature of the photoproducts, photoirradiations (at 365 nm with a continuous source) were carried out in equilibrated solutions of **1** in H_2O/CH_3OH (1/1, v/v) whose composition is a mixture of **Ct**, **Cc**, and **B** in a ratio 8:1:1, as followed by ^{1}H NMR spectroscopy (Figure 6).

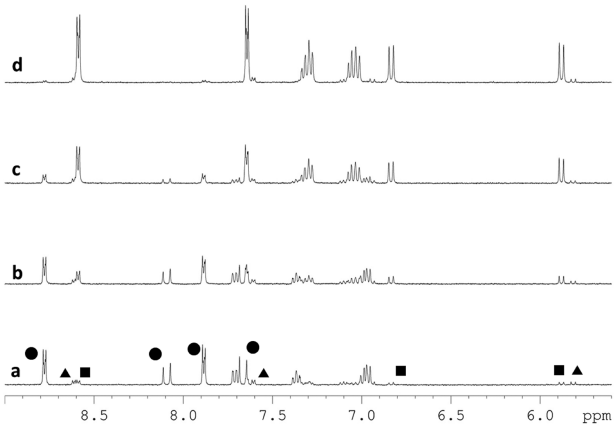

Figure 6. ^{1}H NMR spectra (400 MHz, 298 K) of **1** in D_2O/CD_3OD (1:1, v/v) (a) at thermal equilibrium [(●) 80% **Ct**, (▲) 10% **Cc**, (■) 10% **B**], (b,c) during the course of the irradiation at 365 nm, and (d) after reaching the photostationary state upon irradiation at 365 nm (90% **B**, 10% **Cc**).

^{1}H NMR spectra were run before, during, and after reaching the photostationary state (Figure 6). The initial solution composed of 80% **Ct**, 10% **Cc**, and 10% **B** is converted into a solution composed by 90% **B** and 10% **Cc**. The molar fraction of **Cc** remains stable during the irradiation. The disappearance of **Ct** and concomitant formation of **B** has a global quantum yield of 0.02, which why it was not observed during flash photolysis.

If the photoproduct of the irradiation of **Ct** were **Cc**, which, in a later step, would equilibrate with **B**, then the ratio between **B** and **Cc** would be constant. The ^{1}H NMR data clearly show that the photoproduct of the irradiation of **Ct** is **B** and that the equilibrium between **B** and **Cc** is not attained during the time scale of the experiment.[14] In other words, **Q*** yields **B** (in competition with triplet and **Ct**$^-$ formation) whereas **P*** yields **Cc** plus **Ct**. The formation of **B** in methanol/water solutions (and not **Cc**, as in acetonitrile) must be related with the nature of the new intermediary state **Q***, which is present only in this solvent.

The formation of hydrogen bonds with water can facilitate the proton transfer between the two oxygen atoms, and the most straightforward assignment of **Q*** is the quinoidal tautomer derived from proton transfer (Scheme 4).

Scheme 4. Representation of the Two Distinct Solvent-Dependent Mechanisms for 1[a]

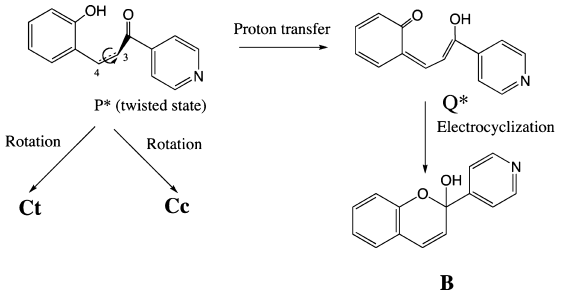

[a]In CH_3CN, the excited state **P*** directly induces the formation of **Ct** or **Cc**, whereas in H_2O/CH_3OH, **B** is promoted from the **Q*** state formed after a solvent-assisted proton transfer.

Whereas **P*** can yield **Ct** or **Cc** through rotation around the C3−C4 bond, after the proton transfer, the most efficient reaction pathway for the quinone is electrocyclization to form **B**. The assignment of **Q*** as a quinone is also in agreement with very efficient formation of the triplet, which was not previously observed in acetonitrile, where **P*** was the only state observed.

A summary of the photophysical events with kinetic parameters leading to the formation of **B** in methanol/water is shown in Scheme 5. Following light excitation, the first steps are identical in acetonitrile and in water: The Franck−Condon excited state rapidly populates the *trans*-chalcone singlet excited state ^{1}**Ct** (LE), which evolves into the twisted state **P*** (τ = 5 ps). In D_2O/CD_3OD, this value reaches 5.4 ps. The state **P*** evolves into **Ct**$^-$ and into the transient **Q***, which leads to **B** and triplets.

CONCLUSIONS

The photochromism of a 2-hydroxychalcone has been studied in CH_3CN and in H_2O/CH_3OH (1/1, v/v) by steady-state (UV−vis absorption, ^{1}H and ^{13}C NMR) and time-resolved (ultrafast transient absorption and nanosecond flow flash photolysis) spectroscopies.

In the two types of media, the first step after excitation is the same and consists of the relaxation of the LE state to a twisted ^{1}**P*** state in a few picoseconds. In acetonitrile, this state deactivates to form **Cc** and **Ct** in identical proportions, the classic situation of double-bond photoisomerization. The final

dx.doi.org/10.1021/jp402761j | J. Phys. Chem. A 2013, 117, 4167−4173

Scheme 5. Jablonski Diagram Showing the Species at Both the Excited and Ground States Intervening in the Photochemistry of Compound 1 (Ct) in H_2O/CH_3OH (1/1, v/v) Solution

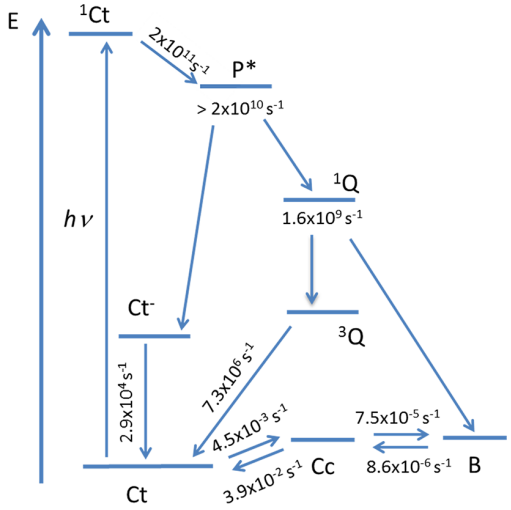

product, **B**, results from tautomerizaton of **Cc** with an observed quantum yield of 0.1

The presence of water, on the other hand, dramatically affects the photochemical pathway by promoting the formation of a tautomeric intermediate, between the ^{1}**P*** state and the photoproducts. The main photochemical pathway from this tautomer is electrocyclization to form chromene **B**, whereas all of the other pathways lead to **Ct** (through **Ct**$^-$ and ^{3}**Q***); that is, no *cis*-isomer is formed photochemically. However, the weight of the pathways leading back to **Ct** is much larger than that of the pathways yielding **B** (ϕ = 0.02).

■ ASSOCIATED CONTENT

Ⓢ Supporting Information

Additional information as noted in text. This material is available free of charge via the Internet at http://pubs.acs.org.

■ AUTHOR INFORMATION

Corresponding Author

*E-mail: yoann.leydet@gmail.com (Y.L.), lima@fct.unl.pt (J.C.L.).

Notes

The authors declare no competing financial interest.

■ ACKNOWLEDGMENTS

This work was supported by the Fundação para a Ciência e Tecnologia, National NMR Network, through Projects PTDC/QUI-QUI/117996/2010 and SFRH/BPD/44230/2008 (Y.L.); the University of Bordeaux, Région Aquitaine; and the PHC Pessoa Franco-Portuguese Programme.

■ REFERENCES

(1) Dimmock, J. R.; Elias, D. W.; Beazely, M. A.; Kandepu, N. M. *Curr. Med. Chem.* **1999**, *6*, 1125−1149.

(2) Ono, M.; Watanabe, R.; Kawashima, H.; Yan, C.; Kimura, H.; Watanabe, H.; Haratake, M.; Saji, H.; Nakayama, M. *J. Med. Chem.* **2009**, *52*, 6394−6401.

(3) Bouas-Laurent, H.; Dürr, H. *Pure Appl. Chem.* **2001**, *73*, 639−665.

(4) (a) Swain, T. In *The Flavonoids*; Harborne, J. B., Mabry, T. J., Mabry, H., Eds.; Chapman and Hall/CRC Press: London, 1975; pp 1096−1129. (b) *Anthocyanins As Food Colors*; Markakis, P., Ed.; Academic Press: New York, 1982. (c) Brouillard, R. O.; Dangles, O. In *The Flavonoids: Advances in Research Since 1986*; Harborne, J. B., Ed.; Chapman and Hall/CRC Press: New York, 1994; pp 565−588.

(5) (a) Yoshida, K.; Mori, M.; Kondo, T. *Nat. Prod. Rep.* **2009**, *26*, 884−915. (b) Goto, T.; Kondo, T. *Angew. Chem., Int. Ed. Engl.* **1991**, *30*, 17−33. (c) Yoshida, K.; Kondo, T.; Okazaki, Y.; Katou, K. *Nature* **1995**, *373*, 291. (d) Kondo, T.; Yoshida, K.; Nakagawa, K. A.; Kawai, T.; Tamura, H.; Goto, T. *Nature* **1992**, *358*, 515−518. (e) Brouillard, R.; Delaporte, B. *J. Am. Chem. Soc.* **1977**, *99*, 8461−8468. (f) Brouillard, R.; Delaporte, B.; Dubois, J.-E *J. Am. Chem. Soc.* **1978**, *100*, 6202−6205. (g) Brouillard, R.; Lang, J. *Can. J. Chem.* **1990**, *68*, 755−761. (h) McClelland, R. A.; Gedge, S. *J. Am. Chem. Soc.* **1980**, *102*, 5838−5848. (i) McClelland, R. A.; McGall, G. H. *J. Org. Chem.* **1982**, *47*, 3730−3736.

(6) Pina, F.; Melo, M. J.; Laia, C. A. T.; Parola, A. J.; Lima, J. C *Chem. Soc. Rev.* **2012**, *41*, 869−908.

(7) Pina, F.; Melo, M. J.; Maestri, M.; Ballardini, R.; Balzani, V. *J. Am. Chem. Soc.* **1997**, *119*, 5556−5561.

(8) Pina, F.; Melo, M. J.; Maestri, M.; Passaniti, P.; Balzani, V. *J. Am. Chem. Soc.* **2000**, *122*, 4496−4498.

(9) Fedorova, O. A.; Gulakova, E. N.; Fedorov, Y. V.; Lobazova, I. E.; Alfimov, M. V.; Jonusauskas, G. *J. Photochem. Photobiol. A* **2008**, *196*, 239−243.

(10) (a) Jiang, Y.-B.; Wang, X.-J.; Lin, L. *J. Phys. Chem.* **1994**, *98*, 12367−12372. (b) Rurack, K.; Dekhtyar, M. L.; Bricks, J. L.; Resch-Genger, U.; Rettig, W. *J. Phys. Chem. A* **1999**, *103*, 9626−9635. (c) Rurack, K.; Bricks, J. L.; Reck, G.; Radeglia, R.; Resch-Genger, U. *J. Phys. Chem. A* **2000**, *104*, 3087−3109. (d) Fayed, T. A.; Awad, M. K. *Chem. Phys.* **2004**, *303*, 317−326.

(11) Waldeck, D. H. *Chem. Rev.* **1991**, *91*, 415−436.

(12) Grabowski, Z. R.; Rotkiewicz, K.; Rettig, W. *Chem. Rev.* **2003**, *103*, 3899−4032.

(13) (a) Diniz, M.; Gomes, R.; Parola, A. J.; Laia, C. A. T.; Pina, F. *J. Phys. Chem. B* **2009**, *113*, 719−727. (b) Jiang, Y.-B.; Wang, X.-J.; Lin, L. *J. Phys. Chem.* **1994**, *98*, 12367−12372. (c) Rurack, K.; Dekhtyar, M. L.; Bricks, J. L.; Resch-Genger, U.; Rettig, W. *J. Phys. Chem. A* **1999**, *103*, 9626−9635. (d) Rurack, K.; Bricks, J. L.; Reck, G.; Radeglia, R.; Resch-Genger, U. *J. Phys. Chem. A* **2000**, *104*, 3087−3109. (e) Fayed, T. A.; Awad, M. K. *Chem. Phys.* **2004**, *303*, 317−326.

(14) Leydet, Y.; Parola, A. J.; Pina, F. *Chem.—Eur. J.* **2010**, *16*, 545−555.

(15) Leydet, Y.; Gavara, R.; Cunha-Silva, L.; Parola, A. J.; Pina, F. *Chem.—Eur. J.* **2011**, *17*, 3663−3671.

(16) Hatchard, C. G.; Parker, C. A *Proc. R. Soc. London, Ser. A* **1956**, *235*, 518−536.

(17) Pina, F.; Maestri, M.; Balzani, V. In *Handbook of Photochemistry and Photobiology*; Nalwa, H. S., Ed.; American Science Publishers: Los Angeles, CA, 2003; Vol. 3, pp 411− 449.

4.5 Chapter Summary

The study of NIR fluorescent *OFF-ON* probes, based on aza-BODIPY dyes, covalently attached to the surface of NP (poly(styrene-co-methacrylic acid)) with characteristic size of $d = 100$ nm was conducted in water solutions. Equally, the model system with pyrene-like units, covalently attached to the surface of same NP was investigated. It was shown that studied systems demonstrate pronounced responses (fluorescence turning *on*) to the presence of surfactant (de-aggregating) agents, such as Triton X-100 and DOPC micelles. Due to the outstanding photostability properties [64], emission properties and good response to stimulus these systems could found more [62] applications in fluorescence cell imaging. The mechanism of fluorescence turn *on* was proposed, which consisted in directed impact of surfactant on spatial organization of fluorophores, attached to the surface of NP, causing elimination of non-radiative deexcitation pathways and as a result increase of fluorescence emission QY, up to 0.13 and 0.4 in case of pyrene and aza-BODIPY dyes, respectively.

Photophysical studies on a novel NIR pH fluorescent probe based on a nitrated variant of Aza-BODIPY molecule were carried out. It was proven that this probe could be used as a lifetime fluorescence pH probe, as well as a pH-sensitive intensity fluorescence probe in fluorescence imaging. The reasonably high FEF value of 80 for **B3** proves that the introduction of the NO_2-group in **B3** fluorophore guaranteed an efficient *OFF* to *ON* switching of the fluorescence signal from physiological to acidic pH. A potential strategy for probe emission improvement was suggested.

Photoisomerization processes for azobenzene-based (azobenzene-lariat ether, azobenzene-BAPTA) ion release/capture systems were investigated by means of ultrafast transient absorption spectroscopy measurements. The rates of the isomerization processes were determined for systems in the presence of Ca^{2+}-ion and without it. It was observed that azobenzene-lariat ether systems did not show any significant difference in the photoisomerization kinetics while binding Ca^{2+} or not, what finds its explanation in weak binding between host complex and guest Ca^{2+} ion ($\log K = 1.7$ at Z-form and $\log K \simeq 0$ at E-form). Azobenzene-BAPTA complex with Ca^{2+}, which has higher binding constant ($\log K \approx 5$ in E-form) shows 4-fold retardation of the photoisomerization rate of azobenzene.

The impact of water on the cis−trans photoisomerization of hydroxychalcones was studied in CH_3CN and in H_2O/CH_3OH (1/1, v/v) by time-resolved subpicosecond and nanosecond spectroscopies. In the two types of media, the first step after excitation is the same and consists of the relaxation of the singlet excited state to a twisted $^1P^*$ state in a few picoseconds. In acetonitrile, this state deactivates to form hydroxychalcone cis-form and trans-from in identical proportions, the classic situation of double-bond photoisomerization. The presence of water dramatically affects the photochemical pathway by promoting the formation of a tautomeric intermediate, between the $^1P^*$ state and the photoproducts. The main photochemical pathway from this tautomer is electrocyclization to form chromene, whereas all of the other pathways lead to hydroxychalcone trans form; that is, no cis-isomer is formed photochemically.

General conclusions

In this thesis photophysical studies were performed on a wealth of molecular systems, notably bi- and multichromophoric supramolecule-based systems, functioning *via* different mechanisms: photoinduced electronic energy and electron transfer, reversible electronic energy transfer, photoinduced isomerization.

- Several applications of the Reversible Electronic Energy Transfer (REET) approach were discussed. The REET approach was used to dramatically enhance emission lifetimes of Ru(II) complexes based on tridentate ligands and cyclometallated Ir(III) complexes, respectively, without diminishing quantum yields. Modulation of photophysical properties of these chromophores can be pertinent for applications in gas sensors (e. g. O_2) and electroluminescence devices. A new approach of REET in the perspective of probing conformation/distance was proposed: to control the efficiency of the REET process by the degree of complexation, exemplified between a host double-helix foldamer and guest thread molecule.
- Time-resolved characterization of charge separation between electron donor (OPV) and acceptor (PB) in the sub-nanosecond timescale through an oligoquinoline bridge in foldamers of increasing oligomeric length (9, 14, 19 units) was carried out in solvents with different polarity: toluene, $CHCl_3$, CH_2Cl_2. The general mechanism of electron transfer in such systems was proposed, consisting of 4 separate steps: acceptor excitation, hole injection from quinoline unit HOMO state to single-occupied HOMO state of electron acceptor; after that hole is transferred to electron donor site by random, reversible hopping between energetically degenerate modular quinoline units, where it is irreversibly trapped by the electron donor. An outstanding long lifetime of OPV^{+}-Q_n-PB^{-} state $\tau_{CSS} > 80\,\mu$s in CH_2Cl_2 was observed. It was also demonstrated that in the studied $OPV^{\bullet+}$-Q_n-$PB^{\bullet-}$ systems, the electron donor OPV site could play a role of light harvesting antenna, transferring excitation energy to a PB site through a dipole-dipole interaction.
- Novel Tb^{3+} and Eu^{3+}-based *in situ* probes for Cu^{+} ions detection, mimicking the CusF peptide structure, were studied. Tb^{3+}-based probes showed pronounced turn *ON* emission of the lanthanide luminophore in the presence of Cu^{+} and Ag^{+} ions. The Eu^{3+}-based probe showed a response only to Ag^{+} ion, which is a promising result, thus far to our knowledge in literature there are no *in situ* probes described that can distinguish between Ag^{+} and Cu^{+} ions. The general mechanism, based on photophysical experimental data, was proposed to explain lanthanide luminescence turn *ON* in the presence of Ag^{+} and Cu^{+} ions, based on cation-π interactions between organic aromatic hydrocarbon fluorophores (tryptophan for Tb^{3+}-based and naphthalene for Eu^{3+}-based probes) and the Ag^{+}, Cu^{+} ions. An explanation for Eu^{3+}-based probe selectivity to Ag^{+}, compared to Cu^{+} ions was also offered.
- The study of NIR fluorescent *OFF-ON* probes, based on aza-BODIPY dyes, covalently attached to the surface of NP (poly(styrene-co-methacrylic acid)) with characteristic size of $d = 100$ nm was conducted in water solutions. Equally, the model system with pyrene-like units, covalently attached to the surface of same NP was investigated. It was shown that studied systems demonstrate pronounced responses (fluorescence turning *ON*) to the presence of surfactant (de-aggregating) agents, such as Triton X-100 and DOPC micelles.

Due to the outstanding photostability properties [64], emission properties and good response to stimulus these systems could find applications in fluorescence cell imaging. The mechanism of fluorescence turn *ON* was proposed, which consisted in direct impact of surfactant on spatial organization of fluorophores, attached to the surface of NP, causing elimination of non-radiative deexcitation pathways and as a result an increase of fluorescence emission QY, up to 0.13 and 0.4 in the case of pyrene and aza-BODIPY dyes, respectively.

Photophysical studies on a novel NIR pH fluorescent probe based on a nitrated variant of aza-BODIPY molecule were carried out. It was proven that this probe could be used as a lifetime fluorescence pH probe, as well as a pH-sensitive intensity fluorescence probe in fluorescence imaging with reasonably high FEF value of 80 for studied molecule. A potential strategy for probe emission improvement was suggested.

- Photoisomerization processes for azobenzene-based (azobenzene-lariat ether, azobenzene-BAPTA) ion release/capture systems were investigated by means of ultrafast transient absorption spectroscopy measurements. The rates of the isomerization processes were determined for systems in the presence of Ca^{2+}-ion and without it. It was observed that azobenzene-lariat ether systems did not show any significant difference in the photoisomerization kinetics while binding Ca^{2+} or not, what finds its explanation in weak binding between host complex and guest Ca^{2+} ion ($\log K = 1.7$ at Z-form and $\log K \simeq 0$ at E-form). azobenzene-BAPTA complex with Ca^{2+}, which has higher binding constant ($\log K \approx 5$ in E-form) shows 4-fold retardation of the photoisomerization rate of azobenzene.

  The impact of water on the cis−trans photoisomerization of hydroxychalcones was studied in CH_3CN and in H_2O/CH_3OH (1/1, v/v) by time-resolved subpicosecond and nanosecond spectroscopies. In the two types of media, the first step after excitation is the same and consists of the relaxation of the singlet excited state to a twisted $^1P^*$ state in a few picoseconds. In acetonitrile, this state deactivates to form hydroxychalcone cis-form and trans-from in identical proportions, the classic situation of double-bond photoisomerization. The presence of water dramatically affects the photochemical pathway by promoting the formation of a tautomeric intermediate, between the $^1P^*$ state and the photoproducts. The main photochemical pathway from this tautomer is electrocyclization to form chromene, whereas all of the other pathways lead to hydroxychalcone trans form.

Appendix A

Supporting information

1.1 Supporting information

The values presented in Table 1.1 in Chapter 1 are discussed in sections: 1.1.1, 1.1.2, 1.1.3.

1.1.1 Time Ranges

To estimate time ranges that chemistry deals with we need to answer these two questions:
1. What is the fastest chemical reaction?
2. What is the slowest chemical reaction?

The fastest reaction to our knowledge is the bond breaking of H_2^+ molecule which is similar to electron movement rate $\sim 10^{15}$ s^{-1}. The slowest reaction is a more difficult question, because a lot of chemical substances could react with each other according to thermodynamic potentials, but kinetics are extremely low at certain temperatures or without catalyst.

To determine time-ranges for physics is easier from general perspective. Physics studies the Universe, the tiniest fraction of time accessible to the pen of theoreticians is 10^{-44} s, just after of Big Bang, and the largest one is the age of our Universe, or approximate age of its death, which is of course very speculative.

1.1.2 Distance ranges

The average chemical bond is about 1 Å, so this is a lower limit for chemistry. The top limit is vague, because an ideal crystal as diamond or Al_2O_3 Czochralski grown, or polymers and of course DNA are giant molecules, so the upper size limit of molecules could be estimated as 10^1 m. But we need to remember that chemistry deals with chemical transformation and they happens on size scales of chemical units: groups or protein structures in biochemistry for example.

Physics works with objects from the Planck length $1.616199(97) \times 10^{-35}$ m to the observable Universe size of 13.8 billion light years $\sim 10^{26}$ m.

1.1.3 Energy ranges

The strength of weak hydrogen bonds lies in the energy range of $8 - 25$ J/mol or $8 \times 10^{-5} - 2.5 \times 10^{-4}$ eV. The top level of energies could be estimated from the temperature of boiling points. The highest temperature of boiling for metals is for rhenium, 5869 K, what correspond to the energy 0.76 eV (calculated using $E = \frac{3}{2}kT$).

Physics deals with all kind of energies from microscopic up to energies of Universe [201].

1.2 Software "DATA-FIT" for data treatment

1.2.1 General description

The "DATA-FIT" software, developed during this thesis in LabVIEW 2012 system-design platform and development environment allowed to:

- Open files:
  - Time explicit format $\begin{matrix} & t_0 & t_i & ... & t_n \\ \lambda_0 \\ \lambda_j \\ ... \\ \lambda_k \end{matrix} \begin{pmatrix} a_{\lambda_0 t_0} & a_{\lambda_0 t_i} & ... & a_{\lambda_0 t_n} \\ a_{\lambda_j t_0} & a_{\lambda_j t_i} & ... & a_{\lambda_0 t_j} \\ ... & ... & ... & ... \\ a_{\lambda_k t_0} & a_{\lambda_k t_i} & ... & a_{\lambda_0 t_k} \end{pmatrix}$;
  - Hamamatsu format *.img*;
  - comma (*.csv*) and tab separated values files.
- Fit experimental data with different mathematical models:
  - single exponential decay/growth $\pm A\exp(-k_{d/g}t)$;
  - stretched exponential decay $A\exp(-(k_d t)^{\beta})$ (see Appendix 1.3);
  - bi-exponential decay/growth:
    - parallel $\pm A\exp(-k_{1d/g}t) \pm B\exp(-k_{2d/g}t)$ (see subsection 1.2.2);
    - serial (see subsection 1.2.2).
  - three-exponential serial decay/growth.
- Save fitted data files as tab-separated values files.
- Additional features:
  - Smoothing experimental 2D-maps data using a Savitzky-Golay FIR smoothing filter;
  - Chirp-correction using a computer program correction with respect to a Lorentzian fit of a Kerr signal generated in a 0.2 mm glass plate used in a place of sample;
  - Calculation of rate-constants from stretched-exponent fit, by inverse Laplace transformation (see Appendix 1.3);
  - Solvation-shift of emission, by tracking extremes in experimental 2D-maps.

Developed software could be run under operational systems: Windows, Mac OS X, Linux, by using a free NI run-time engine.

1.2.2 Fitting

The intensity of the excitation laser beam was described by a Gaussian function with pulse duration of τ_p.

$$I(t) = I_0 \exp\left(-4\ln 2\left(\frac{t-t_0}{\tau_p}\right)^2\right),$$

where I_0 is the intensity at the centre (maximum intensity).

1.2.2.1 One-level model

Iterations

For the one level model, it is assumed that the ensemble of molecules after excitation are excited to S_1 state. The population of this state is described by $N_1(t)$ (eq. A.1) at given time t. The relaxation of excited state S_1 happens with the rate k_1 to ground state S_0. Depopulation of ground state S_0 is negligible ($N_0 \gg N$) during excitation and there is no excited state population

before the excitation pulse arrives ($N(-0)=0$). σ is the absorption cross section for $S_1 \longleftarrow S_0$ transition.

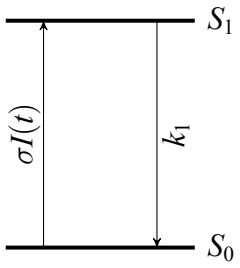

Figure A.1. Scheme for one level model.

$$\frac{dN_1(t)}{dt} = \sigma I(t) - k_1 N_1(t) \tag{A.1}$$

Solution of equation A.1 is expressed in equation A.2:

$$N_1(t) = \frac{\sigma \tau_p I_0}{4} \sqrt{\frac{\pi}{\ln 2}} \exp\left(\frac{k_1^2 \tau_p^2}{16 \ln 2}\right) \left(1 + \mathrm{erf}\left(2\sqrt{\ln 2}\frac{t}{\tau_p} - \frac{k_1 \tau_p}{4\sqrt{\ln 2}}\right)\right) \exp(-k_1 t) \tag{A.2}$$

To extract deexcitation rate k_1 from such function is a complicated mathematical task. Instead of determining k_1 as an analytical function, we determined it in an iterative manner, by fitting experimental data as following:

$$\frac{N_{i+1}(t) - N_i(t)}{\delta t} = \sigma I(t) - k_1 N_i(t),$$

so:

$$N_{i+1}(t) = (\sigma I(t) - k_1 N_i(t)) \times \delta t + N_i(t),$$

where δt is the time step, equalled to $\frac{\text{time-scale}}{N_{points}}$[1].

The trust-region[2] dogleg algorithm [203] (supported by *LabVIEW* 2012) was applied to determine the set of parameters that best fit the set of input data. The trust-region dogleg algorithm was used instead of Levenberg-Marquardt algorithm, the latter being less stable in most cases during optimization process, because trust region methods are robust, and can be applied to ill-conditioned problems.

[1] In case of streak-camera numbers of points was set to 512. In case of data, obtained on sub-pico second set-up (Figure 1.18), the number of experimental points was usually smaller around $100 - 150$. Application of a special algorithm artificially increases a number of fitting points (the number of points were increased in time vector). Despite this artificial increase, the optimization algorithm worked with an amount of points corresponding to experimental number by choosing appropriate values from the fit data.

[2] The trust-region methods are a class of robust and efficient globalization strategies for the numerical calculation of a local minimum of a possibly non-convex, once continuously differentiable function. The trust-region methods are closely related to the Levenberg-Marquardt algorithm, but have significant differences in the problems to be solved quadratic part and are deterministic in the choice of step-size restriction. Trust region is a term used in mathematical optimization to denote the subset of the region of the objective function to be optimized that is approximated using a model function (often an quadratic). If an adequate model of the objective function is found within the trust region then the region is expanded; conversely, if the approximation is poor then the region is contracted. The fit is evaluated by comparing the ratio of expected improvement from the model approximation with the actual improvement observed in the objective function. Simple thresholding of the ratio is used as the criterion for expansion and contraction – a model function is ”trusted” only in the region where it provides a reasonable approximation.[202]

Convolution

Another way to determine the deexcitation rate k_1 was to convolute excitation pulse (Guassian function) with decay function ($A\exp(-k_1 t)$):

$$(\text{exc} * \text{decay})(t) = \int_0^{\tau_{exp}} \text{exc}(\tau)\,\text{decay}(t-\tau)d\tau,$$

where τ_{exp} time of experiment. And again trust-region dogleg algorithm (supported by *LabVIEW* 2012) was applied to determine best fit parameters.

1.2.2.2 Two-level model

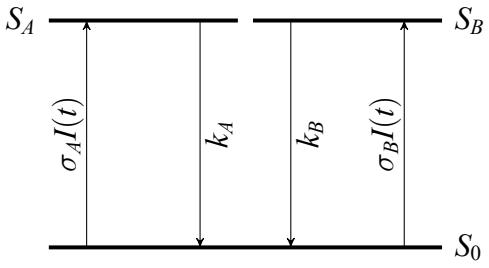

Figure A.2. Scheme for two-level parallel model.

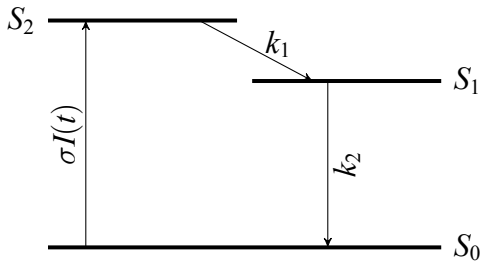

Figure A.3. Scheme for two-level serial model.

Lets consider two-level models Figure A.2 and A.3. Two-level parallel model (Figure A.2), could represent the deexcitation of excited states of two different species in solution or deexcitation of single excited state, which has two different pathways of deexcitation. For such a model these differential equation could be written:

$$\begin{cases} \dfrac{dN_A(t)}{dt} = \sigma_A I(t) - k_A N_A(t) \\ \dfrac{dN_B(t)}{dt} = \sigma_B I(t) - k_A N_B(t) \end{cases} \tag{A.3}$$

The overall temporal evolution $N(t)$ of excited molecules can be written: $N(t) = A_1 N_A(t) + DN_B(t)$, where C and D represent the amplitudes for levels A and B.

The differential equations for serial two-level model (Figure A.3) are written as follows:

$$\begin{cases} \dfrac{dN_1(t)}{dt} = \sigma I(t) - k_1 N_1(t) \\ \dfrac{dN_2(t)}{dt} = k_1 N_1(t) - k_2 N_2(t) \end{cases} \tag{A.4}$$

The overall temporal evolution $N(t)$ of excited molecules can be written: $N(t) = A_1 N_1(t) + A_2 N_2(t)$, where A_1 and A_2 represent the amplitudes for levels 1 and 2.

The equations A.3 and A.4 were solved as described in subsection 1.2.2.1 by iterations and using the trust-region dogleg algorithm for best fit parameters search. Parallel two-level model fit was also treated by convolving Gaussian-shaped excitation pulse and decay function $\pm A\exp(-k_1 t) \pm B\exp(-k_2 t)$ (see subsection 1.2.2.1).

1.2.3 "DATA-FIT" source

The source code of DATA-FIT software can be downloaded from google repository: https://code.google.com/p/datafit-lab/.

1.3 Kohlrausch decay function (stretched exponent)

In the simplest cases, the luminescence decay curves can be satisfactorily described by a sum of discrete exponentials and the pre-exponential factors and decay times have clear physical meaning. But distributions of decay times or rate constants must be anticipated to best account for the observed phenomena in various cases: fluorophores incorporated in micelles, cyclodextrins, rigid solutions, sol–gel matrices, polymers, proteins, vesicles or membranes, biological tissues, fluorophores adsorbed on surfaces, or linked to surfaces, quenching of fluorophores in micellar solutions, energy transfer in assemblies of like or unlike fluorophores, etc.[181]

In such cases, the luminescence decay can be written in the following form:

$$I(t)=\int_0^\infty H(k)e^{-kt}dk, \tag{A.5}$$

with $I(0)=1$. This relation is always valid because $H(k)$ is the inverse Laplase transformation of $I(t)$.The function $H(k)$, also called the eigenvalue spectrum (of a suitable kinetic matrix), is normalized, as $I(0)=1$ implies that $\int_0^\infty H(k)e^{-kt}dk$. In most situations (e. g. in the absence of a rise-time), the function $H(k)$ is nonnegative for all $k>0$, and $H(k)$ can be understood as a distribution of rate constants (strictly, a probability density function).

Recovery of the distribution $H(k)$ from the experimental decay $I(t)$ is very difficult because this is an ill-conditioned problem. In other words, a small change in $I(t)$ can cause an arbitrarily large change in $H(k)$. The quality of the experimental data is of course of major importance. Depending on the level of precision, a decay can be fitted with a sum of two or three exponentials with satisfactory χ^2 values and weighted residuals in spite of the existence of an underlying distribution.[181]

$H(k)$ can be recovered from decay analysis by three approaches: *1)* data analysis with a theoretical model for $H(k)$ that may be supported by Monte-Carlo simulations; *2)* data analysis by methods that do not require an a priori assumption of the distribution shape; *3)* data analysis with a mathematical function describing the distribution [181].

One of the mathematical function allowing to determine the distribution of rate constants is the stretched exponential (or Kohlrausch) function, written as:

$$I(t)=exp[-(t/\tau_0)^\beta], \tag{A.6}$$

where $0<\beta\leq 1$, and τ_0 is a parameter with the dimension of time.

In studies of the relaxation of complex systems, the Kohlrausch function is frequently used as a purely empirical decay law, although there are theoretical arguments to justify its common occurrence.

The Kohlrausch decay law is convenient as a fitting function, even in the absence of a model, given that it allows gauging in simple way deviations to the “canonical” single exponential behaviour through the parameter β.

The general considerations regarding distributions of rate constants can be found in [181] Figure A.4 shows behaviour of stretched-exponent function.

The determination of $H(k)$ for a given $I(t)$ amounts to the computation of the respective inverse Laplace transform. In the case of the Kohlrausch function, eq. A.6, the calculation can be performed with the general inversion formula (Bromwich integral) (Figure A.5).

$$H_\beta(k)=\frac{\tau_0}{\pi}\int_0^\infty \exp(-k\tau_0 u)\times\exp[-u^\beta\cos(\beta\pi)]\sin[u^\beta\sin(\beta\pi)]du \tag{A.7}$$

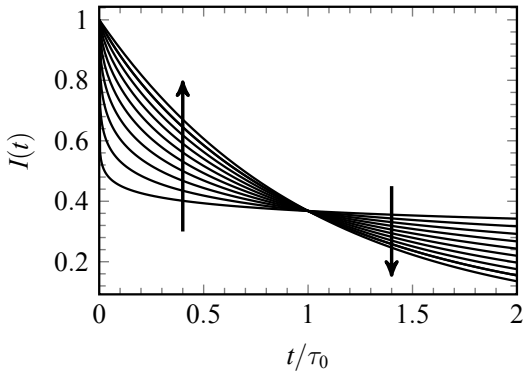

Figure A.4. The Kohlrausch (stretched exponential) decay law for several values of $\beta(0.1, 0.2, ..., 0.9, 1)$. The decay is faster than that of an ordinary exponential ($\beta = 1$) for $t < \tau_0$, and slower afterwards.

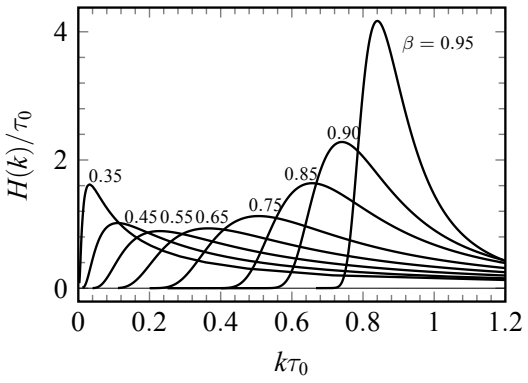

Figure A.5. Distribution of rate constants (probability density function) for the Kohlrausch decay law obtained by numerical integration of equation A.7.

1.4 Photodegradation Quantum Yield

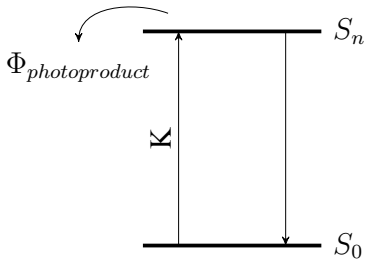

Figure A.6. The reaction scheme to study the photodegradation.

The reaction scheme of photodegradation is presented below (Figure A.6). We suppose that all photoexcited states relax to the ground state except a part denoted Φ_d which represents a quantum yield of photodegradation or other irreversible photoreaction:

The Stark-Einstein law, states that for each photon of light absorbed by a chemical system, only one molecule is activated for subsequent reaction. According to this "photoequivalence law", equation A.8 can be written. Number of excited molecules N_{exc} is equal to number of absorbed photons K_{abs}:

$$K_{abs} = K\left(1 - 10^{-\varepsilon C_0}\right) = N_{exc}, \tag{A.8}$$

where K is incident photon number. It can be found from:

$$K = \frac{Wt}{h\nu}, \tag{A.9}$$

$$[K] = \frac{W \times sec}{J \times sec \times sec^{-1}} = 1,$$

where $W \times t$ (power by time) multiplication gives the energy dose (Joules) of radiation. If we divide it to one photon energy, result is the number of photons.

According to photoreaction scheme, some molecules undergo an irreversible photoreaction (photodegradation) with a quantum yield of Φ_d. This photoreaction yields that corresponds to the number of molecules, reaching the ground state after being excited can be found as follows:

$$N_{relax} = N_{exc}(1 - \Phi_d) \tag{A.10}$$

$$N_{exc} - N_{relax} = N_{exc}\Phi_d \tag{A.11}$$

According to the equation A.11, the changes of the ground state population in time can be

written as:

$$\frac{dN_{ground}}{dt} = N_{exc}\Phi_d \tag{A.12}$$

Substituting equation A.8 into equation A.11 and having in mind the photon flux (equation A.9), one obtains for slowly varying steady state absorption $(1-10^{-N_g l\varepsilon/V})$.

$$\frac{dN_g}{dt} = K\left(1-10^{N_g l\varepsilon/N_A V}\right)\Phi_d = \frac{W}{h\nu}\left(1-10^{-N_g l\varepsilon/N_A V}\right)\Phi_d \tag{A.13}$$

Initial condition is $N_g = N_0$ at the beginning of the experiment ($t=0$), and $c_0 = N_0/V$. If the absorption of initial solution is small (not exceeding 0.3 units), we can develop the exponent into a Taylor series:

$$10^{ax} = e^{xa\ln 10} = 1 + xa\ln 10 + \ldots \tag{A.14}$$

Taking the first term from the series A.14, the differential equation A.13 becomes:

$$\frac{dN_g}{dt} = \frac{W}{h\nu}\left(1-(1-\frac{N_g\varepsilon l}{N_A V}\ln 10)\right)\Phi_d = -\frac{W\varepsilon l\ln 10\Phi_d}{h\nu N_A V}N_g \tag{A.15}$$

The solution of the equation A.15 is:

$$N_g = \exp\left(-\frac{Wl\varepsilon\ln 10\Phi_d}{h\nu N_A V}t\right) \tag{A.16}$$

It corresponds to the exponential relaxation of ground state population with a time constant:

$$\tau = \frac{h\nu N_A V}{W\varepsilon l\Phi_d\ln 10} \tag{A.17}$$

Thus, the quantum yield of irreversible photoreaction (photodegradation) can be found from the exponential kinetic of steady state absorption decay upon irradiation as follows:

$$\Phi_d = \frac{h\nu N_A V}{W\varepsilon l\tau\ln 10} \tag{A.18}$$

In the conditions of real experiment, it is necessary to account for the reflection losses on the input window of the cell as well as permanent stirring of solution is required in order to have an uniform distribution of molecular concentration in the cell.

Bibliography

[1] Denisov, S. A. „Gas-phase modification and electrophysical properties of the detonation nanodiamond“. PhD thesis. A. N. Frumkin Institute of physical chemistry and eletrochemistry RAS, 2013.

[2] Lavie-Cambot, A., Lincheneau, C., Cantuel, M., Leydet, Y., and McClenaghan, N. D. „Reversible electronic energy transfer: a means to govern excited-state properties of supramolecular systems“. *Chem. Soc. Rev.* 39, pp. 506–515, 2010.

[3] Ho, P. K. H., Thomas, D. S., Friend, R. H., and Tessler, N. „All-Polymer Optoelectronic Devices“. *Science* 285, pp. 233–236, 1999.

[4] Hu, W., Bai, F., Gong, X., Zhan, X., Fu, H., and Bjornholm, T. *Organic Optoelectronics*. Wiley, 2012. isbn: 9783527653478.

[5] McClenaghan, N. D., Leydet, Y., Maubert, B., Indelli, M.T., and Campagna, S. „Excited-state equilibration: a process leading to long-lived metal-to-ligand charge transfer luminescence in supramolecular systems“. *Coord. Chem. Rev.* 249, pp. 1336–1350, 2005.

[6] Lavie-Cambot, A., Lincheneau, C., Cantuel, M., Leydet, Y., and McClenaghan, N. D. „Reversible electronic energy transfer: a means to govern excited-state properties of supramolecular systems“. *Chem. Soc. Rev.* 39, pp. 506–515, 2010.

[7] Ragazzon, G., Verwilst, P., Denisov, S. A., Credi, A., Jonusauskas, G., and McClenaghan, N. D. „Ruthenium(ii) complexes based on tridentate polypyridine ligands that feature long-lived room-temperature luminescence“. *Chem. Commun.* 49, pp. 9110–9112, 2013.

[8] Denisov, S. A., Cudré, Y., Verwilst, P., Jonusauskas, G., Marín-Suárez, M., Fernández-Sánchez, J. F., Baranoff, E., and McClenaghan, N. D. „Direct Observation of Reversible Electronic Energy Transfer Involving an Iridium Center“. *Inorg. Chem.* 53, pp. 2677–2682, 2014.

[9] Ramamurthy, V. *Organic and Inorganic Photochemistry*. Taylor & Francis, 1998.

[10] Wang, X.-Y., Del Guerzo, A., and Schmehl, R. H. „Photophysical behavior of transition metal complexes having interacting ligand localized and metal-to-ligand charge transfer states“. *J. Photochem. Photobiol. C* 5, pp. 55–77, 2004.

[11] Ford, W. E. and Rodgers, M. A. J. „Reversible triplet-triplet energy transfer within a covalently linked bichromophoric molecule“. *J. Phys. Chem.* 96, pp. 2917–2920, 1992.

[12] Ji, H.-F., Shen, Y., Hubner, P., Carroll, B., Schmehl, R. H., Simon, J. A., and Schanze, K. „Temperature-Independent Pressure-Sensitive Paint Based on a Bichromophoric Luminophore“. *Appl. Spectrosc.* 54, pp. 856–863, 2000.

[13] Passalacqua, R., Loiseau, F., Campagna, S., Fang, Y.-Q., and Hanan, G. S. „In Search of Ruthenium(II) Complexes Based on Tridentate Polypyridine Ligands that Feature Long-lived Room-Temperature Luminescence: The Multichromophore Approach“. *Angew. Chem. Int. Ed.* 42, pp. 1608–1611, 2003.

[14] Tyson, D. S. and Castellano, F. N. „Intramolecular Singlet and Triplet Energy Transfer in a Ruthenium(II) Diimine Complex Containing Multiple Pyrenyl Chromophores“. *J. Phys. Chem. A* 103, pp. 10955–10960, 1999.

[15] Hissler, M., Harriman, A., Khatyr, A., and Ziessel, R. „Intramolecular Triplet Energy Transfer in Pyrene-Metal Polypyridine Dyads: A Strategy for Extending the Triplet Lifetime of the Metal Complex“. *Chem. Eur. J.* 5, pp. 3366–3381, 1999.

[16] Simon, J. A., Curry, S. L., Schmehl, R.H., Schatz, T. R., Piotrowiak, P., Jin, X., and Thummel, R. P. „Intramolecular Electronic Energy Transfer in Ruthenium(II) Diimine Donor/Pyrene Acceptor Complexes Linked by a Single C–C Bond“. *J. Am. Chem. Soc.* 119, pp. 11012–11022, 1997.

[17] Leydet, Y., Romero-Salguero, F. J., Jimenez-Sanchidrian, C., Bassani, D. M., and McClenaghan, N. D. „Excited-state equilibration in a meso-/microporous material-hosted bichromophoric [Ruthenium (2,2'-bipyridine)$_3$]$^{2+}$: Reversible energy transfer and photosensitized electron pumping“. *Inorg. Chim. Acta* 360, pp. 987–994, 2007.

[18] Yarnell, J. E., Deaton, J. C., McCusker, C. E., and Castellano, F. N. „Bidirectional “Ping-Pong” Energy Transfer and 3000-Fold Lifetime Enhancement in a Re(I) Charge Transfer Complex“. *Inorg. Chem.* 50, pp. 7820–7830, 2011.

[19] Campagna, S., Puntoriero, F., Nastasi, F., Bergamini, G., and Balzani, V. In: „Photochemistry and Photophysics of Coordination Compounds: Ruthenium“. Balzani, Vincenzo and Campagna, Sebastiano, eds. Vol. 280, pp. 117–214. Springer Berlin Heidelberg, 2007.

[20] Imahori, H., Mori, Y., and Matano, Y. „Nanostructured artificial photosynthesis“. *J. Photochem. Photobiol. C* 4, pp. 51–83, 2003.

[21] Balzani, V., Credi, A., and Venturi, M. *Molecular Devices and Machines: Concepts and Perspectives for the Nanoworld, Second Edition*. Wiley-VCH Verlag GmbH & Co. KGaA, 2008.

[22] Grätzel, M. „Recent Advances in Sensitized Mesoscopic Solar Cells“. *Accounts Chem. Res.* 42, pp. 1788–1798, 2009.

[23] Armaroli, N. and Balzani, V. *Energy for a Sustainable World: From the Oil Age to a Sun-Powered Future*. Wiley-VCH Verlag GmbH & Co. KGaA, 2010.

[24] Maestri, M., Armaroli, N., Balzani, V., Constable, E. C., and Thompson, A. M. W. C. „Complexes of the Ruthenium(II)-2,2':6',2"-terpyridine Family. Effect of Electron-Accepting and -Donating Substituents on the Photophysical and Electrochemical Properties“. *Inorg. Chem.* 34, pp. 2759–2767, 1995.

[25] Fang, Y.-Q., Taylor, N. J., Laverdière, F., Hanan, G. S., Loiseau, F., Nastasi, F., Campagna, S., Nierengarten, H., Leize-Wagner, E., and Van Dorsselaer, A. „Ruthenium(II) Complexes with Improved Photophysical Properties Based on Planar 4‘-(2-Pyrimidinyl)-2,2‘:6‘,2“-terpyridine Ligands“. *Inorg. Chem.* 46, pp. 2854–2863, 2007.

[26] Abrahamsson, M., Jäger, M., Kumar, R. J., Österman T.and Persson, P., Becker, H.-C., Johansson, O., and Hammarström, L. „Bistridentate Ruthenium(II)polypyridyl-Type Complexes with Microsecond ^{3}MLCT State Lifetimes: Sensitizers for Rod-Like Molecular Arrays“. *J. Am. Chem. Soc.* 130, pp. 15533–15542, 2008.

[27] Österman, T., Abrahamsson, M., Becker, H.-C., Hammarström, L., and Persson, P. „Influence of Triplet State Multidimensionality on Excited State Lifetimes of Bis-tridentate Ru(II) Complexes: A Computational Study“. *J. Phys. Chem. A* 116, pp. 1041–1050, 2011.

[28] Montalti, M., Credi, A., Prodi, L., and Gandolfi, M. T. *Handbook of Photochemistry, Third Edition*. London: CRC / Taylor & Francis, 2006. P. 633.

[29] Costa, R. D., Ortí, E., Bolink, H.J., Monti, F., Accorsi, G., and Armaroli, N. „Luminescent Ionic Transition-Metal Complexes for Light-Emitting Electrochemical Cells“. *Angew. Chem. Int. Ed.* 51, pp. 8178–8211, 2012.

[30] Lowry, M. S. and Bernhard, S. „Synthetically Tailored Excited States: Phosphorescent, Cyclometalated Iridium(III) Complexes and Their Applications“. *Chem. Eur. J.* 12, pp. 7970–7977, 2006.

[31] Lo, K.K.W., Choi, A.W.-T., and Law, W. H.T. „Applications of luminescent inorganic and organometallic transition metal complexes as biomolecular and cellular probes“. *J. Chem. Soc., Dalton Trans.* 41, pp. 6021–6047, 2012.

[32] Flamigni, L., Barbieri, A., Sabatini, C., Ventura, B., and Barigelletti, F. In: „Photochemistry and Photophysics of Coordination Compounds: Iridium“. Balzani, V. and Campagna, S., eds. Vol. 281, pp. 143–203. Springer Berlin Heidelberg, 2007.

[33] Constable, E. C., Neuburger, M., Rösel, P., Schneider, G. E., Zampese, J.A., Housecroft, C. E., Monti, F., Armaroli, N., Costa, R. D., and Ortí, E. „Ligand-Based Charge-Transfer Luminescence in Ionic Cyclometalated Iridium(III) Complexes Bearing a Pyrene-Functionalized Bipyridine Ligand: A Joint Theoretical and Experimental Study“. *Inorg. Chem.* 52, pp. 885–897, 2012.

[34] Prabhakaran, P., Priya, G., and Sanjayan, G. J. „Foldamers: They’re Not Just for Biomedical Applications Anymore“. *Angew. Chem. Int. Ed.* 51, pp. 4006–4008, 2012.

[35] Ferrand, Y., Gan, Q., Kauffmann, B., Jiang, H., and Huc, I. „Template-Induced Screw Motions within an Aromatic Amide Foldamer Double Helix“. *Angew. Chem.* 123, pp. 7714–7717, 2011.

[36] Royer, C. A. „Probing Protein Folding and Conformational Transitions with Fluorescence“. *Chem. Rev.* 106, pp. 1769–1784, 2006.

[37] Kavarnos, G. J. In: „Fundamental concepts of photoinduced electron transfer“. Mattay, Jochen, ed. Vol. 156chap. 2, pp. 21–58. Springer Berlin Heidelberg, 1990.

[38] Goldsmith, R. H., DeLeon, O., Wilson, T. M., Finkelstein-Shapiro, D., Ratner, M. A., and Wasielewski, M. R. „Challenges in Distinguishing Superexchange and Hopping Mechanisms of Intramolecular Charge Transfer through Fluorene Oligomers“. *J. Phys. Chem. A* 112, pp. 4410–4414, 2008.

[39] May, V. and Kühn, O. *Charge and Energy Transfer Dynamics in Molecular Systems*. Wiley-VCH, 2004. isbn: 9783527403967.

[40] Wolffs, M., Delsuc, N., Veldman, D., Anh, N. V., Williams, R. M., Meskers, S. C. J., Janssen, R. A. J., Huc, I., and Schenning, A. P. H. J. „Helical Aromatic Oligoamide Foldamers as Organizational Scaffolds for Photoinduced Charge Transfer“. *J. Am. Chem. Soc.* 131, pp. 4819–4829, 2009.

[41] Paddon-Row, M. N. „Investigating long-range electron-transfer processes with rigid, covalently linked donor-(norbornylogous bridge)-acceptor systems“. *Accounts Chem. Res.* 27, pp. 18–25, 1994.

[42] Sariciftci, N.S., Wudl, F., Heeger, A.J., Maggini, M., Scorrano, G., Prato, M., Bourassa, J., and Ford, P.C. „Photoinduced electron transfer and long lived charge separation in a donor-bridge-acceptor supramolecular ‘diad’ consisting of ruthenium(II) tris(bipyridine) functionalized C60“. *Chem. Phys. Lett.* 247, pp. 510–514, 1995.

[43] Takada, T., Kawai, K., Tojo, S., and Majima, T. „Hole transfer in DNA: DNA as a scaffold for hole transfer between two organic molecules“. *Tetrahedron Lett.* 44, pp. 3851–3854, 2003.

[44] Benniston, A. C. and Harriman, A. „Charge on the move: how electron-transfer dynamics depend on molecular conformation“. *Chem. Soc. Rev.* 35, pp. 169–179, 2006.

[45] Natali, M., Campagna, S., and Scandola, F. „Photoinduced electron transfer across molecular bridges: electron- and hole-transfer superexchange pathways“. *Chem. Soc. Rev.* 43, pp. 4005–4018, 2014.

[46] Lewis, F. D., Zhu, H., Daublain, P., Fiebig, T., Raytchev, M., Wang, Q., and Shafirovich, V. „Crossover from Superexchange to Hopping as the Mechanism for Photoinduced Charge Transfer in DNA Hairpin Conjugates“. *J. Am. Chem. Soc.* 128, pp. 791–800, 2005.

[47] Hal, P. A. van, Beckers, E. H. A., Peeters, E., Apperloo, J. J., and Janssen, R. A. J. „Photoinduced intermolecular electron transfer between oligo(p-phenylene vinylene)s and N-methylfulleropyrrolidine in a polar solvent“. *Chem. Phys. Lett.* 328, pp. 403–408, 2000.

[48] Beckers, E. H. A., Meskers, S. C. J., Schenning, A. P. H. J., Chen, Z., Würthner, F., and Janssen, R. A. J. „Charge Separation and Recombination in Photoexcited Oligo(p-phenylene vinylene): Perylene Bisimide Arrays Close to the Marcus Inverted Region“. *J. Phys. Chem. A* 108, pp. 6933–6937, 2004.

[49] Würthner, F., Chen, Z., Hoeben, F. J. M., Osswald, P., You, Ch.-Ch., Jonkheijm, P., Herrikhuyzen, J. v, Schenning, A. P. H. J., Schoot, P. P. A. M. van der, Meijer, E. W., Beckers, E. H. A., Meskers, S. C. J., and Janssen, R. A. J. „Supramolecular p−n-Heterojunctions by Co-Self-Organization of Oligo(p-phenylene Vinylene) and Perylene Bisimide Dyes“. *J. Am. Chem. Soc.* 126, pp. 10611–10618, 2004.

[50] Beckers, E. H. A., Jonkheijm, P., Schenning, A. P. H. J., Meskers, S. C. J., and Janssen, R. A. J. „Charge Transfer in Supramolecular Coaggregates of Oligo(p-Phenylene Vinylene) and Perylene Bisimide in Water“. *Chem. Phys. Chem.* 6, pp. 2029–2031, 2005.

[51] Beckers, E. H. A., Meskers, S. C. J., Schenning, A. P. H. J., Chen, Zh., Würthner, F., Marsal, P., Beljonne, D., Cornil, J., and Janssen, R. A. J. „Influence of Intermolecular Orientation on the Photoinduced Charge Transfer Kinetics in Self-Assembled Aggregates of Donor−Acceptor Arrays“. *J. Am. Chem. Soc.* 128, pp. 649–657, 2005.

[52] Beckers, E. H. A., Chen, Zh., Meskers, S. C. J., Jonkheijm, P., Schenning, A. P. H. J., Li, X.-Q., Osswald, P., Würthner, F., and Janssen, R. A. J. „The Importance of Nanoscopic Ordering on

the Kinetics of Photoinduced Charge Transfer in Aggregated π-Conjugated Hydrogen-Bonded Donor−Acceptor Systems“. *J. Phys. Chem. B* 110, pp. 16967–16978, 2006.

[53] Ventura, B., Langhals, H., Bock, B., and Flamigni, L. „Phosphorescent perylene imides“. *Chem. Commun.* 48, pp. 4226–4228, 2012.

[54] Kim, B. E., Nevitt, T., and Thiele, D. J. „Mechanisms for copper acquisition, distribution and regulation“. *Nat. Chem. Biol.* 4, pp. 176–185, 2008.

[55] Gaggelli, E., Kozlowski, H., Valensin, D., and Valensin, G. „Copper Homeostasis and Neurodegenerative Disorders (Alzheimer's, Prion, and Parkinson's Diseases and Amyotrophic Lateral Sclerosis)“. *Chem. Rev.* 106, pp. 1995–2044, 2006.

[56] Fahrni, C. J. „Synthetic fluorescent probes for monovalent copper“. *Curr. Opin. Chem. Biol.* 17, pp. 656–662, 2013.

[57] Loftin, I. R., Franke, S., Roberts, S. A., Weichsel, A., Héroux, A., Montfort, W. R., Rensing, C., and McEvoy, M. M. „A Novel Copper-Binding Fold for the Periplasmic Copper Resistance Protein CusF“. *Biochem.* 44, pp. 10533–10540, 2005.

[58] Ugurbil, K., Maki, A. H., and Bersohn, R. „Study of the triplet state properties of tyrosines and tryptophan in azurins using optically detected magnetic resonance“. *Biochem.* 16, pp. 901–907, 1977.

[59] Xue, Y., Davis, A. V., Balakrishnan, G., Stasser, J. P., Staehlin, B. M., Focia, P., Spiro, T. G., Penner-Hahn, J. E., and O'Halloran, T. V. „Cu(I) recognition via cation-[pi] and methionine interactions in CusF“. *Nat. Chem. Biol.* 4, pp. 107–109, 2008.

[60] Frangioni, J. „In vivo near-infrared fluorescence imaging“. *Curr. Opin. Chem. Biol.* 7, pp. 626–634, 2003.

[61] Leblond, F., Davis, S. C., Valdés, P. A., and Pogue, B. W. „Pre-clinical whole-body fluorescence imaging: Review of instruments, methods and applications.“ *J. Photochem. Photobiol. B, Biol.* 98, pp. 77–94, 2010.

[62] Palma, A., Alvarez, L. A., Scholz, D., Frimannsson, D. O., Grossi, M., Quinn, S. J, and O'Shea, D. F. „Cellular Uptake Mediated Off/On Responsive Near-Infrared Fluorescent Nanoparticles“. *J. Am. Chem. Soc.* 133, pp. 19618–19621, 2011.

[63] Stark, W. J. „Nanoparticles in Biological Systems“. *Angew. Chem. Int. Ed.* 50, pp. 1242–1258, 2011.

[64] Batat, P., Cantuel, M., Jonusauskas, G., Scarpantonio, L., Palma, A., O'Shea, D. F., and McClenaghan, N. D. „BF_2-Azadipyrromethenes: Probing the Excited-State Dynamics of a NIR Fluorophore and Photodynamic Therapy Agent“. *J. Phys. Chem. A* 115, pp. 14034–14039, 2011.

[65] Berezin, M. Y., Guo, K., Akers, W., Northdurft, R. E., Culver, J. P., Teng, B., Vasalatiy, O., Barbacow, K., Gandjbakhche, A., Griffiths, G. L., and Achilefu, S. „Near-infrared fluorescence lifetime pH-sensitive probes.“ *Biophys. J.* 100, pp. 2063–72, 2011.

[66] Wu, D. and O'Shea, D. F. „Synthesis and Properties of BF2-3,3′-Dimethyldiarylazadipyrromethene Near-Infrared Fluorophores“. *Org.Lett.* 15, pp. 3392–3395, 2013.

[67] Ducrot, A., Verwilst, P., Scarpantonio, L., Goudet, S., Kauffmann, B., Denisov, S., Jonusauskas, G., and McClenaghan, N. D. „Photolariats: synthesis, metal ion complexation and photochromism“. *Supramolecular Chemistry* 24, pp. 462–472, 2012.

[68] Lehn, J. M. *Supramol. Chem.: Concepts and Perspectives*. George Fisher Baker lectures in chemistry. Wiley, 1995. isbn: 9783527293117.

[69] Ellis-Davies, G. C. R. „Neurobiology with Caged Calcium“. *Chem. Rev.* 108, pp. 1603–1613, 2008.

[70] Ducrot, A. „Synthèses et études de systèmes supramoléculaires photocommutables : récepteurs à ion et molécules entrelacées“. PhD thesis. Université Bordeaux 1, 2012.

[71] Leydet, Y., Batat, P., Jonusauskas, G., Denisov, S. A., Lima, J. C., Parola, A. J., McClenaghan, N. D., and Pina, F. „Impact of Water on the Cis-Trans Photoisomerization of Hydroxychalcones“. *J. Phys. Chem. A* 117, pp. 4167–4173, 2013.

[72] Dictionary, American Heritage. *The American Heritage Dictionary of the English Language*. Houghton Mifflin Harcourt Publishing Company, 2011.

[73] Stevenson, A. *Oxford Dictionary of English*. OUP Oxford, 2010.

[74] House, Random. *Random House Webster's college dictionary*. (Firm). Random House, 1999.
[75] Bunge, M. „Is chemistry a branch of physics?“ *J. Gen. Philos. Sci.* 13, pp. 209–223, 1982.
[76] Turro, N. J. *Modern Molecular Photochemistry*. Sausalito, California: University Science Books, 1991. P. 628.
[77] Lehn, J. M. „Supramol. Chem.“ *Science* 260, pp. 1762–1763, 1993.
[78] Vögtle, F. and Alfter, F. *Supramolecular Chemistry: an introduction*. Wiley, 1991.
[79] Adamson, A. W. „Properties of excited states“. *J. Chem. Ed.* 60, p. 797, 1983.
[80] Kasha, M. „Characterization of electronic transitions in complex molecules“. *Discuss. Faraday Soc.* 9, pp. 14–19, 1950.
[81] Lakowicz, J. *Principles of Fluorescence Spectroscopy*. Principles of Fluorescence Spectroscopy. New York: Kluwer Academic, 1999.
[82] Valeur, B. *Molecular Fluorescence: Principles and Applications*. Wiley-VCH, 2002. P. 387.
[83] Daintith, J. *A Dictionary of Chemistry*. Oxford Dictionary of Chemistry. Oxford University Press, 2004. isbn: 9780198609186.
[84] Jean, Y., Volatron, F., and Burdett, J. K. *An Introduction to Molecular Orbitals*. Oxford University Press, 1993. isbn: 9780195069181.
[85] Balzani, V. *Electron Transfer in Chemistry: Catalysis of electron transfer, heterogenous systems, gas-phase systems*. Electron Transfer in Chemistry. Wiley-VCH, 2001. isbn: 9783527299126.
[86] Förster, T. „Zwischenmolekulare Energiewanderung und Fluoreszenz“. *Ann. Phys.-Berlin* 437, pp. 55–75, 1948.
[87] Stryer, L. „Fluorescence Energy Transfer as a Spectroscopic Ruler“. *Annu. Rev. Biochem.* 47, pp. 819–846, 1978.
[88] Wu, P. G. and Brand, L. „Resonance Energy Transfer: Methods and Applications“. *Anal. Biochem.* 218, pp. 1–13, 1994.
[89] Rae, M., Fedorov, A., and Berberan-Santos, M. N. „Fluorescence quenching with exponential distance dependence: Application to the external heavy-atom effect“. *J. Chem. Phys.* 119, 2003.
[90] Balzani, V. *Supramolecular Photochemistry*. NATO ASI Series: Mathematical and Physical Sciences. Springer, 1987. P. 486.
[91] Kavarnos, G. J. and Turro, N. J. „Photosensitization by reversible electron transfer: theories, experimental evidence, and examples“. *Chem. Rev.* 86, pp. 401–449, 1986.
[92] Marcus, R. A. „Electron transfer reactions in chemistry. Theory and experiment“. *Rev. Mod. Phys.* 65, pp. 599–610, 1993.
[93] Tkachenko, N. V. *Optical Spectroscopy: Methods and Instrumentations*. Elsevier Science, 2006. isbn: 9780080461724.
[94] Stokkum, I. H. van, Larsen, D. S., and Grondelle, R. van. „Global and target analysis of time-resolved spectra“. *BBA-Bioenergentics* 1657, pp. 82–104, 2004.
[95] Devos, O., Mouton, ., Sliwa, M., and Ruckebusch, C. „Baseline correction methods to deal with artifacts in femtosecond transient absorption spectroscopy“. *Anal. Chim. Acta* 705, pp. 64–71, 2011.
[96] Esposito, R., Altucci, C., and Velotta, R. „Analysis of Simulated Fluorescence Intensities Decays by a New Maximum Entropy Method Algorithm“. *J. Fluo.* 23, pp. 203–211, 2013.
[97] Steinbach, P. J., Chu, K., Frauenfelder, H., Johnson, J. B., Lamb, D. C., Nienhaus, G. U., Sauke, T. B., and Young, R. D. „Determination of rate distributions from kinetic experiments“. *Biophys. J.* 61, pp. 235–245, 1992.
[98] Cornwell, T. J. and Evans, K. F. „A simple maximum entropy deconvolution algorithm“. *Astron. Astrophys.* 143, pp. 77–83, 1985.
[99] Eaton, D. F. „Recommended methods for fluorescence decay analysis“. *Pure Appl. Chem.* 62, pp. 1631–1648, 1990.
[100] Hendler, R. W. and Shrager, R. I. „Deconvolutions based on singular value decomposition and the pseudoinverse: a guide for beginners“. *J. Biochem. Bioph. Meth.* 28, pp. 1–33, 1994.
[101] Cho, M. „Coherent two-dimensional optical spectroscopy“. *Chem. Rev.* 108, pp. 1331–1418, 2008.
[102] Wright, J. C. „Multiresonant coherent multidimensional spectroscopy“. *Annu. Rev. Phys. Chem.* 62, pp. 209–30, 2011.

[103] Ishida, H., Tobita, S., Hasegawa, Y., Katoh, R., and Nozaki, K. „Recent advances in instrumentation for absolute emission quantum yield measurements“. *Coord. Chem. Rev.* 254, pp. 2449–2458, 2010.

[104] Ito, T., Hiramatsu, M., Hosoda, M., and Tsuchiya, Y. „Picosecond time-resolved absorption spectrometer using a streak camera“. *Rev. Sci. Instrum.* 62, pp. 1415–1419, 1991.

[105] Knorr, F. J. and Harris, J. M. „Resolution of multicomponent fluorescence spectra by an emission wavelength-decay time data matrix“. *Anal. Chem.* 53, pp. 272–276, 1981.

[106] Thakker, K. M. „Compartmental models and their application, Keith Godfrey“. *Biopharm. Drug Dispos.* 6, pp. 357–358, 1985.

[107] Meyer, T. J. „Chemical approaches to artificial photosynthesis“. *Accounts Chem. Res.* 22, pp. 163–170, 1989.

[108] Alstrum-Acevedo, J. H., Brennaman, M. K., and Meyer, T. J. „Chemical Approaches to Artificial Photosynthesis. 2“. *Inorg. Chem.* 44, pp. 6802–6827, 2005.

[109] Terazono, Y., Kodis, G., Liddell, P. A., Garg, V., Moore, T. A., Moore, A. L., and Gust, D. „Multiantenna Artificial Photosynthetic Reaction Center Complex“. *J. Phys. Chem. B* 113, pp. 7147–7155, 2009.

[110] Lo, Shih-Chun and Burn, Paul L. „Development of Dendrimers: Macromolecules for Use in Organic Light-Emitting Diodes and Solar Cells“. *Chem. Rev.* 107, pp. 1097–1116, 2007.

[111] Frischmann, P. D., Mahata, K., and Wurthner, F. „Powering the future of molecular artificial photosynthesis with light-harvesting metallosupramolecular dye assemblies“. *Chem. Soc. Rev.* 42, pp. 1847–1870, 2013.

[112] Bäckström, H. L. J. and Sandros, K. „Transfer of Triplet State Energy in Fluid Solutions. I. Sensitized Phosphorescence and Its Application to the Determination of Triplet State Lifetimes.“ *Acta Chem. Scand.* 14, pp. 48–62, 1960.

[113] Sandros, K. and Bäckström, H. L. J. „Transfer of Triplet State Energy in Fluid Solutions. II. Further Studies of the Quenching of Biacetyl Phosphorescence in Solution.“ *Acta Chem. Scand.* 18, pp. 958–968, 1962.

[114] Sandros, K. „Transfer of Triplet State Energy in Fluid Solutions. III. Reversible Energy Transfer.“ *Acta Chem. Scand.* 18, pp. 2355–2374, 1964.

[115] Porter, G. B. „Reversible energy transfer“. *Theor. Chim. Acta* 24, pp. 265–270, 1972.

[116] Nordin, S. and Strong, R. L. „On the conditions necessary for diffusion-controlled energy transfer between triplet states“. *Chem. Phys. Lett.* 2, pp. 429–432, 1968.

[117] Balzani, V. and Carassiti, V. *Photochemistry of coordination compounds*. Academic Press, 1970.

[118] Wagenknecht, P. S. and Ford, P. C. „Metal centered ligand field excited states: Their roles in the design and performance of transition metal based photochemical molecular devices“. *Coord. Chem. Rev.* 255, pp. 591–616, 2011.

[119] Fleischauer, P. D. and Fleischauer, P. „Photoluminescence of transition metal coordination compounds“. *Chem. Rev.* 70, pp. 199–230, 1970.

[120] Juris, A., Balzani, V., Barigelletti, F., Campagna, S., Belser, P., and Zelewsky, A. von. „Ru(II) polypyridine complexes: photophysics, photochemistry, eletrochemistry, and chemiluminescence“. *Coord. Chem. Rev.* 84, pp. 85–277, 1988.

[121] Balzani, V., Juris, A., Venturi, M., Campagna, S., and Serroni, S. „Luminescent and Redox-Active Polynuclear Transition Metal Complexes“. *Chem. Rev.* 96, pp. 759–834, 1996.

[122] Crosby, G. A. „Spectroscopic investigations of excited states of transition-metal complexes“. *Accounts Chem. Res.* 8, pp. 231–238, 1975.

[123] Crosby, G. A., Watts, R. J., and Carstens, D. H. W. „Inversion of Excited States of Transition-Metal Complexes“. *Science* 170, pp. 1195–1196, 1970.

[124] McClenaghan, N. D., Barigelletti, F., Maubert, B., and Campagna, S. „Towards ruthenium(ii) polypyridine complexes with prolonged and predetermined excited state lifetimes“. *Chem. Commun.* Pp. 602–603, 2002.

[125] Österman, T., Abrahamsson, M., Becker, H.-C., Hammarström, L., and Persson, P. „Influence of Triplet State Multidimensionality on Excited State Lifetimes of Bis-tridentate Ru(II) Complexes: A Computational Study“. *J. Phys. Chem. A* 116, pp. 1041–1050, 2011.

[126] Jäger, M., Eriksson, L., Bergquist, J., and Johansson, O. „Synthesis and Characterization of 2,6-Di(quinolin-8-yl)pyridines. New Ligands for Bistridentate Ru(II) Complexes with Microsecond Luminescent Lifetimes“. *J. Org. Chem.* 72, pp. 10227–10230, 2007.

[127] Chelucci, G. „Hydrodehalogenation of halogenated pyridines and quinolines by sodium borohydride/N,N,N',N'-tetramethylethylenediamine under palladium catalysis“. *Tetrahedron Lett.* 51, pp. 1562–1565, 2010.

[128] Jäger, M., Kumar, R. J., Görls, H., Bergquist, J., and Johansson, O. „Facile Synthesis of Bistridentate Ru(II) Complexes Based on 2,6-Di(quinolin-8-yl)pyridyl Ligands: Sensitizers with Microsecond ^{3}MLCT Excited State Lifetimes“. *Inorg. Chem.* 48, pp. 3228–3238, 2009.

[129] Wilson, G. J., Launikonis, A., Sasse, W. H. F., and Mau, A. W. H. „Chromophore-Specific Quenching of Ruthenium Trisbipyridine-Arene Bichromophores by Methyl Viologen“. *J. Phys. Chem. A* 102, pp. 5150–5156, 1998.

[130] Scarpantonio, L., Tron, A., Destribats, C., Godard, P., and McClenaghan, N. D. „Concatenation of reversible electronic energy transfer and photoinduced electron transfer to control a molecular piston“. *Chem. Commun.* 48, pp. 3981–3983, 2012.

[131] McCusker, J. K. „Femtosecond Absorption Spectroscopy of Transition Metal Charge-Transfer Complexes“. *Accounts Chem. Res.* 36, pp. 876–887, 2003.

[132] Peter, L. and Vaubel, G. „Phosphorescence of pure crystalline pyrene“. *Chem. Phys. Lett.* 21, pp. 158–160, 1973.

[133] Tang, K.-C., Liu, K. L., and Chen, I. C. „Rapid intersystem crossing in highly phosphorescent iridium complexes“. *Chem. Phys. Lett.* 386, pp. 437–441, 2004.

[134] Hedley, G. J., Ruseckas, A., and Samuel, I. D. W. „Ultrafast Intersystem Crossing in a Red Phosphorescent Iridium Complex“. *J. Phys. Chem. A* 113, pp. 2–4, 2008.

[135] Marín-Suárez, M., Curchod, B. F. E., Tavernelli, I., Rothlisberger, U., Scopelliti, R., Jung, I., Di Censo, Davide, Grätzel, M., Fernández-Sánchez, J. F., Fernández-Gutiérrez, Al., Nazeeruddin, Md. K., and Baranoff, E. „Nanocomposites Containing Neutral Blue Emitting Cyclometalated Iridium(III) Emitters for Oxygen Sensing“. *Chem. Mat.* 24, pp. 2330–2338, 2012.

[136] Hecht, S. and Huc, I. *Foldamers: Structure, Properties and Applications*. Wiley, 2007. P. 434.

[137] Schmitt, J.-L., Stadler, A.-M., Kyritsakas, N., and Lehn, J.-M. „Helicity-Encoded Molecular Strands: Efficient Access by the Hydrazone Route and Structural Features“. *Helv. Chim. Acta* 86, pp. 1598–1624, 2003.

[138] Bao, C., Gan, Q., Kauffmann, B., Jiang, H., and Huc, I. „A Self-Assembled Foldamer Capsule: Combining Single and Double Helical Segments in One Aromatic Amide Sequence“. *Chem. Eur. J.* 15, pp. 11530–11536, 2009.

[139] Gan, Q., Ferrand, Y., Bao, C., Kauffmann, B., Grélard, A., Jiang, H., and Huc, I. „Helix-Rod Host-Guest Complexes with Shuttling Rates Much Faster than Disassembly“. *Science* 331, pp. 1172–1175, 2011.

[140] Gan, Q. „Foldaxanes: Pseudorotaxanes Hélicoïdaux Auto-Assemblés Structures et Mouvements Moléculaires“. PhD thesis. Université Bordeaux 1, 2012.

[141] Caspar, J. V. and Meyer, T. J. „Photochemistry of MLCT excited states. Effect of nonchromophoric ligand variations on photophysical properties in the series cis-$Ru(bpy)_2L_2^{2+}$“. *Inorg. Chem.* 22, pp. 2444–2453, 1983.

[142] Bolton, James R. „Solar photoproduction of hydrogen: A review“. *Sol. Energy* 57, pp. 37–50, 1996.

[143] Gärtner, F., Sundararaju, B., Surkus, A.-E., Boddien, A., Loges, B., Junge, H., Dixneuf, P. H., and Beller, M. „Light-Driven Hydrogen Generation: Efficient Iron-Based Water Reduction Catalysts“. *Angew. Chem. Int. Ed.* 48, pp. 9962–9965, 2009.

[144] Chen, X., Shen, S., Guo, L., and Mao, S. S. „Semiconductor-based Photocatalytic Hydrogen Generation“. *Chem. Rev.* 110, pp. 6503–6570, 2010.

[145] Chong, M. N., Jin, B., Chow, C. W. K., and Saint, C. „Recent developments in photocatalytic water treatment technology: a review.“ *Water Res.* 44, pp. 2997–3027, 2010.

[146] Veldman, D., Chopin, S. M. A., Meskers, S. C. J., Groeneveld, M. M., Williams, R. M., and Janssen, R. A. J. „Triplet Formation Involving a Polar Transition State in a Well-Defined Intramolecular Perylenediimide Dimeric Aggregate“. *J. Phys. Chem. A* 112, pp. 5846–5857, 2008.

[147] Hippius, C., Stokkum, I. H. M. van, Zangrando, E., Williams, R. M., and Würthner, F. „Excited State Interactions in Calix[4]arene-Perylene Bisimide Dye Conjugates: Global and Target Analysis of Supramolecular Building Blocks“. *J. Phys. Chem. C* 111, pp. 13988–13996, 2007.

[148] Nicolaescu, A. R., Wiest, O., and Kamat, P. V. „Radical-Induced Oxidative Transformation of Quinoline“. *J. Phys. Chem A.* 107, pp. 427–433, 2003.

[149] Ahrens, M. J., Kelley, R. F., Dance, Z. E. X., and Wasielewski, M. R. „Photoinduced charge separation in self-assembled cofacial pentamers of zinc-5,10,15,20-tetrakis(perylenediimide)porphyrin“. *Phys. Chem. Chem. Phys.* 9, pp. 1469–1478, 2007.

[150] Festa, R. A. and Thiele, D. J. „Copper: An essential metal in biology“. *Curr. Biol.* 21, R877–R883, 2011.

[151] Sénèque, O., Bourlés, E., Lebrun, V., Bonnet, E., Dumy, P., and Latour, J. M. „Cyclic peptides bearing a side-chain tail: a tool to model the structure and reactivity of protein zinc sites.“ *Angew. Chem. Int. Ed.* 47, pp. 6888–6891, 2008.

[152] Sénèque, O., Bonnet, E., Joumas, F. L., and Latour, J.-M. „Cooperative Metal Binding and Helical Folding in Model Peptides of Treble-Clef Zinc Fingers“. *Chem. Eur. J.* 15, pp. 4798–4810, 2009.

[153] Jacques, A., Mettra, B., Lebrun, V., Latour, J.-M., and Sénèque, O. „On the Design of Zinc-Finger Models with Cyclic Peptides Bearing a Linear Tail“. *Chem. Eur. J.* 19, pp. 3921–3931, 2013.

[154] Chen, R. F. „Measurements of absolute values in biochemical fluorescence spectroscopy“. *J. Res. Nat. Bur. Stand.* 76A, pp. 593–606, 1972.

[155] Chen, Y., Gai, F., and Petrich, J. W. „Single-Exponential Fluorescence Decay of the Nonnatural Amino Acid 7-Azatryptophan and the Nonexponential Fluorescence Decay of Tryptophan in Water“. *J. Phys. Chem.* 98, pp. 2203–2209, 1994.

[156] Lotte, K., Plessow, R., and Brockhinke, A. „Static and time-resolved fluorescence investigations of tryptophan analogues - a solvent study“. *Photochem. Photobiol. Sci.* 3, pp. 348–359, 2004.

[157] Albani, J. R. „Fluorescence Lifetimes of Tryptophan: Structural Origin and Relation with $S_0 \rightarrow {}^1L_b$ and $S_0 \rightarrow {}^1L_a$ Transitions“. *J. Fluo.* 19, pp. 1061–1071, 2009.

[158] Albani, J. R. „Origin of Tryptophan Fluorescence Lifetimes Part 1. Fluorescence Lifetimes Origin of Tryptophan Free in Solution“. *J. Fluo.* Pp. 1–12, 2013.

[159] Edelhoch, H. „Spectroscopic Determination of Tryptophan and Tyrosine in Proteins“. *Biochem.* 6, pp. 1948–1954, 1967.

[160] Carnall, W. T., Goodman, G. L., Rajnak, K., and Rana, R. S. „A systematic analysis of the spectra of the lanthanides doped into single crystal LaF_3“. *J. Chem. Phys.* 90, pp. 3443–3457, 1989.

[161] Hemmilä, I. and Laitala, V. „Progress in Lanthanides as Luminescent Probes“. *J. Fluo.* 15, pp. 529–542, 2005.

[162] Hynes, J., O'Riordan, T. C., Zhdanov, A. V., Uray, G., Will, Y., and Papkovsky, D. B. „In vitro analysis of cell metabolism using a long-decay pH-sensitive lanthanide probe and extracellular acidification assay.“ *Anal. Biochem.* 390, pp. 21–8, 2009.

[163] Zherdeva, V. V. and Savitsky, A. P. „Using lanthanide-based resonance energy transfer for *in vitro* and *in vivo* studies of biological processes“. *Biochem. (Mosc.)* 77, pp. 1553–1574, 2012.

[164] Anderson, J. H. „The copper-catalysed oxidation of hydroxylamine“. *Analyst* 89, pp. 357–362, 1964.

[165] Yorita, H., Otomo, K., Hiramatsu, H., Toyama, A., Miura, T., and Takeuchi, H. „Evidence for the Cation$-\pi$ Interaction between Cu^{2+} and Tryptophan“. *J. Am. Chem. Soc.* 130, pp. 15266–15267, 2008.

[166] Franz, K. J. „Copper shares a piece of the π“. *Nat. Chem. Biol.* 4, pp. 85–86, 2008.

[167] Brouwer, Al. „Standards for photoluminescence quantum yield measurements in solution (IUPAC Technical Report)“. *Pure Appl. Chem.* 83, pp. 2213–2228, 2011.

[168] Hänninen, P. and Härmä, H. *Lanthanide Luminescence: Photophysical, Analytical and Biological Aspects*. Springer Series on Fluorescence. Springer, 2011. isbn: 9783642210235.

[169] Chen, D., Yu, Y., Wang, Y. H., Huang, P., and Weng, F. „Cooperative Energy Transfer Up-Conversion and Quantum Cutting Down-Conversion in Yb3+:TbF3 Nanocrystals Embedded Glass Ceramics“. *J. Phys. Chem. C* 113, pp. 6406–6410, 2009.

[170] Masuhara, H., Shioyama, H., Saito, T., Hamada, K., Yasoshima, S., and Mataga, N. „Fluorescence quenching mechanism of aromatic hydrocarbons by closed-shell heavy metal ions in aqueous and organic solutions“. *J. Phys. Chem.* 88, pp. 5868–5873, 1984.

[171] Latva, Martti, Takalo, Harri, Mukkala, Veli-Matti, Matachescu, Cristina, Rodríguez-Ubis, Juan C., and Kankare, Jouko. „Correlation between the lowest triplet state energy level of the ligand and lanthanide(III) luminescence quantum yield“. *J. Lumin.* 75, pp. 149–169, 1997.

[172] Haas, Y. and Stein, G. „Pathways of radiative and radiationless transitions in europium(III) solutions. Role of solvents and anions“. *J. Phys. Chem.* 75, 1971.

[173] Berry, M. T., May, P. S., and Xu, H. „Temperature Dependence of the Eu^{3+} $^5D_0$ Lifetime in Europium Tris(2,2,6,6-tetramethyl-3,5-heptanedionato)“. *J. Phys. Chem.* 100, pp. 9216–9222, 1996.

[174] Solarz, P. and Ryba-Romanowski, W. „Effect of temperature and activator concentration on relaxation of excited states of Eu^{3+} in $K_5Li_2La_1{-}xEu_xF_{10}$ crystals“. *J. Phys. Chem. Sol.* 64, pp. 1289–1296, 2003.

[175] Escobedo, J. O., Rusin, O., Lim, S., and Strongin, R. M. „NIR dyes for bioimaging applications.“ *Curr. Opin. Chem. Biol.* 14, pp. 64–70, 2010.

[176] Berlman, I. B. *Handbook of Florescence Spectra of Aromatic Molecules*. Elsevier, 1971. isbn: 9780120926565.

[177] Winnik, F. M. „Photophysics of preassociated pyrenes in aqueous polymer solutions and in other organized media“. *Chem. Rev.* 93, pp. 587–614, 1993.

[178] Porrès, L., Holland, A., Paalsson, L.-O., Monkman, A. P., Kemp, C., and Beeby, A. „Absolute measurements of photoluminescence quantum yields of solutions using an integrating sphere“. *J. Fluo.* 16, pp. 267–72, 2006. doi: 10.1007/s10895-005-0054-8.

[179] Gardner, D. G., Gardner, J. C., Laush, G., and Meinke, W. W. „Method for the Analysis of Multicomponent Exponential Decay Curves“. *J. Chem. Phys.* 31, 1959.

[180] Siemiarczuk, A., Wagner, B. D., and Ware, W. R. „Comparison of the maximum entropy and exponential series methods for the recovery of distributions of lifetimes from fluorescence lifetime data“. *J. Phys. Chem.* 94, pp. 1661–1666, 1990.

[181] Berberan-Santos, M. N., Bodunov, E. N., and Valeur, B. „Mathematical functions for the analysis of luminescence decays with underlying distributions 1. Kohlrausch decay function (stretched exponential)“. *Chem. Phys.* 315, pp. 171–182, 2005.

[182] Metivier, R., Leray, I., Lefevre, J.-P., Roy-Auberger, M., Zanier-Szydlowski, N., and Valeur, B. „Characterization of alumina surfaces by fluorescence spectroscopy Part 2. Photophysics of a bound pyrene derivative as a probe of the spatial distribution of reactive hydroxyl groups“. *Phys. Chem. Chem. Phys.* 5, pp. 758–766, 2003.

[183] Wong, A. L., Harris, J. M., and Marshall, D. B. „Measurements of energy dispersion at liquid–solid interfaces: Fluorescence quenching of pyrene bound to fumed silica“. *Can. J. Phys.* 68, pp. 1027–1034, 1990.

[184] Gillies, R. J., Raghunand, N., Garcia-Martin, M. L., and Gatenby, R. A. *pH imaging. A review of pH measurement methods and applications in cancers.* 2004.

[185] Elson, D., Requejo-Isidro, J., Munro, I., Reavell, F., Siegel, J., Suhling, K., Tadrous, P., Benninger, R., Lanigan, P., McGinty, J., Talbot, C., Treanor, B., Webb, S., Sandison, A., Wallace, A., Davis, D., Lever, J., Neil, M., Phillips, D., Stamp, G., and French, P. „Time-domain fluorescence lifetime imaging applied to biological tissue“. *Photochem. Photobiol. Sci.* 3, pp. 795–801, 2004.

[186] Kuimova, M. K., Yahioglu, G., Levitt, J. A., and Suhling, K. „Molecular Rotor Measures Viscosity of Live Cells via Fluorescence Lifetime Imaging“. *J. Am. Chem. Soc.* 130, pp. 6672–6673, 2008.

[187] Berezin, M. Y. and Achilefu, S. „Fluorescence Lifetime Measurements and Biological Imaging“. *Chem. Rev.* 110, pp. 2641–2684, 2010.

[188] Lopez-Duarte, I., Vu, T. T., Izquierdo, M. A., Bull, J. A, and Kuimova, M. K. „A molecular rotor for measuring viscosity in plasma membranes of live cells“. *Chem. Commun.* 50, pp. 5282–5284, 2014.

[189] Murtagh, J., Frimannsson, D. O., and O'Shea, D. F. „Azide Conjugatable and pH Responsive Near-Infrared Fluorescent Imaging Probes“. *Org. Lett.* 11, pp. 5386–5389, 2009.

[190] Grossi, M., Palma, A., McDonnell, S. O., Hall, M. J., Rai, D. K., Muldoon, J., and O'Shea, D. F. „Mechanistic Insight into the Formation of Tetraarylazadipyrromethenes". *J. Org. Chem.* 77, pp. 9304–9312, 2012.

[191] Ballardini, R., Balzani, V., Credi, A., Gandolfi, M. T., and Venturi, M. „Artificial Molecular-Level Machines: Which Energy To Make Them Work?" *Accounts Chem. Res.* 34, pp. 445–455, 2001.

[192] Lednev, I. K., Ye, T.-Q., Hester, R. E., and Moore, J. N. „Femtosecond Time-Resolved UV−Visible Absorption Spectroscopy of trans-Azobenzene in Solution". *J. Phys. Chem.* 100, pp. 13338–13341, 1996.

[193] Biswas, N. and Umapathy, S. „Early time dynamics of trans-azobenzene isomerization in solution from resonance Raman intensity analysis". *J. Phys. Chem.* 107, 1997.

[194] Nägele, T., Hoche, R., Zinth, W., and Wachtveitl, J. „Femtosecond photoisomerization of cis-azobenzene". *Chem. Phys. Lett.* 272, pp. 489–495, 1997.

[195] Lednev, I. K., Ye, T. Q., Matousek, P., Towrie, M., Foggi, P., Neuwahl, F. V. R., Umapathy, S., Hester, R. E., and Moore, J. N. „Femtosecond time-resolved UV-visible absorption spectroscopy of trans-azobenzene: dependence on excitation wavelength". *Chem. Phys. Lett.* 290, pp. 68–74, 1998.

[196] Cattaneo, P. and Persico, M. „An abinitio study of the photochemistry of azobenzene". *Phys. Chem. Chem. Phys.* 1, pp. 4739–4743, 1999.

[197] Fujino, T., Arzhantsev, S. Yu., and Tahara, T. „Femtosecond/Picosecond Time-Resolved Spectroscopy of trans- Azobenzene: Isomerization Mechanism Following $S_2(\pi\pi^*) \leftarrow S_0$ Photoexcitation". *B. Chem. Soc. Jpn.* 75, pp. 1031–1040, 2002.

[198] Schultz, T., Quenneville, J., Levine, B., Toniolo, A., Martínez, T. J., Lochbrunner, S., Schmitt, M., Shaffer, J. P., Zgierski, M. Z., and Stolow, A. „Mechanism and Dynamics of Azobenzene Photoisomerization". *J. Am. Chem. Soc.* 125, pp. 8098–8099, 2003.

[199] Satzger, H., Root, C., and Braun, M. „Excited-State Dynamics of trans- and cis-Azobenzene after UV Excitation in the π-π* Band". *J. Phys. Chem. A* 108, pp. 6265–6271, 2004.

[200] Monti, S., Orlandi, G., and Palmieri, P. „Features of the photochemically active state surfaces of azobenzene". *Chem. Phys.* 71, pp. 87–99, 1982.

[201] Valev, Dimitar. „Estimations of total mass and energy of the universe". P. 10, 2010. arXiv: 1004.1035.

[202] Yuan, Ya-Xiang. „Trust Region Algorithms For Constrained Optimization". *Math. Prog* 47, pp. 53–63, 1990.

[203] Lourakis, M. L. A. and Argyros, A. A. „Is Levenberg-Marquardt the most efficient optimization algorithm for implementing bundle adjustment?" In: *Computer Vision, 2005. ICCV 2005. Tenth IEEE International Conference on*. Vol. 2. 2005. 1526–1531 Vol. 2.

Abbreviations

BAPTA 1,2-bis(o-aminophenoxy)ethane-N,N,N',N'-tetraacetic acid

BODIPY Boron-dipyrromethene

bpy 2,2'–bipyridine

CD Circular Dichroism

CMC Critical Micelle Concentration

CSS Charge Separated State

DNA Deoxyribonucleic Acid

DOPC 1,2-Dioleoyl-sn-Glycero-3-Phosphocholine

DOTA 1,4,7,10-tetraazacyclododecane-1,4,7,10-tetraacetic acid

EA Electron Affinity

EET Electronic Energy Transfer

FEF Fluorescence Enhancement Factor

FRET Förster Resonance Energy Transfer

GS Ground State

GSB Ground State Bleaching

HEPES 4-(2-hydroxyethyl)-1-piperazineethanesulfonic acid

HOMO Highest Occupied Molecular Orbital

IP Ionization Potential

IRF Instrument Response Function

ISC Intersystem Crossing

LC Ligand Centered

LCAO Linear Combinations of Atomic Orbitals

LEES Lowest Energy Excited State

LMCT Ligand-to-Metal Charge Transfer

LUMO Lowest Unoccupied Molecular Orbital

MC Metal Centered

MLCT Metal-to-Ligand Charge Transfer

MO Molecular Orbital

MSC Multi-Channel Scaling

NIR Near Infra-Red

NMR Nuclear Magnetic Resonance

NP Nanoparticle

O. D. Optical Denisity

OPV Oligo(p-phenylene vinylene)

PB Perylene Bisimide

PBS Phosphate Buffered Saline

PCT Photoinduced Charge Transfer

PEG Polyethylene Glycol

PET Photoinduced Electron Transfer

PIR Proche Infrarouge

QY Quantum Yield

REET Reversible Electronic Energy Transfer

RET Resonance Energy Transfer

RT Room Temperature

TCSPC Time-Correlated Single Photon Counting

TEE Transfert d'Énergie Électronique

TEER Transfert d'Énergie Électronique Réversible

TEP Transfert d'Électron Photoinduit

terpy 2,2';6',2"-terpyridine

TRABS Transient Absorption Spectroscopy

UV Ultraviolet